

**Synthetic Inorganic Chemistry:  
Novel Metallocenes and Inorganic-Fullerenes**

by

Gerald Patrick Clancy

A thesis submitted in part fulfilment of the requirements for  
the degree of Doctor of Philosophy  
at the University of Oxford.

Balliol College

Oxford

June 2000



The work described in this thesis was carried out in the Inorganic Chemistry Laboratory, South Parks Road, Oxford, from September 1997 to May 2000 under the supervision of Professor Malcolm L.H. Green, FRS. All the work is my own unless stated to the contrary, and has not previously been submitted for any degree at this, or any other, university.

**Abstract:**

**Synthetic Inorganic Chemistry:  
Novel Metallocenes and Inorganic-Fullerenes**

Gerald Patrick Clancy  
Balliol College

Trinity Term 2000  
Submitted for D.Phil.

This thesis is divided into two parts. The first part concerns the synthesis and characterisation of substituted metallocene complexes of the transition and main group metals. The second part describes the preparation and characterisation of inorganic fullerene (IF)-related materials.

**Chapter 1** reviews the chemistry of dialkyl- and diaryl-phosphino substituted cyclopentadienyl complexes of the transition metals.

**Chapter 2** describes the synthesis and characterisation of the new ligands  $[M(C_5Me_4)CH_2PMe_2]$  ( $M = H, Li, Na$  and  $K$ ) *via* the precursors  $[(HC_5Me_4)CH_2PHMe_2][X]$  ( $X = Cl$  and  $PF_6$ ). The synthesis, characterisation and chemical reactivity of the compounds  $[Zr\{(\eta-C_5Me_4)CH_2PMe_2\}_2Cl_2]$  and  $[Mn\{(\eta-C_5Me_4)CH_2PMe_2\}_2]$ , is reported together with supporting evidence for the synthesis of the bimetallic complex  $[Zr\{(\eta-C_5Me_4)CH_2PMe_2\}_2Cl_2PtI_2]$  and the complex  $[Mn\{(\eta-C_5Me_4)CH_2PMe_2B(C_6F_5)_3\}_2]$ .

**Chapter 3** provides a brief introduction into the field of main group metallocenes and describes the synthesis and characterisation of the new main group metallocenes  $[M\{(\eta-C_5H_4)CMe_2PMe_2\}_2]$  ( $M = Pb$  and  $Sn$ ). The  $B(C_6F_5)_3$  adduct  $[Pb\{(\eta-C_5H_4)CMe_2PMe_2(B(C_6F_5)_3)_2\}_2]$  has also been synthesised. The main group – transition metal bimetallic complex  $[Pb\{(\eta-C_5H_4)CMe_2PMe_2\}_2PtI_2]$  in which the substituted-plumbocene acts as a bidentate ligand, has been characterised by mass spectrometry and  $^{31}P\{^1H\}$  NMR spectroscopy.

**Chapter 4** provides an introduction into the field of IF-related materials and an overview of the analytical techniques used in their characterisation

**Chapter 5** describes the preparation and characterisation of IF-MoS<sub>2</sub> and IF-(Nb,W)S<sub>2</sub> materials from MoC and the binary oxides Nb<sub>8</sub>W<sub>9</sub>O<sub>47</sub> and Nb<sub>4</sub>W<sub>13</sub>O<sub>47</sub> respectively. A powder X-ray diffraction study of the conversion of WC to WO<sub>3-x</sub> and the subsequent sulfidisation by H<sub>2</sub>S to form novel IF-WS<sub>2</sub> morphologies is also described.

**Chapter 6** describes the preparation of amorphous Group 5 metal (V, Nb and Ta) oxides using the metal vapour synthesis technique. These amorphous precursors have been annealed in a reducing atmosphere to form the oxide phases  $\alpha$ -V<sub>2</sub>O<sub>3</sub>, NbO<sub>2</sub> and TT-Ta<sub>2</sub>O<sub>5</sub> which have been identified by powder X-ray diffraction. Upon reaction with H<sub>2</sub>S, the crystalline oxides afford layered sulfides of the form MS<sub>2</sub> (M = V, Nb and Ta), some of which exhibit behaviour typical of IF-like materials and have been characterised by HRTEM, powder X-ray diffraction and EDX analysis.

**Chapter 7** outlines the experimental details for the synthesis, characterisation, reactions and compounds described in the preceding chapters.

**Chapter 8** presents the characterising data for the new compounds described in chapters 2 and 3.

**Appendix A** contains details of the crystallographic data for the structurally characterised compound [Mn{(η-C<sub>5</sub>Me<sub>4</sub>)CH<sub>2</sub>PMe<sub>2</sub>}<sub>2</sub>].



To my family

## Acknowledgements

I would like to commence by thanking my supervisor Professor Malcolm L. H. Green, F.R.S, for giving me the opportunity to work in his group. For his abilities to enthuse and inspire, for his inexhaustible reserve of ideas and for his financial support in my final year, I am most grateful.

There are many in this group who have helped me over the last few years in some way at some time. Of these I would particularly like to thank Dr. Jeremy Sloan, the Wirral's most famous electron microscopist, for his sub-supervision of the IF-work and for the benefit of his expertise in HRTEM as well as his artistry in the graphics department. Dr. Leigh Rees found time to solve the crystal structure for compound **11** while Dr. Nick Rees was of great assistance in the NMR department, particularly with respect to Sn, Pb and HMQC experiments. Your efforts are greatly appreciated. Dr. Cliff Williams tested his multi-tasking abilities to train me up in a variety of unrelated techniques including NMR spectroscopy, glovebox maintenance and powder X-ray diffraction. For all this and for helping me settle in during my embryonic days in Oxford, I am most grateful. A whole host of doctoral students and post-docs have passed through the revolving doors including Dr. Richard Douthwaite, Dr. Martin Humphries and Dr. Linda Doerrer. Your advice and contributions to matters both chemical and comical has not been forgotten.

I was not alone in making my Third Floor™ debut in October 1996. I soon became good friends with my 'chemical brothers' and I would like to thank the honourable Dr. Peter Silcock and Dr. Ronan Bellabarba for their friendship and boyish banter. I wish them both well as they embark on their academic careers. Also cutting their synthetic teeth at that time were Stephen Conway and Neil Maxted. As the tenants of T8 (Steve being the sitting tenant) our fine collection of contemporary chemical glassware was jealously guarded and having shared a house with him for the last year, I can testify that his cooking is *almost* as good as his chemistry. I thank you both and am privileged to be able to count you among my friends.

Life in the asylum that is the Third Floor™ was rarely uneventful. More recent additions to the group shook things up a little when they were in danger of dropping to an acceptable level. The arrivals of Philip Arnold, Ino Vei, Sofia Pascu and Neale Jones accompanied by those of Chi-Tien Chen and the Mountford Boys ensured that the colourful climate would continue. I thank you all for your help and friendship throughout my time here. In particular I'd like to give a big shout out to Phil for accompanying me on tiring outings to the Pulse and to both Phil and Ino for many mugs of tea and several spontaneous suppers over the last wee while.

There is within the ICL an undercurrent of activity without which the department could not operate. I would like to thank all those at the glassblowers, in the workshop, reception, stores and electronics, particularly Nenad Vranjes, Dave Paul and Steve Brogden, for their help and conviviality. Were proof-reading not the thankless task that it is, my appreciation would also extend to Ino, Jeremy, Malcolm, Pete and Dr. Karl Coleman. My further thanks go to Pete for the generous loan of his laptop (PC) for the duration of the writing of this thesis.

Away from the ICL I am grateful for the distractions afforded by the cosmopolitan Balliol MCR FC and Balliol AFC. Off the football field, I must thank the boys and girls of OUCCC and OUAC for the opportunity to run through knee-deep mud and frozen streams in the depth of winter and for the eventful journeys across the UK under the guise of a wel

organised university sports club. I also take away many fond memories from the cheerful souls at the Chaplaincy. From the ridiculously one-sided 'Varsity Matches' to the many ceilidhs, dinners and countless other occasions where we met and inflicted fun and friendship on one another. I am fortunate indeed to have been part of it all. You all know who you are, thank you.

I have many happy memories of visits to warm places while I've been here in Oxford. For the eventful sabbaticals to the south-west of France, I thank all those from Oxford and Cambridge who shared the experiences. For their friendship, as well as a much needed change of scene just before the final push I am grateful to Louis and Michael d'Arcy. The opportunity to explore a sun-drenched Mediterranean island in early April was much appreciated. *Muchos gracias*. The 'Lisbon Experience' in August 1999 was arguably the most enjoyable chemistry experiment I have undertaken. The Green Group delegates at the conference and principally Dr. Pedro Gomes and Dr. Ana Martins, our hosts for the duration, are to be thanked for making those 12 days most memorable. *Obrigado*.

I am grateful to my friends back home in London, particularly James, Chris, Leo and Tom, for keeping me informed as to recent developments and making the odd reconnaissance trip up here. I am grateful also to my fellow Sussex and Simon Fraser University alumni, particularly Peter Hartley and Jon Boyle. Your efforts in maintaining communication have not been in vain.

Finally, I thank my family for everything they have done to get me this far. Without their support, love and encouragement I would not be where I am. I also appreciate their immense capacity to avoid discussions about laboratory life during my time here in the Green Group.

Meanwhile, somewhere in the state of Colorado, armed to the teeth  
with thousands of flowers,  
two boys entered the front door of their own high school  
and for almost four hours  
gave floral tributes to fellow students and members of staff,  
beginning with red roses  
strewn amongst unsuspecting pupils during their lunch hour,  
followed by posies  
of peace lilies and wild orchids. Most thought the whole show  
was one elaborate hoax  
using silk replicas instead of the real thing, plastic imitations,  
exquisite practical jokes,  
but the flowers were no more fake than you or I,  
and were handed out  
as compliments returned, favours repaid, in good faith,  
straight from the heart.

*Simon Armitage, Killing Time (1999)*

## Contents

Abstract.....	iii
Acknowledgements.....	vi
Contents.....	ix
List of Abbreviations .....	xvii

<b>Chapter 1 : Introduction .....</b>	
1.0 Scope of the Thesis.....	1
1.1 Metallocenes .....	2
1.2 Heteroatomic-Substituted Cyclopentadienyl Ligands .....	2
1.3 Synthesis of Phosphino-Substituted Cyclopentadienyl Complexes .....	3
1.4 Applications of Phosphino-Substituted Cyclopentadienyl Complexes ...	3
1.4.1 Phosphino-Substituted Cyclopentadienyl Ligands in Monometallic Complexes.....	4
1.4.2 Phosphino-Substituted Cyclopentadienyl Ligands in Heterobimetallic Complexes .....	6
1.4.3 Phosphino-Substituted Cyclopentadienyl Ligands in Homobimetallic Complexes .....	14
1.5 Summary.....	17
1.6 References.....	18

<b>Chapter 2 : Dimethylphosphino-substituted Cyclopentadienyl Complexes .....</b>	
2.0 Introduction to Chapter 2.....	23
2.1 Preparation of the Ligand Precursors $[\text{HC}_5\text{Me}_4\text{CH}_2\text{PMe}_2\text{H}][\text{X}]$ (X = Cl, PF <sub>6</sub> ) .....	23
2.1.1 Preparation of $[\text{HC}_5\text{Me}_4\text{CH}_2\text{PMe}_2\text{H}][\text{Cl}]$ (1) .....	23
2.1.2 Characterisation of $[\text{HC}_5\text{Me}_4\text{CH}_2\text{PMe}_2\text{H}][\text{Cl}]$ (1).....	23
2.1.3 Preparation of $[\text{HC}_5\text{Me}_4\text{CH}_2\text{PMe}_2\text{H}][\text{PF}_6]$ (2) .....	26
2.1.4 Characterisation of $[\text{HC}_5\text{Me}_4\text{CH}_2\text{PMe}_2\text{H}][\text{PF}_6]$ (2).....	27
2.2 Preparation of the Ligands $[\text{M}(\text{C}_5\text{Me}_4)\text{CH}_2\text{PMe}_2]$ (M = H, K, Na, Li).....	29
2.2.1 Preparation of $[\text{HC}_5\text{Me}_4\text{CH}_2\text{PMe}_2]$ (3).....	29
2.2.2 Characterisation of $[\text{HC}_5\text{Me}_4\text{CH}_2\text{PMe}_2]$ (3) .....	29
2.2.3 Preparation of $[\text{M}(\text{C}_5\text{Me}_4)\text{CH}_2\text{PMe}_2]$ [M = K (4), Na (5) and Li (6)].....	31

2.2.4 Preparation of $[\text{K}(\text{C}_5\text{Me}_4)\text{CH}_2\text{PMe}_2]$ ( <b>4</b> ) .....	31
2.2.5 Characterisation of $[\text{K}(\text{C}_5\text{Me}_4)\text{CH}_2\text{PMe}_2]$ ( <b>4</b> ) .....	32
2.2.6 Preparation of $[\text{Na}(\text{C}_5\text{Me}_4)\text{CH}_2\text{PMe}_2]$ ( <b>5</b> ) .....	33
2.2.7 Characterisation of $[\text{Na}(\text{C}_5\text{Me}_4)\text{CH}_2\text{PMe}_2]$ ( <b>5</b> ).....	33
2.2.8 Preparation of $[\text{Li}(\text{C}_5\text{Me}_4)\text{CH}_2\text{PMe}_2]$ ( <b>6</b> ) .....	34
2.2.9 Characterisation of $[\text{Li}(\text{C}_5\text{Me}_4)\text{CH}_2\text{PMe}_2]$ ( <b>6</b> ).....	35
2.3 Attempted Preparation of $[\{\text{M}(\eta\text{-C}_5\text{Me}_4)\text{CH}_2\text{PMe}_2\}_2\text{Cl}_2]$ ( $\text{M} = \text{Ti, Zr, Hf}$ ).....	35
2.3.1 Preparation of $[\{\text{Zr}(\eta\text{-C}_5\text{Me}_4)\text{CH}_2\text{PMe}_2\}_2\text{Cl}_2]$ ( <b>7</b> ) .....	36
2.3.2 Characterisation of $[\{\text{Zr}(\eta\text{-C}_5\text{Me}_4)\text{CH}_2\text{PMe}_2\}_2\text{Cl}_2]$ ( <b>7</b> ) .....	36
2.3.3 Attempted Preparation of $[\{\text{Zr}(\eta\text{-C}_5\text{Me}_4)\text{CH}_2\text{PMe}_3\}_2\text{Cl}_2][\text{I}]_2$ .....	38
2.3.4 NMR Scale Reaction between $[\{\text{Zr}(\eta\text{-C}_5\text{Me}_4)\text{CH}_2\text{PMe}_2\}_2\text{Cl}_2]$ ( <b>7</b> ) and Two Equivalents of $\text{B}(\text{C}_6\text{F}_5)_3$ .....	39
2.3.5 Characterisation of $[\{\text{Zr}(\eta\text{-C}_5\text{Me}_4)\text{CH}_2\text{PMe}_2\}_2\text{Cl}]$ $[(\text{C}_6\text{F}_5)_3\text{BClB}(\text{C}_6\text{F}_5)_3]$ ( <b>8</b> ).....	39
2.3.6 Attempted Preparation of $[\{\text{Zr}(\eta\text{-C}_5\text{Me}_4)\text{CH}_2\text{PMe}_2\}_2\text{Me}_2]$ ( <b>9</b> )...41	
2.3.7 Attempted Preparation of $[\{\text{M}(\eta\text{-C}_5\text{Me}_4)\text{CH}_2\text{PMe}_2\}_2\text{Cl}_2]$ ( $\text{M} = \text{Ti, Hf}$ ) .....	42
2.3.8 Attempted Preparation of Mixed Ring Analogues .....	42
2.4 Early-Late Heterobimetallic (ELHB) Transition Metal Complexes Incorporating $[\{\text{Zr}(\eta\text{-C}_5\text{Me}_4)\text{CH}_2\text{PMe}_2\}_2\text{Cl}_2]$ ( <b>7</b> ) .....	42
2.4.1 Preparation of $[\{\text{Zr}(\eta\text{-C}_5\text{Me}_4)\text{CH}_2\text{PMe}_2\}_2\text{Cl}_2\text{PtI}_2]$ ( <b>10</b> ) .....	43
2.4.2 Characterisation of $[\{\text{Zr}(\eta\text{-C}_5\text{Me}_4)\text{CH}_2\text{PMe}_2\}_2\text{Cl}_2\text{PtI}_2]$ ( <b>10</b> ) .....	43
2.5 Later Transition Metal Complexes Incorporating the Ligand $[(\text{C}_5\text{Me}_4)\text{CH}_2\text{PMe}_2]^-$ .....	45
2.6 Chemistry of Manganocenes $[\text{Mn}(\eta\text{-C}_5\text{R}_5)_2]$ .....	46
2.7 Studies on $[\text{Mn}\{(\eta\text{-C}_5\text{Me}_4)\text{CH}_2\text{PMe}_2\}_2]$ ( <b>11</b> ).....	47
2.7.1 Preparation of $[\text{Mn}\{(\eta\text{-C}_5\text{Me}_4)\text{CH}_2\text{PMe}_2\}_2]$ ( <b>11</b> ) .....	47
2.7.2 Characterisation of $[\text{Mn}\{(\eta\text{-C}_5\text{Me}_4)\text{CH}_2\text{PMe}_2\}_2]$ ( <b>11</b> ).....	48
2.7.3 The Molecular Structure of Compound <b>11</b> .....	49
2.7.4 Magnetic Susceptibility Study on Compound <b>11</b> .....	54
2.7.5 Reactivity Studies on Compound <b>11</b> .....	57
2.7.5.1 Reaction between Compound <b>11</b> and $[\text{Na}][\text{C}_8\text{H}_{10}]$ .....	57

2.7.5.2 Reaction between Compound <b>11</b> and	
$[\text{Fe}(\eta\text{-C}_5\text{H}_5)_2][\text{PF}_6]$ .....	57
2.7.5.3 Preparation of	
$[\text{Mn}\{(\eta\text{-C}_5\text{Me}_4)\text{CH}_2\text{PMe}_2\text{B}(\text{C}_6\text{F}_5)_3\}_2]$ ( <b>12</b> ) .....	58
2.7.5.4 Characterisation of	
$[\text{Mn}\{(\eta\text{-C}_5\text{Me}_4)\text{CH}_2\text{PMe}_2\text{B}(\text{C}_6\text{F}_5)_3\}_2]$ ( <b>12</b> ) .....	58
2.7.5.5 Preparation of $[\text{Mn}\{(\eta\text{-C}_5\text{Me}_4)\text{CH}_2\text{PMe}_3\}_2][\text{I}]_2$ ( <b>13</b> ) ....	58
2.8 Attempted Preparation of the Manganocene	
$[\text{Mn}\{(\eta\text{-C}_5\text{H}_4)\text{CMe}_2\text{PMe}_2\}_2]$ .....	59
2.8.1 Preparation of $[\text{Li}(\text{C}_5\text{H}_4)\text{CMe}_2\text{PMe}_2]$ .....	59
2.8.2 Attempted Preparation of $[\text{Mn}\{(\eta\text{-C}_5\text{H}_4)\text{CMe}_2\text{PMe}_2\}_2]$ .....	60
2.9 Attempted Preparation of Heterobimetallic Complexes Incorporating Compound <b>11</b> .....	60
2.9.1 Attempted Preparation of $[\text{Mn}\{(\eta\text{-C}_5\text{Me}_4)\text{CH}_2\text{PMe}_2\}_2\text{PtI}_2]$ ( <b>14</b> ) .....	60
2.10 Summary .....	62
2.11 References for Chapter 2 .....	65
<b>Chapter 3 : Substituted Metallocenes of Group 14 Metals</b> .....	
3.0 Introduction to Chapter 3 .....	68
3.1 Main Group Metallocenes – A Brief Survey .....	68
3.1.1 The Early History of Group 14 Metallocenes .....	68
3.1.2 Review of the Group 14 Metallocenes .....	69
3.1.3 Plumbocenes $[\text{Pb}(\eta\text{-C}_5\text{H}_n\text{R}_{5-n})]$ (R = H, alkyl or aryl group) .....	69
3.1.4 Stannocenes $[\text{Sn}(\eta\text{-C}_5\text{H}_n\text{R}_{5-n})]$ (R = H, alkyl or aryl group) .....	72
3.1.5 Germanocenes $[\text{Pb}(\eta\text{-C}_5\text{H}_n\text{R}_{5-n})]$ (R = H, alkyl or aryl group) .....	73
3.1.6 Silicocenes $[\text{Si}(\eta\text{-C}_5\text{H}_n\text{R}_{5-n})]$ (R = Me, n = 0) .....	73
3.2 Bending in Group 14 Metallocenes .....	74
3.2.1 The Causes of Bending in Group 14 Metallocenes .....	75
3.2.2 The Parallel Group 14 Metallocene ‘Anomaly’ .....	76
3.3 Preparation of New Main Group Metallocenes Containing the	
$[(\text{C}_5\text{H}_4)\text{CMe}_2\text{PMe}_2]^-$ Ligand .....	79
3.3.1 Preparation of $[\text{Pb}\{(\eta\text{-C}_5\text{H}_4)\text{CMe}_2\text{PMe}_2\}_2]$ ( <b>15</b> ) .....	79
3.3.2 Characterisation of $[\text{Pb}\{(\eta\text{-C}_5\text{H}_4)\text{CMe}_2\text{PMe}_2\}_2]$ ( <b>15</b> ) .....	79
3.3.3 $^{207}\text{Pb}$ NMR Spectroscopy .....	82

3.3.4 Preparation of $[\text{Sn}\{(\eta\text{-C}_5\text{H}_4)\text{CMe}_2\text{PMe}_2\}_2]$ ( <b>16</b> ).....	84
3.3.5 Characterisation of $[\text{Sn}\{(\eta\text{-C}_5\text{H}_4)\text{CMe}_2\text{PMe}_2\}_2]$ ( <b>16</b> ) .....	84
3.3.6 $^{119}\text{Sn}$ NMR Spectroscopy .....	86
3.3.7 Attempted Preparation of $[\text{Pb}\{(\eta\text{-C}_5\text{Me}_4)\text{CH}_2\text{PMe}_2\}_2]$ .....	88
3.4 Reactions Between Compounds <b>15</b> and <b>16</b> and $\text{B}(\text{C}_6\text{F}_5)_3$ .....	89
3.4.1 Preparation of $[\text{Pb}\{(\eta\text{-C}_5\text{H}_4)\text{CMe}_2\text{PMe}_2\text{B}(\text{C}_6\text{F}_5)_3\}_2]$ ( <b>17</b> ).....	89
3.4.2 Characterisation of $[\text{Pb}\{(\eta\text{-C}_5\text{H}_4)\text{CMe}_2\text{PMe}_2\text{B}(\text{C}_6\text{F}_5)_3\}_2]$ ( <b>17</b> )...	89
3.4.3 Attempted Preparation of $[\text{Sn}\{(\eta\text{-C}_5\text{H}_4)\text{CMe}_2\text{PMe}_2\text{B}(\text{C}_6\text{F}_5)_3\}_2]$ ( <b>17</b> ).....	91
3.5 Preparation of Heterobimetallic Group 14-Transition Metal Complexes .....	92
3.5.1 Preparation of $[\text{Pb}\{(\eta\text{-C}_5\text{H}_4)\text{CMe}_2\text{PMe}_2\}_2\text{PtI}_2]$ ( <b>18</b> ) .....	92
3.5.2 Characterisation of $[\text{Pb}\{(\eta\text{-C}_5\text{H}_4)\text{CMe}_2\text{PMe}_2\}_2\text{PtI}_2]$ ( <b>18</b> ) .....	93
3.5.3 Attempted Preparation of $[\text{Pb}\{(\eta\text{-C}_5\text{H}_4)\text{CMe}_2\text{PMe}_2\}_2\text{PdCl}_2]$ ( <b>19</b> ) .....	95
3.5.4 Attempted Preparation of $[\text{Sn}\{(\eta\text{-C}_5\text{H}_4)\text{CMe}_2\text{PMe}_2\}_2\text{PtI}_2]$ ( <b>20</b> ) .....	96
3.5.5 Characterisation of $[\text{Sn}\{(\eta\text{-C}_5\text{H}_4)\text{CMe}_2\text{PMe}_2\}_2\text{PtI}_2]$ ( <b>20</b> ) .....	97
3.6 Summary.....	98
3.7 References for Chapter 3 .....	100

## Chapter 4 : Introduction to Inorganic-Fullerenes .....

4.0 Introduction to Chapter 4.....	105
4.1 The Carbon Fullerenes.....	106
4.2 The Structures of Carbon Fullerenes .....	107
4.3 Non-Carbon ‘Fullerene-Like’ Materials.....	109
4.4 Methods of Preparation of IF-Like Materials .....	112
4.4.1 Gas and Solid Phase Synthesis of IF-Like $\text{MS}_2$ ( $\text{M} = \text{Mo}$ and $\text{W}$ ).....	112
4.4.2 STM induction of Amorphous Films.....	113
4.5 Growth of IF-Related Materials: Encapsulation of Metal Oxides Within IF-Like Cages .....	114
4.6 Growth of IF-Related Materials: Encapsulation of WC Within IF-Like Cages .....	117
4.7 Non-Oxide or Carbide Based IF-Like Materials .....	119



4.8 Intercalation of IF-Like Structures .....	121
4.9 Applications of IF-Like Materials .....	122
4.9.1 Solid Lubricants.....	122
4.9.2 Photovoltaic Films.....	123
4.10 Structural Analysis of IF-Like Materials.....	124
4.10.1 Powder X-Ray Diffraction (XRD).....	124
4.10.2 High Resolution Transmission Electron Microscopy (HRTEM).....	125
4.11 Summary.....	128
4.12 References for Chapter 4 .....	129
<b>Chapter 5 : Synthesis of IF-Like Materials (I) .....</b>	
5.0 Introduction to Chapter 5.....	133
5.1 Synthesis of IF-Molybdenum Sulfide (IF-MoS <sub>2</sub> ) from Molybdenum Carbide (MoC).....	133
5.1.1 Sulfidisation of MoC .....	134
5.1.1 Characterisation of Sulfidised Product.....	134
5.2 Mixed-Metal Binary Oxide Systems: Nb <sub>4</sub> W <sub>13</sub> O <sub>47</sub> and Nb <sub>8</sub> W <sub>9</sub> O <sub>47</sub> .....	137
5.2.1 Tetragonal Tungsten Bronzes (TTBs): Nb <sub>4</sub> W <sub>13</sub> O <sub>47</sub> and Nb <sub>8</sub> W <sub>9</sub> O <sub>47</sub> .....	137
5.2.2 Effects of Sulfidisation on the Mixed-Metal Binary Oxides Nb <sub>4</sub> W <sub>13</sub> O <sub>47</sub> and Nb <sub>8</sub> W <sub>9</sub> O <sub>47</sub> .....	140
5.3 Epitaxial and Bulk Formation of IF-WS <sub>2</sub> Structures and Encapsulates from Tungsten Carbide (WC) Precursors .....	144
5.3.1 Oxidation of WC by CO <sub>2</sub> .....	145
5.3.2 Sulfidisation of WC/WO <sub>3-x</sub> Nanoparticles .....	147
5.4 Summary.....	151
5.5 References for Chapter 5 .....	152
<b>Chapter 6 Synthesis of IF-Like Materials (II).....</b>	
6.0 Introduction to Chapter 6.....	154
6.1 Metal Vapour Synthesis .....	154
6.1.1 Introduction to the MVS Technique .....	154
6.2 Preparation of Group 5 Metal Oxides by MVS .....	157
6.2.1 Analysis of MVS Products .....	158
6.3 Preparation of Crystalline Group 5 Metal Oxides .....	161

6.3.1 Preparation of Reduced Vanadium Oxide, $\alpha$ -V <sub>2</sub> O <sub>3</sub> .....	162
6.3.2 Preparation of Reduced Niobium Oxide, NbO <sub>2</sub> .....	163
6.3.3 Preparation of Tantalum Oxide, TT-V <sub>2</sub> O <sub>5</sub> .....	164
6.4 Preparation of the Group 5 Metal Sulfides (MS <sub>2</sub> ) .....	167
6.4.1 Sulfidisation of the Vanadium Oxide $\alpha$ -V <sub>2</sub> O <sub>3</sub> .....	168
6.4.2 Sulfidisation of the Niobium Oxide NbO <sub>2</sub> .....	170
6.4.3 Sulfidisation of the Tantalum Oxide TT-Ta <sub>2</sub> O <sub>5</sub> .....	172
6.5 Attempted Sulfidisation of Amorphous MVS Products .....	175
6.6 Summary .....	177
6.7 References for Chapter 6 .....	178

## Chapter 7 : Experimental Details .....

7.1 General Experimental Details .....	180
7.1.1 Techniques .....	180
7.1.2 Solvents .....	180
7.1.3 General Materials .....	181
7.1.4 Instrumentation .....	181
7.2 Experimental Details for Chapter 2 .....	183
7.2.1 Preparation of [HC <sub>5</sub> Me <sub>4</sub> CH <sub>2</sub> PMe <sub>2</sub> H][Cl] (1) .....	183
7.2.2 Preparation of [HC <sub>5</sub> Me <sub>4</sub> CH <sub>2</sub> PMe <sub>2</sub> H][PF <sub>6</sub> ] (2) .....	183
7.2.3 Preparation of [HC <sub>5</sub> Me <sub>4</sub> CH <sub>2</sub> PMe <sub>2</sub> ] (3) .....	183
7.2.4 Preparation of [K(C <sub>5</sub> Me <sub>4</sub> )CH <sub>2</sub> PMe <sub>2</sub> ] (4) .....	184
7.2.5 Preparation of [Na(C <sub>5</sub> Me <sub>4</sub> )CH <sub>2</sub> PMe <sub>2</sub> ] (5) .....	184
7.2.6 Preparation of [Li(C <sub>5</sub> Me <sub>4</sub> )CH <sub>2</sub> PMe <sub>2</sub> ] (6) .....	184
7.2.7 Preparation of [ {Zr( $\eta$ -C <sub>5</sub> Me <sub>4</sub> )CH <sub>2</sub> PMe <sub>2</sub> } <sub>2</sub> Cl <sub>2</sub> ] (7) .....	185
7.2.8 NMR Scale Reaction between [ {Zr( $\eta$ -C <sub>5</sub> Me <sub>4</sub> )CH <sub>2</sub> PMe <sub>2</sub> } <sub>2</sub> Cl <sub>2</sub> ] (7) and 2 B(C <sub>6</sub> F <sub>5</sub> ) <sub>3</sub> .....	185
7.2.9 Attempted Preparation of [ {Zr( $\eta$ -C <sub>5</sub> Me <sub>4</sub> )CH <sub>2</sub> PMe <sub>2</sub> } <sub>2</sub> Me <sub>2</sub> ] (9) .....	185
7.2.10 Attempted Preparation of [ {Hf( $\eta$ -C <sub>5</sub> Me <sub>4</sub> )CH <sub>2</sub> PMe <sub>2</sub> } <sub>2</sub> Cl <sub>2</sub> ] .....	186
7.2.11 Preparation of [ {Zr( $\eta$ -C <sub>5</sub> Me <sub>4</sub> )CH <sub>2</sub> $\overline{\text{PMe}_2}$ } <sub>2</sub> Cl <sub>2</sub> PtI <sub>2</sub> ] (10) .....	186
7.2.12 Preparation of [Mn{( $\eta$ -C <sub>5</sub> Me <sub>4</sub> )CH <sub>2</sub> PMe <sub>2</sub> } <sub>2</sub> ] (11) .....	186
7.2.13 Attempted Preparation [Na][Mn{( $\eta$ -C <sub>5</sub> Me <sub>4</sub> )CH <sub>2</sub> PMe <sub>2</sub> } <sub>2</sub> ] ....	187
7.2.14 Attempted Preparation of [Mn{( $\eta$ -C <sub>5</sub> Me <sub>4</sub> )CH <sub>2</sub> PMe <sub>2</sub> } <sub>2</sub> ][PF <sub>6</sub> ] .....	187
7.2.15 Preparation of [Mn{( $\eta$ -C <sub>5</sub> Me <sub>4</sub> )CH <sub>2</sub> $\overline{\text{PMe}_2\text{B}(\text{C}_6\text{F}_5)_3}$ } <sub>2</sub> ] (12) .....	187

7.2.16	Preparation of $[\text{Mn}\{(\eta\text{-C}_5\text{Me}_4)\text{CH}_2\text{PMe}_3\}_2][\text{I}]_2$ (13)	188
7.2.17	Attempted Preparation of $[\text{Mn}\{(\eta\text{-C}_5\text{Me}_4)\text{CH}_2\text{PMe}_2\}_2\text{PtI}_2]$ (14)	188
7.2.18	Preparation of $[\text{Li}(\text{C}_5\text{H}_4)\text{CMe}_2\text{PMe}_2]$	188
7.2.19	Attempted Preparation of $[\text{Mn}\{(\eta\text{-C}_5\text{H}_4)\text{CMe}_2\text{PMe}_2\}_2]$	189
7.3	Experimental Details for Chapter 3	190
7.3.1	Attempted Preparation of $[\text{Pb}\{(\eta\text{-C}_5\text{Me}_4)\text{CH}_2\text{PMe}_2\}_2]$	190
7.3.2	Preparation of $[\text{Pb}\{(\eta\text{-C}_5\text{H}_4)\text{CMe}_2\text{PMe}_2\}_2]$ (15)	190
7.3.3	Preparation of $[\text{Sn}\{(\eta\text{-C}_5\text{H}_4)\text{CMe}_2\text{PMe}_2\}_2]$ (16)	190
7.3.4	Preparation of $[\text{Pb}\{(\eta\text{-C}_5\text{H}_4)\text{CMe}_2\text{PMe}_2\text{B}(\text{C}_6\text{F}_5)_3\}_2]$ (17)	191
7.3.5	Attempted Preparation of $[\text{Sn}\{(\eta\text{-C}_5\text{H}_4)\text{CMe}_2\text{PMe}_2\text{B}(\text{C}_6\text{F}_5)_3\}_2]$	191
7.3.6	Preparation of $[\text{Pb}\{(\eta\text{-C}_5\text{H}_4)\text{CMe}_2\text{PMe}_2\}_2\text{PtI}_2]$ (18)	191
7.3.7	Attempted Preparation of $[\text{Pb}\{(\eta\text{-C}_5\text{H}_4)\text{CMe}_2\text{PMe}_2\}_2\text{PdCl}_2]$ (19)	192
7.3.8	Attempted Preparation of $[\text{Sn}\{(\eta\text{-C}_5\text{H}_4)\text{CMe}_2\text{PMe}_2\}_2\text{PtI}_2]$ (20)	192
7.4	Experimental Details for Chapter 5	193
7.4.0	General Procedure	193
7.4.1	Sulfidisation of Molybdenum Carbide (MoC)	193
7.4.2	Sequential Oxidation of Tungsten Carbide (WC) to WC/WO <sub>3-x</sub> by CO <sub>2</sub>	193
7.4.3	Sulfidisation of WC/WO <sub>3-x</sub>	193
7.4.4	Sulfidisation of Nb <sub>4</sub> W <sub>13</sub> O <sub>47</sub>	194
7.4.5	Sulfidisation of Nb <sub>8</sub> W <sub>9</sub> O <sub>47</sub>	194
7.5	Experimental Details for Chapter 6	195
7.5.0	General Procedure	195
7.5.1	Preparation of Amorphous Vanadium Oxide by MVS	195
7.5.2	Preparation of Amorphous Niobium Oxide by MVS	195
7.5.3	Preparation of Amorphous Tantalum Oxide by MVS	195
7.5.4	Preparation of α-V <sub>2</sub> O <sub>3</sub>	196
7.5.5	Preparation of NbO <sub>2</sub>	196
7.5.6	Preparation of TT-Ta <sub>2</sub> O <sub>5</sub>	197
7.5.7	Preparation of VS <sub>2</sub>	197
7.5.8	Preparation of NbS <sub>2</sub>	197

7.5.9 Preparation of TaS <sub>2</sub> .....	198
7.5.10 Preparation of NbS <sub>2</sub> from Amorphous Niobium Oxide .....	198
7.6 References for Chapter 7 .....	199
<b>Chapter 8 : Characterising Data</b> .....	
8.1 Characterising Data for [HC <sub>5</sub> Me <sub>4</sub> CH <sub>2</sub> PMe <sub>2</sub> H][Cl] (1) .....	201
8.2 Characterising Data for [HC <sub>5</sub> Me <sub>4</sub> CH <sub>2</sub> PMe <sub>2</sub> H][PF <sub>6</sub> ] (2) .....	202
8.3 Characterising Data for [H(C <sub>5</sub> Me <sub>4</sub> )CH <sub>2</sub> PMe <sub>2</sub> ] (3) .....	203
8.4 Characterising Data for [K(C <sub>5</sub> Me <sub>4</sub> )CH <sub>2</sub> PMe <sub>2</sub> ] (4) .....	204
8.5 Characterising Data for [Na(C <sub>5</sub> Me <sub>4</sub> )CH <sub>2</sub> PMe <sub>2</sub> ] (5) .....	205
8.6 Characterising Data for [Li(C <sub>5</sub> Me <sub>4</sub> )CH <sub>2</sub> PMe <sub>2</sub> ] (6) .....	206
8.7 Characterising Data for [Zr{(η-C <sub>5</sub> Me <sub>4</sub> )CH <sub>2</sub> PMe <sub>2</sub> } <sub>2</sub> Cl <sub>2</sub> ] (7) .....	207
8.8 Characterising Data for [Zr{(η-C <sub>5</sub> Me <sub>4</sub> )CH <sub>2</sub> PMe <sub>2</sub> } <sub>2</sub> Cl] [(C <sub>6</sub> F <sub>5</sub> ) <sub>3</sub> BClB(C <sub>6</sub> F <sub>5</sub> ) <sub>3</sub> ] (8) .....	208
8.9 Characterising Data for [Zr{(η-C <sub>5</sub> Me <sub>4</sub> )CH <sub>2</sub> PMe <sub>2</sub> } <sub>2</sub> Cl <sub>2</sub> PtI <sub>2</sub> ] (10) .....	209
8.10 Characterising Data for [Mn{(η-C <sub>5</sub> Me <sub>4</sub> )CH <sub>2</sub> PMe <sub>2</sub> } <sub>2</sub> ] (11) .....	210
8.11 Characterising Data for [Mn{(η-C <sub>5</sub> Me <sub>4</sub> )CH <sub>2</sub> PMe <sub>2</sub> B(C <sub>6</sub> F <sub>5</sub> ) <sub>3</sub> } <sub>2</sub> ] (12) .....	211
8.12 Characterising Data for [Pb{(η-C <sub>5</sub> H <sub>4</sub> )CMe <sub>2</sub> PMe <sub>2</sub> } <sub>2</sub> ] (15) .....	212
8.13 Characterising Data for [Sn{(η-C <sub>5</sub> H <sub>4</sub> )CMe <sub>2</sub> PMe <sub>2</sub> } <sub>2</sub> ] (16) .....	213
8.14 Characterising Data for [Pb{(η-C <sub>5</sub> H <sub>4</sub> )CMe <sub>2</sub> PMe <sub>2</sub> B(C <sub>6</sub> F <sub>5</sub> ) <sub>3</sub> } <sub>2</sub> ] (17) .....	214
8.15 Characterising Data for [Pb{(η-C <sub>5</sub> H <sub>4</sub> )CMe <sub>2</sub> PMe <sub>2</sub> } <sub>2</sub> PtI <sub>2</sub> ] (18) .....	215
<b>Appendix A</b> .....	216
Crystal Data and Structure Refinement for [Mn{(η-C <sub>5</sub> Me <sub>4</sub> )CH <sub>2</sub> PMe <sub>2</sub> } <sub>2</sub> ] (11) .....	217

---

## List of Abbreviations

### *General abbreviations*

Ar	aryl group
b. p.	boiling point
<sup>n</sup> Bu	normal-butyl
<sup>t</sup> Bu	<i>tertiary</i> -butyl
calc.	calculated
C <sub>ipso</sub>	<i>ipso</i> -carbon
COD	1,5-cyclooctadiene
Cp	cyclopentadienyl
Cp <sup>*</sup>	pentamethylcyclopentadienyl
Cp <sub>cent</sub>	cyclopentadienyl ring centroid
DME	1,2-dimethoxyethane
EDX	energy dispersive X-ray
EI	electron impact (mass spectrometry)
Et	ethyl
FAB	fast atom bombardment (mass spectrometry)
FFT	fast Fourier transform
HRTEM	high resolution transmission electron microscopy
IF	inorganic fullerene
<sup>i</sup> Pr	<i>iso</i> -propyl
IR	infra-red
L	two electron donor ligand
<i>m</i> -	<i>meta</i> - position of an aryl ring
M	metal atom
M <sup>+</sup>	molecular ion
MAO	methylaluminoxane
Me	methyl
MO	molecular orbital
MVS	metal vapour synthesis
MWNTs	multi-walled nanotubes
<i>m/z</i>	atomic mass units per unit charge
nbd	norbornadiene
NMR	nuclear magnetic resonance

---

<i>o</i> -	<i>ortho</i> - position of an aryl ring
<i>p</i> -	<i>para</i> - position of an aryl ring
Ph	phenyl
py	pyridine
R	alkyl or aryl group
RT	room temperature
STM	scanning tunnelling microscopy
SWNTs	single-walled nanotubes
TEM	transmission electron microscopy
THF	tetrahydrofuran
vdW	van der Waals
X	generic ligand
XRD	X-ray diffraction

*NMR spectroscopic abbreviations*

br	broad
$\delta$	chemical shift
d	doublet
$\{^1\text{H}\}$	proton decoupled
HMQC	heteronuclear multiple quantum coherence
I	nuclear spin quantum number
$^nJ_{\text{A-B}}$	n bond coupling constant between A and B
m	multiplet
$\{^{31}\text{P}\}$	phosphorus decoupled
ppm	parts per million
q	quartet
sp	septet

# Chapter 1

## Introduction

## 1.0 Scope of the Thesis

The scope of this thesis covers two areas of synthetic inorganic chemistry. The first part describes the synthesis, structure and reactivity of new organometallic compounds (transition and main group metals) containing dimethylphosphino-substituted cyclopentadienyl ligands. This research excludes compounds containing iron, such as dimethylphosphinoferrocene (dmpf) and diphenylphosphinoferrocene (dppf) which have already been widely reported in the literature.<sup>[1-5]</sup> Chapter 1 provides a brief review of the chemistry of dialkyl- and diaryl-phosphinocyclopentadienyl complexes and in particular, their utility as bifunctional ligands. The following two chapters describe the synthesis and characterisation of a range of complexes incorporating these bifunctional ligands.

The second part of this thesis concerns the synthesis and characterisation of novel, inorganic fullerene (IF)-like materials. A review of the recent developments in this relatively new field, including methods of preparation and the techniques for structural characterisation is given in Chapter 4. Chapters 5 and 6 describe the preparation of some IF-like materials from a range of precursors.



## 1.1 Metallocenes

The perhapto mode of bonding in the  $\eta^5\text{-C}_5\text{H}_5$  cyclopentadienyl ring in ferrocene was discovered in 1952.[6, 7] Since then, the chemistry of this ligand has contributed enormously to the development of organometallic chemistry and especially to the area of transition metal complexes, of which nearly 80% include a cyclopentadienyl moiety. Compounds containing two  $\eta^5\text{-C}_5\text{H}_5$  rings bonded to a metal are known as metallocenes, and in most cases the cyclopentadienyl ligand behaves as an inert spectator ligand. The steric and electronic properties of the cyclopentadienyl ligand may be tuned, however, by substitution of the hydrogen atoms with other hydrocarbon or heteroatomic groups. In this way, the ligand provides ample opportunity to control the stereoelectronic properties of the metal centre.

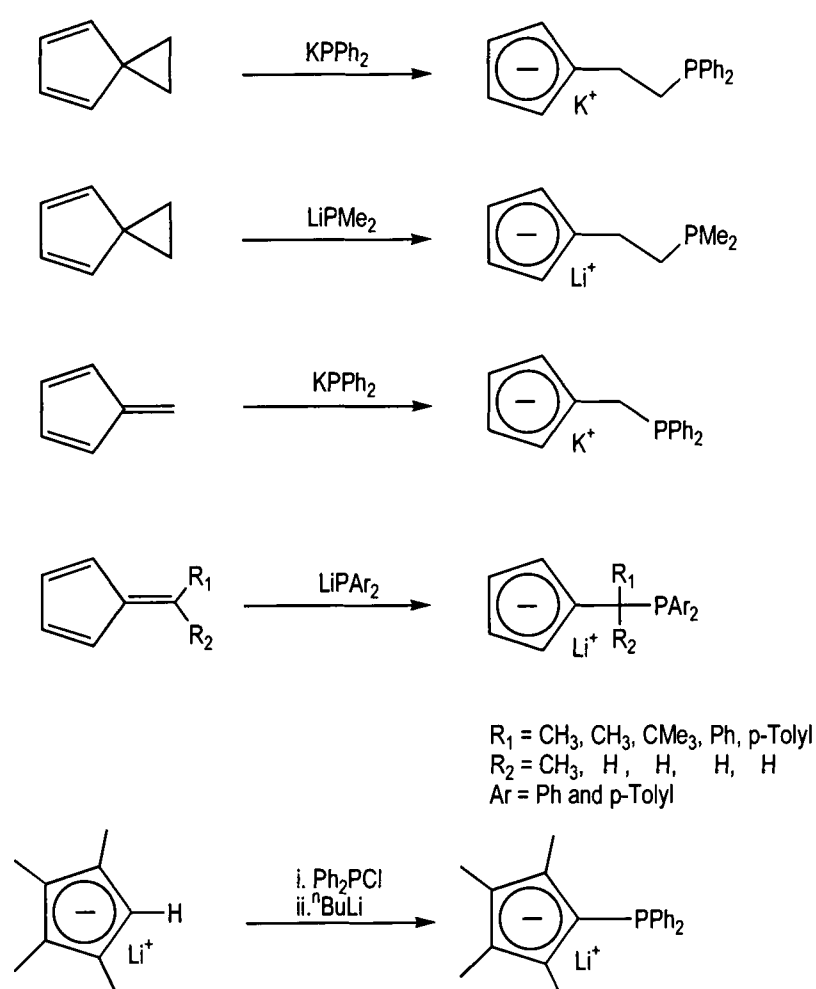
## 1.2 Heteroatomic Substituted-Cyclopentadienyl Species

Alkyl, aryl and silyl substituents have commonly been utilised to effect stabilisation of transition metal centres in cyclopentadienyl complexes.[8] More recently cyclopentadienyl complexes containing substituents which are themselves capable of binding to metals have been reported. These side-chain functionalised ligands or *bifunctional* ligands are used mainly for the construction of homo- or hetero-oligomeric complexes for the study of intramolecular metal-metal interactions.

The chemistry of side-chain functionalised cyclopentadienyl systems is a rapidly developing area currently under investigation by a number of groups and two of the most useful functionalities are the dialkylamino- and diaryl- and dialkylphosphino moieties. The following review encompasses some recent developments in the chemistry of diaryl- and dialkylphosphino-substituted cyclopentadienyl ligands.

### 1.3 Synthesis of Phosphino-substituted Cyclopentadienyl Ligands

The synthesis of dialkyl- and diarylphosphino substituted cyclopentadienyl ligands can be achieved *via* reaction between spiro[2.4]hepta-4,6-diene[9, 10] or a fulvene[10-12] and a lithium or potassium dimethyl- or diarylphosphide reagent. Additionally, synthesis can occur *via* reaction between a protonated cyclopentadienyl moiety ( $C_5H_6$  or  $C_5Me_4H$ ) and  $Ph_2PCl$ . [13, 14] Some examples are shown below in **Scheme 1.1**.



**Scheme 1.1** Some preparative methods for obtaining dialkyl- or diaryl-substituted cyclopentadienyl ligands

In addition, the longer chain compounds such as  $Ph_2P(CH_2)_3C_5Me_4H$  can be obtained by analogous routes but starting with  $LiC_5Me_4H$  and  $TsO(CH_2)_2Cl$  followed by reaction with a  $LiPR_2$  salt (  $R$  = alkyl or aryl group). [14]

### 1.4 Applications of Phosphino-Substituted Cyclopentadienyl Ligands

Dialkyl- and diarylphosphino-substituted cyclopentadienyl complexes were designed to act as ligands for the synthesis of new mono- or bi-metallic complexes. [15] For example, the  $[C_5H_4PPh_2]^-$  ligand has been utilised to afford both homo- [16-18] and

hetero-bimetallic[19, 20] complexes in which the bifunctional species acts as a bridging moiety between the metal centres. This section provides a brief review of the three main areas in which these bifunctional ligands have been used.

#### 1.4.1 Phosphino-substituted Cyclopentadienyl Ligands in Monometallic Complexes

The use of the phosphino functionality on a substituted cyclopentadienyl ligand for *intramolecular* co-ordination to a metal centre is described in this section. Complexes containing both cyclopentadienyl and phosphine functionalities are widely known in organometallic chemistry. In systems in which the Cp and  $\text{PR}_2$  groups are separated by an alkyl spacer group, it is possible to maintain the individual properties of both the Cp and phosphine moieties while at the same time allowing for formation of a chelate complex.[21]

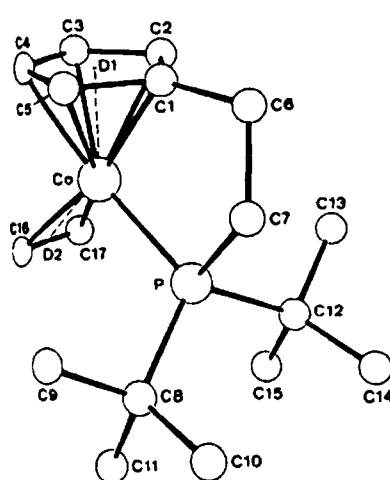
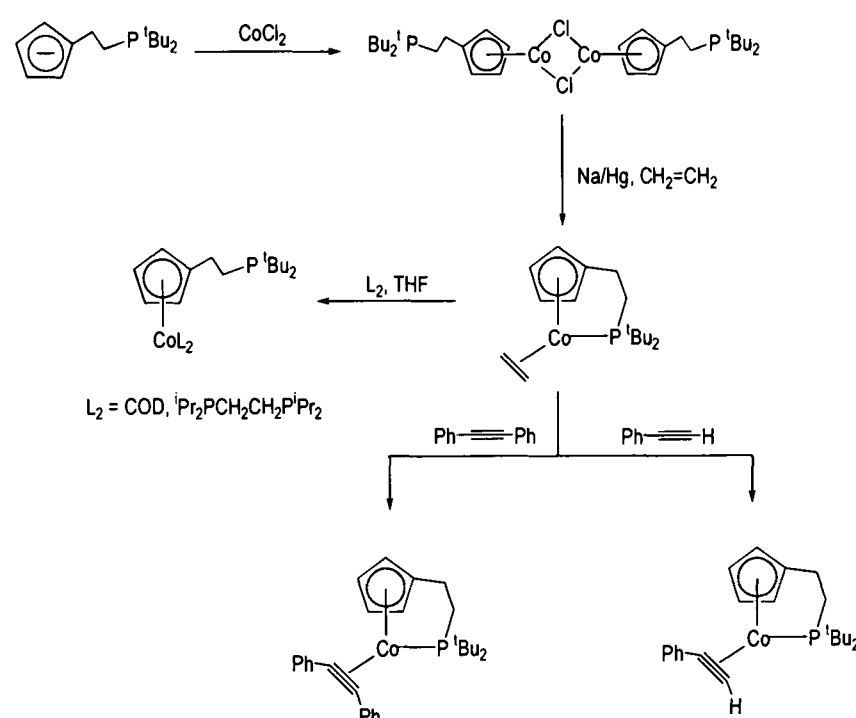


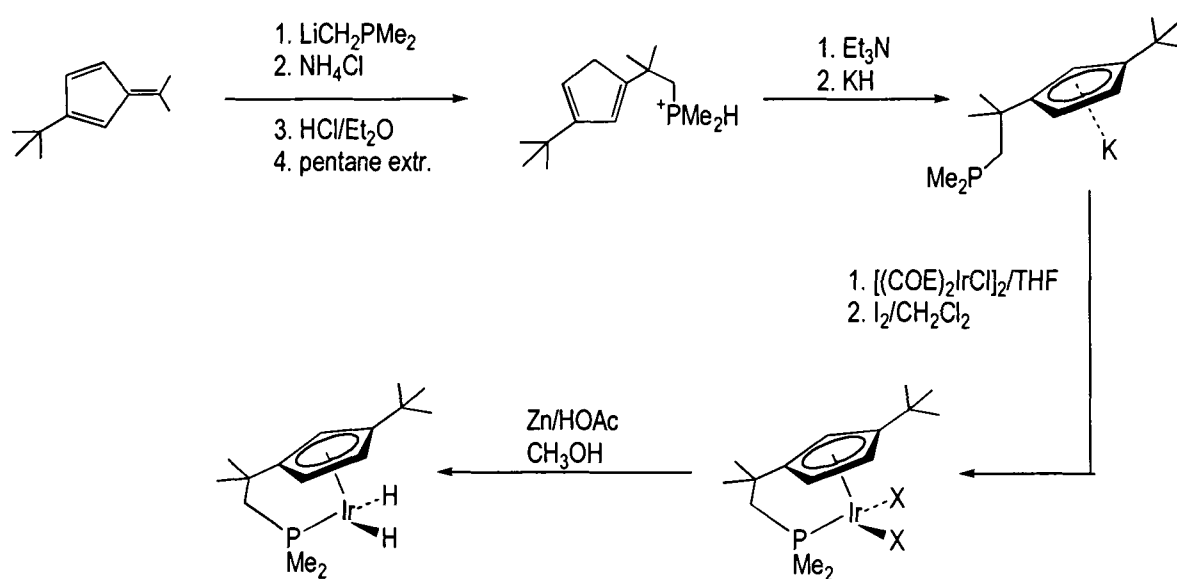
**Figure 1.1** Molecular structure diagram of  $[(\eta\text{-C}_5\text{H}_4)\text{CH}_2\text{CH}_2\text{P}^t\text{Bu}_2\text{Co}(\eta\text{-CH}_2\text{CH}_2)]$

Studies by Butenschon *et al.* have demonstrated the capability of the phosphine group on these bifunctional ligands to selectively bind to the metal centre, preventing co-ordination by unwanted ligands. In this way, the chelating phosphine moiety acts as an intramolecular protection group for a vacant co-ordination site. For example, the phosphine group in the complex  $[(\eta\text{-C}_5\text{H}_4)\text{CH}_2\text{CH}_2\text{P}^t\text{Bu}_2\text{Co}(\eta\text{-CH}_2\text{CH}_2)]$  shown in **Figure 1.1**, dissociates in the presence of chelating bidentate ligands such as 1,5-COD or diphosphinoalkyl reagents, as a result of competition between the chelate effects of the two ligands. In contrast, reaction with an alkyne species results solely in the replacement of the ethene molecule.[22, 23] Further reactions are shown in **Scheme 1.2**.



**Scheme 1.2** Synthesis of the complex  $[(\eta\text{-C}_5\text{H}_4)\text{CH}_2\text{CH}_2\text{P}^i\text{Bu}_2\text{Co}(\eta\text{-CH}_2\text{CH}_2)]$  and behaviour of the chelating phosphine group depending on the nature of the alternative ligand

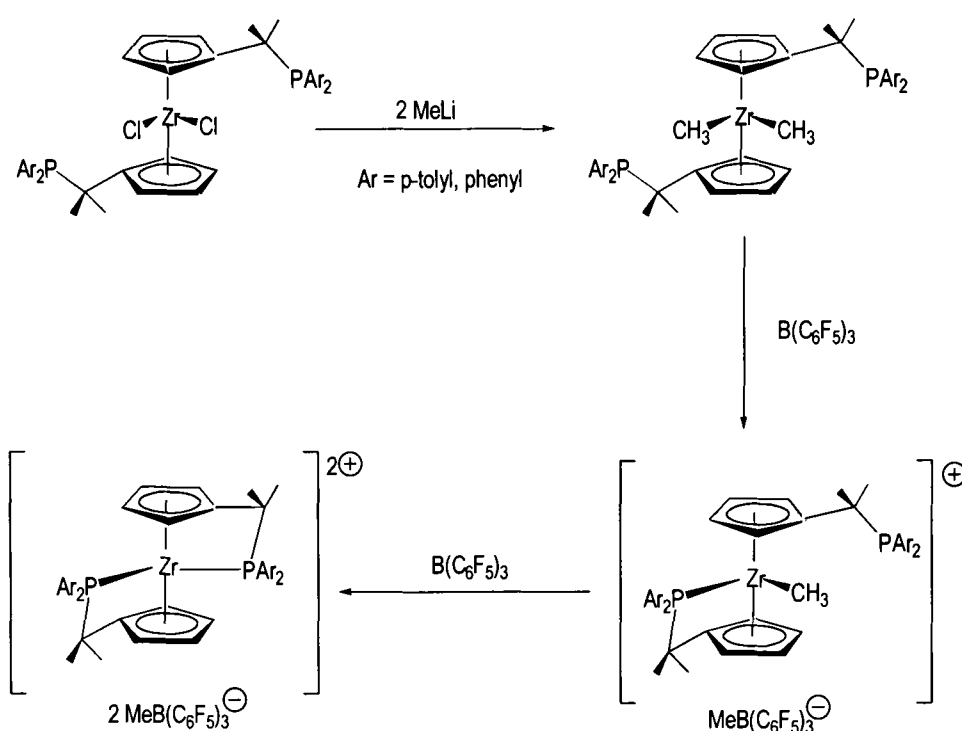
The synthesis of a disubstituted cyclopentadienyl ligand has been reported by Bergman *et al.* The synthesis and subsequent reactions of this prochiral ligand are shown in **Scheme 1.3**.<sup>[24]</sup> Utilising this ligand, an asymmetric iridium dihydride complex was synthesised, which was found to activate the C-H bond in cyclohexane with stereoselectivity.



**Scheme 1.3** Preparation of the complex  $[(\eta\text{-C}_5\text{H}_3^i\text{Bu})\text{CH}_2\text{PMe}_2\text{IrH}_2]$

The synthesis of a series of diphenylphosphino-substituted zirconocene complexes was reported by Erker in 1997 (**Scheme 1.4**).<sup>[25]</sup> The work demonstrates the intramolecular chelating ability of the diarylphosphino substituent containing a one-carbon bridge spacer. It was shown that following abstraction a methide group  $[\text{CH}_3]^-$  by the

Lewis acid  $B(C_6F_5)_3$ , chelation of the phosphino substituents could be induced resulting in a cationic complex, stabilised by the nucleophilic nature of the  $-PAr_2$  substituents. In addition, mutual exchange of the diphenylphosphine groups was observed.[25]



**Scheme 1.4** Synthesis of  $B(C_6F_5)_3$  adducts of zirconocene complexes containing arylphosphino-substituted cyclopentadienyl groups.

#### 1.4.2 Phosphino-substituted Cyclopentadienyl Ligands in Heterobimetallic complexes

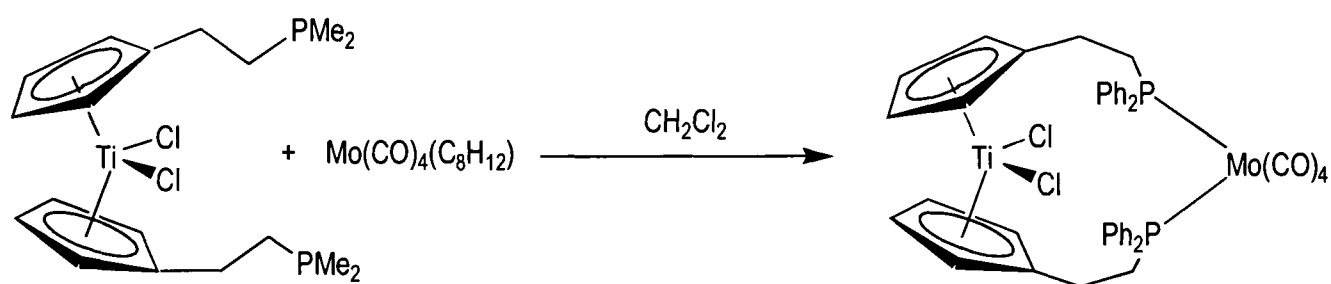
The interest in early-late heterobimetallic (ELHB) complexes is primarily based upon the objective of utilising two metals, each with widely divergent properties, to induce transformations otherwise unattainable by a single metal species. The presence of two different metals in bimetallic compounds seems to provide an important co-operative reactivity, particularly between early (electron deficient) and late (electron rich) metals.[10, 26] Many of these heterobimetallic compounds combine *bis*(cyclopentadienyl) derivatives of Group 4 metals containing alkyl- or arylphosphino substituents with later transition metals, bridging through the phosphorus atom.[27-29]

A commonly used method for the synthesis of ELHB complexes uses a bifunctional ligand template that is capable of binding strongly to both metal types. This eliminates the need for metal-metal bonds, which are normally required to hold the

metals close enough to ensure a co-operative interaction. Additionally, this technique maintains the integrity of the complex during interesting reactions. The phosphine functionality in these ligands forms favourable interactions with the late transition metal while the cyclopentadienyl moiety binds to the early transition metal.<sup>[10]</sup>

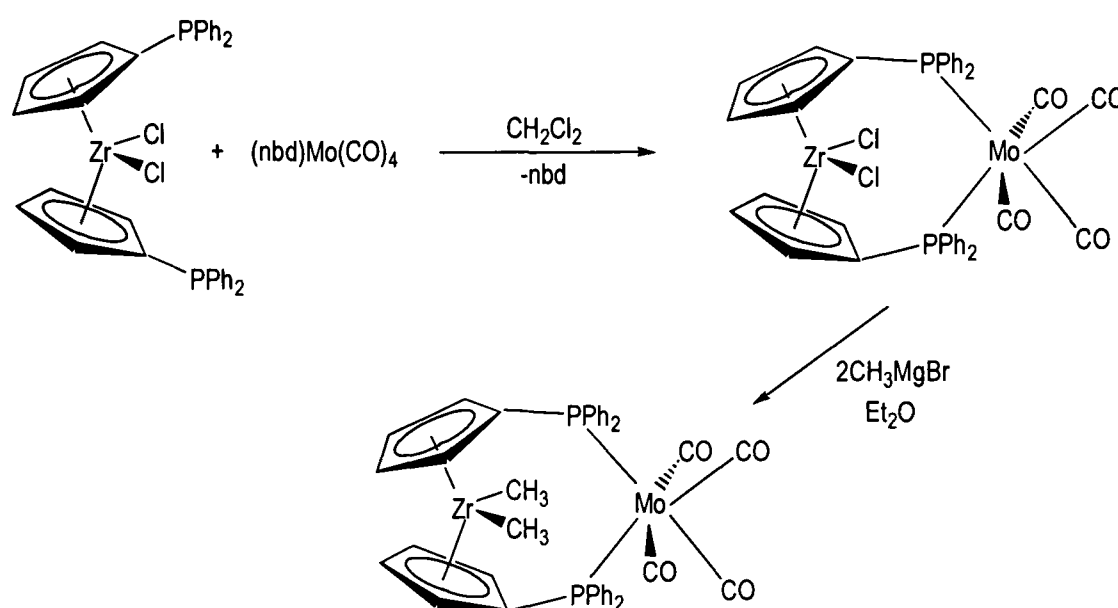
The general strategy for the preparation of these complexes begins with synthesis of the early-metal metallocene species in which the cyclopentadienyl rings have already been derivatised with a dialkyl- or diarylphosphino functionality. These monomers are then reacted with late transition metal sources with displaceable ligands such as CO,<sup>[10]</sup> COD<sup>[10]</sup> or MeCN.<sup>[30]</sup>

The earliest report of successful synthesis of a complex containing this genre of bifunctional ligand was by Poilblanc and Moise in 1982 and is illustrated in **Scheme 1.5**.<sup>[31]</sup> The complex is synthesised from a reaction between the metallo-ligand  $[\text{Ti}(\eta\text{-C}_5\text{H}_4\text{CH}_2\text{CH}_2\text{PMe}_2)_2\text{Cl}_2]$  and  $\text{Mo}(\text{CO})_4(\text{C}_8\text{H}_{12})$ . Following displacement of one molecule of the COD, the diphenylphosphinoethyl substituents co-ordinate to  $\text{Mo}(\text{CO})_4$  forming a heterobimetallic species.



**Scheme 1.5** Preparation of the first early-late heterobimetallic complex incorporating phosphino-substituted cyclopentadienyl ligands

Treatment of  $[(\text{nbd})\text{Mo}(\text{CO})_4]$  with the bidentate ligand  $[\text{Zr}(\eta\text{-C}_5\text{H}_4\text{PPh}_2)_2\text{Cl}_2]$  results in the isolation of the heterobimetallic complex  $[\text{Zr}(\eta\text{-C}_5\text{H}_4\text{PPh}_2)_2\text{Cl}_2\text{Mo}(\text{CO})_4]$  which has been characterised by X-ray crystallography. Further reaction with methyl magnesium bromide yields the dimethyl analogue  $[\text{Zr}(\eta\text{-C}_5\text{H}_4\text{PPh}_2)_2\text{Me}_2\text{Mo}(\text{CO})_4]$  (**Scheme 1.6**).<sup>[28]</sup> The compounds exhibit a *cis*-geometry and the  $^{31}\text{P}\{^1\text{H}\}$  NMR spectrum displays a singlet at  $\delta$  30.9 compared with a chemical shift of -18.2 for the parent zirconocene, indicating that the two phosphorus atoms are equivalent on the NMR timescale.

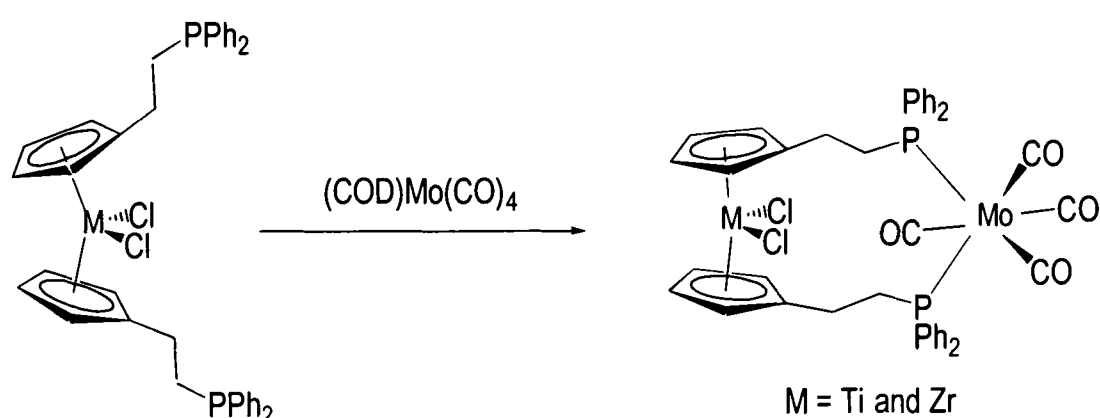


**Scheme 1.6** Synthesis of  $[\text{Zr}(\eta\text{-C}_5\text{H}_4\text{PPh}_2)_2\text{Cl}_2\text{Mo}(\text{CO})_4]$  and  $[\text{Zr}(\eta\text{-C}_5\text{H}_4\text{PPh}_2)_2\text{Me}_2\text{Mo}(\text{CO})_4]$

The use of spacer groups between the alkylphosphino functionality and that of the cyclopentadienyl ligand purportedly alleviates the geometric constraints, which may inhibit reactivity in  $\text{Cp-PR}_2$  ( $\text{R} = \text{alkyl or aryl group}$ ) type complexes. The inclusion of a carbon chain may allow for greater conformational freedom of the two coordination spheres of the two metals.<sup>[10]</sup>

Recently, independent work by both Erker and Graham has demonstrated the uses of a variety of substituted cyclopentadienyl zirconocene and titanocene dichlorides in conjunction with complexes of rhodium, palladium and platinum. The complexes synthesised include both bimetallic and tetrametallic species with structures dependent on the substituents available on the methylene spacer group.<sup>[10, 12]</sup>

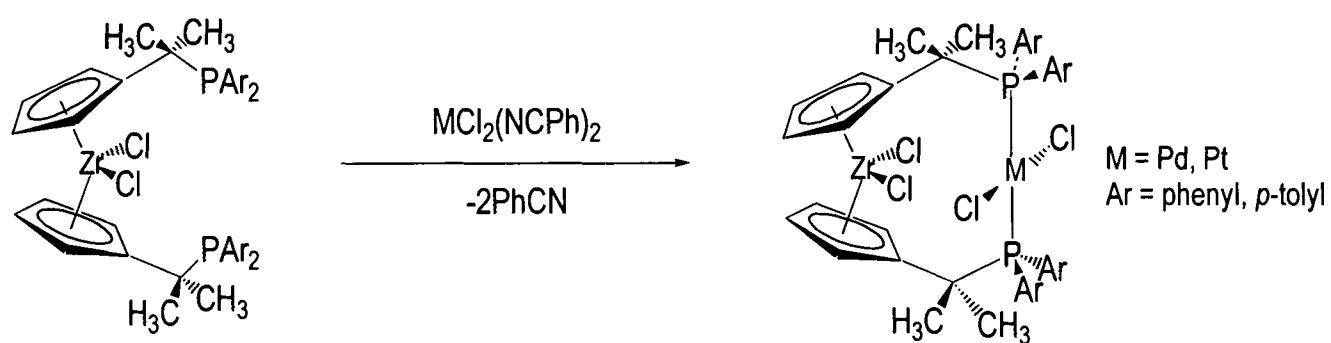
The compounds  $[(\eta\text{-C}_5\text{H}_4\text{CH}_2\text{CH}_2\text{PPh}_2)_2\text{TiCl}_2]$  and  $[(\eta\text{-C}_5\text{H}_4\text{CH}_2\text{CH}_2\text{PPh}_2)_2\text{ZrCl}_2]$  were synthesised *via* reactions between  $\text{K}[\text{C}_5\text{H}_4\text{CH}_2\text{CH}_2\text{PPh}_2]$  and THF adducts of the respective metal chlorides  $\text{MCl}_4(\text{THF})_2$  ( $\text{M} = \text{Ti and Zr}$ ). Both the  $^{31}\text{P}\{^1\text{H}\}$  and  $^1\text{H}$  NMR spectra of the metallocene dichlorides are very similar to those observed for the free ligand which suggests that the phosphine group does not co-ordinate to the metal centre. Synthesis of ELHB complexes was achieved by reaction of the metallocene dichlorides with the metal carbonyl compound  $(\text{COD})\text{Mo}(\text{CO})_4$ . Displacement of the labile COD group results and co-ordination of the two phosphino groups occurs in a *cis*-fashion as shown in **Scheme 1.7**.<sup>[10]</sup>



**Scheme 1.7** Synthesis of  $[\text{M}\{(\eta\text{-C}_5\text{H}_4)(\text{CH}_2)_2\text{PPh}_2\}_2\text{Cl}_2\text{Mo}(\text{CO})_4]$  ( $\text{M} = \text{Ti and Zr}$ )

In the resultant bimetallic Zr-Mo and Ti-Mo complexes, the metal<sub>1</sub>-metal<sub>2</sub> separations of 6.895 and 6.945 Å ruled out any metal-metal interactions. Additionally, it was shown that the orientation of methylene protons on the C<sub>2</sub>H<sub>4</sub> spacer group inhibits access between the two metals.

Related studies were reported by Erker *et al.* utilising the metallo-ligand  $[(\eta\text{-C}_5\text{H}_4\text{CMe}_2\text{PPh}_2)_2\text{ZrCl}_2]$  containing a methyl-substituted one-carbon spacer.[12] Upon reaction with the palladium(II) and platinum(II) salts  $\text{MCl}_2(\text{NCPh})_2$  ( $\text{M} = \text{Pt and Pd}$ ) the bimetallic complexes  $[(\eta\text{-C}_5\text{H}_4\text{CMe}_2\text{PPh}_2)_2\text{ZrCl}_2\text{MCl}_2]$  ( $\text{M} = \text{Pd and Pt}$ ) were obtained. In these examples, the phosphine groups chelate in a *trans*-arrangement around the Group 10 metal, which exhibits a ‘square planar’ co-ordination geometry as shown in **Scheme 1.8**.

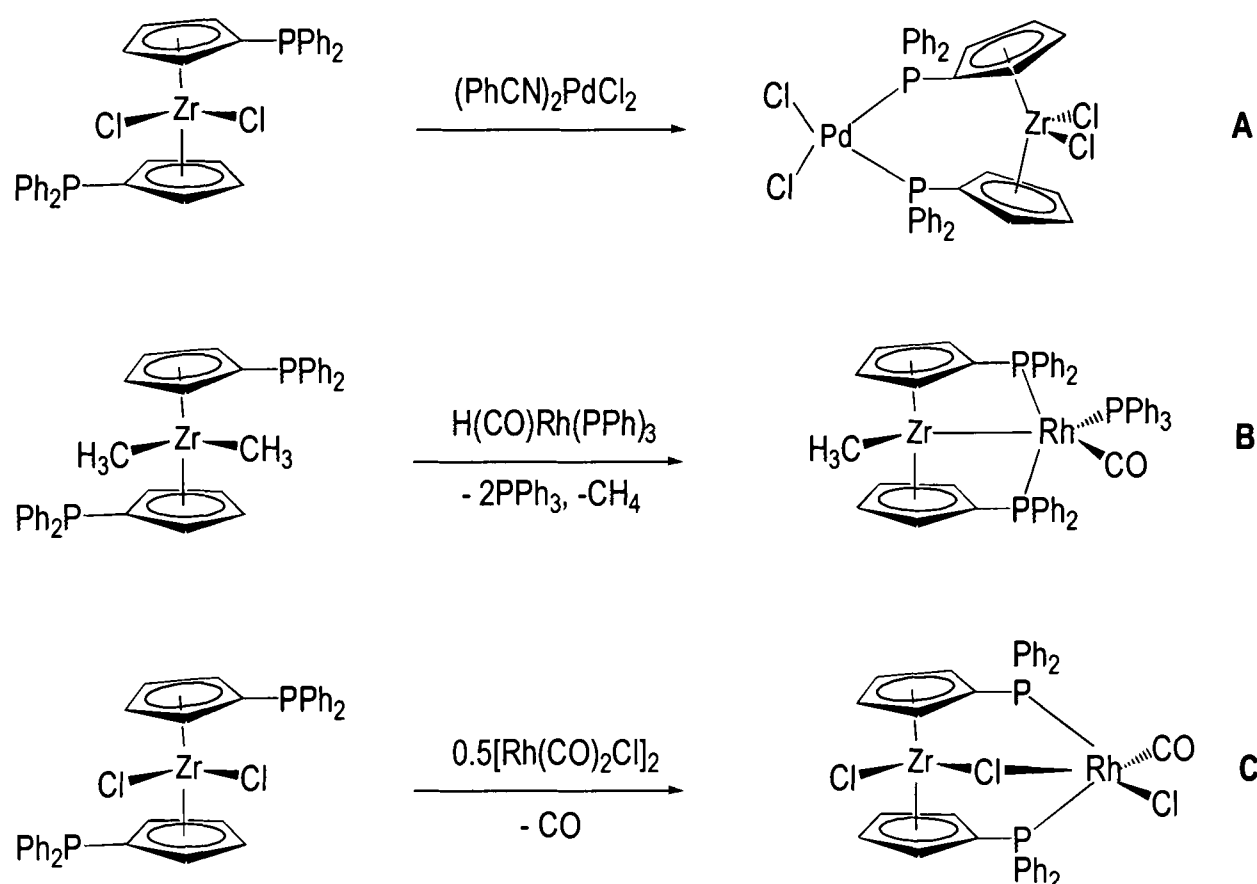


**Scheme 1.8** Bimetallic complexes formed from the reactions between  $\text{MCl}_2(\text{PhCN})_2$  ( $\text{M} = \text{Pt, Pd}$ ) and  $[\text{Zr}\{(\eta\text{-C}_5\text{H}_4)(\text{CR}_2)_n\text{PAr}_2\}_2\text{Cl}_2]$



The presence of a  $^{195}\text{Pt}$  isotope (natural abundance 33.7 %,  $I = \frac{1}{2}$ ) results in a  $^{31}\text{P}$ - $^{195}\text{Pt}$  coupling, the magnitude of which is diagnostic for the identification of *cis*- or *trans*-isomers. In these cases, the observed coupling constants ( $J_{\text{Pt-P}}$ ) for the two platinum analogues were 2605 (Ar = Ph) and 2631 Hz (Ar = *p*-tolyl) indicating that *trans*-structures were present.[12, 32, 33]

Further studies by Erker have resulted in the synthesis of several bimetallic Zr/Pd and Zr/Rh compounds, which have shown potential as catalysts (**Scheme 1.9**). The compound **A** catalyses cross-coupling between *sec*-butylmagnesium bromide and bromobenzene to afford *sec*-butylbenzene while compound **B** has been shown to be an active catalyst for the hydroformylation process.[34]



**Scheme 1.9** Synthesis of novel zirconium/rhodium and zirconium/palladium ELHB complexes

The compound **C** has been characterised by X-ray crystallography and the two metal centres (Zr and Rh) are shown to be connected by the bridging  $\eta\text{-C}_5\text{H}_4\text{-PPh}_2$  ligands as expected. In addition, the metal centres are joined by a  $\mu$ -chloride bridge and the Zr---Rh separation of 2.997(2) Å is only slightly greater than the sum of the covalent radii.[34] An illustration is shown below in **Figure 1.2**.

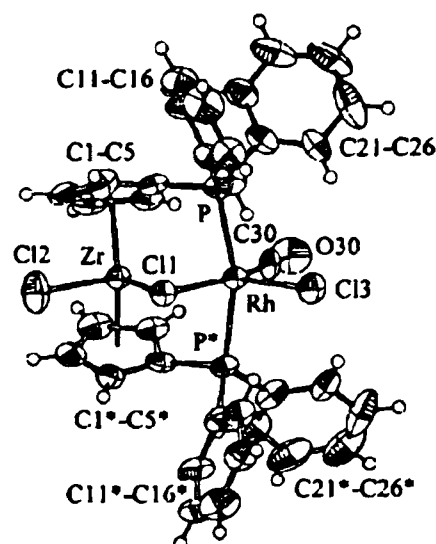
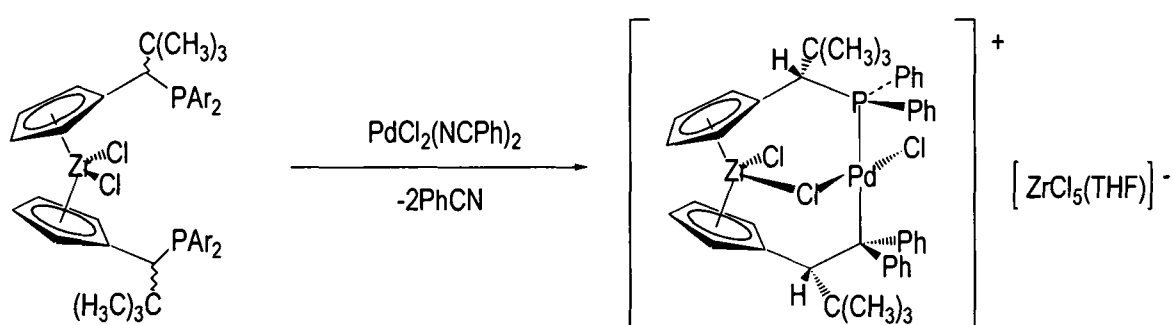


**Figure 1.2** Illustration of the early-late heterobimetallic complex  $[\text{Zr}(\eta\text{-C}_5\text{H}_4\text{PPh}_2)_2\text{Cl}(\mu\text{-Cl})\text{Rh}(\text{CO})\text{Cl}]$

In a similar vein, the reaction between the chelating phosphine system  $[\text{Zr}\{(\eta\text{-C}_5\text{H}_4)\text{CH}(\text{CH}_3)_3\text{PPh}_2\}_2]$  and  $\text{PdCl}_2(\text{PhCN})_2$  results in the cationic complex  $[\text{Zr}(\eta\text{-C}_5\text{H}_4\text{PPh}_2)_2\text{Cl}(\mu\text{-Cl})\text{PdCl}]^+$  (**Scheme 1.10**). The structure of the complex has been determined by X-ray crystallography and the counter anion identified as  $[\text{ZrCl}_5(\text{THF})]^-$ . The two metal centres are bridged by both the bifunctional cyclopentadienyl ligands and the  $\mu$ -chloride moiety as in the Zr/Rh system described earlier. An illustration of the crystal structure is shown in **Figure 1.3**.



**Scheme 1.10** Synthesis of the early-late heterobimetallic complex  $[\text{Zr}(\eta\text{-C}_5\text{H}_4\text{PPh}_2)_2\text{Cl}(\mu\text{-Cl})\text{PdCl}]^+[\text{ZrCl}_5]^-$

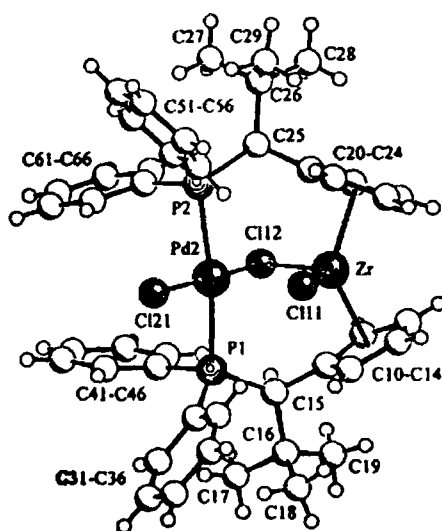


**Figure 1.3** Illustration of the early-late heterobimetallic complex  $[\text{Zr}(\eta\text{-C}_5\text{H}_4\text{CH}(\text{CH}_3)_3\text{PPh}_2)_2\text{Cl}(\mu\text{-Cl})\text{PdCl}]^+$

The synthesis of the compound  $[\text{Zr}\{(\eta\text{-C}_5\text{H}_4)\text{C}_2\text{H}_4\text{PPh}_2\}_2\text{Cl}_2]\text{Mo}(\text{CO})_4$  has been reported by Graham *via* the reaction between  $[\text{Zr}\{(\eta\text{-C}_5\text{H}_4)\text{C}_2\text{H}_4\text{PPh}_2\}_2\text{Cl}_2]$  and  $\text{Mo}(\text{CO})_4(\text{COD})$ .<sup>[10]</sup> Later work by the same author in an effort to incorporate Group 9 metals in bimetallic complexes with the same metallo-ligand resulted in the unexpected formation of tetrametallic complexes.<sup>[30]</sup> However, successful attempts to synthesise bimetallic Zr/Rh complexes have been reported by Erker utilising the analogous bridging bifunctional ligands  $[(\eta\text{-C}_5\text{H}_4)\text{CRR}'\text{PAr}_2]^-$  ( $\text{R} = \text{H}$ ,  $\text{R} = \text{'Bu}$ ;  $\text{R} = \text{R}' = \text{Me}$ ;  $\text{Ar} = \text{Ph, Tol}$ ).<sup>[12]</sup>

The reasons proposed for this difference in behaviour are thought to be a result of the presence or absence of alkyl substituents on the spacer carbon. Using as an example the tetramer shown in **Figure 1.4**, the hydrogen moieties on the methylene spacer carbon come into close contact with the Cl-ligands on the Ti or Rh metal centres. By substituting either or both hydrogens with alkyl groups, the corresponding substituents would come into unacceptably close contact with the Cl-ligands, destabilising the tetrameric structure and favouring the bimetallic arrangement observed by Erker.<sup>[12, 30]</sup>

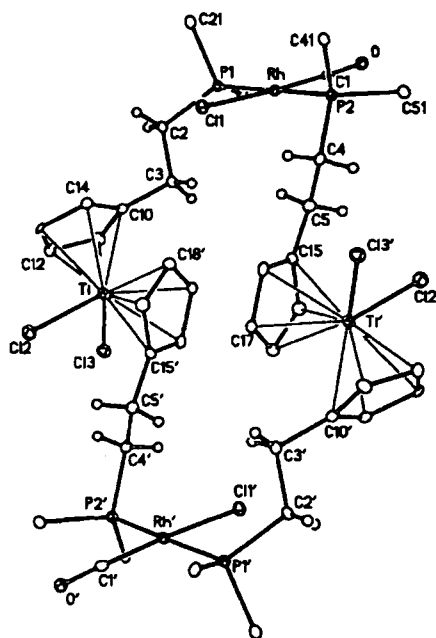
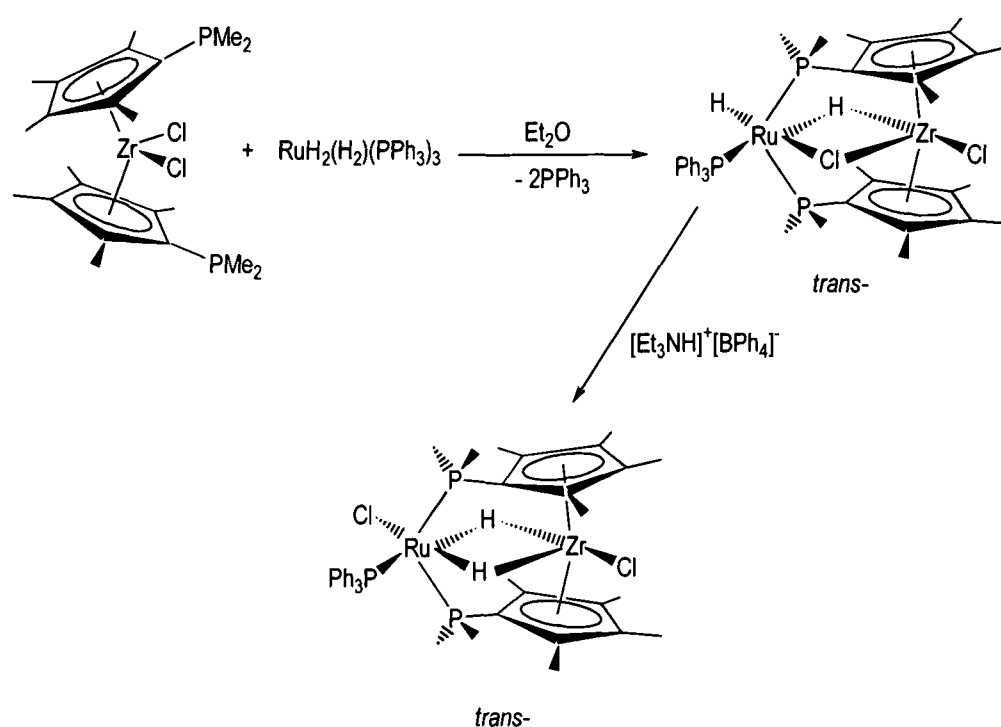


**Figure 1.4** Molecular structure diagram of the dimer complex  $[\text{Ti}(\eta\text{-C}_5\text{H}_4\text{C}_2\text{H}_4\text{PPh}_2)_2\text{Cl}_2\text{Rh}(\text{CO})\text{Cl}]_2$

Bakmutov made an interesting addition to the area of ELHB complexes.<sup>[35]</sup> The reaction between the zirconocene  $[\text{Zr}(\eta\text{-C}_5\text{Me}_4\text{PMe}_2)_2\text{Cl}_2]$  and  $[\text{Ru}(\text{H}_2)\text{H}_2(\text{PPh}_3)_3]$  resulted in the formation of  $[\text{ZrCl}(\mu\text{-C}_5\text{Me}_4\text{PMe}_2)(\mu\text{-H})(\mu\text{-Cl})\text{RuH}(\text{PPh}_3)]$  which undergoes isomerisation, in the presence of the non-coordinating acid  $[\text{HEt}_3\text{N}][\text{BPh}_4]$ , to afford the compound  $[\text{ZrCl}(\mu\text{-C}_5\text{Me}_4\text{PMe}_2)(\mu\text{-H})_2\text{RuCl}(\text{PPh}_3)]$  (**Scheme 1.11**). The bimetallic structure with bifunctional phosphino-cyclopentadienyl ligands and bridging H and Cl bridges was confirmed by an X-ray crystal structure.



**Scheme 1.11** Synthesis of  $[\text{ZrCl}(\eta\text{-C}_5\text{Me}_4\text{PMe}_2)(\mu\text{-H})_2\text{RuCl}(\text{PPh}_3)]$

The compound  $[\text{Ti}(\eta\text{-C}_5\text{H}_5)(\eta\text{-C}_7\text{H}_7)]$ , when treated with  $^n\text{BuLi}$  and  $\text{PMe}_2\text{Cl}$  produces the substituted complex  $[\text{Ti}(\eta\text{-C}_5\text{H}_4\text{PMe}_2)(\eta\text{-C}_7\text{H}_6\text{PMe}_2)]$  and as such is an interesting variation on the bifunctional compounds described above.<sup>[36]</sup> Upon reaction with the carbonyl complexes  $\text{Cr}(\text{CO})_6$  and  $\text{Mo}(\text{CO})_6$ , the heterobimetallic compounds  $[\text{Ti}(\eta\text{-C}_5\text{H}_4\text{PMe}_2)(\eta\text{-C}_7\text{H}_6\text{PMe}_2)\text{Mo}(\text{CO})_4]$  and  $[\text{Ti}(\eta\text{-C}_5\text{H}_4\text{PMe}_2)(\eta\text{-C}_7\text{H}_6\text{PMe}_2)\text{Cr}(\text{CO})_4]$  were obtained in greater than 90 % yields. In both cases, the  $^{31}\text{P}$  NMR resonances of the two non-equivalent phosphorus nuclei were, as expected, shifted to lower field compared to the analogous resonances for the starting material. Moreover, the two phosphorus resonances for the compounds appeared as doublets, providing strong evidence for the co-ordination of the dimethylphosphino groups to the same metal.

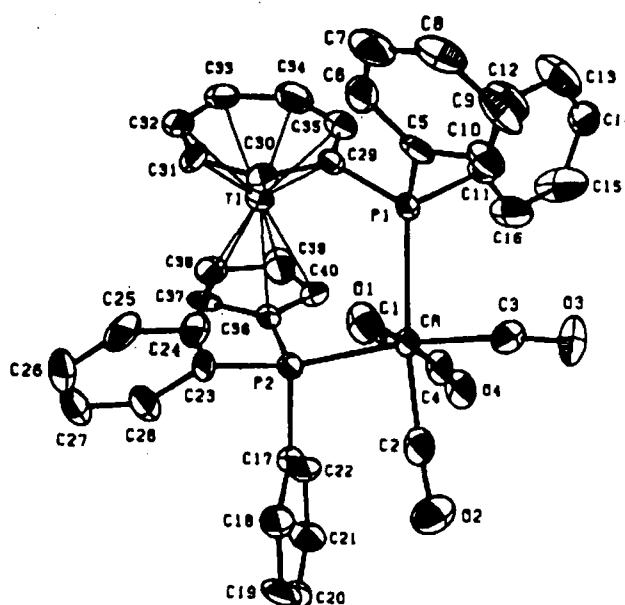


**Figure 1.5** Illustration of the mixed ring bimetallic complex  $[\text{Ti}(\mu\text{-}\eta\text{-C}_5\text{H}_4\text{PPh}_2)(\mu\text{-}\eta\text{-C}_7\text{H}_6\text{PPh}_2)\text{Cr}(\text{CO})_4]$

These conclusions were substantiated by an X-ray structural study on  $[\text{Ti}(\eta\text{-C}_5\text{H}_4\text{PMe}_2)(\eta\text{-C}_7\text{H}_6\text{PMe}_2)]\text{Cr}(\text{CO})_4$ . Thus, the use of inequivalent ring-moieties can be exploited to obtain structural information from  $^{31}\text{P}\{^1\text{H}\}$  NMR studies. Further reaction of the parent ligand with  $\text{Ni}(\text{COD})_2$  afforded the compound  $[\text{Ti}(\eta\text{-C}_5\text{H}_4\text{PMe}_2)(\eta\text{-C}_7\text{H}_6\text{PMe}_2)]_2\text{Ni}$ , after displacement of both COD ligands.[36]

In addition to ELHB complexes, there are also reports of the synthesis of heterobimetallic complexes containing two later transition metals such as W and Mo, Mn and Mo[37] or W and Pd.[38, 39]

#### 1.4.3 Phosphino-substituted Cyclopentadienyl Ligands in Homobimetallic Complexes

In addition to the range of heterobimetallic complexes synthesised utilising the bifunctional ligands described above, a number homobimetallic species have also been reported. Unlike the compounds containing two different metal centres, these complexes often contain metal-metal bonds.[16-18, 20, 40] One of the earliest homobimetallic complexes was reported by Leblanc *et al.*[31] Reaction of the ligand  $[\text{Li}(\text{C}_5\text{H}_4)(\text{CH}_2)_2\text{PPh}_2]$  with the compound  $[\text{Ti}(\eta\text{-C}_5\text{H}_5)\text{Cl}_3]$  affords the complex  $[\text{Ti}(\eta\text{-C}_5\text{H}_5)(\eta\text{-C}_5\text{H}_4)(\text{CH}_2)_2\text{PPh}_2]_2\text{Cl}_2$  in good yield. The compound is a dimer, containing two Ti(III) metal centres.

There are, however, far more examples of homobimetallic complexes formed using the later transition metals. Anderson has reported dimeric complexes of palladium and platinum containing the diphenylphosphinocyclopentadienyl ligand. In these cases, the bifunctional ligand co-ordinates to one metal *via* the phosphino group and to the other through the  $\eta^5$ -cyclopentadienyl moiety (**Figure 1.6**).[29, 41]

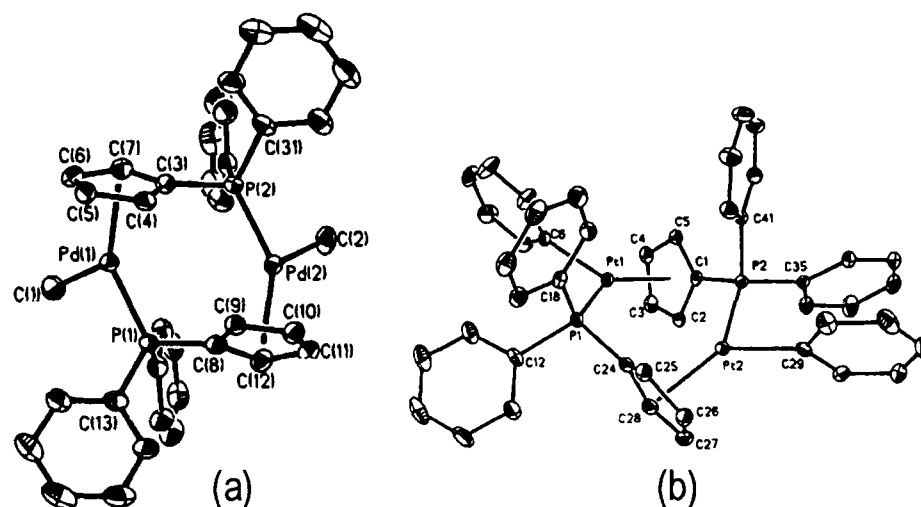


**Figure 1.6** Molecular structure diagrams of the complexes  $[M_2R_2(\mu\text{-}\eta\text{-C}_5\text{H}_4\text{PPh}_2)_2]$   
(a)  $M = \text{Pt}$ ,  $R = \text{Ph}$  (b)  $M = \text{Pd}$ ,  $R = \text{Me}$

Rausch has reported nickel analogues of the complexes shown in **Figure 1.6**, synthesised *via* a reaction between  $[\text{Ti}(\eta\text{-C}_5\text{H}_4)\text{PPh}_2]$  and  $\text{NiBr}_2 \cdot 2\text{DME}$ . The green dimethyl analogue was synthesised *via* reaction between the purple dibromo-compound and two equivalents of methyllithium.[42]

A number of dimeric molybdenum complexes containing bifunctional ligands have been reported,[17, 18] some of which contain a Mo-Mo bond, such as  $[\text{Mo}_2(\mu\text{-}\eta^5\text{-C}_5\text{H}_4\text{PPh}_2)_2(\text{CO})_4]$  illustrated in **Figure 1.7**. [16]

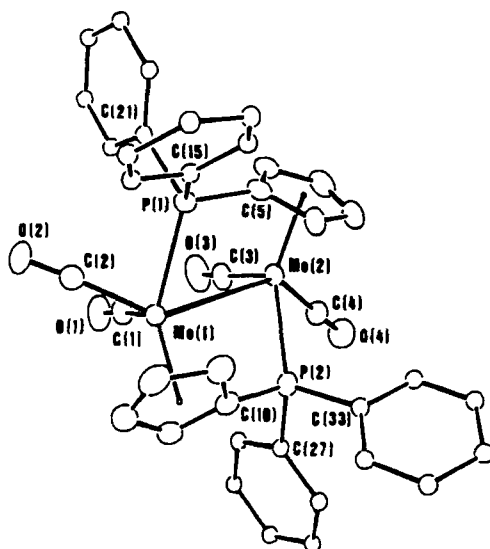


**Figure 1.7** Illustration of the dimolybdenum complex  $[\text{Mo}_2(\text{CO})_4(\mu\text{-}\eta\text{-C}_5\text{H}_4\text{PPh}_2)_2]$

Similar behaviour is also demonstrated by Ir and Rh analogues<sup>[43]</sup>, which are synthesised *via* reaction between *trans*-[RhCl(CO)PPh<sub>3</sub>]<sub>2</sub> or *trans*-IrCl(CO)(PPh<sub>3</sub>)<sub>2</sub> and the bifunctional ligand Li[(C<sub>5</sub>H<sub>4</sub>)PPh<sub>2</sub>]. In each case, the phosphorus atom is bonded to an 18-electron rhodium centre in a 'head to tail' arrangement. An alternative preparation involves heating the monomeric complex [Rh(η-C<sub>5</sub>H<sub>4</sub>)PPh<sub>2</sub>(CO)PPh<sub>3</sub>] (in which the phosphino substituent cannot co-ordinate to the metal centre) to 60°C in toluene. Elimination of the PPh<sub>3</sub> group allows for co-ordination of the phosphino-substituent from another Rh(η-C<sub>5</sub>H<sub>4</sub>)PPh<sub>2</sub>(CO) fragment.

The resulting dimeric complex [Rh(η-C<sub>5</sub>H<sub>4</sub>)PPh<sub>2</sub>(CO)]<sub>2</sub> has a metal-metal distance of 4.3029 (6) Å which seemed too long to suggest co-operative reactivity between the two metal sites.<sup>[40]</sup> However, further studies on this compound by He *et al.* resulted in the complex [Rh<sub>2</sub>{(η-C<sub>5</sub>H<sub>4</sub>)PPh<sub>2</sub>}<sub>2</sub>(CO)(COCH<sub>3</sub>)] [SO<sub>3</sub>CF<sub>3</sub>] after reaction with methyl triflate. The resulting cation contains a Rh-Rh bond measuring 2.7319 Å (**Figure 1.8**). The mechanism is postulated to include fast attack of one of the Rh atoms by CH<sub>3</sub><sup>+</sup> followed by formation of a dative metal-metal bond, leading to migration of the methyl-group, resulting in product formation. Thus, this is an example of *intra* molecular promotion of alkyl migration resulting from co-operation between the two metal centres.<sup>[40]</sup>

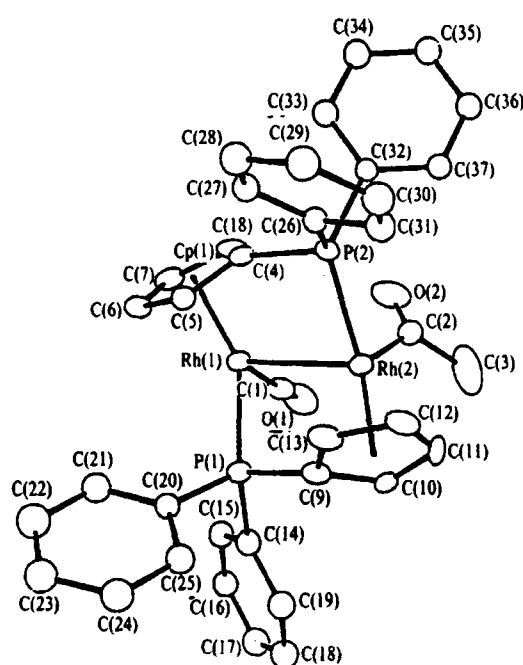


**Figure 1.8** Illustration of the dirhodium complex [Rh<sub>2</sub>(η-C<sub>5</sub>H<sub>4</sub>PPh<sub>2</sub>)<sub>2</sub>(CO)(COCH<sub>3</sub>)]<sup>+</sup>

## 1.5 Summary

This chapter has provided a brief review of recent developments in the field of dialkyl- and diaryl-phosphino substituted cyclopentadienyl complexes. The different examples illustrate the variety of complexes available using this type of ligand. Essentially, there are three different classes of complex possible. The monometallic species, as typified by the cobalt complex  $[(\eta\text{-C}_5\text{H}_4)\text{CH}_2\text{CH}_2\text{P}^t\text{Bu}_2\text{Co}(\eta\text{-CH}_2\text{CH}_2)]$  can exhibit *intramolecular* co-ordination of the pendant phosphine functionality depending on the nature of other substituents. The bifunctional ligands have more recently been utilised to synthesise heterobimetallic complexes such as  $[(\eta\text{-C}_5\text{H}_4)\text{C}_2\text{H}_4\text{PPh}_2]_2\text{ZrCl}_2\text{Mo}(\text{CO})_4$  and  $[(\eta\text{-C}_5\text{H}_4\text{CMe}_2\text{PPh}_2)_2\text{ZrCl}_2\text{PdCl}_2]$ , which incorporate both early and later transition metals and finally homobimetallic complexes of the later transition metals including  $[\text{Pd}_2\text{Me}_2(\mu\text{-}\eta\text{-C}_5\text{H}_4\text{PPh}_2)_2]$  have been reported.

The remainder of this part of the thesis describes the synthesis of some novel dialkylphosphino-substituted cyclopentadienyl ligands and the preparation of a number transition metal complexes thereof. Studies into the potential for these complexes to act as metallo-ligands are also described.



## 1.6 References for Chapter 1

- [1] T. Ireland, G. Grossheimann, C. Wieser-Jeunesse and P. Knochel, *Angew. Chem. Int. Ed. Engl.*, **38** (1999) 3212.
- [2] N. J. Goodwin, W. Henderson and B. K. Nicholson, *Inorg. Chim. Acta.*, **295** (1999) 18.
- [3] H. C. L. Abbenhuis, U. Burckhardt, V. Gramlich, A. Togni, A. Albinati and B. Muller, *Organometallics*, **13** (1994) 4481.
- [4] I. M. Lorkovic, M. S. Wrighton and W. M. Davis, *J. Am. Chem. Soc.*, **116** (1994) 6220.
- [5] M. Viotte, B. Gautheron, M. M. Kubicki, Y. Mugnier and R. V. Parish, *Inorg. Chem.*, **34** (1995) 3465.
- [6] G. Wilkinson, M. Rosenblum, M. C. Whiting and R. B. Woodward, *J. Am. Chem. Soc.*, **74** (1952) 2125.
- [7] E. O. Fischer, *Z. Naturforsch.*, **7b** (1952) 377.
- [8] P. Jutzi and U. Siemeling, *J. Organomet. Chem.*, **500** (1995) 175.
- [9] S. Ciruelos, U. Englert and A. Salzer, *Organometallics*, **19** (2000) 2240.
- [10] T. W. Graham, A. Llamazares, R. McDonald and M. Cowie, *Organometallics*, **18** (1999) 3490.
- [11] D. M. Bensley, E. A. Mintz and S. J. Sussangkarn, *J. Org. Chem.*, **53** (1988) 4417.
- [12] B. Bosch, G. Erker and R. Fröhlich, *Inorg. Chim. Acta.*, **270** (1998) 446.
- [13] F. Mathey and J.-P. Lampin, *Tetrahedron*, **31** (1975) 2685.
- [14] J. Szymoniak, J. Besancon, A. Dormond and C. Moise, *J. Org. Chem.*, **55** (1990) 1429.
- [15] I. Lee, F. Dahan, A. Maisonnat and R. Poilblanc, *J. Organomet. Chem.*, **532** (1997) 159.
- [16] B. Brumas-Soula, D. de Montauzon and R. Poilblanc, *New J. Chem.*, **19** (1995) 757.
- [17] B. Brumas, D. de Caro, F. Dahan, D. de Montauzon and R. Poilblanc, *Organometallics*, **12** (1993) 1502.
- [18] B. Brumas, F. Dahan, D. de Montauzon and R. Poilblanc, *J. Organomet. Chem.*, **453** (1993) C13.

- 
- [19] D. DuBois, C. W. Eigenbrot, A. Miedaner, J. C. Smart and R. C. Haltiwanger, *Organometallics*, **5** (1986) 1405.
- [20] X.-D. He, A. Maisonnat, F. Dahan and R. Poilblanc, *Organometallics*, **8** (1989) 2618.
- [21] R. T. Kettenbach, W. Bonrath and H. Butenschon, *Chem. Ber.*, **126** (1993) 1657.
- [22] R. T. Kettenbach and H. Butenschon, *New. J. Chem.*, **14** (1990) 599.
- [23] H. Butenschon, R. T. Kettenbach and C. Krüger, *Angew. Chem. Int. Ed. Engl.*, **31** (1992) 166.
- [24] T. A. Mobley and R. G. Bergman, *J. Am. Chem. Soc.*, **120** (1998) 3253.
- [25] B. E. Bosch, G. Erker, R. Fröhlich and O. Meyer, *Organometallics*, **16** (1997) 5449.
- [26] I. Ara, E. Delgado, J. Fornies, E. Hernandez, E. Lalinde, N. Mansilla and M. T. Moreno, *J. Chem. Soc., Dalton Trans.*, (1996) 3201.
- [27] R. M. Bullock, *Acc. Chem. Res.*, **20** (1987) 167.
- [28] W. Tikkanen, Y. Fujita and J. L. Petersen, *Organometallics*, **5** (1986) 888.
- [29] F. T. Ladipo, G. K. Anderson and N. P. Rath, *Organometallics*, **13** (1994) 4741.
- [30] T. W. Graham, A. Llamazares, R. McDonald and M. Cowie, *Organometallics*, **18** (1999) 3502.
- [31] J. C. Leblanc, C. Moise, A. Maisonnat, R. Poilblanc, C. Charrier and F. Mathey, *J. Organomet. Chem.*, **231** (1982) C43.
- [32] R. G. Pregosin, in J. G. Verkade and, L. D. Quin (Eds.): *Stereochemistry of Metal Complexes: Unidentate Phosphorus Ligands, Phosphorus-31 NMR Spectroscopy in Stereochemical Analysis; Organic Compounds and Metal Complexes*, VCH, Weinheim 1987, p. 465.
- [33] R. Favez, R. Roulet, A. A. Pinkerton and D. Schwarzenbach, *Inorg. Chem.*, **19** (1980) 1356.
- [34] B. E. Bosch, I. Brummer, K. Künz, G. Erker, R. Fröhlich and S. Kotila, *Organometallics*, **19** (2000) 1255.
- [35] V. I. Bakhmutov, M. Visseaux, D. Baudry, A. Dormond and P. Richard, *Inorg. Chem.*, **35** (1996) 7316.
- [36] M. Ogasa and M. D. Rausch, *J. Organomet. Chem.*, **403** (1991) 279.
- [37] C. P. Casey and R. M. Bullock, *Organometallics*, **1** (1982) 1591.

- [38] L. Spadoni, C. L. Sterzo, R. Crescenzi and G. Frachley, *Organometallics*, *14* (1995) 3149.
- [39] S. Rigny, V. I. Bakhumotov, B. Nuber, J.-C. Leblanc and C. Moise, *Inorg. Chem.*, *35* (1996) 3202.
- [40] X. He, A. Maissonat, F. Dahan and R. Poilblanc, *New J. Chem.*, *14* (1990) 313.
- [41] G. K. Anderson, M. Lin and M. Y. Chiang, *Organometallics*, *9* (1990) 288.
- [42] M. S. Blais, R. D. Rogers and M. D. Rausch, *J. Organomet. Chem.*, *593* (2000) 142.
- [43] X.-D. He, A. Maisonnat, F. Fahan and R. Poilblanc, *Organometallics*, *6* (1987) 678.

## **Chapter 2**

### **Dimethylphosphino-Substituted Cyclopentadienyl Complexes**

## 2.0 Introduction to Chapter 2

This chapter describes the preparation of a novel, dimethylphosphino-substituted tetramethylcyclopentadienyl ligand  $[(C_5Me_4)CH_2PMe_2]^-$  and the synthesis of several transition metal metallocene complexes incorporating this new ligand. In addition, some reactivity studies of the new complexes, particularly with respect to forming bimetallic complexes, are described.

The use of 1-(diphenylphosphino)cyclopentadienide as a bridging ligand in the synthesis of homo- and hetero-bimetallic complexes has been utilised by a number of research groups.[1-6] The interest in the area stems from the possibility that heterobimetallic complexes may demonstrate unusual catalytic activity as a result of their ability to activate substrate molecules at two different metal sites. A second attractive feature is that heterobimetallic complexes derived from  $C_5H_4PR_2$  ligands may also exhibit redox catalytic properties.

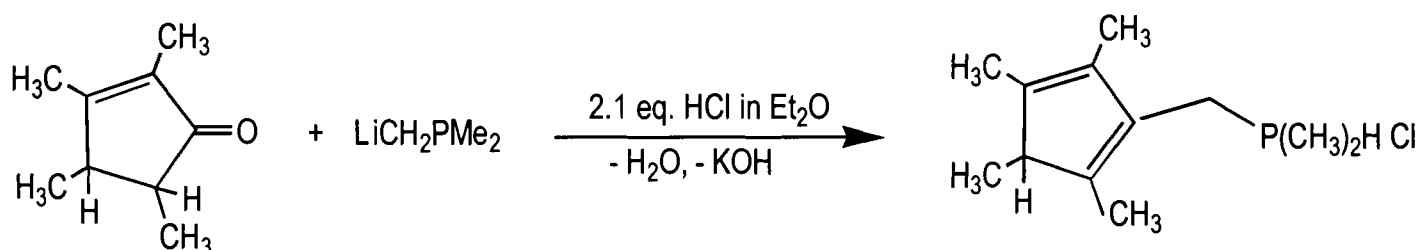
In this study, the introduction of an alkyl-spacer methylene group between the phosphinodialkyl and cyclopentadienyl groups was investigated in anticipation that it might alleviate the geometric restrictions placed upon ligands where the  $PR_2$  moiety is directly bound to the cyclopentadienyl ring.[1, 4, 7-9] The presence of the spacer group might allow for increased conformational freedom of both metal co-ordination spheres. As a result, a dimethylphosphino-substituted cyclopentadienyl ring containing a “C<sub>1</sub>” methylene spacer between the two functionalites was chosen. The one-carbon bridge has been exploited by several other groups, although none of these have reported the  $-CH_2PMe_2$  moiety as a substituent.[1, 3, 10]

A number of synthetic routes to the ligands described above have been detailed in the introductory chapter. The route devised for the preparation of the ligand used in this chapter utilises  $LiCH_2PMe_2$  and its addition to tetramethylcyclopentene-2-one. The subsequent acid work-up gives  $[HC_5Me_4CH_2PMe_2H][Cl]$  (1) which is then converted to  $[HC_5Me_4CH_2PMe_2H][PF_6]$  (2) before further conversion to the compounds  $[M(C_5Me_4)CH_2PMe_2]$  {M = H (3), K (4), Na (5), Li (6)}.

## 2.1 Preparation of Ligand Precursors $[\text{HC}_5\text{Me}_4\text{CH}_2\text{PMe}_2\text{H}][\text{X}]$ ( $\text{X} = \text{Cl}, \text{PF}_6$ )

### 2.1.1 Preparation of $[\text{H}(\text{C}_5\text{Me}_4)\text{CH}_2\text{PMe}_2\text{H}][\text{Cl}]$ (1)

A THF solution of 1,2,3,4-tetramethylcyclopentene-2-one was added slowly to a THF solution of  $\text{LiCH}_2\text{PMe}_2$  at  $-78^\circ\text{C}$ . After warming to room temperature and stirring for twelve hours, the yellow solution was again cooled to  $-78^\circ\text{C}$ . A solution of hydrogen chloride in diethyl ether (1.0 M) was added dropwise over thirty minutes and the resulting white suspension stirred for 6 hours before being filtered through a glass frit and washed several times with pentane. Removal of remaining volatiles under reduced pressure afforded the compound  $[\text{HC}_5\text{Me}_4\text{CH}_2\text{PMe}_2\text{H}][\text{Cl}]$  (1) as a flocculant white solid in approximately 80% yield (**Scheme 2.1**).



**Scheme 2.1** Synthesis of  $[\text{H}(\text{C}_5\text{Me}_4)\text{CH}_2\text{PMe}_2\text{H}][\text{Cl}]$  (1)

### 2.1.2 Characterisation of $[\text{H}(\text{C}_5\text{Me}_4)\text{CH}_2\text{PMe}_2\text{H}][\text{Cl}]$ (1)

The compound **1** is a moderately air-sensitive white solid, which is soluble in acetone, methanol and degassed water. Characterising data are given in **Section 8.1**. Although a number of isomers are possible as a result of the protonated Cp-ring, the NMR studies suggest that only one isomer is present.

The  $^1\text{H}$  NMR spectrum of **1** in  $\text{d}^6$ -acetone exhibits eight resonances. The signal for the single ring proton appears as a multiplet at  $\delta$  2.85, while the associated methyl group resonates as a doublet [ $^3J_{\text{H-H}} = 8.0$  Hz] at  $\delta$  1.08. The protons on the methylene backbone are diastereotopic and are represented by a pair of triplets at  $\delta$  3.51 and 3.90, each affording an integration value consistent with that for a single proton. A selective  $^1\text{H}\{^31\text{P}\}$  NMR decoupling experiment was used to identify the resonance and determine the magnitude of the geminal coupling, [ $^2J_{\text{Ha-Hb}} = 15$  Hz], for the methylene protons.

Assignment of the two sets of phosphinodimethyl protons was also made *via* use of a selective  $^1\text{H}\{^3\text{P}\}$  NMR experiment. On increasing the decoupler power, the doublets at  $\delta$  2.06 and 2.10 collapsed to singlets and therefore the phosphinodimethyl protons are assigned as a pair of doublets at  $\delta$  2.06 and 2.10 [ $^2J_{\text{H-P}} = 14.5$  Hz]

The  $^{13}\text{C}\{^1\text{H}\}$  NMR spectrum displays twelve chemically distinct  $^{13}\text{C}$  environments and displays couplings to  $^3\text{P}$ . The  $^{13}\text{C}$  resonances of the Cp-ring are observed at  $\delta$  49.93, 127.1, 127.2, 134.3 and 143.3. The four substituent methyl groups on the Cp-ring are observed as singlets at  $\delta$  9.97, 10.83, 11.14 and 13.10 while the dimethylphosphino  $^{13}\text{C}$  signals resonate as doublets at  $\delta$  2.51 and 2.93 [ $J_{\text{P-C}} = 28.9$  Hz] and the methylene spacer group at  $\delta$  17.96 [ $J_{\text{P-C}} = 28.9$  Hz] (**Figure 2.1**).

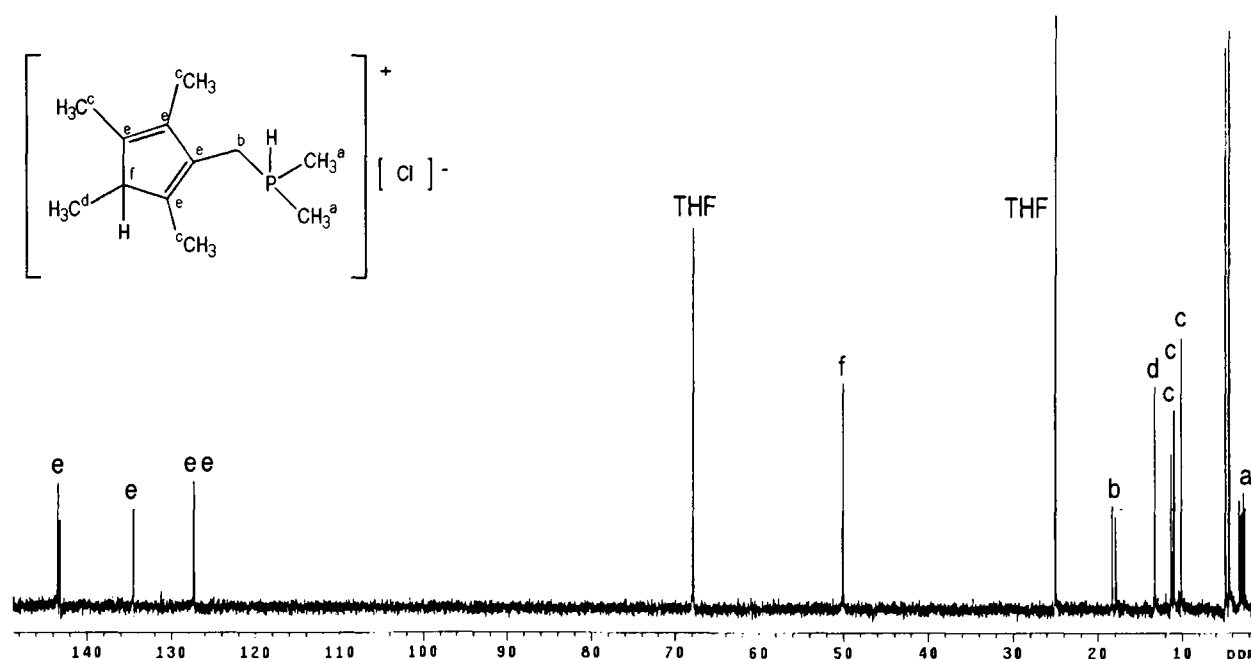


**Figure 2.1**  $^{13}\text{C}\{^1\text{H}\}$  NMR spectrum of  $[\text{H}(\text{C}_5\text{Me}_4)\text{CH}_2\text{PMe}_2\text{H}][\text{Cl}]$  (**1**) ( $\text{D}_2\text{O}$ ) (THF refers to signals due to residual THF from the reaction mixture)

An HMQC (Heteronuclear Multiple Quantum Coherence) 2D-correlation NMR spectroscopy technique was performed, in order to unambiguously assign the  $^{13}\text{C}$  and  $^1\text{H}$  signals of the ligand (**Figure 2.2**). The  $^1\text{H}$  resonance at  $\delta$  1.08 for the methyl group on the protonated cyclopentadienyl carbon correlates to the  $^{13}\text{C}$  signal at  $\delta$  13.10, while the remaining ring-methyl groups with the  $^1\text{H}$  resonances at  $\delta$  1.77, 1.86 and 1.93 show correlation to the  $^{13}\text{C}$  signals at  $\delta$  9.97, 10.86 and 11.14, respectively. Finally, the dimethylphosphino protons, resonating at  $\delta$  2.06 and 2.10, display strong

correlations to the  $^{13}\text{C}$  signals at  $\delta$  2.53 and 2.91 respectively. On the basis of these observations, the  $^1\text{H}$  and  $^{13}\text{C}$  spectra have been assigned.

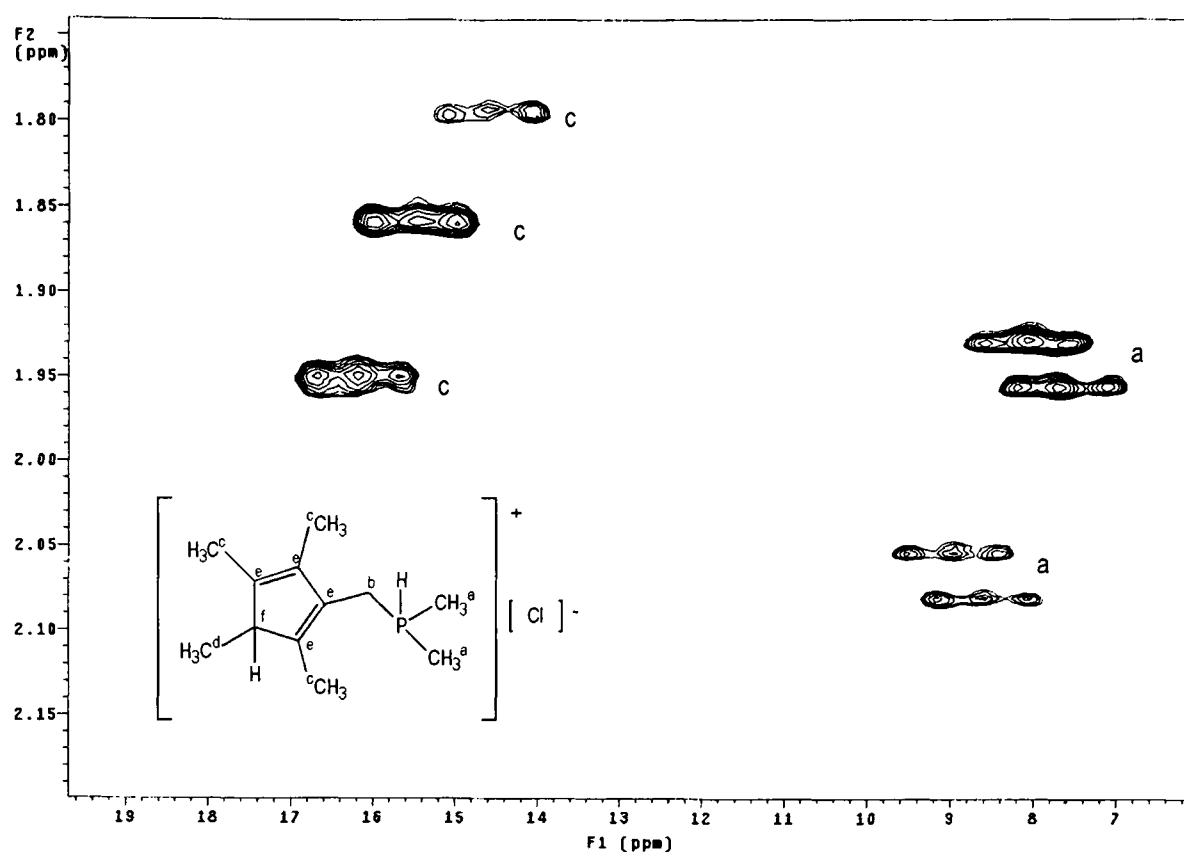
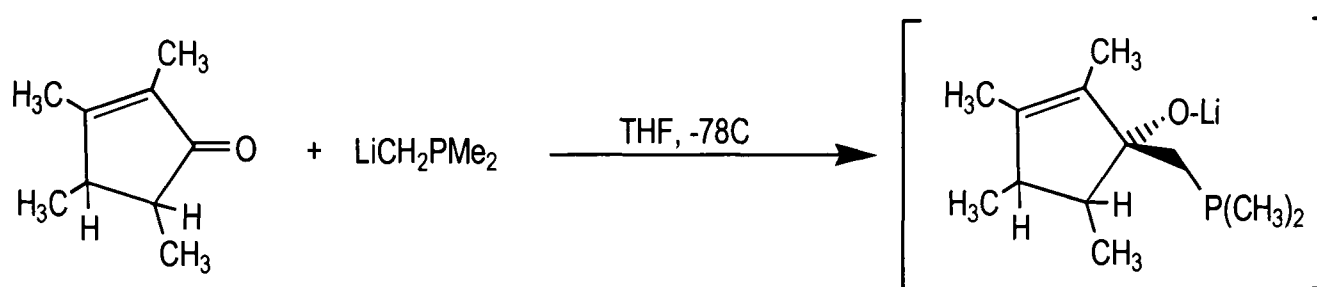


**Figure 2.2**  $^{13}\text{C}$ - $^1\text{H}$  HMQC NMR spectrum of  $[\text{H}(\text{C}_5\text{Me}_4)\text{CH}_2\text{PMe}_2\text{H}][\text{Cl}]$  (**1**)

The  $^{31}\text{P}\{^1\text{H}\}$  NMR spectrum displays a phosphorus signal at  $\delta$  40.4, which is a comparable chemical shift with tetravalent phosphonium ions. Failure to obtain the compound as an analytically pure sample, however, led to the preparation of the hexafluorophosphate salt (**2**), which is described fully in **Section 2.2.1** below.

The mechanism of formation of compound **1** is thought to proceed *via* a molecular intermediate containing an  $\text{O}^-\text{Li}^+$  pendant group, which is subsequently acidified and hydrolysed with HCl in diethyl ether (**Scheme 2.2**). Attempts to isolate the intermediate part way through the reaction by removing an aliquot followed by removal of solvents under reduced pressure yielded a viscous, yellow oil. However, the  $^1\text{H}$  NMR spectrum ( $d^8$ -toluene) was complex and demonstrated the presence of a number of species in the mixture.



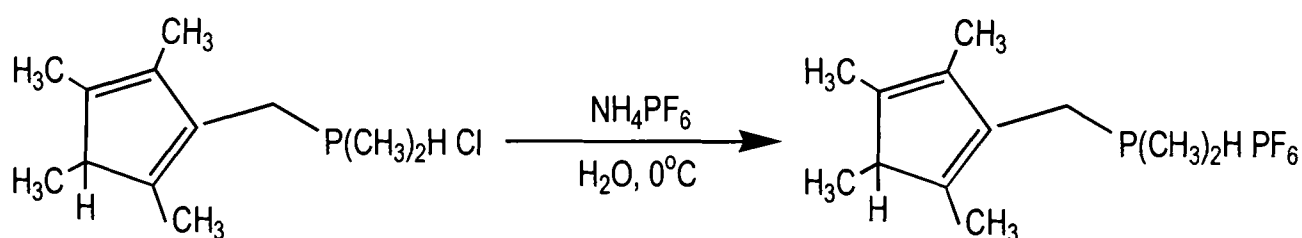


**Scheme 2.2** Possible formation of intermediate species in the reaction between  $\text{LiPCH}_2\text{Me}_2$  and 1,2,3,4-tetramethylcyclopentene-2-one

### 2.1.3 Preparation of $[\text{H}(\text{C}_5\text{Me}_4)\text{CH}_2\text{PMe}_2\text{H}][\text{PF}_6]$ (2)

An analytically pure sample of compound **1** was not obtained. Hence, replacement of the chloride counter-anion with a larger species,  $[\text{PF}_6]^-$ , which is less soluble in water, was attempted in the expectation of being able to achieve precipitation of a pure compound.

To a pale yellow solution of compound **1** in degassed water was added *via* cannula an aqueous solution of ammonium hexafluorophosphate  $[\text{NH}_4][\text{PF}_6]$  at  $0^\circ\text{C}$ . Immediately upon addition, precipitation of a white solid occurred. The product was transferred onto a glass frit, filtered and then washed several times with cold water. Residual water was removed from the resulting white solid under reduced pressure to yield the compound  $[\text{H}(\text{C}_5\text{Me}_4)\text{CH}_2\text{PMe}_2\text{H}][\text{PF}_6]$  (**2**) as a white solid in 85 % yield (**Scheme 2.3**).



**Scheme 2.3** Synthesis of the compound  $[\text{H}(\text{C}_5\text{Me}_4)\text{CH}_2\text{PMe}_2\text{H}][\text{PF}_6]$  (**2**)

### 2.1.4 Characterisation of $[\text{H}(\text{C}_5\text{Me}_4)\text{CH}_2\text{PMe}_2\text{H}][\text{PF}_6]$ (**2**)

The compound **2**, like the hydrochloride analogue **1**, is a moderately air-sensitive white solid, soluble in acetone and methanol. Microanalysis results are consistent with the empirical formula  $\text{C}_{12}\text{H}_{22}\text{F}_6\text{P}_2$ . Characterising data are given in **Section 8.2**.

The  $^1\text{H}$  NMR spectrum of **2** in  $\text{d}^6$ -acetone is shown in **Figure 2.3** and exhibits nine resonances. The signal for the single ring proton appears as a multiplet at  $\delta$  2.86, while the associated methyl group resonates as a doublet [ $^2J_{\text{H-H}} = 15.0$  Hz] at  $\delta$  1.07. The protons on the methylene backbone are inequivalent and are represented by a pair of triplets at  $\delta$  3.35 and 3.69, each affording an integration value consistent with that for a single proton. A selective  $^1\text{H}\{^{31}\text{P}\}$  NMR decoupling experiment was used to assign the resonance and determine the magnitude of the geminal coupling for the methylene protons [ $^2J_{\text{Ha-Hb}} = 15$  Hz].

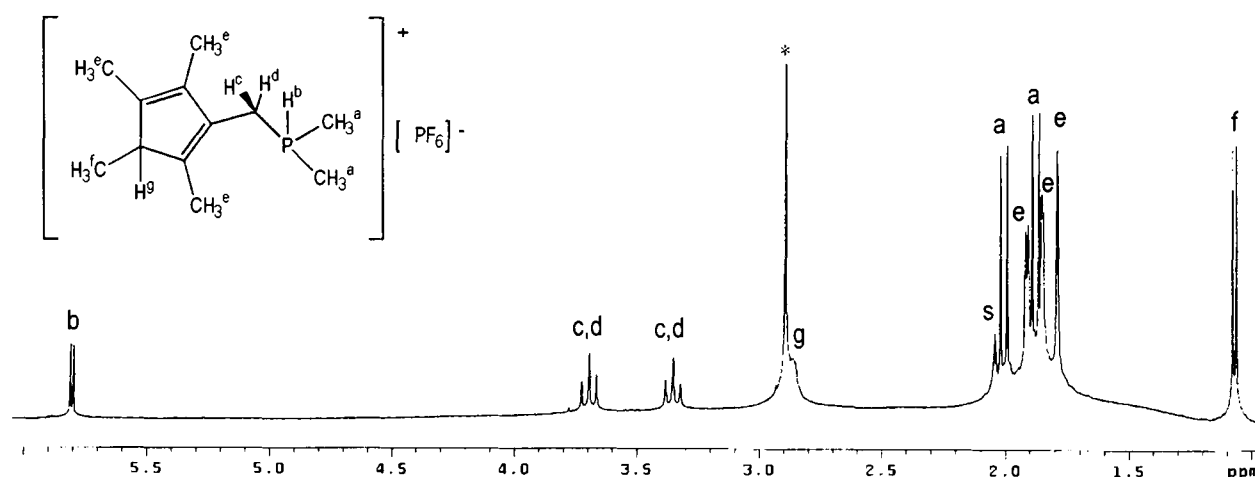


**Figure 2.3**  $^1\text{H}$  NMR spectrum of  $[\text{H}(\text{C}_5\text{Me}_4)\text{CH}_2\text{PMe}_2\text{H}][\text{PF}_6]$  (**2**) ('s' denotes  $\text{d}^6$ -acetone) (the asterisk \* denotes signal due to residual water)

Assignment of the two sets of phosphinodimethyl protons was also made *via* use of a selective  $^1\text{H}\{^{31}\text{P}\}$  NMR experiment. On increasing the decoupler power, the doublets at  $\delta$  1.88 and 2.00 collapsed to singlets and so the phosphinodimethyl protons are assigned as a pair of doublets at  $\delta$  1.88 and 2.00 [ $^2J_{\text{H-P}} = 13.5$  Hz].

The  $^{13}\text{C}\{^1\text{H}\}$  NMR spectrum displays twelve chemically distinct  $^{13}\text{C}$  environments and exhibits couplings to  $^{31}\text{P}$ . The  $^{13}\text{C}$  resonances of the Cp-ring are observed at  $\delta$  50.7, 127.3, 134.3, 142.5 and 143.2. The four substituent methyl groups are observed as singlets at  $\delta$  11.3, 11.8, 12.4 and 13.8 while the dimethylphosphino  $^{13}\text{C}$  signals

resonate as doublets at  $\delta$  2.50 and 3.32 [ $J_{\text{P-C}} = 47.8$  Hz] and the methylene spacer group at  $\delta$  17.8 [ $J_{\text{P-C}} = 46.5$  Hz].

An HMQC NMR spectroscopy 2D-correlation technique was performed, in order to unambiguously assign the  $^{13}\text{C}$  and  $^1\text{H}$  signals of the ligand (**Figure 2.4**). The  $^1\text{H}$  resonance at  $\delta$  1.07 for the methyl group on the protonated cyclopentadienyl carbon correlates to the  $^{13}\text{C}$  signal at  $\delta$  13.8, while the remaining ring-methyl groups with the  $^1\text{H}$  resonances at  $\delta$  1.07,  $\delta$  1.80 and  $\delta$  1.86 show correlation to the  $^{13}\text{C}$  signals at  $\delta$  9.97, 10.86 and 11.14, respectively. Finally, the dimethylphosphino protons resonating at  $\delta$  1.88 and 2.00 display strong correlations to the  $^{13}\text{C}$  signals at  $\delta$  2.50 and 3.32. On the basis of these observations, the  $^1\text{H}$  and  $^{13}\text{C}$  spectra have been assigned.

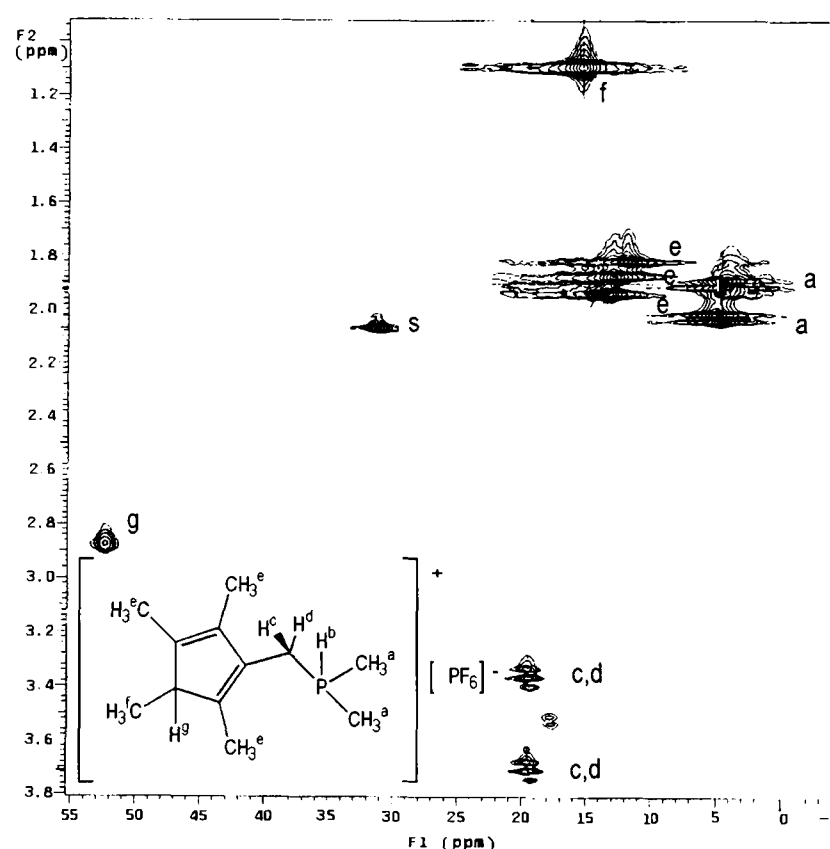


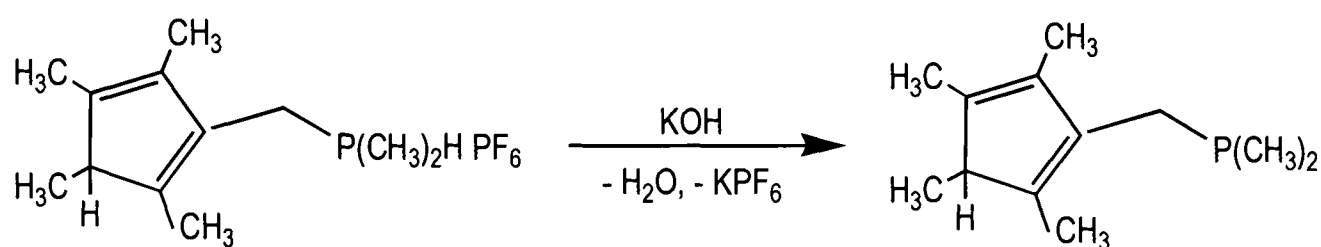
**Figure 2.4**  $^{13}\text{C}$ - $^1\text{H}$  HMQC NMR spectrum of  $[\text{H}(\text{C}_5\text{Me}_4)\text{CH}_2\text{PMe}_2\text{H}][\text{PF}_6]$  (**2**) ('s' denotes  $\text{d}^6$ -acetone signal)

The  $^{31}\text{P}\{^1\text{H}\}$  NMR spectrum displays the phosphino-methyl phosphorus as a singlet at  $\delta$  37.5 which is comparable to the shift value obtained for compound **1** and the hexafluorophosphate moiety as a septet centred on  $\delta$  -144.6 [ $J_{\text{P-F}} = 710$  Hz]. The  $^{19}\text{F}$  spectrum consists of a doublet, attributable to the  $[\text{PF}_6]^-$  counter anion at  $\delta$  -195.5 [ $J_{\text{F-P}} = 710$  Hz].

## 2.2 Preparation of the ligands $[M(C_5Me_4)CH_2PMe_2]$ ( $M = H, K, Na, Li$ )

### 2.2.1 Preparation of $[HC_5Me_4CH_2PMe_2]$ (3)

To a saturated solution of compound **2** in degassed methanol at room temperature was added a methanol solution of potassium hydroxide (**Scheme 2.4**). On addition, the suspension changed to a cloudy solution with the concomitant evolution of a phosphine odour. Several aliquots of pentane were then added to extract the neutral ligand. Upon separation of the two layers, the resulting pale yellow pentane layer was removed and dried with anhydrous magnesium sulfate. After filtration and removal of solvents under reduced pressure the compound  $[H(C_5Me_4)CH_2PMe_2]$  (**3**) was isolated in 45 % yield as a very pale-yellow oil.



**Scheme 2.4** Synthesis of the compound  $[HC_5Me_4CH_2PMe_2]$  (**3**)

### 2.2.2 Characterisation of $[HC_5Me_4CH_2PMe_2]$ (**3**)

The compound **3** is a water stable, air sensitive, pale-yellow oil at room temperature. It is soluble in pentane, toluene, benzene, THF and diethyl ether. Exposure to air results in the formation of an insoluble white solid which is presumably the phosphine oxide complex. Satisfactory elemental analyses were precluded by the air-sensitive nature of the compound. Characterising data are given in **Section 8.3**.

The  $^1H$  NMR spectrum of **3** in  $d^6$ -benzene is shown in **Figure 2.5** and displays nine resonances. The signal for the single ring proton appears as a multiplet at  $\delta$  2.85, while the associated methyl group resonates as a doublet [ $^2J_{H-H} = 12.5$  Hz] at  $\delta$  1.07. The two protons on the methylene backbone are inequivalent, giving rise to signals at  $\delta$  2.31 and 2.41 [ $^2J_{Ha-Hb} = 12.5$  Hz] and [ $^2J_{H-P} = 3.5$  Hz]. A selective  $^1H\{^{31}P\}$  decoupling experiment was used to determine the magnitude of the geminal coupling, [ $^2J_{Ha-Hb} = 14.5$  Hz].

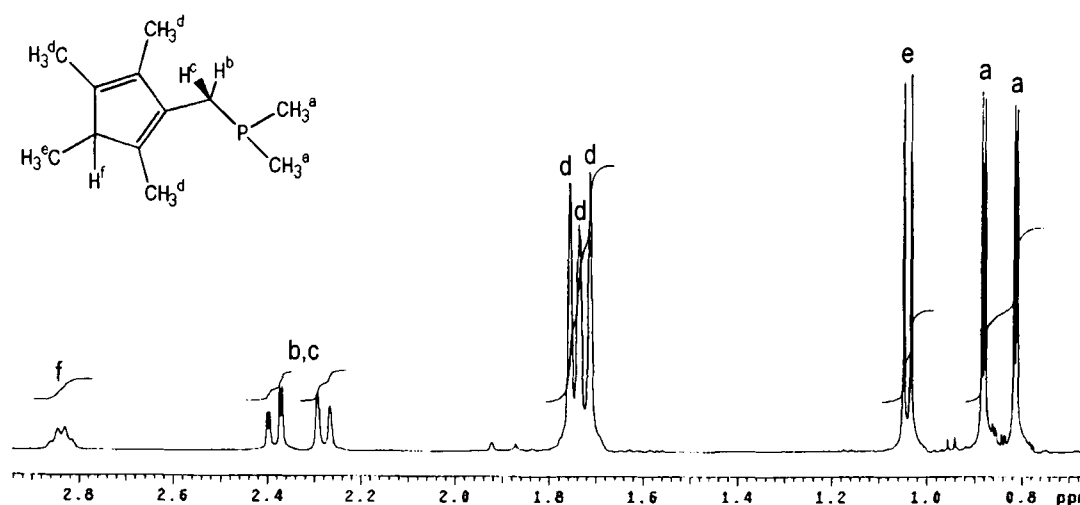


**Figure 2.5**  $^1\text{H}$  NMR spectrum of  $[\text{HC}_5\text{Me}_4\text{CH}_2\text{PMe}_2]$  (**3**) ( $\text{d}^6$ -benzene)

The  $^{31}\text{P}\{^1\text{H}\}$  NMR spectrum exhibits a singlet at  $\delta$  -46, which is consistent with values known for similar tertiary phosphines.[2, 4, 10, 11] Assignment of the two sets of phosphinodimethyl protons was confirmed *via* use of a selective  $^1\text{H}\{^{31}\text{P}\}$  NMR experiment. On increasing the decoupler power, the doublets at  $\delta$  0.85 and 0.93 [ $^2J_{\text{H-P}} = 3.5$  Hz] collapsed to singlets and so the resonances arising from the phosphinodimethyl protons have been assigned to these signals.

The  $^{13}\text{C}\{^1\text{H}\}$  NMR spectrum displays twelve chemically distinct  $^{13}\text{C}$  environments and exhibits several couplings to  $^{31}\text{P}$ . The  $^{13}\text{C}$  resonances of the Cp-ring are observed at  $\delta$  50.4, 134.0, 135.8, 138.2 and 138.6. The four substituent methyl groups are observed as singlets at  $\delta$  11.2, 11.8, 12.4 and 14.5 while the dimethylphosphino  $^{13}\text{C}$  signals resonate as doublets at  $\delta$  14.46 and 14.57 [ $J_{\text{P-C}} = 11.5$  Hz] and the methylene group at  $\delta$  31.1 [ $J_{\text{P-C}} = 10$  Hz] (**Figure 2.6**). These assignments have been made by analogy with those determined for compounds **1** and **2**.

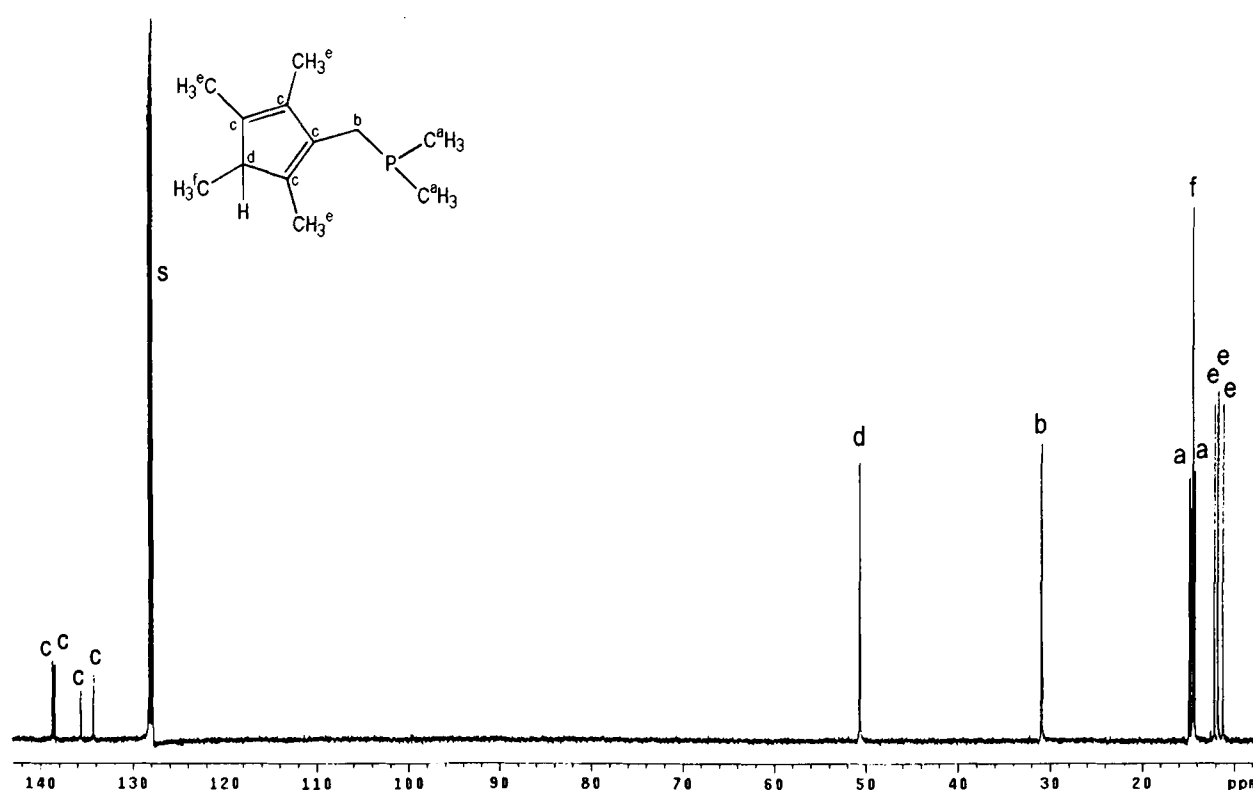


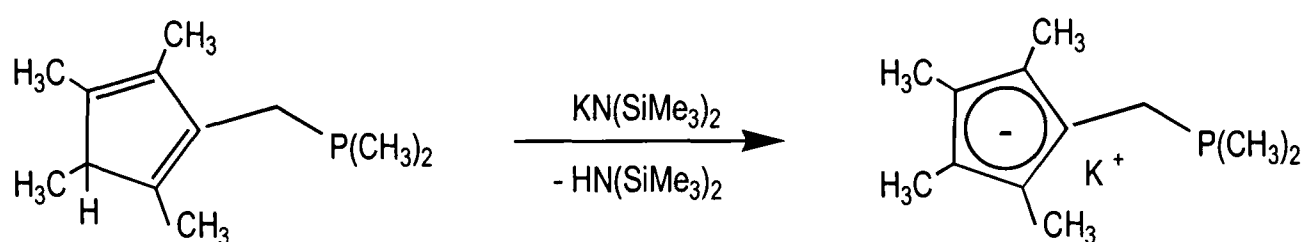
**Figure 2.6**  $^{13}\text{C}\{^1\text{H}\}$  NMR spectrum of  $[\text{HC}_5\text{Me}_4\text{CH}_2\text{PMe}_2]$  (**3**) ( $\text{d}^6$ -benzene)

### 2.2.3 Preparation of $[\text{M}(\text{C}_5\text{Me}_4)\text{CH}_2\text{PMe}_2]$ ( $\text{M} = \text{K}, \text{Na}, \text{Li}$ ) (**4**), (**5**) and (**6**)

The syntheses of the alkali metal salts of the compound **3** were attempted with a number of different metallating agents including potassium hydride, potassium metal and *n*-butyllithium. However, the products proved to be of a complex nature. The  $^{31}\text{P}\{^1\text{H}\}$  NMR spectra displayed a number of signals suggesting that a number of products had been formed, probably as a result of the reagents being too basic. Ultimately, the less basic alkali metal *bis*(trimethylsilylamide) salts  $[\text{MN}(\text{SiMe}_3)_2]$  ( $\text{M} = \text{K}, \text{Na}, \text{Li}$ ) were found to be the most suitable deprotonating agents, affording the desired products in acceptable yields.

### 2.2.4 Preparation of $[\text{K}(\text{C}_5\text{Me}_4)\text{CH}_2\text{PMe}_2]$ (**4**)

A solution of potassium *bis*(trimethylsilylamide)  $[\text{KN}(\text{SiMe}_3)_2]$  in THF was added dropwise to a solution of compound **3** in THF at  $-78^\circ\text{C}$  (**Scheme 2.5**). The pale yellow solution was allowed to warm to room temperature and stirred for 12 hours. Solvents were removed under reduced pressure and the off-white product was washed with pentane and isolated by filtration. After residual solvents were removed under reduced pressure, compound  $[\text{K}(\text{C}_5\text{Me}_4)\text{CH}_2\text{PMe}_2]$  (**4**) was obtained as a pyrophoric, fine white powder in 70 % yield.

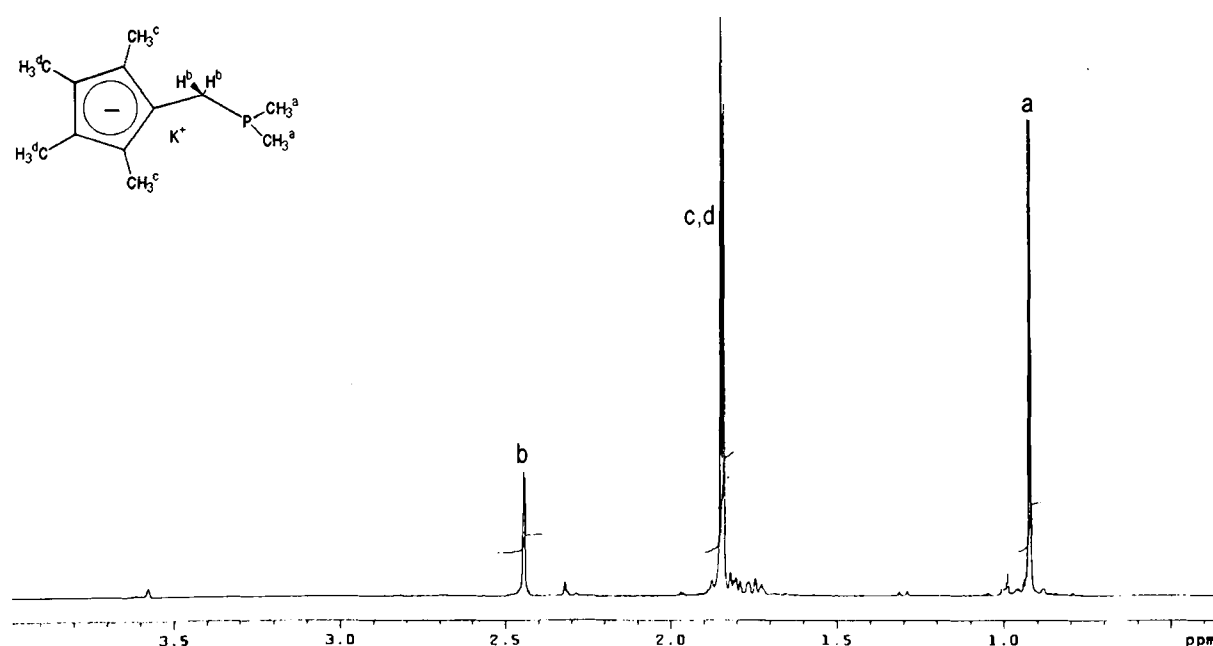
Scheme 2.5 Synthesis of the compound  $[K(C_5Me_4)CH_2PMe_2]$  (**4**)

### 2.2.5 Characterisation of $[K(C_5Me_4)CH_2PMe_2]$ (**4**)

The compound **4** is a pyrophoric, white powder, which is soluble in THF and pyridine. Satisfactory elemental analyses were precluded by the air sensitive nature of the compound. Characterising data are given in **Section 8.4**.

The  $^1H$  NMR spectrum of **4** in  $d^8$ -THF is shown in **Figure 2.7** and is greatly simplified in comparison with those of the preceding three complexes. The phosphinodimethyl signals resonate as a doublet at  $\delta$  0.92 [ $^2J_{H-P} = 2.5$  Hz] while the two *equivalent* methylene protons appear at  $\delta$  2.44 as a doublet [ $^2J_{H-P} = 1.5$  Hz]. Singlets at  $\delta$  1.84 and 1.85 account for the two pairs of methyl groups on the cyclopentadienyl ring.

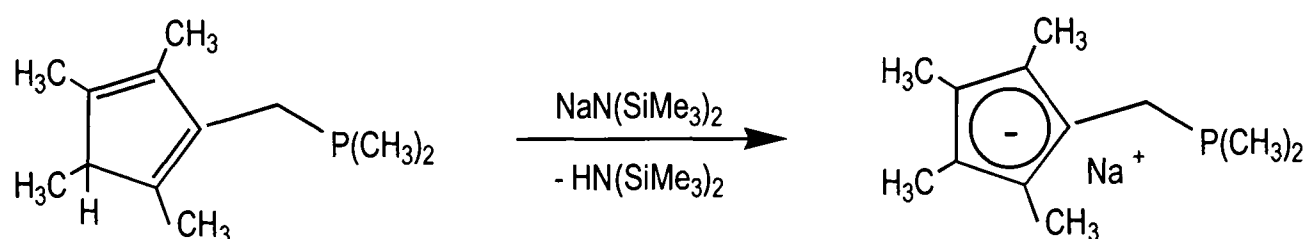
The  $^{31}P\{^1H\}$  NMR spectrum ( $d^8$ -THF) displays a single signal at  $\delta$  -45.4, which is in the expected region for an uncoordinated tertiary phosphine species.[2, 4, 10]

Figure 2.7  $^1H$  NMR spectrum of  $[K(C_5Me_4)CH_2PMe_2]$  (**4**) ( $d^8$ -THF)

The  $^{13}\text{C}\{^1\text{H}\}$  NMR spectrum displays seven chemically distinct  $^{13}\text{C}$  environments and demonstrates couplings to  $^{31}\text{P}$ . The  $^{13}\text{C}$  resonances of the Cp-ring are observed at  $\delta$  106.4, 107.1 and 107.9. The two types of substituent methyl groups are observed as singlets at  $\delta$  11.6 and 12.1 while the dimethylphosphino  $^{13}\text{C}$  signal appears as a doublet at  $\delta$  15.7 [ $J_{\text{P-C}} = 17$  Hz] and the methylene spacer group at  $\delta$  31.6 [ $J_{\text{P-C}} = 8$  Hz].

### 2.2.6 Preparation of $[\text{Na}(\text{C}_5\text{Me}_4)\text{CH}_2\text{PMe}_2]$ (**5**)

A solution of sodium *bis*(trimethylsilylamide)  $[\text{NaN}(\text{SiMe}_3)_2]$  in THF was added dropwise to a solution of compound **3** in THF at  $-78^\circ\text{C}$  (**Scheme 2.6**). The pale yellow solution was allowed to warm to room temperature and stirred for 12 hours. Solvents were removed under reduced pressure and the off-white product was washed with pentane and isolated by filtration. After residual solvents were removed under reduced pressure, compound  $[\text{Na}(\text{C}_5\text{Me}_4)\text{CH}_2\text{PMe}_2]$  (**5**) was obtained as a pyrophoric, fine white powder in 70 % yield.



**Scheme 2.6** Synthesis of the compound  $[\text{Na}(\text{C}_5\text{Me}_4)\text{CH}_2\text{PMe}_2]$  (**5**)

### 2.2.7 Characterisation of $[\text{Na}(\text{C}_5\text{Me}_4)\text{CH}_2\text{PMe}_2]$ (**5**)

The compound **5** is a pyrophoric, white powder, which is soluble in THF and pyridine. The main difference between the sodium and potassium salts is that the former tends to react far more cleanly. Once again satisfactory elemental analysis was precluded by the air sensitive nature of the compound. Characterising data are given in **Section 8.5**.

The  $^1\text{H}$  NMR spectrum of **5** in  $d^5$ -pyridine is analogous with that of compound **4** and displays four resonances. Similarly, the  $^{13}\text{C}\{^1\text{H}\}$  NMR spectrum (**Figure 2.8**) displays the expected seven chemically distinct  $^{13}\text{C}$  environments. The  $^{13}\text{C}$  resonances of the Cp-ring are observed at  $\delta$  105.3, 105.4 and 105.6. The two types of substituent methyl groups are observed as singlets at  $\delta$  11.96 and 12.40 while the



dimethylphosphino  $^{13}\text{C}$  signal appears as a doublet at  $\delta$  14.4 [ $J_{\text{P-C}} = 16$  Hz] and the methylene spacer group at  $\delta$  31.1 [ $J_{\text{P-C}} = 7.5$  Hz].

The  $^3\text{P}\{^1\text{H}\}$  NMR spectrum in  $d^5$ -pyridine displays a single signal at  $\delta$  -46.0, which is in the same region as that found for compound 4.

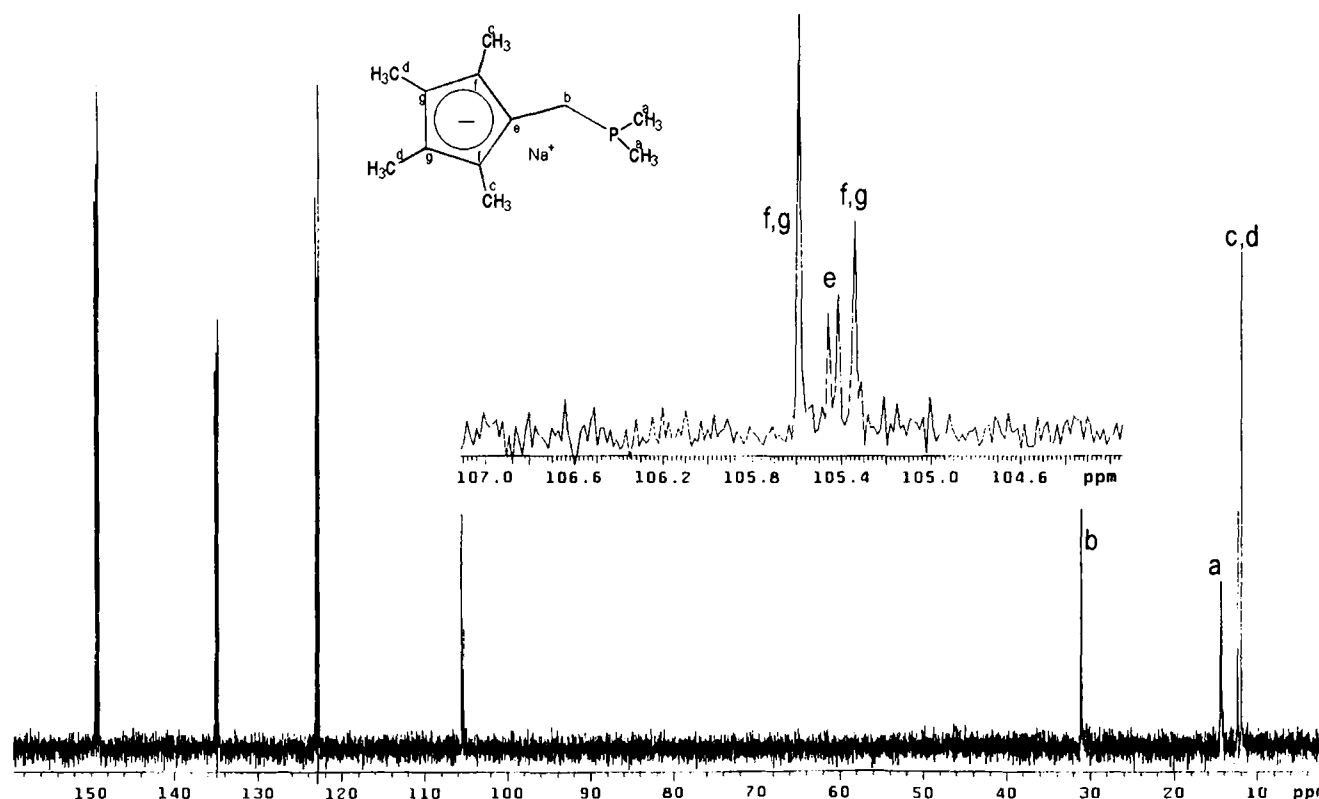
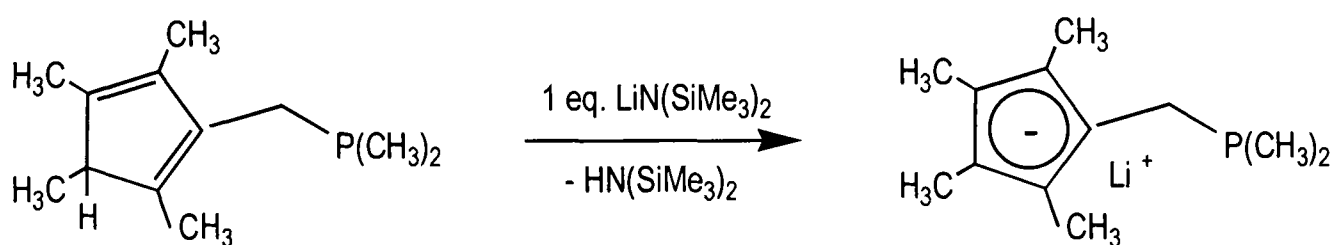


**Figure 2.8**  $^{13}\text{C}\{^1\text{H}\}$  NMR spectrum of  $[\text{Na}(\text{C}_5\text{Me}_4)\text{CH}_2\text{PMe}_2]$  (**5**) ( $d^5$ -pyridine)

### 2.2.8 Preparation of $[\text{Li}(\text{C}_5\text{Me}_4)\text{CH}_2\text{PMe}_2]$ (**6**)

A solution of recrystallised lithium *bis*(trimethylsilylamide)  $[\text{LiN}(\text{SiMe}_3)_2]$  in THF was added dropwise to a solution of compound **3** in THF at  $-78^\circ\text{C}$  (**Scheme 2.7**). The pale yellow solution was allowed to warm to room temperature and stirred for 12 hours. Solvents were removed under reduced pressure and the off-white product was washed with pentane and isolated by filtration. After residual solvents were removed under reduced pressure, compound  $[\text{Li}(\text{C}_5\text{Me}_4)\text{CH}_2\text{PMe}_2]$  (**6**) was obtained as a pyrophoric, fine white powder in 70 % yield.



**Scheme 2.7** Synthesis of the compound  $[\text{Li}(\text{C}_5\text{Me}_4)\text{CH}_2\text{PMe}_2]$  (**6**)

### 2.2.9 Characterisation of $[\text{Li}(\text{C}_5\text{Me}_4)\text{CH}_2\text{PMe}_2]$ (**6**)

The compound **6** is a pyrophoric, white powder, which is soluble in THF and pyridine. The formation of the lithium salt is achieved more cleanly than that for the potassium analogue, but less so than for the sodium analogue. Satisfactory elemental analysis was precluded by the air sensitive nature of the compound. Characterising data are given in **Section 8.6**.

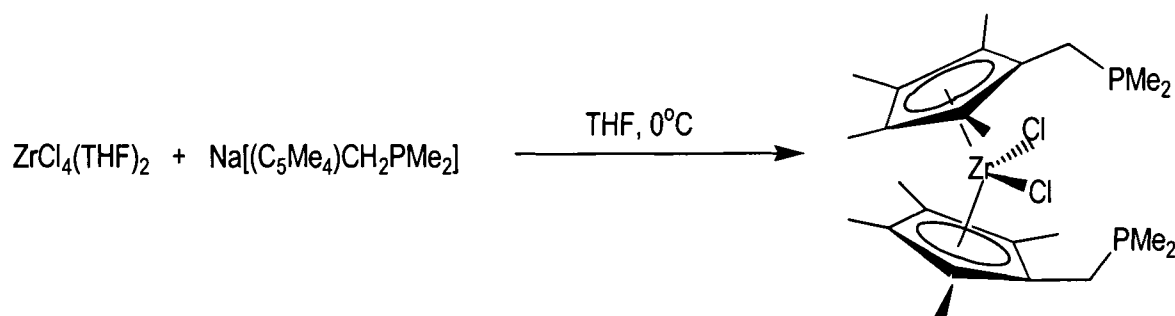
The  $^1\text{H}$  NMR spectrum of **6** in  $d^8$ -THF is analogous with those of compounds **4** and **5** and displays four resonances. The  $^{13}\text{C}\{^1\text{H}\}$  NMR spectrum displays the expected seven chemically distinct  $^{13}\text{C}$  environments with the  $^{13}\text{C}$  resonances of the Cp-ring observed at  $\delta$  104.8, 104.9 and 105.2. The two types of substituent methyl groups are observed as singlets at  $\delta$  10.37 and 10.87 while the dimethylphosphino  $^{13}\text{C}$  signal appears as a doublet at  $\delta$  13.4 [ $J_{\text{P-C}} = 17$  Hz] and the methylene spacer group at  $\delta$  29.2 [ $J_{\text{P-C}} = 7.8$  Hz]. The  $^{31}\text{P}\{^1\text{H}\}$  NMR spectrum in  $d^5$ -pyridine displays the expected signal at  $\delta$  -46.

### 2.3 Attempted Preparation of $[\text{M}\{(\text{C}_5\text{Me}_4)\text{CH}_2\text{PMe}_2\}_2\text{Cl}_2]$ ( $\text{M} = \text{Ti}, \text{Zr}, \text{Hf}$ )

There are numerous reported examples of (dialkylphosphino)alkyl and (diarylphosphino)alkyl substituted zirconocenes and their derivatives as evidenced by the review in **Chapter 1**. The organometallic chemistry of the Cp-PPh<sub>2</sub> ligand in Group 4 metal complexes has been particularly well reported and the field developed to a significant extent.[7, 12, 13] Currently, there is great interest in the use of phosphine-substituted cyclopentadienyl ligands to form Group 4 metallocenes containing an additional functional moiety, which may then co-ordinate to another metallic centre. Such bimetallic complexes, which incorporate, for example, both Zr and Rh metal centres have been synthesised as catalyst precursors with potential in homogeneous catalysis.[5, 10, 14] Given the increased basicity of the -PMe<sub>2</sub> group over the more sterically demanding -PPh<sub>2</sub> substituent, and the relative paucity of (dimethylphosphino)alkyl complexes relative to their diaryl- counterparts, the synthesis of a related (dimethylphosphino)methyl zirconocene complex  $[\text{Zr}\{(\eta\text{-C}_5\text{Me}_4)\text{CH}_2\text{PMe}_2\}_2\text{Cl}_2]$  was an attractive target.[14]

### 2.3.1 Preparation of $[\text{Zr}\{(\eta\text{-C}_5\text{Me}_4)\text{CH}_2\text{PMe}_2\}_2\text{Cl}_2]$ (7)

To a stirred THF solution of  $\text{ZrCl}_4(\text{THF})_2$  at  $0^\circ\text{C}$  was added dropwise a THF solution of compound **5** over a period of thirty minutes. The orange solution was stirred overnight, solvents were removed under reduced pressure and the pale-yellow product was triturated with pentane. Extraction into dichloromethane and filtration yielded a yellow solution from which solvents were removed. The compound  $[\text{Zr}\{(\eta\text{-C}_5\text{Me}_4)\text{CH}_2\text{PMe}_2\}_2\text{Cl}_2]$  (**7**) was isolated as pale-yellow microcrystals in 72 % yield.



**Scheme 2.8** Synthesis of  $[\text{Zr}\{(\eta\text{-C}_5\text{Me}_4)\text{CH}_2\text{PMe}_2\}_2\text{Cl}_2]$  (**7**)

### 2.3.2 Characterisation of $[\text{Zr}\{(\eta\text{-C}_5\text{Me}_4)\text{CH}_2\text{PMe}_2\}_2\text{Cl}_2]$ (**7**)

The compound **7** is an air-sensitive, pale-yellow, microcrystalline solid, which is soluble in dichloromethane, pyridine and THF. Microanalysis results are consistent with those calculated for a compound with the empirical formula  $\text{C}_{24}\text{H}_{40}\text{P}_2\text{ZrCl}_2$ . Characterising data are given in **Section 8.7**.

The  $^1\text{H}$  NMR spectrum of **7** in  $d^5$ -pyridine is similar to those of the preceding three complexes (**4** - **6**) and displays four resonances. The phosphinodimethyl protons resonate as a broad singlet at  $\delta$  0.62 (in  $\text{CD}_2\text{Cl}_2$  the doublet can be resolved with a  $^2J_{\text{H-P}}$  value of 3.0 Hz). Further singlets at  $\delta$  1.65 and 1.81 account for the two pairs of methyl groups on the cyclopentadienyl ring.

The most noticeable difference between the  $^1\text{H}$  NMR spectrum of compound **7** and those of the free ligand (compounds **4**, **5** and **6**) is the increase in magnitude of the frequency difference ( $\Delta\delta$ ) between the two Cp-methyl group signals. In the compound **7**, the signals are observed at  $\delta$  1.65 and  $\delta$  1.81 with  $\Delta\delta = 83.0$  Hz. In the starting material compounds **4**, **5** and **6**, they appear with  $\Delta\delta$  values between 27.5 and 30.0 Hz (**Table 2.1**).

Compound		Cp-Me <sub>1</sub> (δ)	Cp-Me <sub>2</sub> (δ)	Δδ (Hz)
[K(C <sub>5</sub> Me <sub>4</sub> )CH <sub>2</sub> PMe <sub>2</sub> ]	(4)	1.85	1.84	28.0
[Na(C <sub>5</sub> Me <sub>4</sub> )CH <sub>2</sub> PMe <sub>2</sub> ]	(5)	2.17	2.22	30.0
[Li(C <sub>5</sub> Me <sub>4</sub> )CH <sub>2</sub> PMe <sub>2</sub> ]	(6)	1.98	2.04	27.5
[Zr{(η-C <sub>5</sub> Me <sub>4</sub> )CH <sub>2</sub> PMe <sub>2</sub> } <sub>2</sub> Cl <sub>2</sub> ]	(7)	1.65	1.81	83.0

**Table 2.1** Comparison between the <sup>1</sup>H NMR Cp-Me chemical shifts of the compounds **4**, **5**, **6** and **7**

The <sup>13</sup>C{<sup>1</sup>H} NMR spectrum (**Figure 2.9**) displays seven chemically distinct <sup>13</sup>C environments with several couplings to <sup>31</sup>P. The <sup>13</sup>C resonances of the Cp-ring are observed at δ 121.6, 121.9 and 125.3. The two types of Cp-methyl groups are observed as a singlet and a doublet at δ 10.5 1 and δ 11.6 [<sup>4</sup>J<sub>P-C</sub> = 4.2 Hz] respectively, while the dimethylphosphino <sup>13</sup>C signal resonates as a doublet at δ 13.3 [J<sub>P-C</sub> = 15.0 Hz]. The methylene carbon resonates as a doublet at δ 30.1 [J<sub>P-C</sub> = 14.0 Hz]. Both the proton and carbon NMR spectra are very similar to those of the free ligand, however, the increased J<sub>P-H</sub> and J<sub>P-C</sub> coupling constants are indicative of ligand coordination to the Zr metal centre.[3, 10]

The <sup>31</sup>P{<sup>1</sup>H} spectrum for compound **7** consists of a singlet at δ -44.5 and is very similar to that obtained for the free ligand. This suggests that the phosphine moiety is not co-ordinated to the metal centre. Upon co-ordination, it would be expected that the chemical shift of the phosphorus signal would move downfield as a result of an increase in the co-ordination number.[5] The resemblance between the <sup>1</sup>H and <sup>31</sup>P{<sup>1</sup>H} NMR spectra of the zirconocene and the free ligand is not unusual in complexes of this type. In some cases, the zirconocene displays an identical <sup>31</sup>P{<sup>1</sup>H} chemical shift to that of the ligand.[10]

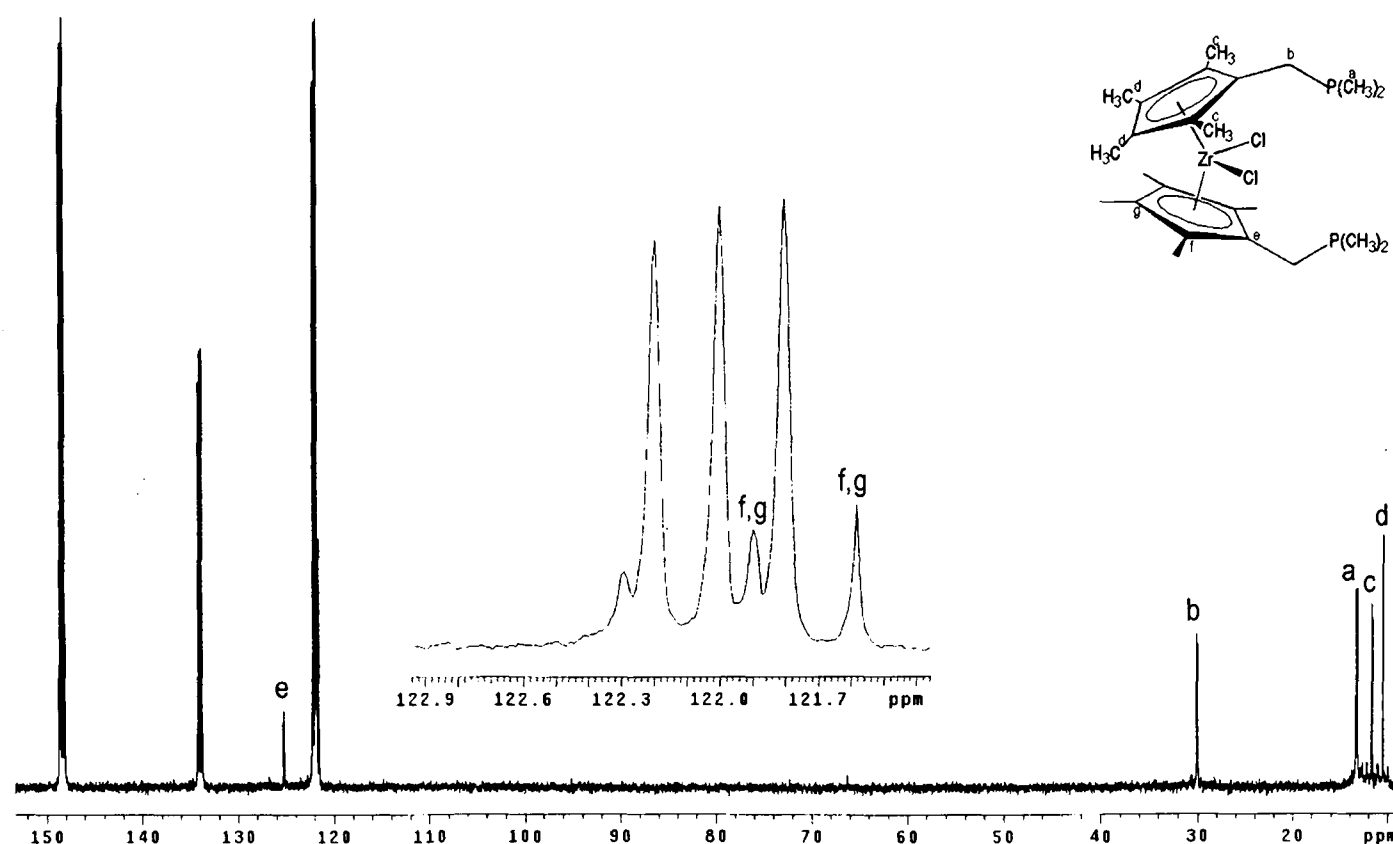
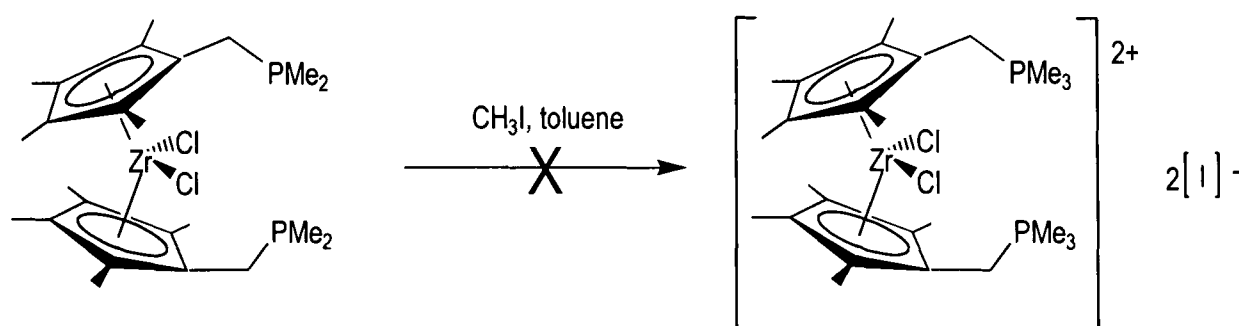


**Figure 2.9**  $^{13}\text{C}\{^1\text{H}\}$  NMR spectrum of  $[\text{Zr}\{(\eta\text{-C}_5\text{Me}_4)\text{CH}_2\text{PMe}_2\}_2\text{Cl}_2]$  (**7**) ( $d^5$ -pyridine)

In addition to NMR studies, a signal is observed at  $m/z$  547 in the FAB mass spectrum with the correct isotope pattern for the parent ion with the loss of a chloride ligand and addition of two oxygen atoms. This oxidation is unsurprising for air sensitive compounds such as this. The same signal and isotope pattern is observed in the electrospray (ES) mass spectrum.

### 2.3.3 Attempted Preparation of $[\text{Zr}\{(\eta\text{-C}_5\text{Me}_4)\text{CH}_2\text{PMe}_3\}_2\text{Cl}_2][\text{I}]_2$

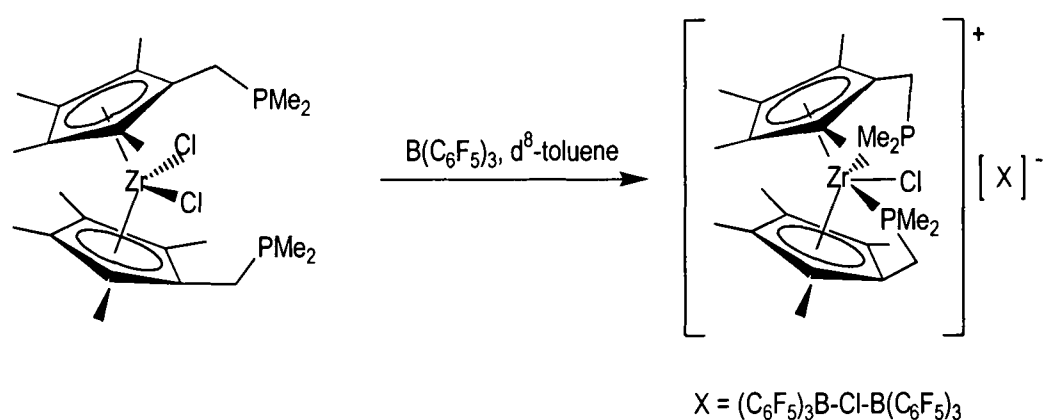
The attempted synthesis of the methyl iodide adduct  $[\text{Zr}\{(\eta\text{-C}_5\text{Me}_4)\text{CH}_2\text{PMe}_3\}_2\text{Cl}_2][\text{I}]_2$  by the addition of an excess of methyl iodide to a toluene solution of **7** at room temperature resulted in isolation of an off-white solid, insoluble in all common solvents including  $\text{D}_2\text{O}$ . Elemental analyses were inconsistent with the empirical formula  $\text{C}_{26}\text{H}_{46}\text{I}_2\text{P}_2\text{Zr}$  so further studies were discontinued.



**Scheme 2.9** Attempted synthesis of  $[\text{Zr}\{(\eta\text{-C}_5\text{Me}_4)\text{CH}_2\text{PMe}_2\}_2\text{Cl}_2][\text{I}]_2$

### 2.3.4 NMR scale reaction between $[\text{Zr}\{(\eta\text{-C}_5\text{Me}_4)\text{CH}_2\text{PMe}_2\}_2\text{Cl}_2]$ (7) and two equivalents of $\text{B}(\text{C}_6\text{F}_5)_3$

Reactions between the strong Lewis acid  $\text{B}(\text{C}_6\text{F}_5)_3$  and transition metal metallocene dichlorides or dimethyl analogues often show interesting outcomes.<sup>[15]</sup> Work by Erker described in **Chapter 1** demonstrates how methyl-abstraction from the molecule  $[\text{Zr}(\eta\text{-C}_5\text{H}_4\text{CMe}_2\text{PAr}_2)_2\text{Me}_2]$  results in the double ‘tuck-in’ complex where both diarylphosphino moieties coordinate to the cationic metal centre and one methide group is eliminated as  $[\text{MeB}(\text{C}_6\text{F}_5)_3]$ .<sup>[15]</sup> With this in mind, a reaction between compound 7 and  $\text{B}(\text{C}_6\text{F}_5)_3$  was attempted. To a Young’s tap NMR tube was added a solution of the zirconocene (7) and two equivalents of  $\text{B}(\text{C}_6\text{F}_5)_3$  in  $\text{d}^8$ -toluene (**Scheme 2.10**).



**Scheme 2.10** Preparation of  $[\text{Zr}\{(\eta\text{-C}_5\text{Me}_4)\text{CH}_2\text{PMe}_2\}_2\text{Cl}][(\text{C}_6\text{F}_5)_3\text{BClB}(\text{C}_6\text{F}_5)_3]$  (8)

### 2.3.5 Characterisation of $[\text{Zr}\{(\eta\text{-C}_5\text{Me}_4)\text{CH}_2\text{PMe}_2\}_2\text{Cl}][(\text{C}_6\text{F}_5)_3\text{BClB}(\text{C}_6\text{F}_5)_3]$ (8)

The compound 8 forms a yellow solution in  $\text{d}^8$ -toluene. Characterising data are given in **Section 8.8**. The  $^1\text{H}$  NMR spectrum is similar to that of the parent compound 7, consisting of four resonances. These resonances are remarkably similar to those found for compound 7, although a major difference is the size of the  $J_{\text{H-P}}$  coupling constants, which have increased considerably. The phosphinodimethyl protons now resonate as a doublet at  $\delta$  0.62 with  $^2J_{\text{H-P}}$  value of 10.6 Hz – more than three times that found for the analogous signal in compound 7. In addition, the signal corresponding to that at  $\delta$  2.52 in 7 is now a doublet [ $^2J_{\text{H-P}} = 7.0$  Hz]. Singlets at  $\delta$  1.65 and 1.66 account for the two pairs of methyl groups on the cyclopentadienyl ring.

	$[\text{Zr}\{(\eta\text{-C}_5\text{Me}_4)\text{CH}_2\text{PMe}_2\}_2\text{Cl}][\text{X}]$ ( <b>8</b> ) ( $\delta$ )	$[\text{Zr}\{(\eta\text{-C}_5\text{Me}_4)\text{CH}_2\text{PMe}_2\}_2\text{Cl}_2]$ ( <b>7</b> ) ( $\delta$ )
$\text{P}(\text{CH}_3)_2$	d, 6H, 0.62 ( $^2J_{\text{H-P}} = 10.6$ Hz)	d, 6H, 0.62 ( $^2J_{\text{H-P}} = 3.0$ Hz)
$\text{C}_5(\text{CH}_3)_4$	s, 6H, 1.65	s, 6H, 1.65
$\text{C}_5(\text{CH}_3)_4$	s, 6H, 1.66	s, 6H, 1.81
$-\text{CH}_2-$	d, 2H, 2.52 ( $^2J_{\text{H-P}} = 7.0$ Hz)	s, 2H, 2.52

Table 2.2 Comparison between the  $^1\text{H}$  NMR chemical shifts ( $\delta$ ) of the compounds **7** and **8**

The  $^{13}\text{C}\{^1\text{H}\}$  NMR spectrum displays seven chemically distinct  $^{13}\text{C}$  environments with several couplings to  $^{31}\text{P}$ . The  $^{13}\text{C}$  resonances of the Cp-ring are observed at  $\delta$  118.0, 123.4 and 124.4. The two types of Cp-methyl groups are observed as singlets at  $\delta$  11.6 and 13.9, while the dimethylphosphino  $^{13}\text{C}$  signal resonates as a doublet at  $\delta$  7.89 [ $J_{\text{P-C}} = 36.7$  Hz]. The methylene carbon resonates as a doublet at  $\delta$  22.4 [ $J_{\text{P-C}} = 31.4$  Hz]. There are also doublets for the  $\text{B}(\text{C}_6\text{F}_5)_3$  carbon atoms at  $\delta$  137.8 [ $J_{\text{C-F}} = 257.3$  Hz], 140.7 [ $J_{\text{C-F}} = 252.4$  Hz] and 149.2 [ $J_{\text{C-F}} = 247.3$  Hz] assigned to the *ortho*-, *para*- and *meta*- carbons respectively,<sup>[16]</sup> with the *ipso*-carbon resonating as a broad singlet at  $\delta$  115.4.

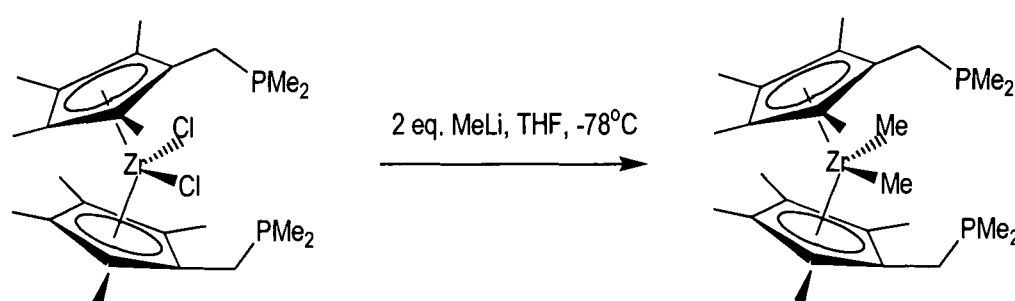
The  $^{31}\text{P}\{^1\text{H}\}$  NMR spectrum for compound **8** consists of a singlet at  $\delta$  8.26. This suggests that the phosphine moiety is co-ordinated to the metal centre and the magnitude of the downfield shift ( $\Delta\delta = +53$  ppm) is consistent with both an increase in coordination number as well as the effect of the cationic nature of the zirconocene ion.<sup>[5]</sup> The  $^{11}\text{B}\{^1\text{H}\}$  NMR spectrum displays a single peak at  $\delta$  -13.0. The usual value for  $[\text{ClB}(\text{C}_6\text{F}_5)_3]^-$  anions is around  $\delta$  -3.0 while the value of -13.0 resembles more closely the resonance found for  $[\text{MeB}(\text{C}_6\text{F}_5)_3]^-$  which clearly cannot be the case. Given that the chemical shift does not match the expected value for  $[\text{ClB}(\text{C}_6\text{F}_5)_3]^-$  and that two equivalents of  $\text{B}(\text{C}_6\text{F}_5)_3$  were utilised in the reaction and only one set of signals is observed in the  $^{19}\text{F}$ ,  $^{11}\text{B}$  and  $^{13}\text{C}$  NMR spectra, a possible counter-anion could be the  $[(\text{C}_6\text{F}_5)_3\text{B-Cl-B}(\text{C}_6\text{F}_5)_3]^-$  species, which is currently unreported.

	$[\text{Zr}\{(\eta\text{-C}_5\text{Me}_4)\text{CH}_2\text{PMe}_2\}_2\text{Cl}][\text{X}]$ ( <b>8</b> ) ( $\delta$ )	$[\text{Zr}\{(\eta\text{-C}_5\text{Me}_4)\text{CH}_2\text{PMe}_2\}_2\text{Cl}_2]$ ( <b>7</b> ) ( $\delta$ )
$\text{P}(\underline{\text{C}}\text{H}_3)_2$	d, 7.89 ( $J_{\text{C-P}} = 36.7$ Hz)	d, 11.6 ( $^4J_{\text{C-P}} = 4.2$ Hz)
$\text{C}_5(\underline{\text{C}}\text{H}_3)_4$	s, 11.6	s, 10.5
$\text{C}_5(\underline{\text{C}}\text{H}_3)_4$	s, 13.9	d, 13.3
$-\underline{\text{C}}\text{H}_2-$	d, 22.4 ( $J_{\text{C-P}} = 31.4$ Hz)	d, 30.1 ( $J_{\text{C-P}} = 14.0$ Hz)
$\underline{\text{C}}_5(\text{CH}_3)_4$	s, 123.4	s, 121.6
$\underline{\text{C}}_5(\text{CH}_3)_4$	s, 124.4	s, 121.9
$\underline{\text{C}}_{\text{ipso}}$	d, 118.0 ( $^2J_{\text{C-P}} = 7.25$ Hz)	d, 125.3 ( $^2J_{\text{C-P}} = 12.9$ Hz)

Table 2.3 Comparison between the  $^{13}\text{C}\{^1\text{H}\}$  NMR chemical shifts ( $\delta$ ) of the compounds **7** and **8**

### 2.3.6 Attempted Preparation of $[\text{Zr}\{(\eta\text{-C}_5\text{Me}_4)\text{CH}_2\text{PMe}_2\}_2\text{Me}_2]$ (**9**)

To a stirred THF solution of **7** at  $-78^\circ\text{C}$  was added *via* microsyringe a solution of MeLi in diethyl ether. After stirring overnight at room temperature, solvents were removed under reduced pressure and the pale-yellow product was washed with pentane. Extraction into dichloromethane and filtration yielded a pale-yellow solution from which solvents were removed to afford a white solid (**Scheme 2.11**).

Scheme 2.11 Attempted synthesis of  $[\text{Zr}\{(\eta\text{-C}_5\text{Me}_4)\text{CH}_2\text{PMe}_2\}_2\text{Me}_2]$  (**9**)

The  $^1\text{H}$  NMR spectrum ( $\text{d}^8\text{-toluene}$ ) of the product **9** displays signals consistent with those expected for the compound at  $\delta$  0.85 [d, 6H,  $\text{P}(\underline{\text{C}}\text{H}_3)_2$ ], 1.71 [s, 6H,  $\text{C}_5(\underline{\text{C}}\text{H}_3)_4$ ], 1.87 [s, 6H,  $\text{C}_5(\underline{\text{C}}\text{H}_3)_4$ ] and 2.48 [s, 2H,  $-\underline{\text{C}}\text{H}_2-$ ]. Two signals were also observed in the  $^{31}\text{P}\{^1\text{H}\}$  NMR spectrum at  $\delta$  -45.5 and -45.8. Attempts to purify the material failed to afford the compound **9** in an analytically pure form. As a result, synthesis *via* an alternative route utilising  $\text{ZnMe}_2$ , was attempted. However, this method also failed to afford the desired compound. Deprotonation of the methylene backbone is



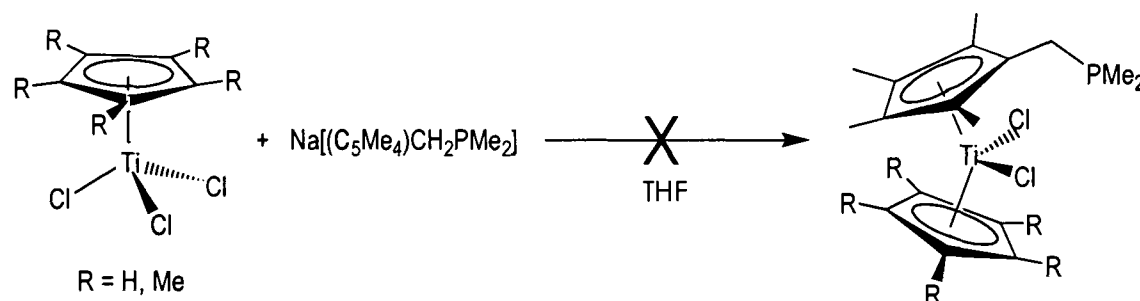
suggested as the source of the impurities in the NMR spectrum of **9**. Further studies were therefore discontinued. Characterising data are given in **Section 7.2.9**.

### 2.3.7 Attempted Preparation of $[M\{(\eta\text{-C}_5\text{Me}_4)\text{CH}_2\text{PMe}_2\}_2\text{Cl}_2]$ ( $M = \text{Ti, Hf}$ )

Attempts to synthesise the other Group 4 *bis*(cyclopentadienyl) analogues were undertaken. In the case of the hafnium analogue, the isolated product was shown by  $^{31}\text{P}\{^1\text{H}\}$  NMR spectroscopy to contain a number of different phosphorus environments and the  $^1\text{H}$  NMR spectrum confirmed this, although analogous signals to those found for compound **7** were observed within the spectrum. Characterising data are given in **Section 7.2.10**. No further attempts were made to isolate the hafnium species. Attempts to prepare the titanium analogue also failed to produce a single, isolable compound.

### 2.3.8 Attempted Preparation of Mixed Ring Analogues

Syntheses of mixed-ring titanium systems were also attempted. The starting reagents utilised were the half-sandwich complexes  $[\text{Ti}(\eta\text{-C}_5\text{H}_5)\text{Cl}_3]$  and  $[\text{Ti}(\eta\text{-C}_5\text{Me}_5)\text{Cl}_3]$  and the compound **5**. In the case of the non-methylated titanium reagent, a red, crystalline product was obtained from which X-ray quality crystals were isolated. The X-ray crystal structure analysis, however, showed that the product was simply *bis*(cyclopentadienyl) titanium. As a result, further studies into this area were discontinued.



**Scheme 2.12** Attempted preparation of  $[\text{Ti}(\eta\text{-C}_5\text{R}_5)\{(\eta\text{-C}_5\text{Me}_4)\text{CH}_2\text{PMe}_2\}\text{Cl}_2]$  ( $\text{R} = \text{H, Me}$ )

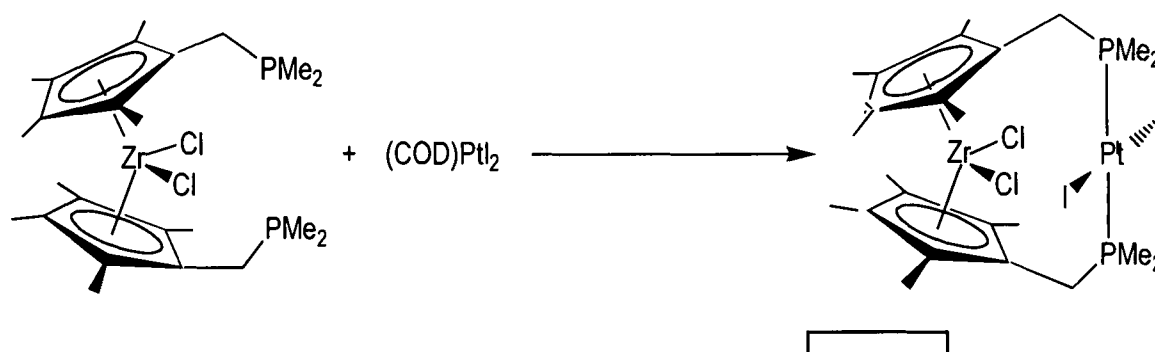
## 2.4 Early-Late Heterobimetallic (ELHB) Transition Metal Complexes Incorporating $[\text{Zr}\{(\eta\text{-C}_5\text{Me}_4)\text{CH}_2\text{PMe}_2\}_2\text{Cl}_2]$ (**7**)

As described in **Chapter 1**, the bifunctional nature of the ligand incorporated in compound **7** might make it suitable for the synthesis of complexes containing both an early transition metal and one from Group 8, 9 or 10 of the periodic table. In recent

work by Graham[5, 10] and Erker[3, 14] the strategy for preparing the ELHB complexes was first to complex the Cp-unit of the bifunctional ligands to an early transition metal followed by reaction of these metallocene derivatives with later transition metal sources such as  $\text{PtCl}_2(\text{PhCN})_2$ ,  $\text{PdCl}_2(\text{PhCN})_2$  and  $(\text{COD})\text{Mo}(\text{CO})_4$ , forming the bimetallic complex as a result of displacement of the donor ligands COD and PhCN by the chelating action of the substituted metallocenes. This methodology was utilised in the attempted preparation of bimetallic complexes incorporating compound 7.

#### 2.4.1 Preparation of $[\text{Zr}\{(\eta\text{-C}_5\text{Me}_4)\text{CH}_2\text{PMe}_2\}_2\text{Cl}_2\text{PtI}_2]$ (10)

To a Schlenk tube containing THF at  $-40^\circ\text{C}$  was added dropwise THF solution of compound 7 and a THF solution of  $\text{Pt}(\text{COD})\text{I}_2$  (one equivalent) with stirring. The orange solution was stirred overnight at room temperature. Solvent was removed under reduced pressure and the product washed with pentane. The complex  $[\text{Zr}\{(\eta\text{-C}_5\text{Me}_4)\text{CH}_2\text{PMe}_2\}_2\text{Cl}_2\text{PtI}_2]$  (10) was isolated as a yellow powder in 45 % yield (Scheme 2.13).



Scheme 2.13 Synthesis of  $[\text{Zr}\{(\eta\text{-C}_5\text{Me}_4)\text{CH}_2\text{PMe}_2\}_2\text{Cl}_2\text{PtI}_2]$  (10)

#### 2.4.2 Characterisation of $[\text{Zr}\{(\eta\text{-C}_5\text{Me}_4)\text{CH}_2\text{PMe}_2\}_2\text{Cl}_2\text{PtI}_2]$ (10)

The compound 10 is an orange solid, poorly soluble in common solvents and decomposes in the presence of air. Microanalysis results are consistent with those calculated for a compound with the empirical formula  $\text{C}_{24}\text{Cl}_2\text{H}_{40}\text{P}_2\text{PtZrI}_2$ . The  $^{31}\text{P}\{^1\text{H}\}$  NMR spectrum in  $\text{d}^8\text{-THF}$  exhibits a weak signal at  $\delta$  -12 (Figure 2.10). In comparison with the spectrum obtained for 7, this represents a significant downfield shift ( $\Delta = +32$  ppm), which is consistent with co-ordination of the phosphine moiety to another metal species.[3] The presence of a pair of  $^{195}\text{Pt}$  satellites [ $J_{\text{P-Pt}} = 2304$  Hz]

implies that the phosphine groups are co-ordinated to the platinum moiety which is an NMR active nucleus, ( $I = \frac{1}{2}$ , 34 % abundant).

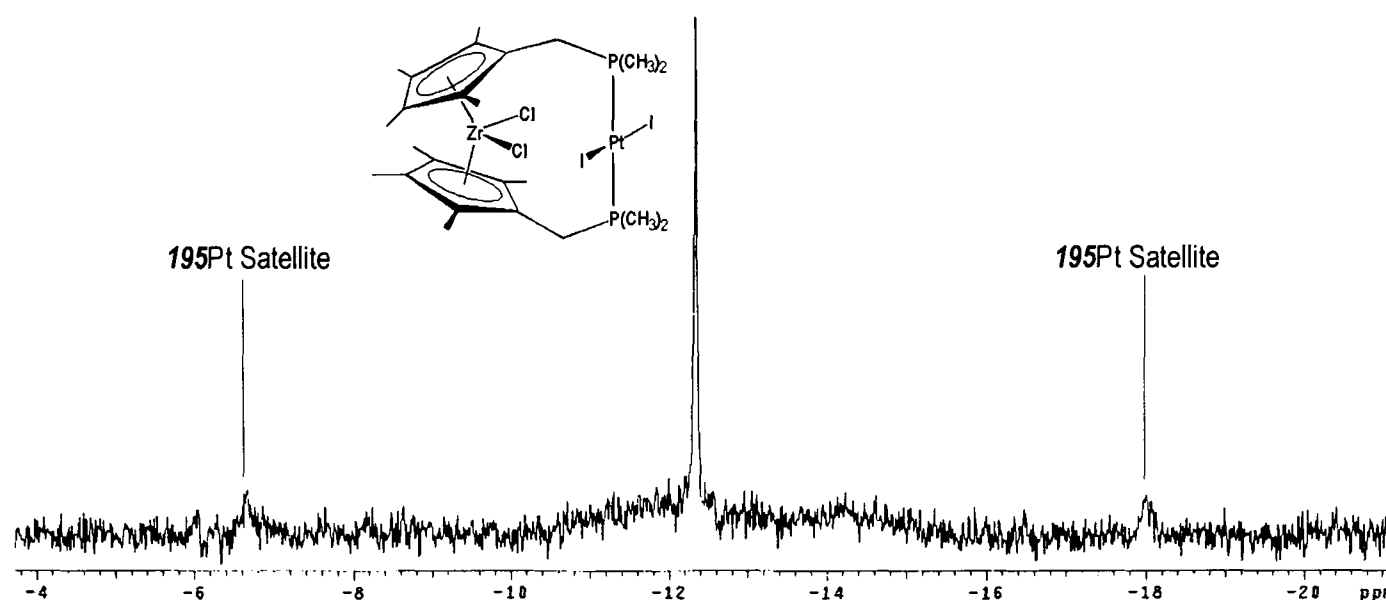


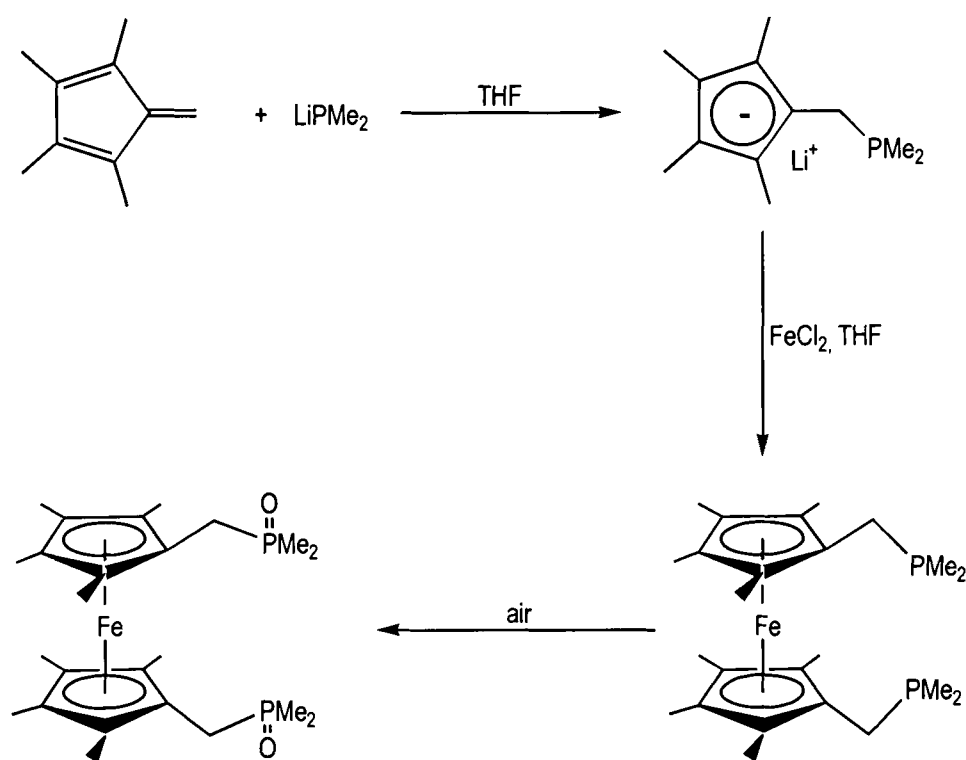
**Figure 2.10**  $^{31}\text{P}\{^1\text{H}\}$  NMR spectrum of  $[\text{Zr}\{(\eta\text{-C}_5\text{Me}_4)\text{CH}_2\text{PMe}_2\}\text{Cl}_2\text{PtI}_2]$  (**10**) ( $\text{d}^8\text{-THF}$ )

The magnitude of  $J_{\text{P-Pt}}$  is demonstrative of a *trans*-arrangement of phosphine groups around the platinum centre given that the *cis*- isomers are normally of the magnitude of 3500 Hz.<sup>[17-19]</sup> This is consistent with results reported by Erker<sup>[3]</sup> in the synthesis of heterobimetallic systems utilising  $[\text{Zr}\{(\eta\text{-C}_5\text{H}_4)\text{CMe}_2\text{PAr}_2\}_2\text{Cl}_2]$  (Ar = phenyl, *p*-tolyl) as the chelating phosphine. In the reaction between this ligand and  $\text{Pt/PdCl}_2(\text{PhCN})_2$ , displacement of the benzonitrile ligands by the organometallic chelating phosphine-system generates *trans*-co-ordinated systems. In addition, the Zr/Pd- and Zr/Pt-complexes have been structurally characterised and shown to exhibit the arrangement suggested by the  $J_{\text{P-Pt}}$  coupling constant values.

Supporting the formation of a bimetallic complex is the positive mode Fast Atom Bombardment (FAB) mass spectrum which displays a signal at  $m/z$  747 with the correct isotope pattern for the  $[\text{M}^+ - 2\text{I}]$  fragment. The low solubility of the compound **10** means that it is not impossible to rule out formation of an oligomeric species *via* the substituted zirconocene acting in a bridging mode rather as a chelating ligand. However, there is no evidence in the mass spectrum of signals that are assignable to larger fragments as might be expected for an oligomeric species.

## 2.5 Later Transition Metal Complexes Incorporating the Ligand $[(C_5Me_4)CH_2PMe_2]^+$

At the same time as the research described in this thesis was being carried out, R.M. Bellabarba of this laboratory was also investigating the reactivity of the compound **4**, which was prepared *via* a different route utilising tetramethylfulvalene and lithium dimethylphosphide as starting materials (**Scheme 2.14**).<sup>[20]</sup> Synthesis of a number of later transition metal compounds, including the novel ferrocenyl complexes  $[Fe\{(\eta-C_5Me_4)CH_2PMe_2\}_2]$  and  $[Fe\{(\eta-C_5Me_4)CH_2P(O)Me_2\}_2]$  was described.



**Scheme 2.14** Alternative preparation of the ligand (**6**) and synthesis of two substituted ferrocene complexes.

As a result of the successful synthesis of the ferrocene complexes illustrated in **Scheme 2.14**, it was decided to prepare other metallocene complexes of later transition metals as described below.

## 2.6 Chemistry of Manganocenes $[\text{Mn}(\eta\text{-C}_5\text{R}_5)_2]$

Manganocene  $[\text{Mn}(\eta\text{-C}_5\text{H}_5)_2]$  was one of the first organometallic complexes of manganese to be prepared and characterised.[21] It is synthesised from a metathesis reaction between anhydrous  $\text{MnX}_2$  ( $\text{X} = \text{Cl}, \text{Br}, \text{I}$ ) and sodium cyclopentadienide in THF.  $\text{Mn(II)}$  is a high-spin  $d^5$  ion with zero crystal field splitting energy and behaves like a hard cation such as  $\text{Zn}^{2+}$  or  $\text{Mg}^{2+}$ . For these reasons, the  $\text{C}_5\text{H}_5^-$  ligand in  $[\text{Mn}(\eta\text{-C}_5\text{H}_5)_2]$  is less covalently bonded than in other metallocenes and manganocene is unique among the first row transition metals in adopting a polymeric structure at room temperature. B nder and Weiss[22] have demonstrated that  $[\text{Mn}(\eta\text{-C}_5\text{H}_5)_2]$  exists as an ionic structure, which forms polymer chains in a zig-zag arrangement of  $\text{Mn-C}_5\text{H}_5$  units and additional  $\text{C}_5\text{H}_5$  bridges between adjacent ions. At  $158^\circ\text{C}$ , the pink, polymeric structure gives way to amber crystals of the monomeric, standard metallocene sandwich structure (**Figure 2.11**).

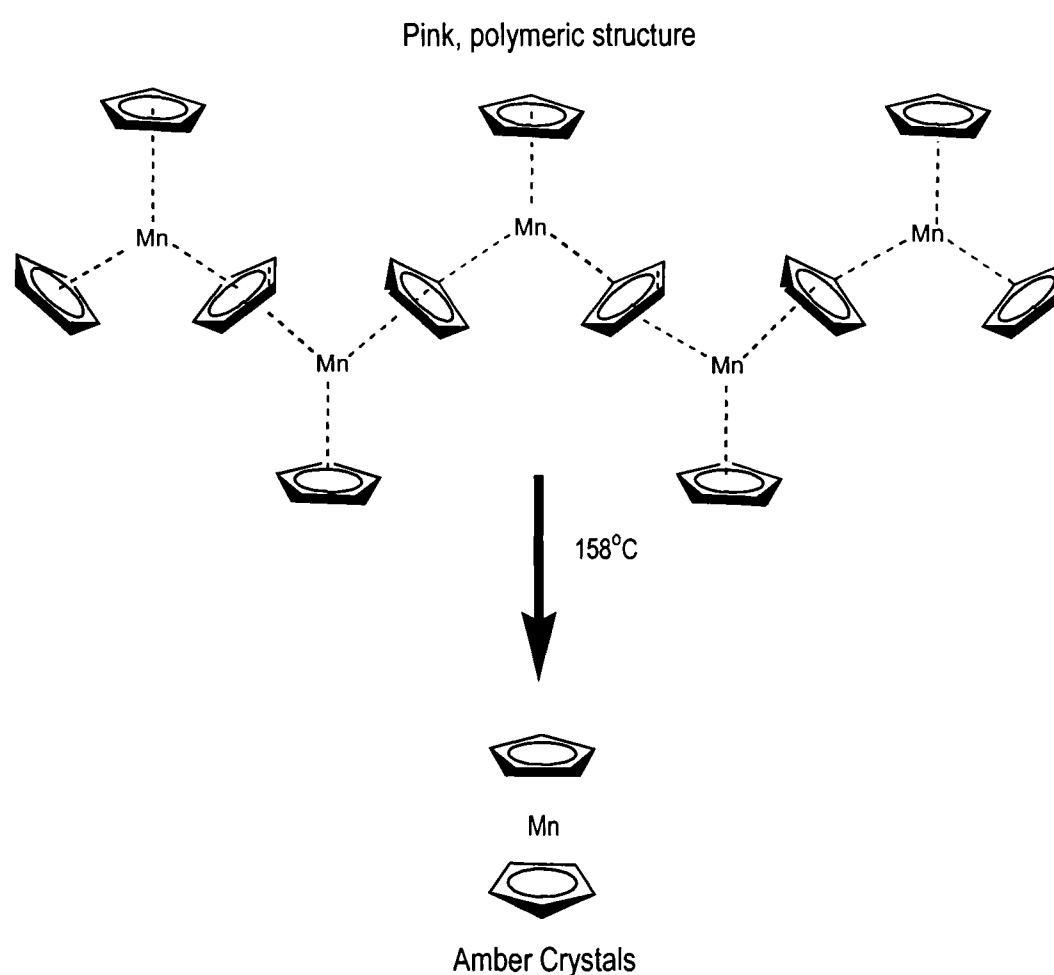


**Figure 2.11** Polymeric and monomeric structures of manganocene  $[\text{Mn}(\eta\text{-C}_5\text{H}_5)_2]$

Among first row transition metals, manganocenes are unique in that they contain two energetically accessible spin states – either the high spin  ${}^6\text{A}_{1g}$  [ $e_{2g}^2 a_{1g}^1 e_{1g}^2$ ] or the low

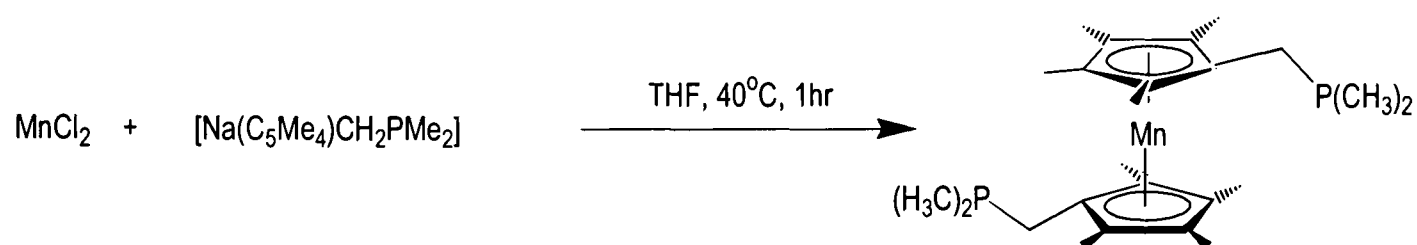
spin  $^2E_{2g}$  [ $e_{2g}^3 a_{1g}^2$ ] configuration. These states can be readily interconverted by changing the electronic or steric properties of the cyclopentadienyl ring. The magnetic behaviour of  $[Mn(\eta-C_5H_5)_2]$  is unusual in that it is a high-spin molecule at room temperature, but is close to the high-spin / low spin crossover point with a small energy difference of around  $2 \text{ kJ mol}^{-1}$ .<sup>[23]</sup>

A number of studies have demonstrated some dramatic differences between the structure and chemistry of alkylated and non-alkylated cyclopentadienyl complexes of manganese.<sup>[24-26]</sup> Magnetic studies on  $[Mn(\eta-C_5Me_5)_2]$  show that permethylation of the Cp-ring leads to the exclusive formation of a low-spin  $^2E_{2g}$  configuration, in contrast to other manganocenes where the  $^6A_{1g}$  state is thermally populated. In addition, despite the fact that the pentamethylcyclopentadienyl ligand is almost twice as sterically demanding as the Cp-moiety, the metal-to-ring carbon distances [ $r(M-C)$ ] in  $[Mn(\eta-C_5Me_5)_2]$  are approximately  $0.3 \text{ \AA}$  shorter than in  $[Mn(\eta-C_5H_5)_2]$ . Manganocenes with low-spin electronic configurations have been shown to be far less reactive towards hydrolysis and the permethylated complex uniquely undergoes one-electron oxidation and reduction reactions to the 16 and 18 electron derivatives respectively.<sup>[25]</sup> The compound 1,1'-dimethylmanganocene  $[Mn(\eta-C_5H_4Me)_2]$  is known to exist in a thermal equilibrium between the high- and low-spin electronic configurations, with the  $^2E_{2g}$  predominating at lower temperatures.<sup>[27]</sup>

## 2.7 Studies on $[Mn\{(\eta-C_5Me_4)CH_2PMe_2\}_2]$ (11)

### 2.7.1 Preparation of $[Mn\{(\eta-C_5Me_4)CH_2PMe_2\}_2]$ (11)

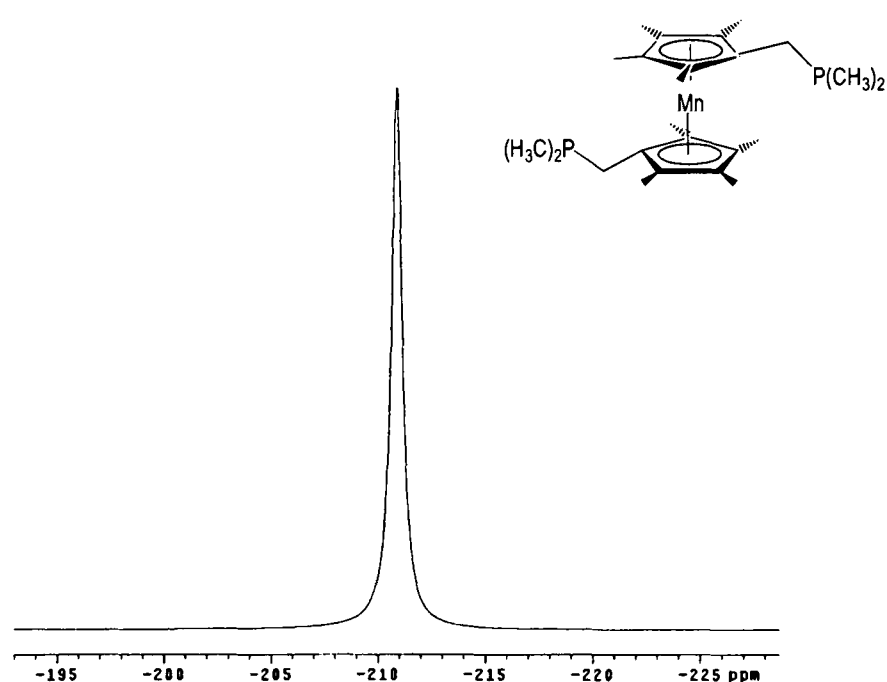
To a stirred THF solution of compound **5** in THF at  $-78^\circ\text{C}$  was added *via* a solid addition Schlenk tube, manganese dichloride ( $MnCl_2$ ) (**Scheme 2.15**). The mixture was warmed to  $40^\circ\text{C}$  for 1 hour and the resulting orange solution was then stirred for a further 12 hours at room temperature. Solvents were removed under reduced pressure and the oily, orange product triturated with and then extracted into pentane. Filtration yielded a deep orange solution from which volatiles were removed and a concentrated solution (*ca.* 20 ml) was cooled to  $4^\circ\text{C}$ . The compound  $[Mn\{(\eta-C_5Me_4)CH_2PMe_2\}_2]$  (**11**) was isolated in 66 % yield as cubic, orange, X-ray quality crystals.

Scheme 2.15 Synthesis of  $[\text{Mn}\{(\eta\text{-C}_5\text{Me}_4)\text{CH}_2\text{PMe}_2\}_2]$  (**11**)

### 2.7.2 Characterisation of $[\text{Mn}\{(\eta\text{-C}_5\text{Me}_4)\text{CH}_2\text{PMe}_2\}_2]$ (**11**)

The compound **11** is a red-orange, crystalline material, which decomposes in the presence of air. Microanalysis results are consistent with the empirical formula  $\text{C}_{24}\text{H}_{40}\text{MnP}_2$ . The FAB mass spectrum displays a signal at  $m/z$  445 with the correct isotope pattern for the molecular ion and another at  $m/z$  195 demonstrating loss of one ligand  $[\text{M}^+ - \text{C}_5\text{Me}_4\text{CH}_2\text{PMe}_2]$ . Characterising data are given in **Section 8.10**.

The  $^{31}\text{P}\{^1\text{H}\}$  NMR spectrum in  $d^6$ -benzene is shown in **Figure 2.12**. The tertiary phosphine group resonating as a singlet at  $\delta$  -210.0, which is relatively high-field. However, the compound is expected to be paramagnetic. The  $^1\text{H}$  NMR spectrum exhibits the expected number of signals with appropriate integrals. The signal at  $\delta$  4.96 can be assigned to the phosphinodimethyl protons, with further signals at  $\delta$  -2.51, -4.21 and -11.29 assigned to the two pairs of cyclopentadienyl methyl groups and the backbone methylene protons respectively.

Figure 2.12  $^{31}\text{P}\{^1\text{H}\}$  NMR spectrum of  $[\text{Mn}\{(\eta\text{-C}_5\text{Me}_4)\text{CH}_2\text{PMe}_2\}_2]$  (**11**) ( $d^8$ -toluene)

### 2.7.3 The Molecular Structure of Compound 11

The cooling to  $-40^{\circ}\text{C}$  of a pentane solution of **11** afforded cubic orange crystals suitable for single crystal X-ray diffraction. A crystal of dimensions  $0.3 \times 0.3 \times 0.4$  mm was selected and mounted on a glass fibre using a drop of Paratone oil. Data collection and structure solution were performed by Dr L.H. Rees of the Chemical Crystallographic Laboratory, Oxford. Data were collected at 293 K and indexed on a monoclinic cell with systematic absences consistent with the space group  $P2_1/c$ . The structure was solved using a direct methods package (SIR92). Full matrix least squares refinement was performed on the structure using SHELXL-93. Hydrogen atoms were placed in geometrically calculated positions yielding a final R value of 5.66 % with a weighted R value of 9.47 %. The structure is shown in **Figure 2.13**. Full details are contained within **Appendix A**.

The view of the crystal structure of **11** given in **Figure 2.13** shows that the parallel cyclopentadienyl rings are arranged in a staggered formation such that the pendant dimethylphosphino groups are as far away from each other as possible. The view afforded by **Figure 2.14** demonstrates that in addition to being located on opposite sides of the molecule, both  $-\text{PMe}_2$  groups also point up and away from the molecule in a fashion that minimises any steric strain resulting from interaction between the many bulky substituents on the cyclopentadienyl rings.

Selected Mn-C<sub>ring</sub> bond lengths of **11** are shown in **Table 2.4** below. The  $r(\text{M}-\text{C})$  values found for **11** broadly agree with the Mn-C bond lengths found for low-spin  $[\text{Mn}(\eta\text{-C}_5\text{Me}_5)_2]$  with Mn-C bond lengths in the range of 2.092(2) to 2.127(2) Å. Taken on their own, these bond length data could suggest that **11** has a low-spin,  $^2\text{E}_{2g}$  character.



Bond	Distance (Å)	Bonds	Angle (°)
Mn – C(1)	2.099(2)	C(1) – Mn - C(1)	180.0
Mn – C(3)	2.120(2)	C(1) – C(7) – C(9)	107.9(2)
Mn – C(5)	2.127(2)	C <sub>centroid</sub> – Mn - C <sub>centroid</sub>	180.0
Mn – C(7)	2.105(2)		
Mn – C(9)	2.092(2)		
Mn – C <sub>centroid</sub>	1.725		

**Table 2.4** Selected bond data from the crystal structure of [Mn{(η-C<sub>5</sub>Me<sub>4</sub>)CH<sub>2</sub>PMe<sub>2</sub>}<sub>2</sub>] (**11**)

The crystal structure of [Fe{(η-C<sub>5</sub>Me<sub>4</sub>)CH<sub>2</sub>PMe<sub>2</sub>}<sub>2</sub>]<sup>[20]</sup> demonstrates that the Fe analogue consists of two parallel cyclopentadienyl rings supporting the central metal atom with the pendant dimethylphosphine groups almost eclipsed. This is in contrast with the compound **11** where the two dialkylphosphino groups are 180° apart.

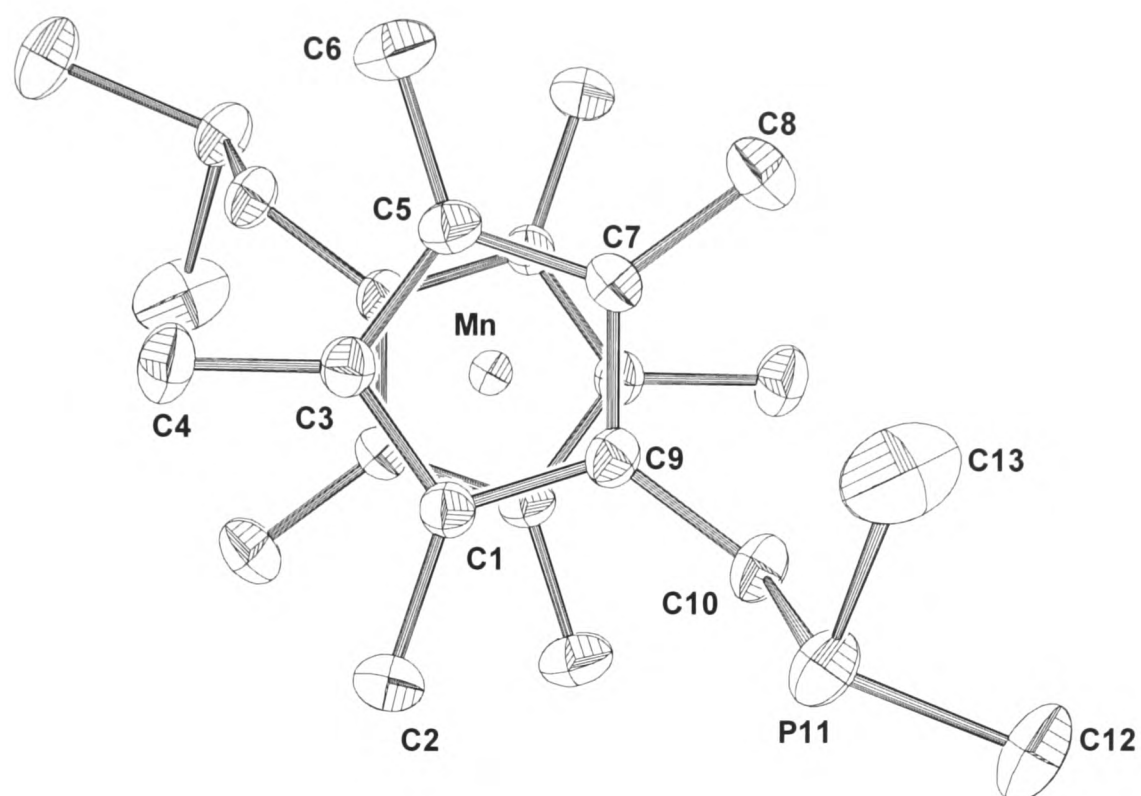


**Figure 2.13** Crystal structure view of  $[\text{Mn}\{(\eta\text{-C}_5\text{Me}_4)\text{CH}_2\text{PMe}_2\}_2]$  (**11**) along the Cp-Mn-Cp axis demonstrating the 'staggered' nature of the Cp-ligands

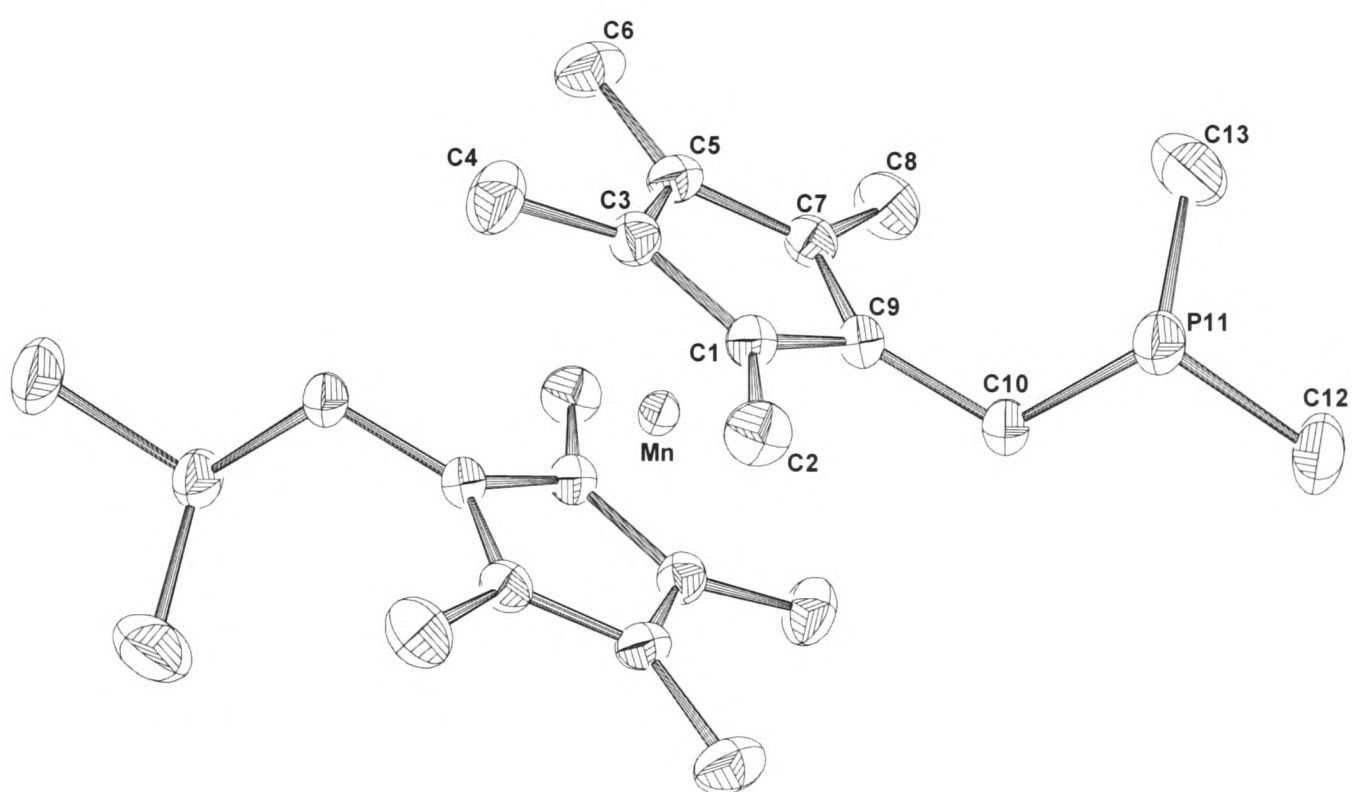


**Figure 2.14** 'Side-On' Crystal structure view of  $[\text{Mn}\{(\eta\text{-C}_5\text{Me}_4)\text{CH}_2\text{PMe}_2\}_2]$  (**11**)

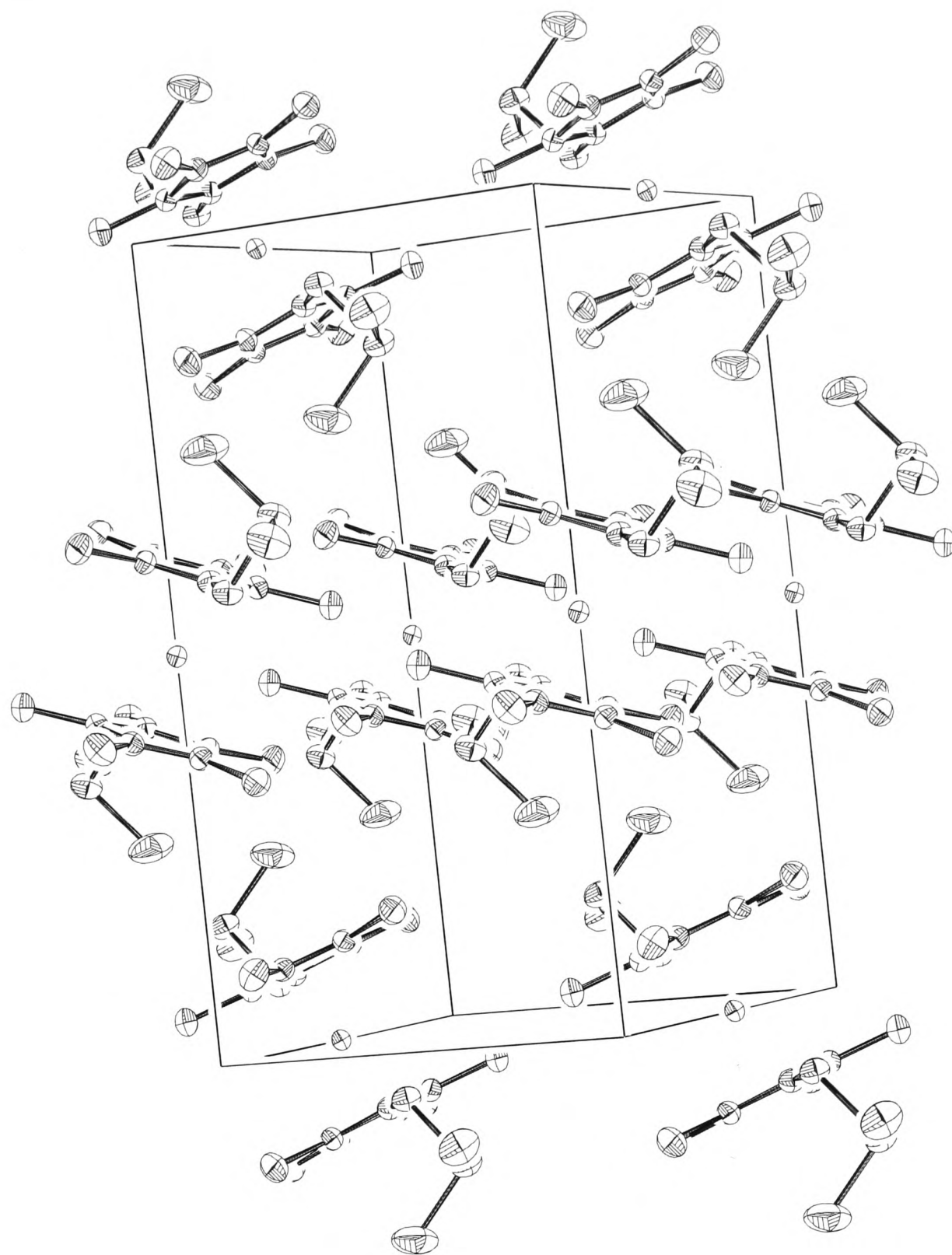


**Figure 2.15** Crystal structure packing view of  $[\text{Mn}\{(\eta\text{-C}_5\text{Me}_4)\text{CH}_2\text{PMe}_2\}_2]$  (**11**)

The packing diagram above shows that the crystal packing arrangement consists of two types of layer, each containing molecular units aligned in the opposite orientation to that of the other.

Sitzmann has reported the synthesis and magnetic behaviour of a number of highly substituted manganocenes.[29] The compounds  $[\text{Mn}(\eta\text{-C}_5^i\text{Bu}_3\text{H}_2)_2]$  and  $[\text{Mn}(\eta\text{-C}_5^i\text{Pr}_4\text{H})_2]$  exhibit high-spin behaviour while  $[\text{Mn}(\eta\text{-C}_5^i\text{Pr}_3\text{Me}_2)_2]$  displays a spin-crossover from high-spin to low-spin below  $-106^\circ\text{C}$ . The compound  $[\text{Mn}(\eta\text{-C}_5^i\text{Pr}_3\text{H}_2)_2]$  is consistent with a completely low spin arrangement. These data support the argument that steric effects can overrule an electronic spin-state preference and also that it is possible to alter the spin-state through slight structural modifications.

Further work by Hanusa *et al.* supports this argument.[30] Following the studies by Sitzmann, the compound  $[\text{Mn}(\eta\text{-C}_5^i\text{Pr}_4\text{H})_2]$  has been structurally characterised and the Mn-C bond length data are consistent with those found for high-spin complexes, even though it might be expected to demonstrate low-spin structural characteristics similar to those of complexes like  $[\text{Mn}(\eta\text{-C}_5\text{Me}_5)_2]$  and  $[\text{Mn}(\eta\text{-C}_5\text{Me}_4\text{H})_2]$ . [25, 28] Thus, the type as well as the extent of substitution is an important variable in determining the electronic configuration. **Table 2.5** gives some examples of comparisons between Mn-C bond length and spin-state.

Compound	Selected Mn-C Bond Lengths (Å)	Spin State	Reference
$[\text{Mn}(\eta\text{-C}_5\text{Me}_5)_2]$	2.105 (2)	$^2\text{E}_{2g}$	[25]
$[\text{Mn}(\eta\text{-C}_5^i\text{Pr}_4\text{H})_2]$	2.450 (5)	$^6\text{A}_{1g}$	[30]
$[\text{Mn}(\eta\text{-C}_5\text{Me}_4\text{H})_2]$	-	$^2\text{E}_{2g}$	[28]
$[\text{Mn}(\eta\text{-MeC}_5\text{H}_4)_2]$	2.114 (12) and 2.433 (8)	$^2\text{E}_{2g} \leftrightarrow ^6\text{A}_{1g}$	[23]
$[\text{Mn}(\eta\text{-C}_5\text{H}_5)_2]$	2.380 (6)	$^6\text{A}_{1g}$	[23]
$[\text{Mn}(\eta\text{-C}_5^i\text{Pr}_3\text{H}_2)_2]$	2.131 (3)	$^2\text{E}_{2g}$	[29]
$[\text{Mn}(\eta\text{-C}_5^i\text{Bu}_3\text{H}_2)_2]$	-	$^6\text{A}_{1g}$	[29]
$[\text{Mn}(\eta\text{-C}_5^i\text{PrMe}_4)_2]$	-	$^2\text{E}_{2g}$	[29]
$[\text{Mn}(\eta\text{-C}_5^i\text{Pr}_3\text{Me}_2)_2]$	-	$^2\text{E}_{2g} \leftrightarrow ^6\text{A}_{1g}$	[29]

**Table 2.5** Comparison between Mn-C bond lengths in structurally characterised manganocenes and their electronic spin-state

### 2.7.4 Magnetic Susceptibility Study of Compound 11

Due to the potential for a mixture or equilibrium of electronic spin-states in substituted manganocene complexes,[23, 25, 27-29, 31-34] a magnetic susceptibility study was undertaken to determine the spin-state of the compound **11**.

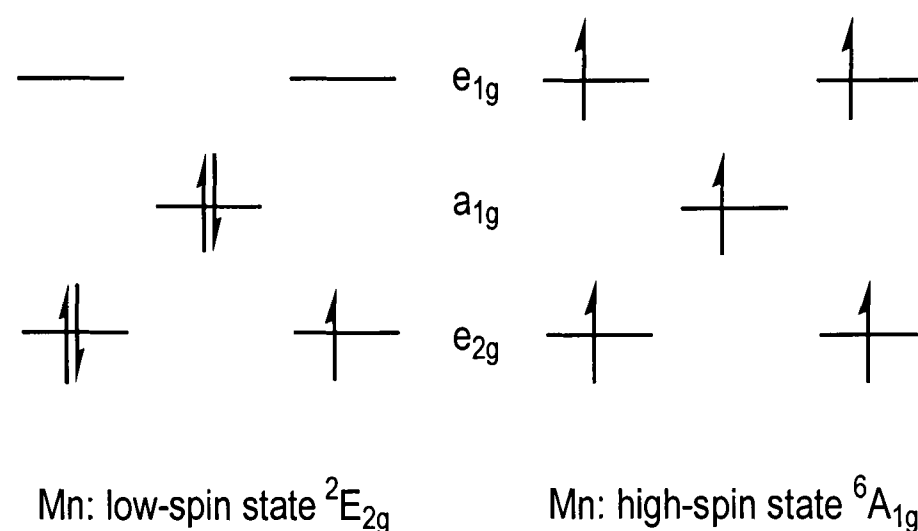


**Figure 2.16** Schematic of energy level diagrams for high- and low-spin manganocenes[35]

The magnetic susceptibility of **11** was determined in a toluene solution as a function of temperature by Evans' NMR method.[36, 37] A capillary containing a solution of  $d^8$ -toluene and tetramethylsilane (TMS) was placed in a Young's tap NMR tube containing a known concentration of **11** in  $d^8$ -toluene. The differences between the chemical shifts of the toluene *o*-, *m*- and *p*-protons in the standard solution and those in the solution of the paramagnetic complex ( $\Delta f$ ) were measured. From these values, it was possible to calculate the magnetic susceptibility and the effective magnetic moment of the paramagnetic species. Using the general equations:

$$\chi = \frac{3\Delta f}{2\pi f m} \quad \text{equation 2.1}$$

$$\chi_A = \frac{3\Delta f A}{2\pi f m'} \quad \text{equation 2.2}$$

$$\mu_{\text{eff}} = (8\chi_A T)^{1/2} \quad \text{equation 2.3}$$

where  $\chi$  is the magnetic susceptibility,  $\chi_A$  is the atomic magnetic susceptibility,  $\mu_{\text{eff}}$  is the effective magnetic moment,  $A$  is the atomic mass of manganese,  $\Delta f$  is the frequency separation between corresponding frequencies (Hz),  $f$  is the operating frequency of the spectrometer (Hz),  $m$  is the mass of solid sample per unit of solvent ( $\text{g ml}^{-1}$ ),  $m'$  is the molarity of the solution ( $\text{mol l}^{-1}$ ) and  $T$  is the temperature (K), it is possible to calculate the magnetic susceptibility ( $\chi_A$ ) and the effective magnetic moment ( $\mu_{\text{eff}}$ ).

Magnetic susceptibility calculations using Evans' method result in a calculated effective magnetic moment (298 K) of 2.64 BM. This value is higher than that expected for a system with one unpaired electron (1.73 BM).[34] Thus, the complex **11** seems to exhibit behaviour which suggests that the manganocene has predominantly low-spin character as evidenced by the similarity of bond-length data to those of  $[\text{Mn}(\eta\text{-C}_5\text{Me}_5)_2]$ , but also contains a contribution from the high-spin  ${}^6\text{A}_{1g}$  configuration. **Figure 2.17** shows the plot of effective magnetic moment ( $\mu_{\text{eff}}$ ) versus temperature (T) obtained from the data. The graph shows a minor decrease in  $\mu_{\text{eff}}$  with increasing temperature levelling off at around 2.5 BM.

In addition to the plot of effective magnetic moment versus temperature, a plot of magnetic susceptibility versus temperature, shown in **Figure 2.18**, exhibits behaviour typical of a normal paramagnetic species where  $\chi \propto 1/T$ . [34]



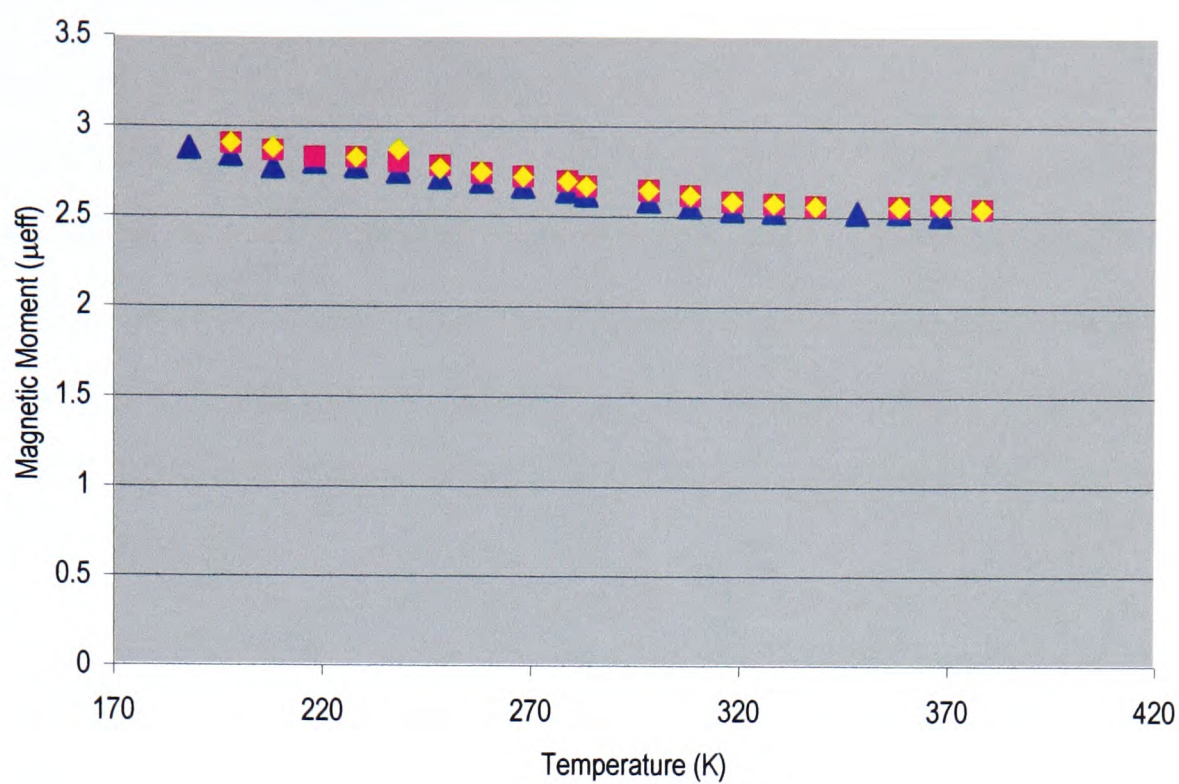


**Figure 2.17** Plot of the effective magnetic moment ( $\mu_{\text{eff}}$ ) of compound **11** in  $d^8$ -toluene at a range of temperatures.

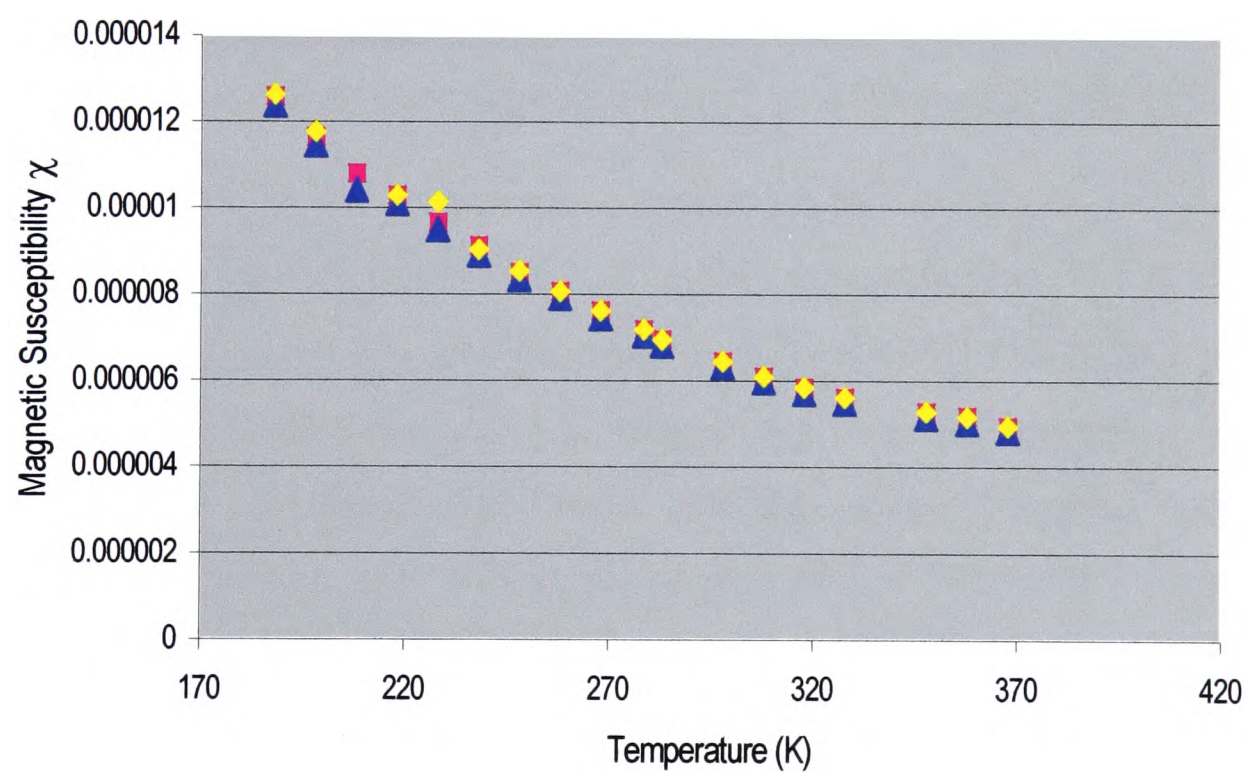


**Figure 2.18** Plot of the Magnetic Susceptibility ( $\chi$ ) of compound **11** in  $d^8$ -toluene at a range of temperatures.

### 2.7.5 Reactivity Studies on Compound 11

A number of reactions were attempted between compound **11** and a variety of oxidation and reduction agents. The compound  $[\text{Mn}(\eta\text{-C}_5\text{Me}_5)_2]$  is known to undergo both oxidation to a 16 electron metallocene and reduction to an 18 electron complex.<sup>[25]</sup> However, the reactions between **11** and a variety of reagents did not lead to any isolable compounds. The failure to isolate the expected products may be a result of reactions between the phosphinodimethyl substituent and the oxidation and reduction agents.

#### 2.7.5.1 Reaction Between Compound 11 and $[\text{Na}][\text{C}_{10}\text{H}_8]$

In an attempt to reduce the manganocene **11** to the eighteen electron complex  $[\text{11}][\text{Na}]^+$  a THF solution of compound **11** was added to a freshly prepared THF solution of sodium naphthalide at room temperature. The orange solution was stirred for 30 minutes after which time solvents were removed under reduced pressure to yield an intractable brown solid. Microanalysis results were inconsistent with the proposed formula. Further studies were discontinued.

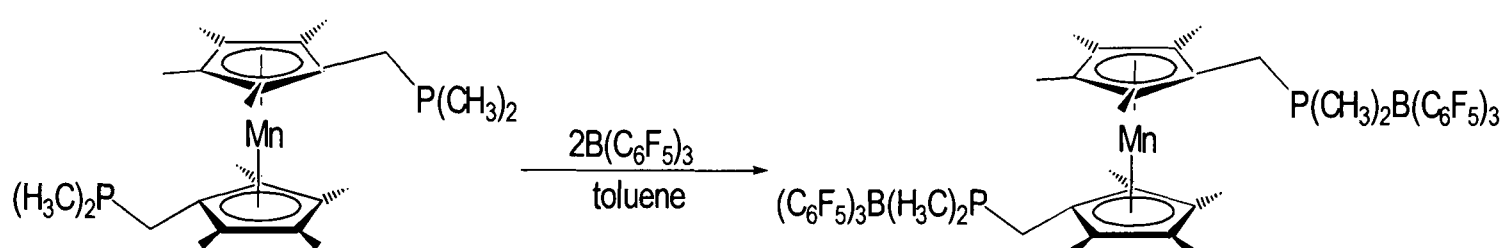
#### 2.7.5.2 Reaction Between Compound 11 and $[\text{Fe}(\eta\text{-C}_5\text{H}_5)_2][\text{PF}_6]$

Attempts to oxidise the manganese complex **11** to the sixteen electron complex  $[\text{11}]^+[\text{PF}_6]^-$  also proved unsuccessful. In an analogous procedure to that described by Robbins,<sup>[25]</sup> THF was added to a mixture of the two solids **11** and  $[\text{FeCp}_2][\text{PF}_6]$  and then acetone was added to dissolve all the solids. The resulting orange-red solution was stirred for 30 minutes after which time solvent was removed under reduced pressure. The orange solid was extracted into pentane, solvents were removed to yield a pink solid. The  $^1\text{H}$  and  $^{31}\text{P}$  NMR spectra exhibited a large number of signals indicating that a large number of species were present so further studies in this area were discontinued.



### 2.7.5.3 Preparation of $[\text{Mn}\{(\eta\text{-C}_5\text{Me}_4)\text{CH}_2\text{PMe}_2\text{B}(\text{C}_6\text{F}_5)_3\}_2]$ (**12**)

To a toluene solution of **11** was added a toluene solution containing two equivalents of  $\text{B}(\text{C}_6\text{F}_5)_3$ . The orange solution was stirred overnight and solvents were removed and the product washed with pentane to yield the compound  $[\text{Mn}\{(\eta\text{-C}_5\text{Me}_4)\text{CH}_2\text{PMe}_2\text{B}(\text{C}_6\text{F}_5)_3\}_2]$  (**12**) as an orange powder in quantitative yield (Scheme 2.16).



Scheme 2.16 Synthesis of  $[\text{Mn}\{(\eta\text{-C}_5\text{Me}_4)\text{CH}_2\text{PMe}_2\text{B}(\text{C}_6\text{F}_5)_3\}_2]$  (**12**)

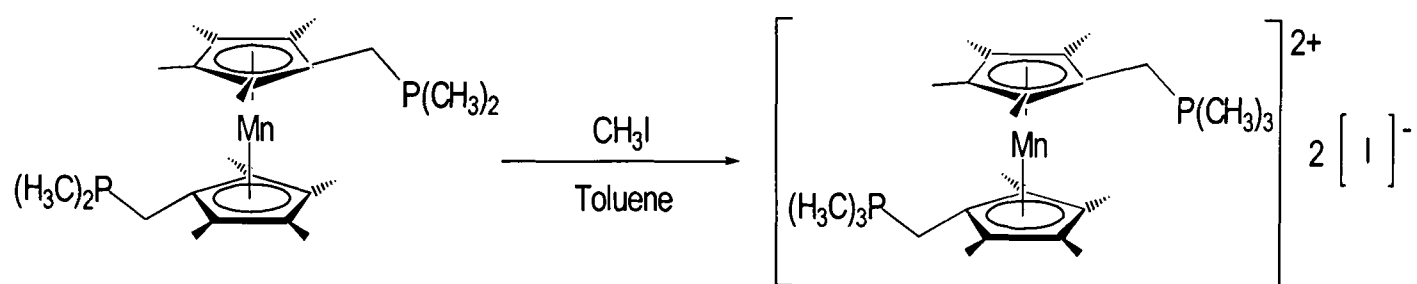
### 2.7.5.4 Characterisation of $[\text{Mn}\{(\eta\text{-C}_5\text{Me}_4)\text{CH}_2\text{PMe}_2\text{B}(\text{C}_6\text{F}_5)_3\}_2]$ (**12**)

The compound **12** is an orange solid, relatively stable in air but insoluble in common solvents. Microanalysis results are consistent with the empirical formula  $\text{C}_{60}\text{H}_{40}\text{B}_2\text{MnP}_2$ . The low solubility of the complex precluded solution NMR studies.

In addition to the microanalysis, the FAB mass spectrum provides further evidence for the formation of **12**. A signal at  $m/z$  1469 with the correct isotope pattern demonstrates the presence of the molecular ion  $[\text{M}^+]$ . Further signals at  $m/z$  957 and  $m/z$  445 are attributable to fragments resulting from the loss of one and two molecules of  $\text{B}(\text{C}_6\text{F}_5)_3$  respectively. Characterising data are given in Section 8.11.

### 2.7.5.5 Preparation of $[\text{Mn}\{(\eta\text{-C}_5\text{Me}_4)\text{CH}_2\text{PMe}_3\}_2][\text{I}]_2$ (**13**)

To a toluene solution of the compound **11** was added *via* syringe an excess of methyl iodide. The orange solution was stirred overnight and an orange-yellow solid precipitated. The supernatant solution was removed and the solid was washed with pentane. Remaining volatiles were removed under reduced pressure and the product  $[\text{Mn}\{(\eta\text{-C}_5\text{Me}_4)\text{CH}_2\text{PMe}_3\}_2][\text{I}]_2$  (**13**) was isolated as a pale orange solid (Scheme 2.17).



**Scheme 2.17** Synthesis of  $[\text{Mn}\{(\eta\text{-C}_5\text{Me}_4)\text{CH}_2\text{PMe}_3\}_2][\text{I}]_2$  (**13**)

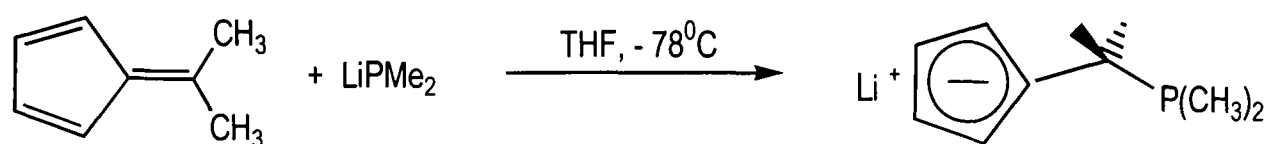
The compound **13** is a pale orange solid, which decomposes in air and is insoluble in common solvents. Microanalysis results are consistent with the empirical formula  $\text{C}_{26}\text{H}_{46}\text{I}_2\text{MnP}_2$ . Once again, the poor solubility of the complex precluded any NMR studies and attempts to obtain a mass spectrum containing peaks for either the molecular ion or identifiable fragments failed to give the desired result. Characterising data are given in **Section 7.2.16**.

## 2.8 Attempted Preparation of the Manganocene, $[\text{Mn}\{(\eta\text{-C}_5\text{H}_4)\text{CMe}_2\text{PMe}_2\}_2]$

We were interested to compare the properties of compound **11** with the analogous compound  $[\text{Mn}\{(\eta\text{-C}_5\text{H}_4)\text{CMe}_2\text{PMe}_2\}_2]$ . Hence, the ligand  $[\text{Li}(\text{C}_5\text{H}_4)\text{CMe}_2\text{PMe}_2]$  was prepared and reacted with manganese dichloride.

### 2.8.1 Preparation of $[\text{Li}(\text{C}_5\text{H}_4)\text{CMe}_2\text{PMe}_2]$

The ligand  $[\text{Li}(\text{C}_5\text{H}_4)\text{CMe}_2\text{PMe}_2]$  was synthesised following a published procedure developed in this laboratory.<sup>[20]</sup> To a THF solution at  $-78^\circ\text{C}$  containing lithium dimethylphosphide was added a THF solution of dimethylfulvene. The yellow solution was stirred overnight, solvents were removed under reduced pressure and the white product washed with pentane (**Scheme 2.18**). Satisfactory microanalysis data were obtained and the  $^1\text{H}$  NMR spectrum was consistent with that published for the compound.

Scheme 2.18 Preparation of the ligand  $[\text{Li}(\text{C}_5\text{H}_4)\text{CMe}_2\text{PMe}_2]$ 

### 2.8.2 Attempted Preparation of $[\text{Mn}\{(\eta\text{-C}_5\text{H}_4)\text{CMe}_2\text{PMe}_2\}_2]$

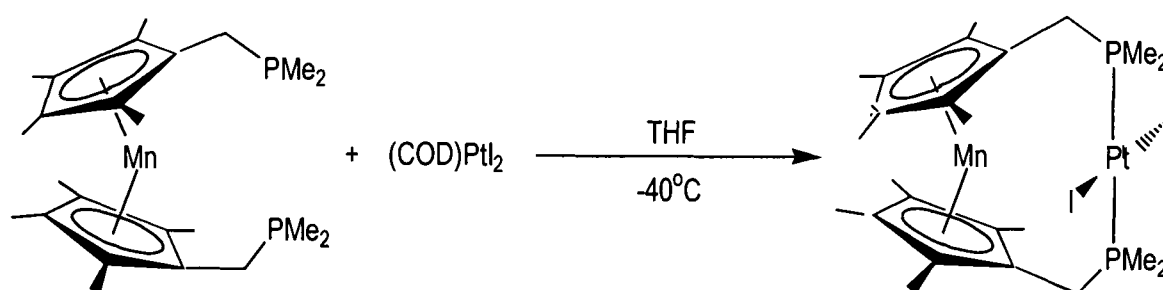
To an intimate mixture of  $\text{MnCl}_2$  and  $[\text{Li}(\text{C}_5\text{H}_4)\text{CMe}_2\text{PMe}_2]$  at  $-78^\circ\text{C}$  was added THF. The resulting suspension was allowed to warm to room temperature and stirred overnight. Solvent was removed under reduced pressure and the resulting oily orange solid was triturated with and then extracted into pentane. Removal of solvents under reduced pressure yielded an oily orange solid. The  $^{31}\text{P}\{^1\text{H}\}$  NMR spectrum demonstrated the presence of a number of species in the isolated product, while the  $^1\text{H}$  NMR spectrum was also suggestive of a mixture of species. Further work on this system was discontinued.

## 2.9 Attempted Preparation of a Bimetallic Complex Incorporating Compound 11

As described in Section 2.4, it is possible to form bimetallic complexes utilising the chelating ability of the phosphinodimethyl group. It was decided, therefore to attempt a reaction between **11** and one of the Group 8 metal(II) complexes such as  $\text{Pt}(\text{COD})\text{I}_2$  or  $\text{Pd}(\text{COD})\text{Cl}_2$  in accordance with this previously reported synthetic route to heterobimetallic transition metal complexes.[5, 10, 12]

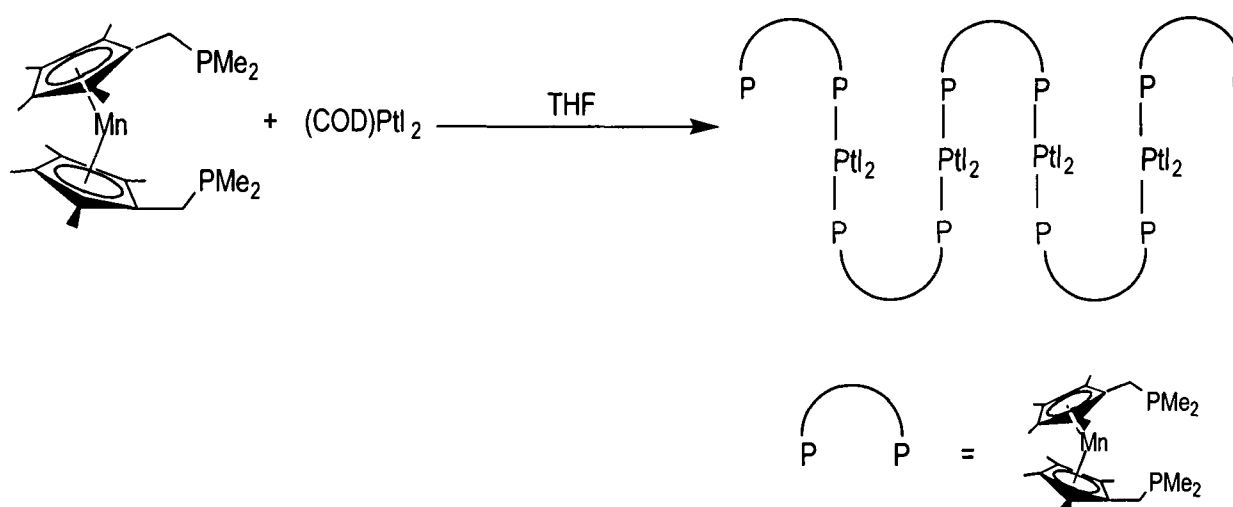
### 2.9.1 Attempted Preparation of $[\text{Mn}\{\eta\text{-C}_5\text{Me}_4\text{CH}_2\text{PMe}_2\}\text{PtI}_2]$ (**14**)

To a Schlenk tube containing THF at  $-40^\circ\text{C}$  was added dropwise a THF solution of compound **11** and a THF solution of  $\text{Pt}(\text{COD})\text{I}_2$  (one equivalent) with stirring. The orange solution was stirred overnight at room temperature, solvent was removed under reduced pressure and the product was washed with pentane. The compound **14** was isolated as an orange powder in 45 % yield (Scheme 2.19).



**Scheme 2.19** Synthesis of  $[\text{Mn}\{\eta\text{-C}_5\text{Me}_4\text{CH}_2\text{PMe}_2\}\text{PtI}_2]$  (**14**)

The compound **14** is an orange solid, relatively stable in air but insoluble in common solvents. Microanalysis results are consistent with the empirical formula  $\text{C}_{24}\text{H}_{40}\text{I}_2\text{MnP}_2\text{Pt}$ . The low solubility of the complex, precluded NMR studies on the complex and the FAB mass spectrum did not display signals for either the parent ion or fragments thereof. The combination of consistent elemental analysis and very low solubility infer that the product may be oligomeric or polymeric. This could arise from the binding mode of the manganocene as a *bridging* ligand rather than *chelating* to a single platinum centre to form a species or a mixture of species of the form shown in **Scheme 2.20**. Characterising data are given in **Section 7.2.17**.



**Scheme 2.20** Possible formation of a polymeric structure of compound **14**

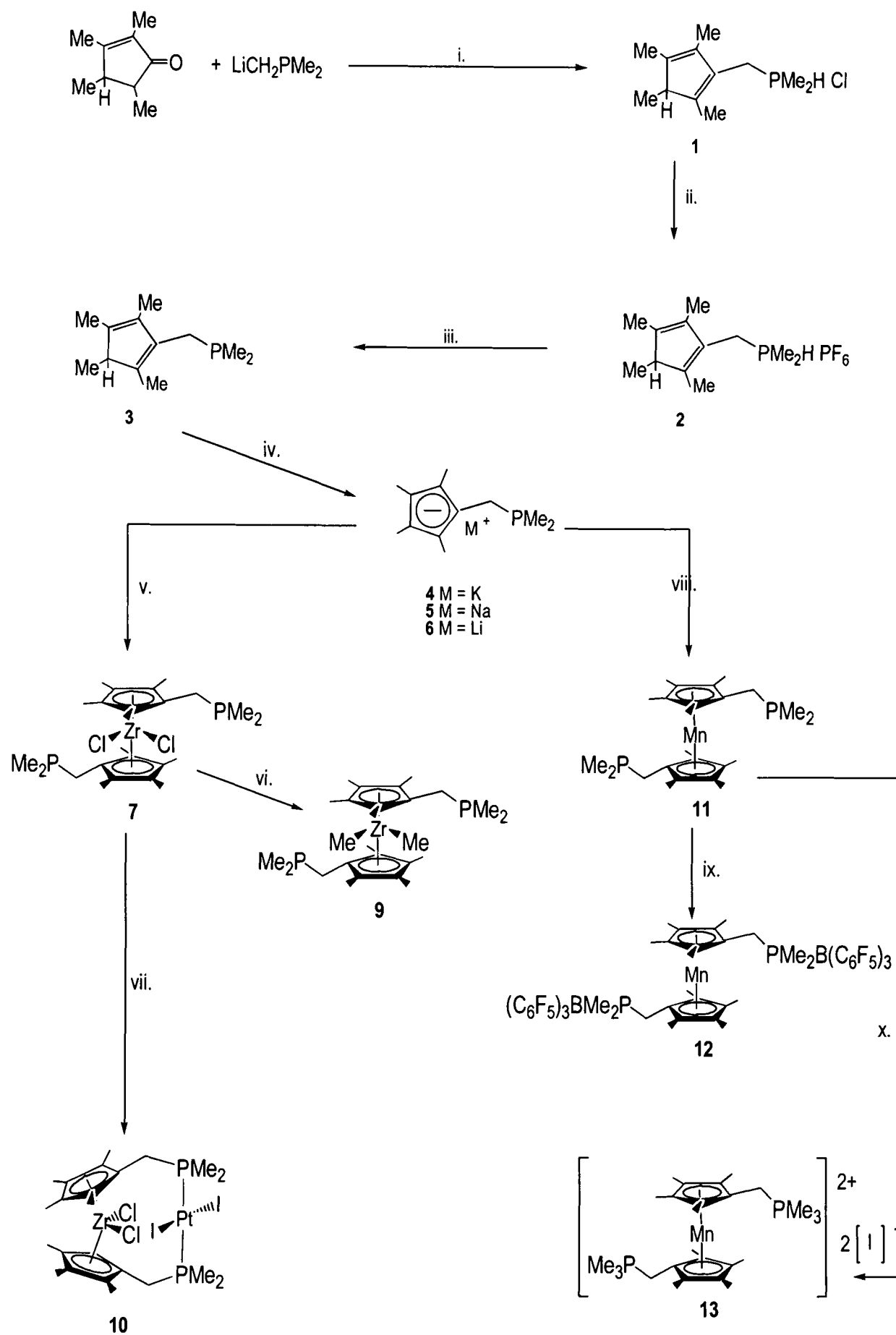
## 2.10 Summary

The work in this chapter describes the development of a novel, phosphinodimethyl substituted cyclopentadienyl ligand  $M(C_5Me_4)CH_2PMe_2$   $\{M = H$  (**3**), Li (**4**), Na (**5**), K(**6**) $\}$  *via* synthesis of the precursor complexes  $[H(C_5Me_4)CH_2PMe_2H][Cl]$  (**1**) and  $[H(C_5Me_4)CH_2PMe_2H][PF_6]$  (**2**). The compound **5** has been used to synthesise the zirconocene derivative  $[Zr\{(\eta-C_5Me_4)CH_2PMe_2\}_2Cl_2]$  (**7**). In addition, formation of the early-late bimetallic complex *trans*- $[Zr\{(\eta-C_5Me_4)CH_2PMe_2\}_2Cl_2PtI_2]$  (**10**) is supported by  $^{31}P\{^1H\}$  NMR spectroscopy, elemental analysis and mass spectrometry and displays evidence, through the magnitude of the  $J_{P-Pt}$  coupling constant, that the bidentate phosphine ligand binds with a *trans*-geometry.

The sodium salt of the ligand (**5**) has also been used to synthesise the substituted managnocene  $[Mn\{(\eta-C_5Me_4)CH_2PMe_2\}_2]$  (**11**) for which the X-ray crystal and molecular structure has been obtained. The compound **11** is a paramagnetic  $d^5$ -complex which exhibits a magnetic moment ( $\mu_{eff}$ ) of 2.64 BM, which suggests a mixture of high- and low-spin electronic arrangements. The Mn-C bond lengths as determined from the molecular structure are consistent with those expected of a compound with the proposed low-spin  $^2E_{2g}$  state and are comparable with those of other known low-spin manganocenes  $[Mn(\eta-C_5Me_5)_2]$  and  $[Mn(\eta-C_5^iPr_4Me)_2]$ . Attempts to obtain respectively the one electron oxidation and reduction products  $[Mn\{(\eta-C_5Me_4)CH_2PMe_2\}_2]^+$  and  $[Mn\{(\eta-C_5Me_4)CH_2PMe_2\}_2]^-$  proved unsuccessful.

Further reactions of **11** with the strong Lewis acid  $B(C_6F_5)_3$  yielded the adduct  $[Mn\{(\eta-C_5Me_4)CH_2PMe_2B(C_6F_5)_3\}_2]$  (**12**) characterised by elemental analysis and mass spectrometry and a reaction with an excess of methyl iodide yielded a highly insoluble product with microanalysis results consistent with those calculated for a complex of the formula  $[Mn\{(\eta-C_5Me_4)CH_2PMe_3\}_2][I]_2$  (**13**). Attempts to prepare the heteronuclear bimetallic manganese-platinum complex  $Mn\{(\eta-C_5Me_4)CH_2PMe_2PtI_2\}$  (**14**) produced a species which provided satisfactory elemental analysis, but which exhibited other characteristics suggestive of the formation of a polymeric product incorporating **11** in a bridging mode rather than as a chelating ligand.

The new chemistry described in this chapter is summarised in **Scheme 2.21**.



Scheme 2.21 Summary of the new chemistry described in Chapter 2

Reagents and conditions for **Scheme 2.21**:

- |      |  |       |   |
|------|--|-------|---|
| i.   | THF, -78°C, HCl in Et <sub>2</sub> O                       | ii.   | [NH <sub>4</sub> ][PF <sub>6</sub> ], H <sub>2</sub> O                |
| iii. | KOH, MeOH, pentane   | iv.   | MN(SiMe <sub>3</sub> ) <sub>2</sub> , THF, -78°C<br>(M = K, Na or Li) |
| v.   | ZrCl <sub>4</sub> (thf) <sub>2</sub> , THF, 0°C            | vi.   | MeLi, THF, -78°C  |
| vii. | PtI <sub>2</sub> (COD), THF, -40°C                         | viii. | MnCl <sub>2</sub> , THF, 40°C   |
| ix.  | 2 B(C <sub>6</sub> F <sub>5</sub> ) <sub>3</sub> , toluene | x.    | Excess CH <sub>3</sub> I, pentane                                     |

## 2.11 References for Chapter 2

- [1] J. C. Leblanc, C. Moise, A. Maisonnat, R. Poilblanc, C. Charrier and F. Mathey, *J. Organomet. Chem.*, 231 (1982) C43.
- [2] C. Charrier and F. Mathey, *Tetrahedron Lett.*, 27 (1978) 2407.
- [3] B. Bosch, G. Erker and R. Fröhlich, *Inorg. Chim. Acta.*, 270 (1998) 446.
- [4] W. Tikkanen, A. L. Kim, K. B. Lam and K. Ruekert, *Organometallics*, 14 (1995) 1525.
- [5] T. W. Graham, A. Llamazares, R. McDonald and M. Cowie, *Organometallics*, 18 (1999) 3502.
- [6] N. J. Goodwin, W. Henderson and B. K. Nicholson, *Inorg. Chim. Acta.*, 295 (1999) 18.
- [7] V. I. Bakmutov, M. Visseaux, D. Baudry, A. Dormond and P. Richard, *Inorg. Chem.*, 35 (1996) 7316.
- [8] X.-D. He, A. Maisonnat, F. Dahan and R. Poilblanc, *Organometallics*, 8 (1989) .
- [9] C. P. Casey and F. Nief, *Organometallics*, 4 (1985) 1218.
- [10] T. W. Graham, A. Llamazares, R. McDonald and M. Cowie, *Organometallics*, 18 (1999) 3490.
- [11] F. T. Ladipo, K. Anderson and N. P. Rath, *Organometallics*, 13 (1994) 4741.
- [12] M. D. Rausch, B. H. Edwards, R. D. Rogers and J. L. Atwood, *J. Am. Chem. Soc.*, 105 (1983) 3882.
- [13] W. Tikkanen, Y. Fujita and J. L. Petersen, *Organometallics*, 5 (1986) 888.
- [14] B. E. Bosch, I. Brummer, K. Künz, G. Erker, R. Frölich and S. Kotila, *Organometallics*, 19 (2000) 1255.
- [15] B. E. Bosch, G. Erker, R. Fröhlich and O. Meyer, *Organometallics*, 16 (1997) 5449.
- [16] A. J. Graham, *D.Phil. Thesis*, University of Oxford, (1998) *and references therein*.
- [17] R. G. Pregosin, in J. G. Verkade and L. D. Quin (Eds.): *Stereochemistry of Metal Complexes: Unidentate Phosphorus Ligands, Phosphorus-31 NMR Spectroscopy in Stereochemical Analysis; Organic Compounds and Metal Complexes*, VCH, Weinheim 1987, p. 465.



- [18] P. L. Goggin, R. J. Goodfellow, S. R. Haddock, J. R. Knight, F. J. S. Reed and B. F. Taylor, *J. Chem. Soc., Dalton Trans.*, (1974) 523.
- [19] R. Favez, R. Roulet, A. A. Pinkerton and D. Schwarzenbach, *Inorg. Chem.*, **19** (1980) 1356.
- [20] R. M. Bellabarba, *D.Phil. Thesis*, University of Oxford (2000).
- [21] G. Wilkinson, F. A. Cotton and J. M. Birmingham, *J. Inorg. Nucl. Chem.*, **2** (1956) 95.
- [22] W. Bünder and E. Weiss, *Z. Naturforsch., Teil B.* **33** (1978) 1235.
- [23] J. H. Ammeter, R. Bucher and N. Oswals, *J. Am. Chem. Soc.*, **94** (1974) 7833.
- [24] C. G. Howard, G. S. Girolami, G. Wilkinson, M. Thornton-Pett and M. B. Hursthouse, *J. Am. Chem. Soc.*, **106** (1984) 2033.
- [25] J. L. Robbins, N. M. Edelstein, S. R. Cooper and J. C. Smart, *J. Am. Chem. Soc.*, **101** (1979) 3853.
- [26] J. Heck, W. Massa and P. Weinig, *Angew. Chem. Int. Ed. Engl.*, **23** (1984) 722.
- [27] M. E. Switzer, R. Wang, M. F. Rettig and A. H. Maki, *J. Am. Chem. Soc.*, **96** (1974) 7669.
- [28] D. Cozak, F. Gauvin and J. Demers, *Can. J. Chem.*, **64** (1986) 71.
- [29] H. Sitzmann and M. Schar, *Z. Anorg. Allg. Chem.*, **623** (1997) 1609.
- [30] M. L. Hays, D. J. Burkey, J. S. Overby, T. P. Hanusa, S. P. Sellers, G. T. Yee and J. Young, *Organometallics*, **17** (1998) 5521.
- [31] D. Cozak and F. Gauvin, *Organometallics*, **6** (1987) 1912.
- [32] N. Hebenanz, F. H. Köhler, G. Müller and J. Reide, *J. Am. Chem. Soc.*, **108** (1986) 3281.
- [33] F. H. Köhler and B. Schlesinger, *Inorg. Chem.*, **31** (1992) 2853.
- [34] D. Nicholls, *Complexes and First Row Transition Metals*, Macmillan Education Ltd., London 1974.
- [35] D. P. Freyberg, J. L. Robbins, K. N. Raymond and J. C. Smart, *J. Am. Chem. Soc.*, **101** (1979) 892.
- [36] D. F. Evans, *J. Chem. Soc.*, (1959) 2003.
- [37] D. F. Evans and T. A. James, *J. Chem. Soc. Dalton Trans.*, (1979) 723.

## **Chapter 3**

### **Substituted metallocenes of Group 14 metals**

### 3.0 Introduction to Chapter 3

This chapter describes the synthesis of some new main group metallocenes containing the  $[(C_5H_4)CMe_2PMe_2]^-$  ligand. There are relatively few examples of main group metallocenes compared with the plethora of transition metal complexes reported in the literature. The first part of this chapter therefore, provides a brief review of the area including examples and a description of the bonding and reactivity of main group metallocenes.

### 3.1 Main Group Metallocenes - A Brief Survey

Transition metal metallocenes have been a keystone in the development of modern organometallic chemistry and continue to provide major insights into the structure and reactivity of organometallic complexes.[1] Main group metallocene chemistry on the other hand has remained relatively underdeveloped. Recently, however, there has been a renaissance in the chemistry of *p*-block (Groups 13-15) metallocenes which has provided new insights into the chemistry of these species.[2] The less restrictive electronic requirements of the main group metals allows greater diversity in structure and reactivity which contrasts radically with that of transition metal metallocenes.[2]

#### 3.1.1 The Early History Group 14 Metallocenes

The first reported main group metallocenes were the cyclopentadienyl tin(II) and cyclopentadienyl lead(II) complexes  $[Sn(\eta-C_5H_5)_2]$  and  $[Pb(\eta-C_5H_5)_2]$  prepared by Fischer and co-workers in 1956.[3, 4] At the time, it was suggested that they had a  $\sigma$ -bonded structure, a theory supported by the dipole moments measured for each complex.[3, 4] It was the similarity of the IR spectra of these complexes to that of ferrocene that led the workers to conclude that the lead and tin complexes had a similar  $\pi$ -bonded sandwich structure, with both cyclopentadienyl rings bound in an  $\eta^5$ -fashion to the central metal atom.

The solution  $^1H$  NMR spectra of  $[Pb(\eta-C_5H_5)_2]$  and  $[Sn(\eta-C_5H_5)_2]$  in cyclohexane were reported by Wilkinson *et al.* in 1959.[5] In both cases, the spectrum displays only one signal, thus supporting the 'sandwich' metallocene arrangement also

preferred by Wilkinson. The  $\sigma$ -bonded structure originally postulated by Fischer would have given rise to a more complicated spectrum. In addition, the tin complex also exhibited  $^{117}\text{Sn}$  and  $^{119}\text{Sn}$  satellites, which too were consistent with a sandwich structure. Although the NMR data supported a sandwich structure, it was a gas phase electron diffraction study by Allmenningen that finally confirmed that the compound exists as a bent metallocene with an interplanar angle of  $55^\circ$ .<sup>[6]</sup>

### 3.1.2 Review of the Group 14 Metallocenes

Of all Group 14 metallocenes, stannocenes are the most prevalent in the literature. There are far fewer plumbocenes and germanocenes while examples of silicocenes are very rare. The following section provides a review of the reported complexes by element type. Group 14 metallocenes are almost always sensitive towards air and moisture. Increasing the steric bulk of the cyclopentadienyl ring, however, affords additional stability through shielding of the metal centre.<sup>[1, 7-9]</sup> Air sensitivity increases appreciably once a moderate amount of access to the metal is available. For example, in  $[\text{Sn}(\eta\text{-C}_5\text{Ph}_4\text{H})_2]$  and  $[\text{Sn}(\eta\text{-C}_5^i\text{Pr}_3\text{H}_2)_2]$  derivatives, decomposition occurs within minutes of exposure to air.<sup>[1]</sup>

### 3.1.3 Plumbocenes $[\text{Pb}(\eta\text{-C}_5\text{H}_n\text{R}_{5-n})_2]$ ( $\text{R} = \text{H}$ , alkyl or aryl group)

Although all known neutral metallocenes are monomeric in the gas phase, many exist as associated polymeric or molecular arrangements in the solid state. Simple non-substituted metallocenes often form polymeric strand-like structures in which the metal atoms are linked by metal-( $\mu\text{-Cp}$ )-metal interactions.<sup>[2]</sup> The orthorhombic form of  $[\text{Pb}(\eta\text{-C}_5\text{H}_5)_2]$  displays this type of structure, and the tendency of plumbocenes to polymerise is unique among the Group 14 elements. This arrangement contrasts with the monomeric structure exhibited by  $[\text{Sn}(\eta\text{-C}_5\text{H}_5)_2]$ .<sup>[2]</sup>

An interesting range of geometries are exhibited by  $[\text{Pb}(\eta\text{-C}_5\text{H}_5)_2]$ ,<sup>[1]</sup> from the bent monomer observed in the gaseous phase,<sup>[6]</sup> to the zig-zag polymeric structure in  $[\text{Pb}(\eta\text{-C}_5\text{H}_5)_2]_n$  crystals grown by sublimation.<sup>[10]</sup> More recently it has been demonstrated that the solvent from which the plumbocene is crystallised also has an

effect on the structure adopted.[2, 11] If the crystals are grown from the vapour phase *via* sublimation then the orthorhombic form with the zig-zag structure is formed **Figure 3.1(a)**. If the solvent used is toluene, the major product becomes the inclusion compound  $[\{\text{Pb}(\eta\text{-C}_5\text{H}_5)_2\}_3\cdot\text{toluene}]_\infty$  shown in **Figure 3.1(b)**. The other morphology is the minor product from this crystallisation, which is a hexagonal phase of plumbocene containing six  $[\text{Pb}(\eta\text{-C}_5\text{H}_5)_2]$  units linked together in a doughnut arrangement as shown in **Figure 3.1(c)**.

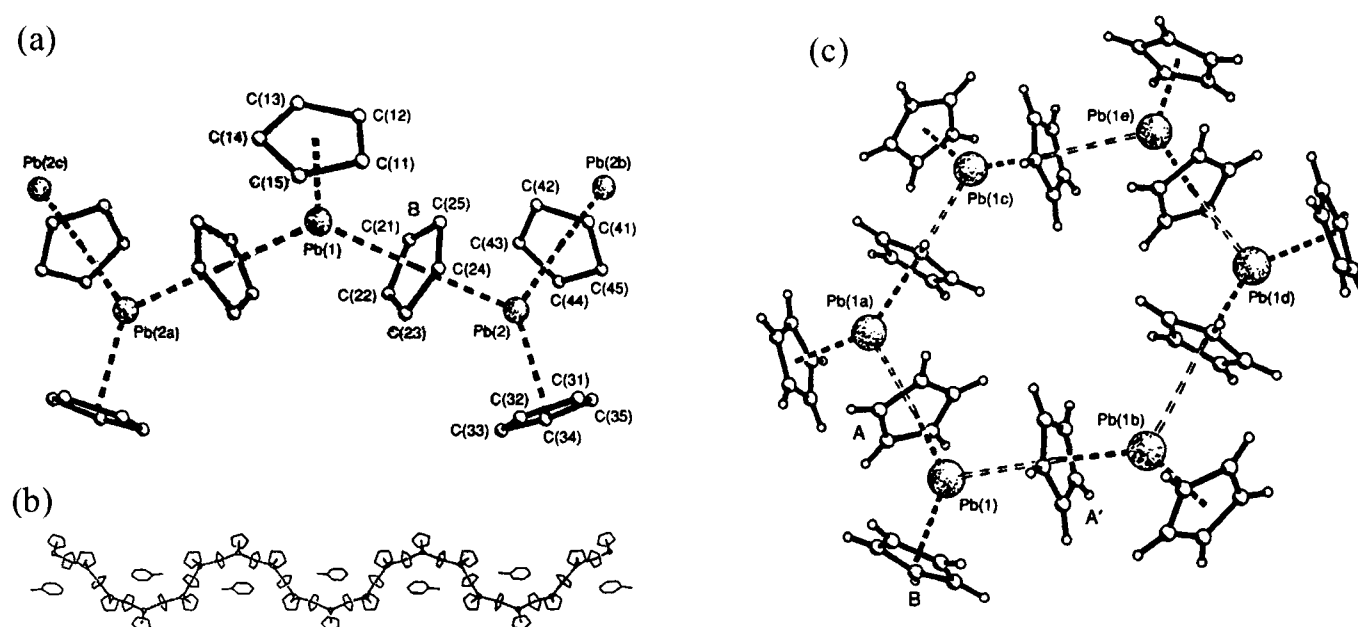


**Figure 3.1** Alternative morphologies of  $[\text{Pb}(\eta\text{-C}_5\text{H}_5)_2]$

According to the literature, there are only twelve known cyclopentadienyl complexes of divalent lead, and these are summarised in **Table 3.1** below.

Compound	Year	Reference
$[\text{Pb}(\eta\text{-C}_5\text{H}_5)_2]$	1956	[10]
$[\text{Pb}(\eta\text{-C}_5\text{Me}_5)_2]$	1981	[12]
$[\text{Pb}\{\eta\text{-C}_5(\text{CH}_2\text{Ph})_5\}_2]$	1986	[13]
$[\text{Pb}(\eta\text{-C}_5\text{Ph}_4\text{H})_2]$	1988	[14]
$[\text{Pb}\{\eta\text{-C}_5(\text{tBuPh})\text{Ph}_4\}_2]$	1988	[14]
$[\text{Pb}(\eta\text{-C}_5\text{Ph}_5)_2]$	1988	[8]
$[\text{Pb}(\eta\text{-C}_5\text{tBu}_2\text{H}_3)_2]$	1989	[15]
$[\text{Pb}\{\eta\text{-C}_5\text{Me}_4(\text{SiMe}_2\text{tBu})\}_2]$	1996	[16]
$[\text{Pb}(\eta\text{-C}_5\text{Me}_4\text{Et})_2]$	1996	[17]
$[\text{Pb}(\eta\text{-C}_5\text{Me}_4\text{nBu})_2]$	1999	[18]
$[\text{Pb}(\eta\text{-C}_5\text{Me}_4\text{H})_2]$	1999	[18]
$[\text{Pb}(\eta\text{-C}_5\text{iPr}_3\text{H}_2)_2]$	2000	[19]

**Table 3.1** Reported plumbocene complexes of the form  $[\text{Pb}(\eta\text{-C}_5\text{H}_{5-n}\text{R}_n)_2]$

The most recently reported plumbocene is  $[\text{Pb}(\eta\text{-C}_5\text{iPr}_3\text{H}_2)_2]$ , which has a parallel structure as shown by X-ray crystallography.[19] The low temperature crystal structure shows that the molecule contains a centre of inversion and is only the second structurally characterised plumbocene to exhibit a parallel structure. The symmetrical perhapto co-ordination of the cyclopentadienyl rings is similar to that found in decamethylsilicocene,  $[\text{Si}(\eta\text{-C}_5\text{Me}_5)_2]$ . [20] The other linear plumbocene which has been structurally characterised is  $[\text{Pb}\{\eta\text{-C}_5\text{Me}_4(\text{SiMe}_2\text{tBu})\}_2]$ , reported by Lawless *et al.* in 1996.[16]

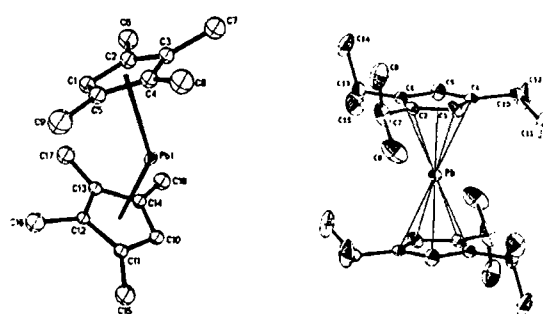
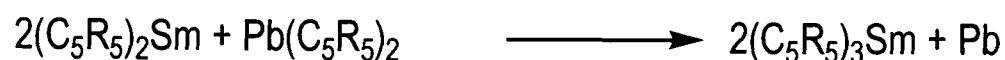


**Figure 3.2** Examples of structurally characterised bent and parallel plumbocenes

The compounds  $[\text{Pb}(\eta\text{-C}_5\text{Me}_4^i\text{Pr})_2]$ ,  $[\text{Pb}(\eta\text{-C}_5\text{Me}_4^n\text{Bu})_2]$  and  $[\text{Pb}(\eta\text{-C}_5\text{Me}_4\text{H})_2]$  were synthesised for use as Cp-transfer reagents for converting sterically crowded  $\text{Sm}(\text{Cp})_2$  complexes to  $\text{Sm}(\text{Cp})_3$  complexes as shown in **Scheme 3.1**.<sup>[18]</sup>



**Scheme 3.1** Use of substituted  $[\text{Pb}(\eta\text{-C}_5\text{R}_5)_2]$  complexes as Cp-transfer agents

### 3.1.4 Stannocenes $[\text{Sn}(\eta\text{-C}_5\text{H}_n\text{R}_{5-n})_2]$ (R = H, alkyl or aryl group)

The first substituted stannocene, 1,1'-dimethylstannocene  $\text{Sn}(\eta\text{-C}_5\text{H}_4\text{Me})_2$  was reported in 1959, the same year that Wilkinson first reported the unsubstituted analogue. These two complexes were, for a long time, the only known examples of thermally stable bivalent organotin species.<sup>[21]</sup> Since then there have been a large number of examples reported, most of which incorporate 'bent' cyclopentadienyl rings with the angle dependent on the degree and type of ring-substitution. Most of these have been described in recent reviews by Burkey<sup>[1]</sup> and Jutzi.<sup>[21]</sup> The synthesis of decaphenylstannocene  $[\text{Sn}(\eta\text{-C}_5\text{Ph}_5)_2]$  was reported in 1984 and structural characterisation demonstrated it to be the first example of a main group metallocene containing parallel cyclopentadienyl rings.<sup>[9]</sup>

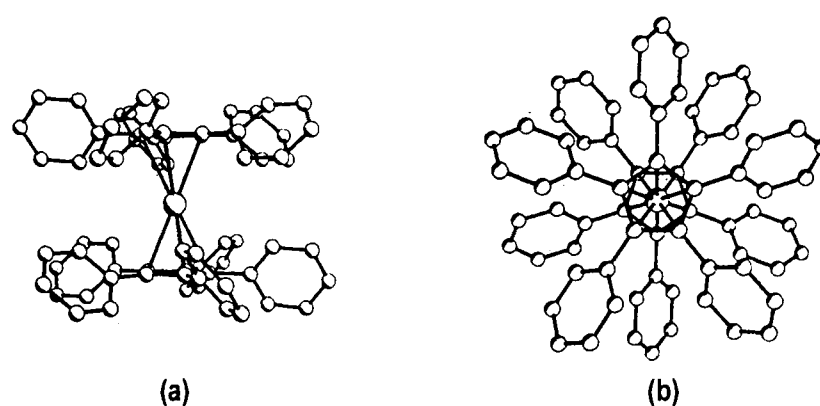


**Figure 3.3** Two views of  $[\text{Sn}(\eta\text{-C}_5\text{Ph}_5)_2]$  demonstrating the (a) parallel and (b) staggered nature of the molecule

Since then, two more stannocene complexes,  $[\text{Sn}\{\eta\text{-C}_5\text{Me}_4(\text{SiMe}_2^t\text{Bu})\}_2]$  <sup>[22, 23]</sup> and  $[\text{Sn}(\eta\text{-C}_5^i\text{Pr}_5)_2]$  <sup>[24]</sup> have been shown to exhibit a parallel-ring structure.

### 3.1.5 Germanocenes $[\text{Ge}(\eta\text{-C}_5\text{H}_n\text{R}_{5-n})_2]$ ( $\text{R} = \text{H}$ , alkyl or aryl group)

The first reported example of a *bis*(cyclopentadienyl)germanium complex was synthesised by Curtis and Scibelli *via* a reaction between germanium dibromide and sodium cyclopentadienide.[25] The resultant *bis*(cyclopentadienyl)germanium(II) complex is a colourless compound, stable in its pure state. Germanocenes are all air-sensitive compounds stable under ambient conditions with the most stable being the permethylated compound  $[\text{Ge}(\eta\text{-C}_5\text{Me}_5)_2]$ . Recent reviews by Burkey[1] and Jutzi[26] detail new developments in the area. The compounds exist as monomers in the gaseous, solution and solid states. The general structure of the compounds is similar to those found for plumbocenes and stannocenes, consisting of bent sandwich structures, although Lawless *et al.* reported the first example of a structurally characterised parallel germanocene,  $[\text{Ge}\{\eta\text{-C}_5\text{Me}_4(\text{SiMe}_2^t\text{Bu})\}_2]$  in 2000.[23] It was shown to be isomorphous with the Sn and Pb analogues published earlier (*vide supra*).[16, 22] In addition, the powder X-ray diffraction pattern found for  $\text{Ge}(\eta\text{-C}_5\text{Ph}_5)_2$  was almost identical to that found for the tin analogue  $[\text{Sn}(\eta\text{-C}_5\text{Ph}_5)_2]$ , so it is very likely that this compound also exhibits a parallel structure.[8]

### 3.1.6 Silicocenes $[\text{Si}(\eta\text{-C}_5\text{H}_n\text{R}_{5-n})_2]$ ( $\text{R} = \text{Me}$ )

In 1989, the synthesis of the silicon analogue, decamethylsilicocene from reduction of the *bis*( $\eta^1$ -pentamethylcyclopentadienyl)silicon(IV) dihalides as a monomeric crystalline material was reported.[27] The compound was the first divalent silicon species known to be stable under normal conditions. The crystal structure determination showed the unit cell to contain two geometrical isomers in the ratio 1:2 (Figure 3.4).

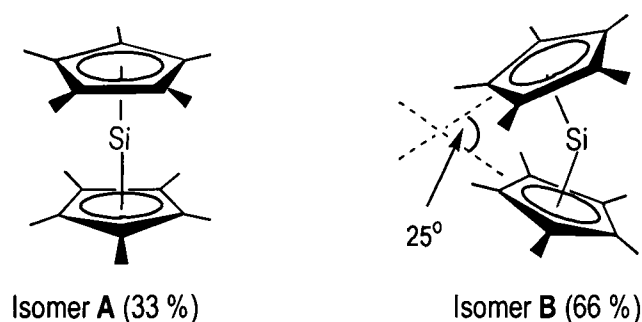


**Figure 3.4** The two geometrical isomers of decamethylsilicocene  $[\text{Si}(\eta\text{-C}_5\text{Me}_5)_2]$



The first isomer (**A**) is isostructural with decamethylferrocene,[28] containing staggered, parallel pentamethylcyclopentadienyl rings with the silicon atom occupying a centre of inversion. The other isomer (**B**) is of a bent-metallocene type structure, more typical of heavier group 14 metallocenes,[5, 29] with an interplanar angle of  $25^\circ$  and with staggered pentamethylcyclopentadienyl rings. At the time of writing, it remains the only reported example of a *bis*(cyclopentadienyl)silicon species.

### 3.2 Bending in Group 14 Metallocenes

There are close similarities between the structures of Group 2 metallocenes and those of Group 14.[1] For example, there is a strong linear correlation between the bending angles and metal radii (larger metal centres tend to have longer M-C distances). There is however, one major geometrical difference between the two sets of metallocenes. In Group 2 metallocenes, the plane of the Cp-rings is orthogonal to the metal-ring centroid vectors, while in Group 14 metallocenes, the rings are substantially tilted relative to these same vectors (**Figure 3.5**).[1]

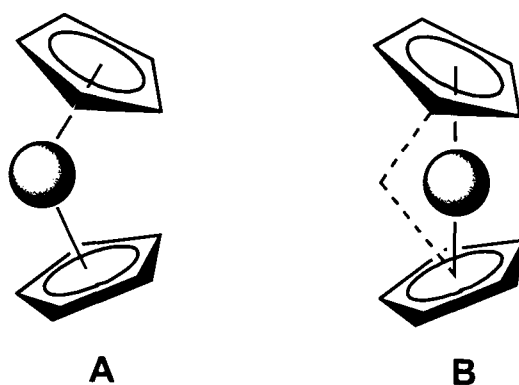


**Figure 3.5** Geometrical characteristics of main group metallocenes. The bending in **A** is typical for Group 2 metallocenes, while the distortion away from symmetrical  $\eta^5$ -ring co-ordination in **B** occurs in Group 14 metallocenes.[1]

These differences are evident in the large spreads in the M-C distances found for Group 14 metallocenes. For example, in the bent silicocene species  $[\text{SiCp}^*_2]$  the M-C range is  $2.347 - 2.730 \text{ \AA}$  and the stannocene  $[\text{SnCp}^*_2]$  the M-C distances vary between  $2.57$  and  $2.78 \text{ \AA}$ . [20, 29, 30] Compare these values with the uniform values obtained for  $[\text{CaCp}^*_2]$  and  $[\text{BaCp}^*_2]$  where the ranges are  $2.597\text{--}2.653 \text{ \AA}$  and  $2.915\text{--}3.074 \text{ \AA}$  respectively indicate a much smaller spread.[30, 31]

### 3.2.1 The Causes of Bending in Group 14 Metallocenes

Prior to 1984 and the reported preparation of decaphenylstannocene  $[\text{Sn}(\eta\text{-C}_5\text{Ph}_5)_2]$ ,<sup>[9]</sup> all structurally characterised Group 14 metallocenes demonstrated non-planarity between their cyclopentadienyl rings and were classified as ‘bent’ metallocenes.<sup>[1, 19]</sup> The source of bending was ascribed to a ‘stereochemically active’ lone pair of electrons on the metal centre. The seminal paper<sup>[5]</sup> by Wilkinson *et al.* reporting the sandwich structure of  $[\text{Sn}(\eta\text{-C}_5\text{H}_5)_2]$  and  $[\text{Pb}(\eta\text{-C}_5\text{H}_5)_2]$ , described the two compounds as having ‘angular sandwich structures’ in which the tin and lead atoms were considered to be in an  $sp^2$  hybridised state. The two hybrid orbitals, each containing one electron, formed two single covalent bonds by overlapping with one, electron-containing orbital on each Cp-ring. The third  $sp^2$  hybrid then contains the remaining two electrons as a lone pair. Further, a parallel structure like that of ferrocene was ruled out because such a structure would contain ‘linear  $sp$  hybrid bonds which would have the two non-bonding electrons in degenerate  $p_x$  and  $p_y$  orbitals.’<sup>[5]</sup> This arrangement would have resulted in a triplet ground state, which was not observed.

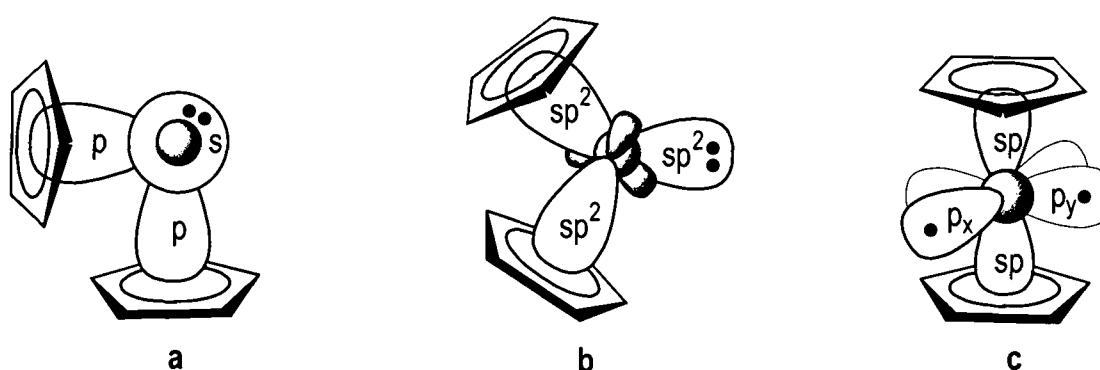


**Figure 3.6** Valence bond interpretation of bending in Group 14 metallocenes; the hybridisation of the metal centre varies with the bending angle

The valence bond approach to explaining the bonding in main group metallocenes was first proposed by Wilkinson in 1959.<sup>[5]</sup> Using this practice, three regions of electron density are associated with the metal centre. One of the regions represents the non-bonding valence electron density while the other two are associated with the M-Cp bonds. The Cp-rings bend to minimise electron-electron interactions between bonding and non-bonding stereochemically-active valence electrons. As explained above, this is achieved by considering the orbitals to be  $sp^2$  hybridised with the lone pair of electrons occupying one of the orbitals. **Figure 3.6** above, illustrates the

different hybridisation possibilities available. The angle between the Cp-rings is diagnostic of the degree of hybridisation of the metal centre and most metallocenes lie near the  $sp^2$  option (**b**). As the angle increases, the  $p$ -character of the lone-pair orbitals would increase until the limit of a parallel geometry is reached, at which point the metallocene would have non-bonding electrons in degenerate  $p_x$  and  $p_y$  orbitals. In such an arrangement a triplet ground state is expected, however, the structurally characterised stannocene  $[\text{Sn}(\eta\text{-C}_5\text{Ph}_5)_2]$  is known to be parallel and diamagnetic.[9] The valence bond approach cannot account for these two conflicting facts. [1] It has since been postulated that van der Waals forces resulting from the cyclopentadienyl ligands affect the geometry of the molecule. Such an approach has been used to explain the planarity of the Cp-rings in  $[\text{Sn}(\eta\text{-C}_5\text{Ph}_5)_2]$  and also ‘may be responsible, in part’ for the bent nature of the germanocene  $[\text{Ge}\{(\eta\text{-C}_5\text{H}_5(\text{Me}_3\text{Si})_3)_2\}]$ . [9, 26]

### 3.2.2 The Parallel Group 14 Metallocene ‘Anomaly’

Plumbocene,  $[\text{Pb}(\eta\text{-C}_5\text{H}_5)_2]$  and stannocene,  $[\text{Sn}(\eta\text{-C}_5\text{H}_5)_2]$  demonstrate what is known as a typical main group metallocene structure. That is to say that they exist as bent or non-parallel metallocenes in the solid state.[11, 12, 19, 32] As stated in the previous section, the operation of the stereochemically-active lone pair or inert pair is often cited as the source of the bending[5] and this theory was reinforced by early MO calculations performed by Jutzi.[33]

As a result of the concept of the stereochemically-active lone pair of electrons, the first structurally authenticated parallel Group 14 metallocene, the sterically demanding complex  $[\text{Sn}(\eta\text{-C}_5\text{Ph}_5)_2]$ , reported by Heeg *et al.* in 1984, was greeted with great interest but came under no little scrutiny.[9] Subsequently, other linear Group 14 metallocenes have been reported to possess planar cyclopentadienyl rings including the rare  $\text{Si}^{\text{II}}$  complex, decamethylsilicocene  $[\text{Si}(\eta\text{-C}_5\text{Me}_5)_2]$ , [20] two further stannocenes  $[\text{Sn}\{\eta\text{-C}_5\text{Me}_4(\text{SiMe}_2^t\text{Bu})\}_2]$  [22, 23] and  $[\text{Sn}(\eta\text{-C}_5^i\text{Pr}_5)_2]$ , [24] two plumbocenes  $[\text{Pb}\{\eta\text{-C}_5\text{Me}_4(\text{SiMe}_2^t\text{Bu})\}_2]$  [16, 23] and  $[\text{Pb}(\eta\text{-C}_5^i\text{Pr}_3\text{H}_2)_2]$  [19] and a germanocene  $[\text{Ge}\{\eta\text{-C}_5\text{Me}_4(\text{SiMe}_2^t\text{Bu})\}_2]$ . [23] In addition to this, the powder X-ray diffraction pattern exhibited by the compound  $[\text{Ge}(\eta\text{-C}_5\text{Ph}_5)_2]$  is virtually identical to

that found for the analogous stannocene,  $[\text{Sn}(\eta\text{-C}_5\text{Ph}_5)_2]$ , so it is very likely that this compound too contains parallel cyclopentadienyl rings.[8] A summary of structurally characterised, parallel ring Group 14 metallocenes is given below in **Table 3.2**.

Compound	Year	Example (Figure 3.7)	Reference
$[\text{Sn}(\eta\text{-C}_5\text{Ph}_5)_2]$	1984	(a)	[9]
$[\text{Si}(\eta\text{-C}_5\text{Me}_5)_2]$	1985	(e)	[20]
$[\text{Sn}\{\eta\text{-C}_5\text{Me}_4(\text{SiMe}_2^t\text{Bu})\}_2]$	1996	(b)	[22],[23]
$[\text{Sn}\{\eta\text{-C}_5(\text{iPr})_5\}_2]$	1996	-	[24]
$[\text{Pb}\{\eta\text{-C}_5\text{Me}_4(\text{SiMe}_2^t\text{Bu})\}_2]$	1996	(c)	[16],[23]
$[\text{Ge}(\eta\text{-C}_5\text{Ph}_5)_2]$	1998	-	[8]
$[\text{Pb}\{\eta\text{-C}_5(\text{iPr})_3\text{H}_2\}_2]$	2000	(d)	[19]
$[\text{Ge}\{\eta\text{-C}_5\text{Me}_4(\text{SiMe}_2^t\text{Bu})\}_2]$	2000	-	[23]

**Table 3.2** List of structurally characterised parallel Group 14 metallocenes

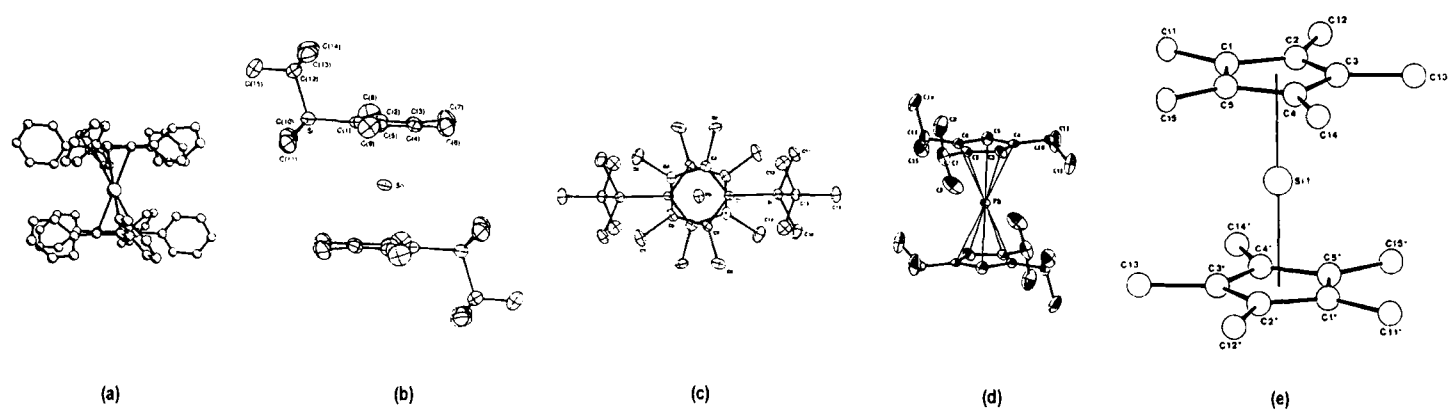


**Figure 3.7** Examples of structurally characterised, parallel Group 14 metallocenes

The growing volume of structural data on parallel metallocenes has led Hanusa to refine the rule of the stereochemically-active lone pair in Group 14 metallocenes.[19] In a recent report, he re-evaluates the importance of intramolecular crowding as a contributory factor in the bending of metallocene structures. The link between the metal centred lone pair and the bent nature of Group 14 metallocenes, he argues, is more subtle than that originally thought.[1]

Indirect support for the lack of correlation between the lone pair electrons and the structural characteristics of Group 14 metallocenes is provided by the bent geometries of most Group 2 metallocenes<sup>[34]</sup> as well as those of the lanthanide group, neither of which possess valence electrons.<sup>[35]</sup> For these complexes, the calculated energy difference between the bent and linear structure is very small ( $< 20 \text{ kJ mol}^{-1}$ ). For example, the stabilisation energies for the bent metallocenes versus the linear molecules for  $[\text{Sn}(\eta\text{-C}_5\text{H}_5)_2]$  and  $[\text{Pb}(\eta\text{-C}_5\text{H}_5)_2]$  are  $15 \text{ kJmol}^{-1}$  and  $2.8 \text{ kJmol}^{-1}$  respectively.<sup>[36]</sup> Allinger has suggested that van der Waals forces between the cyclopentadienyl ligands contribute to the stabilisation of bent structures.<sup>[30]</sup> The low energy barrier between rearrangements thus contributes to the characterisation of these molecules as conformationally ‘floppy’ systems.

Photoelectron spectroscopy studies of compounds of the general formula  $[\text{M}(\eta\text{-C}_5\text{R}_5)_2]$  ( $\text{M} = \text{Pb}, \text{Sn}$  or  $\text{Ge}$ ) indicate that the metal valence electrons are bound tightly relative to the Cp-ring electrons. This demonstrates that their interaction with the ring-electrons is minimal and that the metal-ring bonding in Group 14 metallocenes is more ionic than was previously recognised.<sup>[1, 37-39]</sup> Such findings cast doubt on the relevance of the distinction between stereochemically ‘active’ or ‘inactive’ electron pairs because such a distinction is based on the existence of substantial covalent interaction between the metal valence electrons and those of the cyclopentadienyl rings. In addition to these data,  $^{119}\text{Sn}$  Mössbauer studies by Dory<sup>[40]</sup> have demonstrated that the valence electrons in stannocenes are largely confined to the spherically symmetrical  $5s$ -orbital. Hanusa suggests, therefore, that it seems more likely that the metal valence electrons in divalent Group 14 metals are confined to non-directional orbitals ( $s$ -character) and that they neither strongly influence the orientation of the cyclopentadienyl ligands nor offer themselves as an available electron lone pair to electrophiles.<sup>[1]</sup>

Of the twenty-one structurally characterised Group 14 metallocenes, approximately one third are now known to exist in a geometry where the cyclopentadienyl rings are parallel. These statistics lend weight to the argument such linear metallocenes should no longer be regarded as anomalous.<sup>[19]</sup>

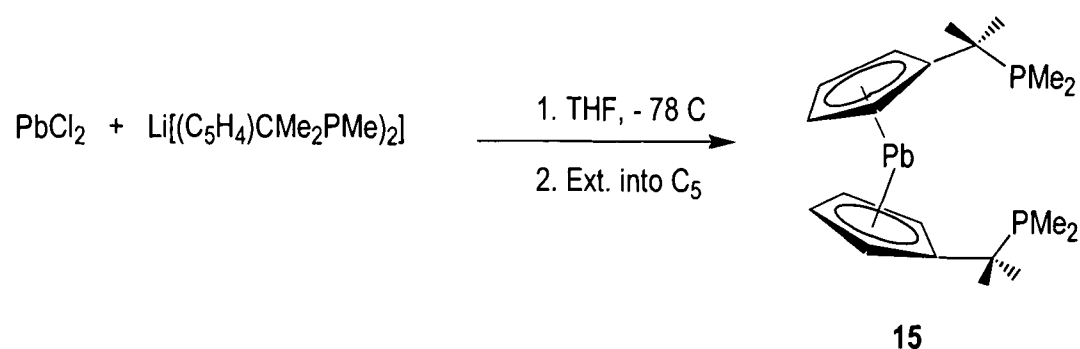
### 3.3 Preparation of New Main Group Metallocenes Containing the $[(C_5H_4)CMe_2PMe_2]$ Ligand

At the commencement of the work contained in this thesis, there were no publications citing the synthesis of main group metallocenes containing ligands in the class  $[(C_5H_4)CR'_2PR''_2]$  ( $R = H$ , alkyl- or aryl-group).

The general method for the preparation of the Group 14 metallocenes employed the methathesis reaction between the tin(II) and lead(II) chloride salts and the lithium cyclopentadienide salt of the ligand  $[Li(C_5H_4)CMe_2PMe_2]$  in THF.[8, 16, 18, 22, 23, 41-43] The additional advantage of working with complexes of tin and lead is the NMR active nuclei contained in both  $^{207}Pb$  and  $^{119}Sn$ . [44, 45]

#### 3.3.1 Preparation of $[Pb\{(\eta-C_5H_4)CMe_2PMe_2\}_2]$ (**15**)

In the absence of light, a mixture of  $[PbCl_2]$  and  $[Li(C_5H_4)CMe_2PMe_2]$  in THF was stirred at  $-78^\circ C$  and warmed to room temperature overnight. The resulting orange solution containing a white precipitate was filtered *via* cannula to yield a dark yellow solution from which solvents were removed under reduced pressure. An orange, oily solid resulted, which was triturated with pentane and the compound  $[Pb\{(\eta-C_5H_4)CMe_2PMe_2\}_2]$  (**15**) was isolated as a microcrystalline, orange solid in 78 % yield. (Scheme 3.2)



Scheme 3.2 Synthesis of  $[Pb\{(\eta-C_5H_4)CMe_2PMe_2\}_2]$  (**15**)

#### 3.3.2 Characterisation of $[Pb\{(\eta-C_5H_4)CMe_2PMe_2\}_2]$ (**15**)

The compound **15** is an orange-yellow crystalline solid, which is moderately stable towards light in the solid state but decomposes in solution after a few minutes. It is soluble in pentane, toluene, pyridine and tetrahydrofuran. Attempts to grow crystals

from a variety of solvents were unsuccessful. Microanalysis results are consistent with the empirical formula  $C_{20}H_{32}P_2Pb$ .

The  $^1H$  NMR spectrum of **15** ( $d^8$ -toluene, 298 K) is shown in **Figure 3.8**. The backbone methyl protons resonate as a doublet  $\delta$  1.21 [ $^3J_{H-P} = 3.5$  Hz], which is slightly upfield from those found in the free ligand anion. The two phosphino-methyl groups on are represented by a doublet at  $\delta$  0.73 [ $^2J_{H-P} = 12.5$  Hz] and while the cyclopentadienyl protons are accounted for by two multiplets at  $\delta$  5.68 and  $\delta$  5.73 with a typical AA'BB' pattern expected for mono-substituted cyclopentadienyl rings.

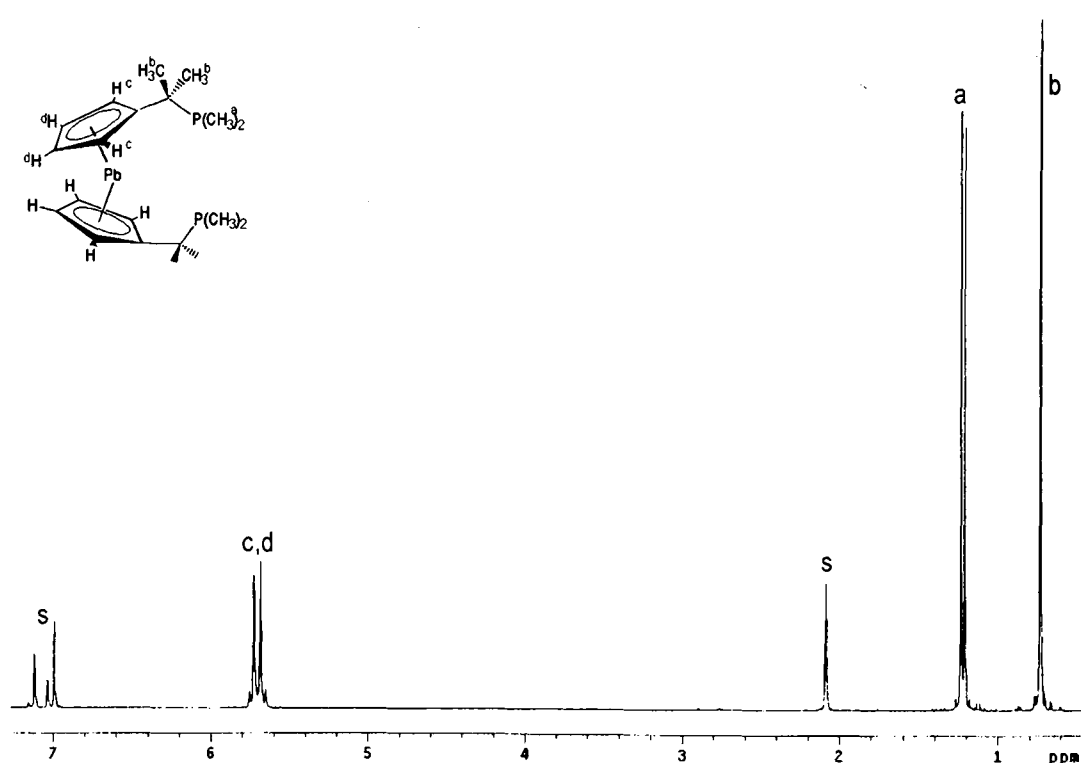


**Figure 3.8**  $^1H$  NMR spectrum of  $[Pb\{(\eta-C_5H_4)CMe_2PMe_2\}_2]$  (**15**) ( $d^8$ -toluene)

The  $^{13}C\{^1H\}$  NMR spectrum displays three doublets for the bridging methyl, phosphinodimethyl and methylene carbons at  $\delta$  11.8 [ $^2J_{C-P} = 21$  Hz],  $\delta$  26.8 [ $^2J_{C-P} = 13$  Hz] and  $\delta$  31.7 [ $J_{C-P} = 16$  Hz] respectively. The *ipso*-carbon appears as a singlet at  $\delta$  139.5 while the cyclopentadienyl carbons resonate at  $\delta$  108.8 and  $\delta$  109.4. In the case of the latter two signals, there is evidence of coupling between the carbon and lead atoms through the presence of  $^{207}Pb$  satellites where  $\delta$  108.8 [ $J_{C-Pb} = 82$  Hz] and  $\delta$  109.4 [ $J_{C-Pb} = 106$  Hz] respectively.

The  $^{31}\text{P}\{^1\text{H}\}$  NMR spectrum of **15** shown in **Figure 3.9** is diagnostic of plumbocene formation given that the signal at  $\delta$  -15.6 is accompanied by  $^{207}\text{Pb}$  satellites ( $I = 1/2$ , 22.6 % abundance) with a coupling of 276 Hz. This value is indicative of a  $^3J_{\text{P-Pb}}$  or  $^4J_{\text{P-Pb}}$  coupling and about one tenth the size of direct metal-phosphorus couplings found in tertiary phosphine-lead complexes.[46] Based on this evidence it seems highly unlikely that the pendant phosphinodimethyl moiety is co-ordinated to the central lead atom. Examples of similar complexes are not readily available from the literature given that this is not a particularly well studied area.

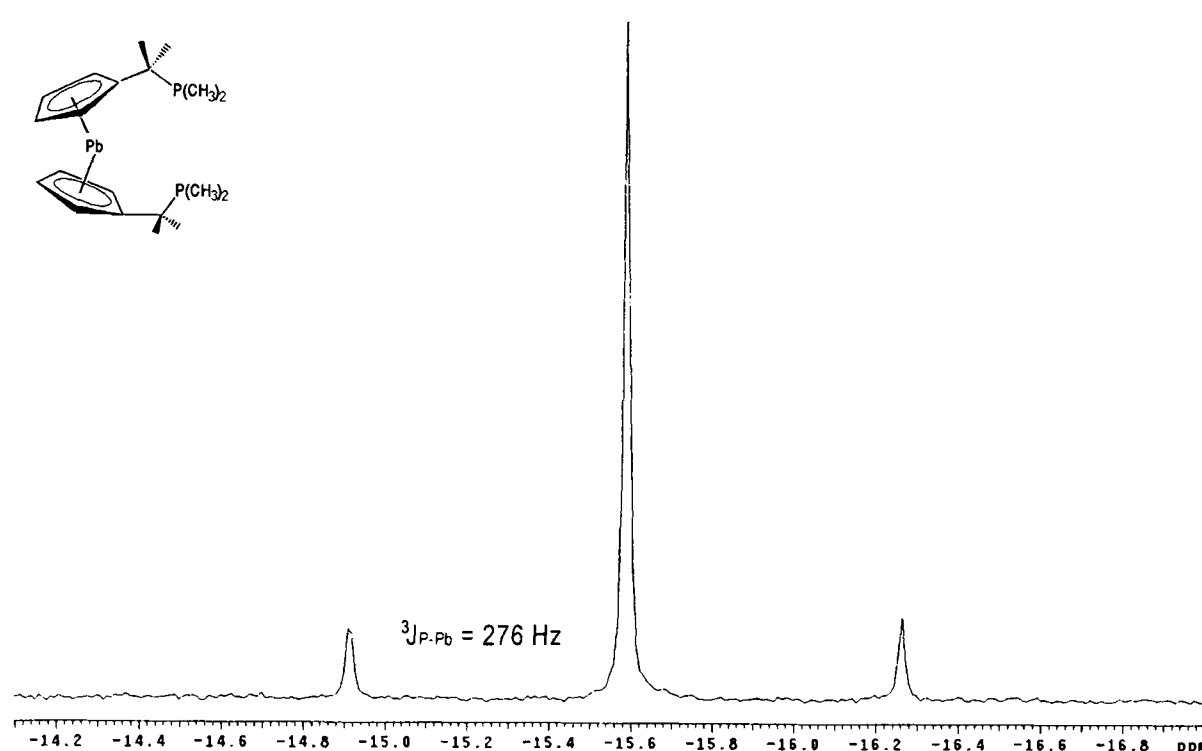


**Figure 3.9**  $^{31}\text{P}\{^1\text{H}\}$  NMR spectrum of  $[\text{Pb}\{(\eta\text{-C}_5\text{H}_4)\text{CMe}_2\text{PMe}_2\}_2]$  (**15**) ( $\text{d}^8$ -toluene)

An HMQC 2D-correlation spectroscopy technique was performed, in order to unambiguously assign the  $^{13}\text{C}$  and  $^1\text{H}$  signals of the ligand (**Figure 3.10**). The  $^1\text{H}$  resonance at  $\delta$  0.77 shows a single, strong correlation to the  $^{13}\text{C}$  resonance at  $\delta$  11.8, while the  $^1\text{H}$  resonance at  $\delta$  1.21 displays a strong correlation with the  $^{13}\text{C}$  resonance at  $\delta$  26.8. Finally, the cyclopentadienyl protons, resonating at  $\delta$  5.68 and  $\delta$  5.73 display strong correlations to the  $^{13}\text{C}$  signals at  $\delta$  108.8 and  $\delta$  109.4 respectively. On the basis of these observations, the  $^1\text{H}$  and  $^{13}\text{C}$  spectra have been assigned.



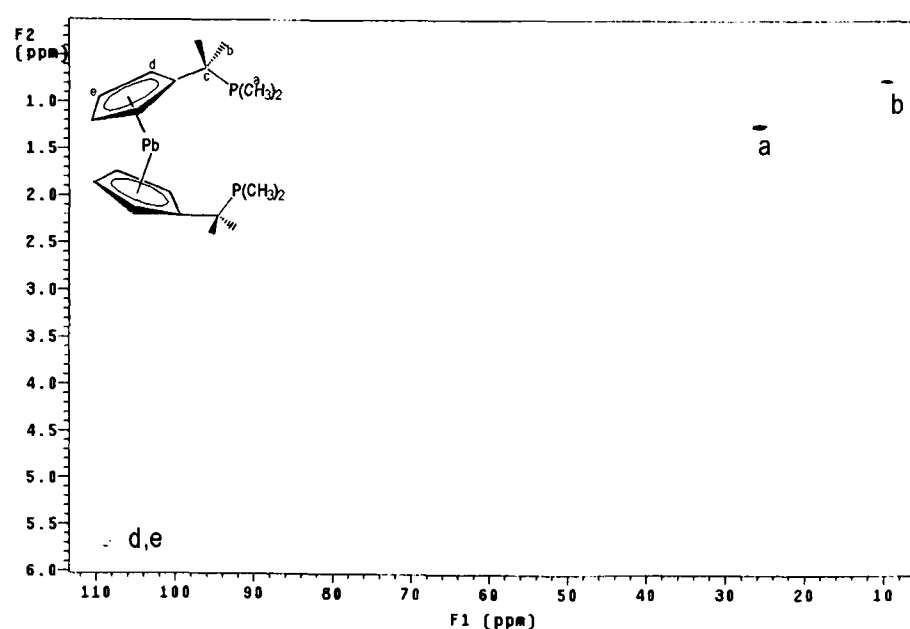


**Figure 3.10**  $^{13}\text{C}$ - $^1\text{H}$  HMQC NMR spectrum of  $[\text{Pb}\{(\eta\text{-C}_5\text{H}_4)\text{CMe}_2\text{PMe}_2\}_2]$  (**15**) ( $\text{d}^8$ -toluene)

### 3.3.3 $^{207}\text{Pb}$ NMR Spectroscopy

$^{207}\text{Pb}$  NMR Spectroscopy provides additional characterising information for characterising plumbocenes.  $^{207}\text{Pb}$  NMR measurements are relatively easy to perform for solutions.[47] The chemical shift range for  $^{207}\text{Pb}$  covers approximately 16000 ppm from  $\delta \sim >10000$  to  $-6500$  with  $\delta^{207}\text{Pb}$  for  $\text{Me}_4\text{Pb}$  at zero.

				$\mathcal{E}(^{207}\text{Pb}), \text{Me}_4\text{Pb}$	Receptivity
	Spin	Natural Abundance	Magnetogyric ratio $\gamma$ ( $\text{s}^{-1} \text{T}^{-1}$ )	$(\mathcal{E}(^1\text{H}), \text{Me}_4\text{Si} = 100 \text{ MHz})$	$D^c(^{13}\text{C} = 1)$
$^{207}\text{Pb}$	$\frac{1}{2}$	22.6 %	$5.59 \times 10^7$	20 920 597 Hz	11.7

**Table 3.3** NMR properties of the magnetically active isotope  $^{207}\text{Pb}$

The  $^{207}\text{Pb}\{^1\text{H}\}$  NMR spectrum of **15** in solution ( $\text{d}^8$ -toluene, 298 K) shown in **Figure 3.11** consists of a binomial triplet at  $\delta - 4963$  [ $^3J_{\text{Pb-P}} = 270 \text{ Hz}$ ] referenced to  $\text{Pb}(\text{OAc})_4$  ( $\delta = -2675$ ), which compares favourably with the chemical shifts recorded for other metallocenes of  $\text{Pb}^{\text{II}}$  (see **Table 3.4**). The coupling value for  $^3J_{\text{Pb-P}}$  is consistent with that found in the  $^{31}\text{P}\{^1\text{H}\}$  NMR spectrum (**Section 3.3.2**),  $^3J_{\text{P-Pb}} = 276 \text{ Hz}$ ) and confirms that the pendant phosphine groups are not directly attached to the  $\text{Pb}^{\text{II}}$  centre.

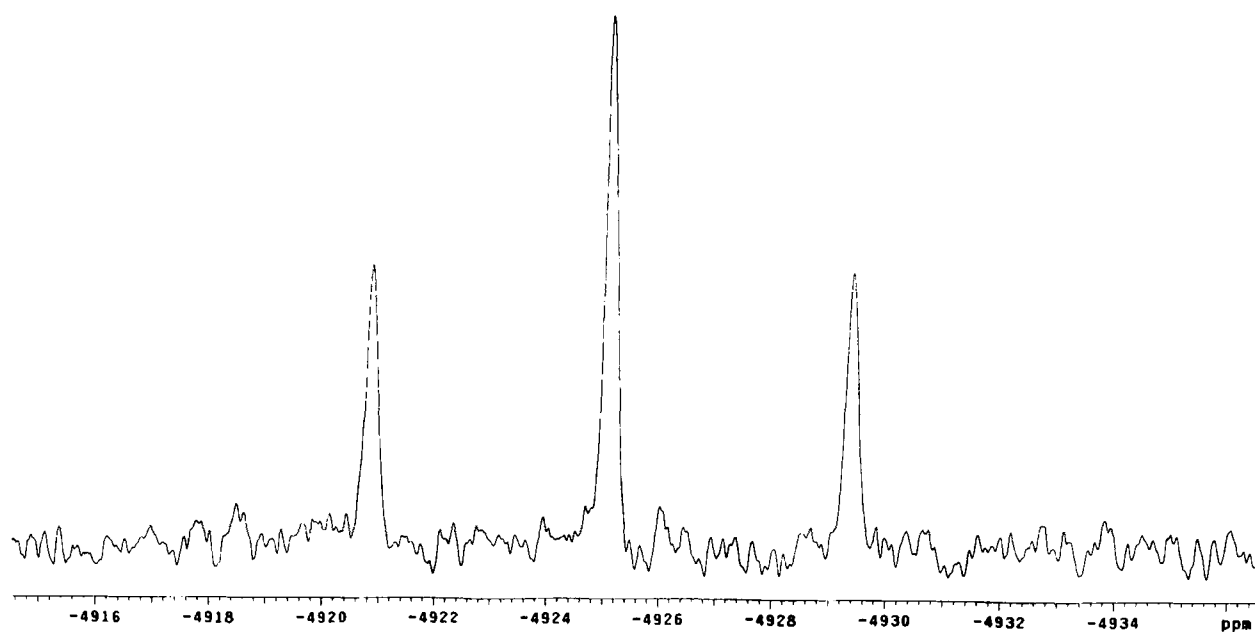


**Figure 3.11**  $^{207}\text{Pb}\{^1\text{H}\}$  NMR spectrum of  $[\text{Pb}\{(\eta\text{-C}_5\text{H}_4)\text{CMe}_2\text{PMe}_2\}_2]$  (**15**) ( $d^8$ -toluene)

Compound	$\delta$ ( $^{207}\text{Pb}$ )	Reference
$[\text{Pb}(\eta\text{-C}_5\text{Me}_5)_2]$	- 4390	[48]
$[\text{Pb}\{\eta\text{-(C}_5\text{Me}_4(\text{SiMe}_2(\text{C}_5\text{HMe}_4)))\}_2]$	- 4538	[49]
$[\text{Pb}\{\eta\text{-C}_5\text{Me}_4(\text{SiMe}_2^t\text{Bu})\}_2]$	- 4595	[23]
$[\text{Pb}(\eta\text{-C}_5\text{H}_3^t\text{Bu}_2)_2]$	- 4756	[15]
$[\text{Pb}(\eta\text{-C}_5\text{H}_5)_2]$	- 5030	[45]
$[\text{Pb}(\eta\text{-C}_5\text{Ph}_5)_2]$	- 4794	[23, 50]
$[\text{Pb}\{(\eta\text{-C}_5\text{H}_4)\text{CMe}_2\text{PMe}_2\}_2]$ ( <b>15</b> )	- 4963	This work

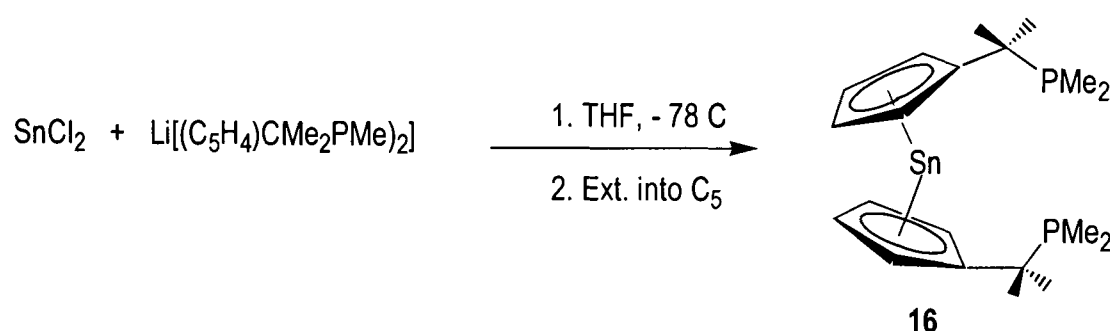
\* No solution data were available for  $\text{Pb}(\eta\text{-C}_5\text{Ph}_5)_2$  so the solid state value is quoted

**Table 3.4** Selected  $^{207}\text{Pb}$  NMR Solution and Solid State Chemical Shift Data for  $\text{Pb}^{\text{II}}$  metallocenes

In the absence of a crystal structure, it was not possible to assign a bent or parallel structure to compound **15**.

### 3.3.4 Preparation of $[\text{Sn}\{(\eta\text{-C}_5\text{H}_4)\text{CMe}_2\text{PMe}_2\}_2]$ (**16**)

In the absence of light, a mixture of  $[\text{SnCl}_2]$  and  $[\text{Li}(\text{C}_5\text{H}_4)\text{CMe}_2\text{PMe}_2]$  in THF was stirred at  $-78^\circ\text{C}$  and warmed to room temperature overnight. The yellow solution containing a white precipitate was filtered *via* cannula to yield a pale yellow solution from which solvents were removed under reduced pressure. The compound  $[\text{Sn}\{(\eta\text{-C}_5\text{H}_4)\text{CMe}_2\text{PMe}_2\}_2]$  (**16**) was isolated as yellow, waxy solid, which was triturated with pentane and obtained as a fine yellow powder in 70 % yield (**Scheme 3.3**).



**Scheme 3.3** Synthesis of  $[\text{Sn}\{(\eta\text{-C}_5\text{H}_4)\text{CMe}_2\text{PMe}_2\}_2]$  (**16**)

### 3.3.5 Characterisation of $[\text{Sn}\{(\eta\text{-C}_5\text{H}_4)\text{CMe}_2\text{PMe}_2\}_2]$ (**16**)

The compound **16** is a yellow solid, which is unstable towards light in the solid state and decomposes if left standing in solution for more than a few minutes. It is soluble in toluene, pyridine and THF. Attempts to grow crystals from a variety of solvents were unsuccessful. Microanalysis results are consistent with the empirical formula  $\text{C}_{20}\text{H}_{32}\text{P}_2\text{Sn}$ .

The  $^1\text{H}$  NMR spectrum of **16** ( $d^8$ -toluene, 298 K) is shown in **Figure 3.12**. The backbone methyl protons resonate as a doublet  $\delta$  0.74 [ $^3J_{\text{H-P}} = 3.5$  Hz], which is slightly upfield from those found in the corresponding free ligand. The two phosphino-methyl groups are represented by a doublet at  $\delta$  1.26 [ $^2J_{\text{H-P}} = 11.5$  Hz] and while the cyclopentadienyl protons are accounted for by two multiplets at  $\delta$  5.62 and 5.67 with the typical AA'BB' pattern expected for mono-substituted cyclopentadienyl rings.

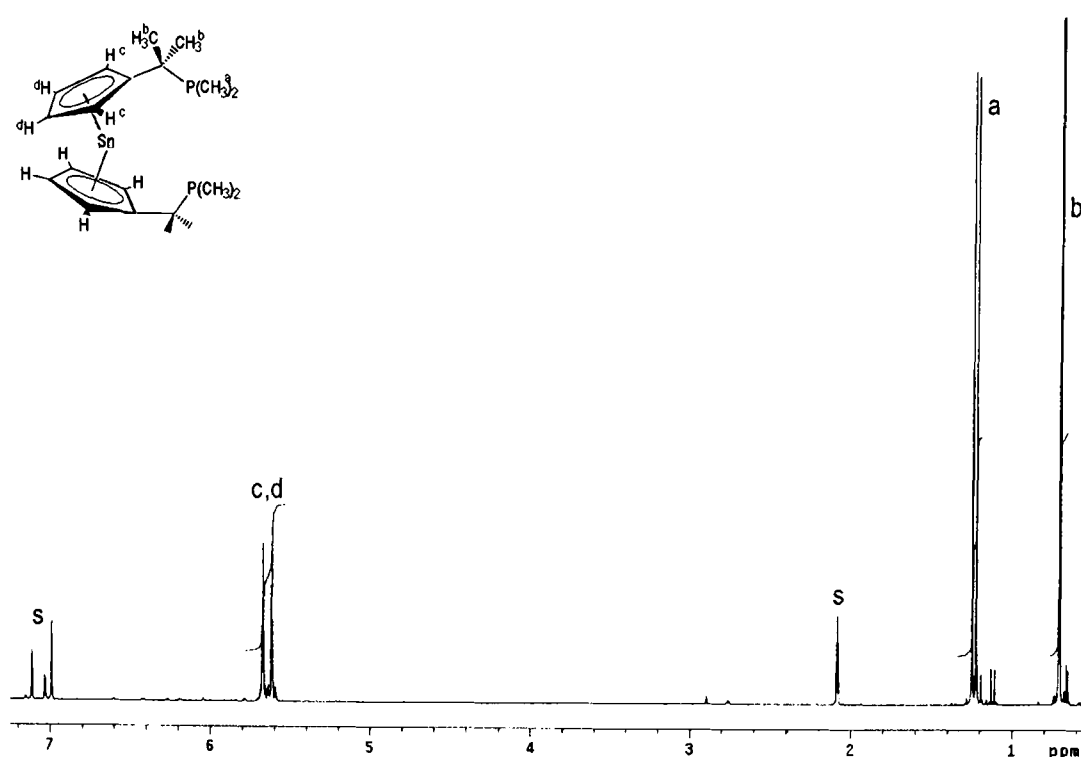


**Figure 3.12**  $^1\text{H}$  NMR spectrum of  $[\text{Sn}\{(\eta\text{-C}_5\text{H}_4)\text{CMe}_2\text{PMe}_2\}_2]$  (**16**) ( $\text{d}^8\text{-toluene}$ )

The  $^{31}\text{P}\{^1\text{H}\}$  NMR spectrum (**Figure 3.13**) is diagnostic of formation of a stannocene given that the signal at  $\delta$  -21.4 is accompanied by  $^{119}\text{Sn}$  satellites ( $I = 1/2$ , 8.68 % abundance) [ $^3J_{\text{P-Sn}119} = 111$  Hz]. Resolution of the two sets of satellites was not possible. The coupling value of 111 Hz is in keeping with other  $^3J_{\text{P-Sn}}$  values reported in the literature.[46, 51, 52]

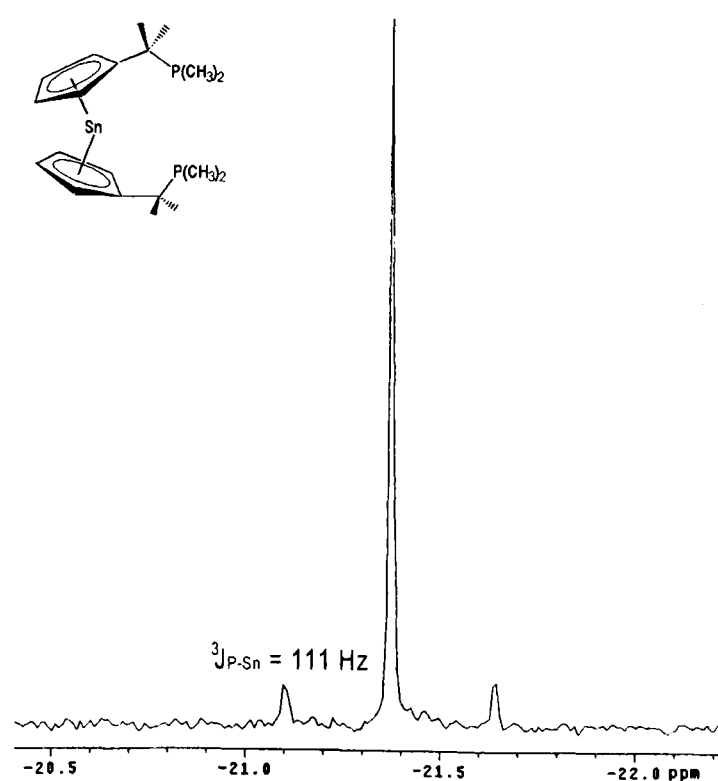


**Figure 3.13**  $^{31}\text{P}\{^1\text{H}\}$  NMR spectrum of  $[\text{Sn}\{(\eta\text{-C}_5\text{H}_4)\text{CMe}_2\text{PMe}_2\}_2]$  (**16**) ( $\text{d}^8\text{-toluene}$ )

An HMQC 2D-correlation spectroscopy technique was performed, in order to unambiguously assign the  $^{13}\text{C}$  and  $^1\text{H}$  signals of the ligand (**Figure 3.14**). The  $^1\text{H}$  resonance at  $\delta$  0.74 shows a single, strong correlation to the  $^{13}\text{C}$  resonance at  $\delta$  10.0, while the  $^1\text{H}$  resonance at  $\delta$  1.26 displays a strong correlation with the  $^{13}\text{C}$  resonance at  $\delta$  26.6. Finally, the cyclopentadienyl protons resonating at  $\delta$  5.68 and 5.73 display strong correlations to the  $^{13}\text{C}$  signals at  $\delta$  107.9 and  $\delta$  109.9 respectively. On the basis of these observations, the  $^1\text{H}$  and  $^{13}\text{C}$  spectra have been assigned.

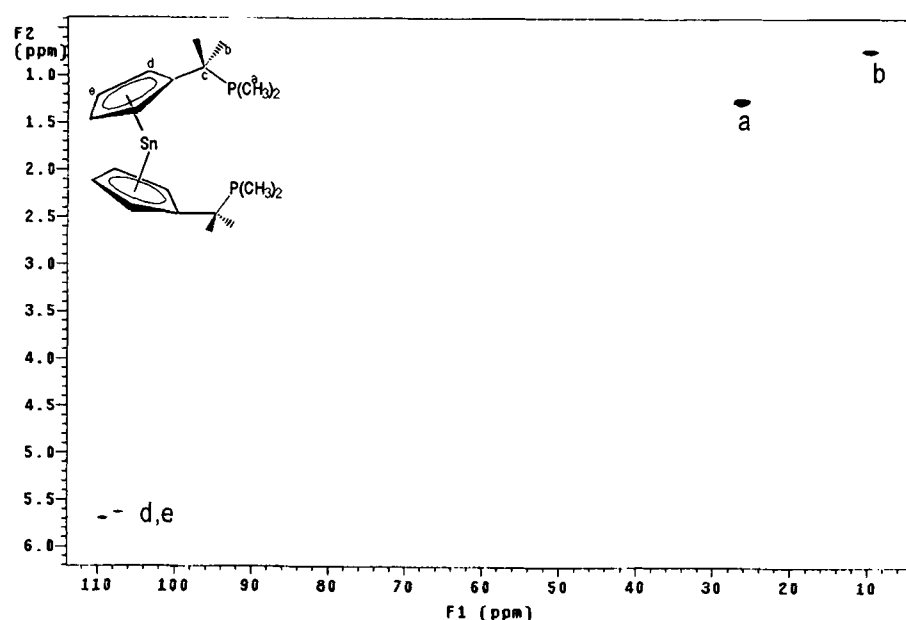


**Figure 3.14**  $^{13}\text{C}$ - $^1\text{H}$  HMQC NMR spectrum of  $[\text{Sn}\{(\eta\text{-C}_5\text{H}_4)\text{CMe}_2\text{PMe}_2\}_2]$  (**16**) ( $d^8$ -toluene)

### 3.3.6 $^{119}\text{Sn}$ NMR Spectroscopy

Tin possesses three isotopes, which have magnetically active, spin =  $\frac{1}{2}$  nuclei ( $^{115}\text{Sn}$ ,  $^{117}\text{Sn}$  and  $^{119}\text{Sn}$ ). The natural abundance of the latter two isotopes is relatively high and the NMR receptivity is sufficient to obtain most  $^{119}\text{Sn}$  spectra within a reasonable time in both the solution and solid states. Most  $^{119}\text{Sn}$  spectra are referenced with respect to tetramethyltin,  $\text{Me}_4\text{Sn}$ . The chemical shift range for  $^{119}\text{Sn}$  covers approximately 6500 ppm from  $\delta \sim >4000$  to - 2500 with  $\delta^{119}\text{Sn}$  for  $\text{Me}_4\text{Sn}$  at zero. **Table 3.5** below contains some information about the three Sn isotopes. A recent review by Wrackmeyer contains a wealth of data collected over the past 10 years.[44]

				$\mathcal{E}^{(207\text{Pb}), \text{Me}_4\text{Pb}}$	Receptivity
	Spin	Natural Abundance	Magnetogyric ratio $\gamma$ (s <sup>-1</sup> T <sup>-1</sup> )	( $\mathcal{E}^{(1\text{H})}$ , Me <sub>4</sub> Si = 100 MHz)	$D^c(^{13}\text{C} = 1)$
<sup>115</sup> Sn	$\frac{1}{2}$	0.35 %	-8.014 x 10 <sup>7</sup>	32 718 780 Hz	0.7
<sup>117</sup> Sn	$\frac{1}{2}$	7.61 %	-9.59 x 10 <sup>7</sup>	35 632 295 Hz	19.5
<sup>119</sup> Sn	$\frac{1}{2}$	8.58 %	-10.0 x 10 <sup>7</sup>	37 290 665 Hz	25.2

**Table 3.5** NMR properties of the magnetically active isotopes <sup>115</sup>Sn, <sup>117</sup>Sn and <sup>119</sup>Sn

The <sup>119</sup>Sn{<sup>1</sup>H} NMR spectrum of **16** in solution (d<sup>8</sup>-toluene, 298 K) shown in **Figure 3.15** consists of a binomial triplet at  $\delta$  - 2163 [<sup>3</sup>*J*<sub>Sn-P</sub> = 110 Hz] referenced to SnMe<sub>4</sub> ( $\delta$  = 0), which compares favourably with the chemical shifts recorded for other metallocenes of Sn<sup>II</sup> (see **Table 3.6**). The coupling value for <sup>3</sup>*J*<sub>Sn-P</sub> is consistent with that found in the <sup>31</sup>P{<sup>1</sup>H} spectrum (**Section 3.3.5**, 111 Hz) and confirms that the pendant phosphine groups are not directly attached to the Sn<sup>II</sup> centre.

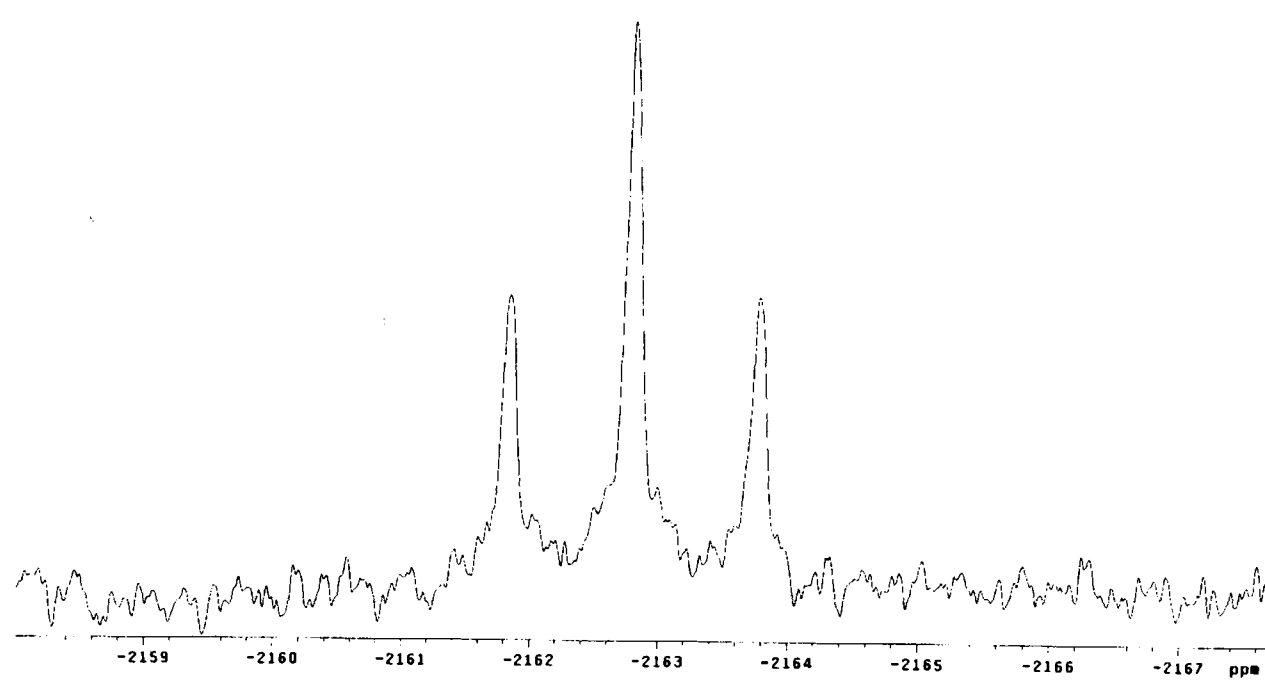


**Figure 3.15** <sup>119</sup>Sn{<sup>1</sup>H} NMR spectrum of [Sn{(η-C<sub>5</sub>H<sub>4</sub>)CMe<sub>2</sub>PMe<sub>2</sub>}<sub>2</sub>] (**16**) (d<sup>8</sup>-toluene)

Compound	$\delta$ ( $^{119}\text{Sn}$ )	Reference
$[\text{Sn}(\eta\text{-C}_5\text{Me}_5)_2]$	- 2129	[29]
$[\text{Sn}\{\eta\text{-C}_5(\text{CH}_2\text{Ph})_5\}_2]$	- 2188	[50]
$[\text{Sn}(\eta\text{-C}_5\text{H}_5)_2]$	- 2199	[53]
$[\text{Sn}(\eta\text{-C}_5\text{Ph}_5)_2]$	- 2215*	[50]
$[\text{Sn}\{\eta\text{-C}_5\text{Me}_4(\text{SiMe}_3)\}_2]$	- 2171	[54]
$[\text{Sn}\{\eta\text{-C}_5\text{Me}_4(\text{SiMe}_2^t\text{Bu})\}_2]$	- 2204	[23]
$[\text{Sn}\{(\eta\text{-C}_5\text{H}_4)\text{CMe}_2\text{PMe}_2\}_2]$ ( <b>16</b> )	- 2163	This work

\* No solution data were available for  $\text{Sn}(\eta\text{-C}_5\text{Ph}_5)_2$  so the solid state value is quoted

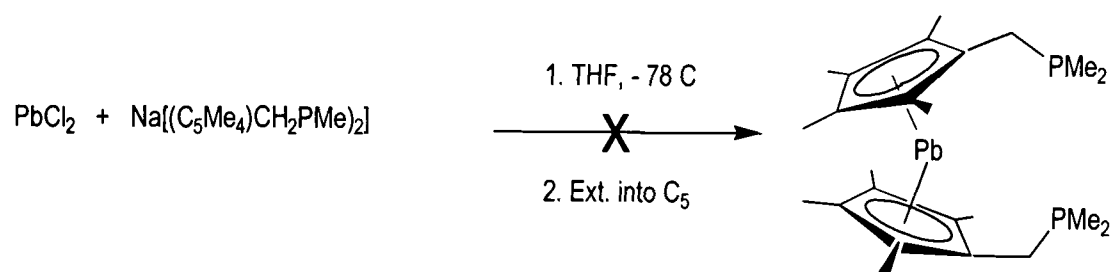
**Table 3.6** Selected  $^{119}\text{Sn}$  NMR solution and solid state chemical shift data for  $\text{Sn}^{\text{II}}$  metallocenes

In the absence of a crystal structure, it is not possible to assign a bent or parallel structure to compound **16**.

### 3.3.7 Attempted Preparation of $[\text{Pb}\{(\eta\text{-C}_5\text{Me}_4)\text{CH}_2\text{PMe}_2\}_2]$

Following the successful syntheses of the compounds **15** and **16**, an attempt was made to prepare analogous complexes containing the ligand  $[(\text{C}_5\text{Me}_4)\text{CH}_2\text{PMe}_2]^-$ .

In the absence of light, a mixture of  $[\text{PbCl}_2]$  and the compound **5** was stirred in THF at  $-78^\circ\text{C}$  and warmed to room temperature overnight. The resulting orange solution was filtered and solvent was removed to yield an oily orange solid. The solid was triturated with pentane to and then extracted into pentane. Removal of solvent from the resulting orange solution yielded a red-orange oily solid. The  $^1\text{H}$  and  $^{31}\text{P}\{^1\text{H}\}$  NMR spectra ( $d^8$ -toluene) demonstrated the presence of a number of different products in the oily solid, which could not be separated, so further studies were discontinued.



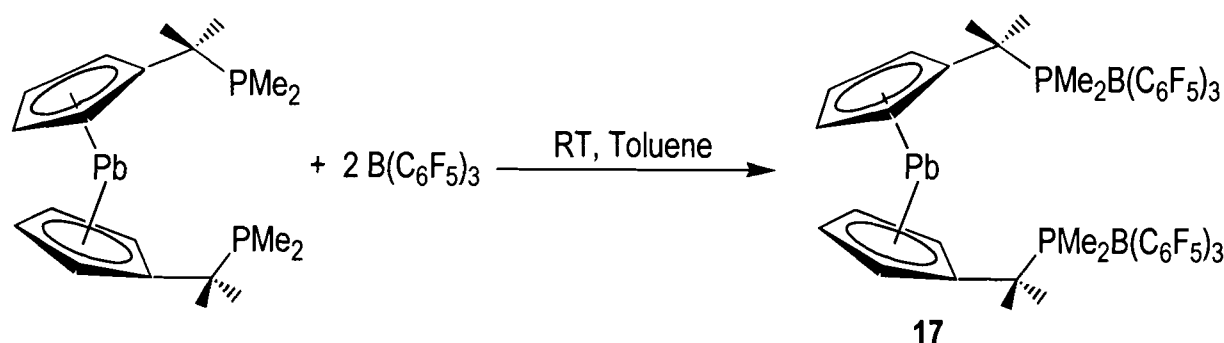
**Scheme 3.4** Attempted synthesis of  $[\text{Pb}\{(\eta\text{-C}_5\text{Me}_4)\text{CH}_2\text{PMe}_2\}_2]$

### 3.4 Reactions Between Compounds 15 and 16 and $B(C_6F_5)_3$

The compounds **15** and **16** were each reacted with two equivalents of the strong Lewis acid  $B(C_6F_5)_3$ . It was expected that the Lewis acid would react with the pendant phosphine to form a  $P-B(C_6F_5)_3$  adduct.

#### 3.4.1 Preparation of $[Pb\{(\eta-C_5H_4)CMe_2PMe_2B(C_6F_5)_3\}_2]$ (**17**)

A solution of two equivalents of  $B(C_6F_5)_3$  in toluene was added dropwise to a solution of **15** at room temperature and the resulting solution was stirred for 12 hours. Volatiles were removed under reduced pressure from the yellow solution and the yellow solid washed with pentane. Final removal of volatiles under reduced pressure yielded the compound  $[Pb\{(\eta-C_5H_4)CMe_2PMe_2B(C_6F_5)_3\}_2]$  (**17**) as a yellow powder in quantitative yield. (Scheme 3.5)



Scheme 3.5 Synthesis of  $[Pb\{(\eta-C_5H_4)CMe_2PMe_2B(C_6F_5)_3\}_2]$  (**17**)

#### 3.4.2 Characterisation of $[Pb\{(\eta-C_5H_4)CMe_2PMe_2B(C_6F_5)_3\}_2]$ (**17**)

The compound **17** is a yellow solid, which decomposes in air and is soluble in polar solvents. Microanalysis results are consistent with the empirical formula  $B_2C_{56}F_{30}H_{32}P_2Pb$ .

The  $^1H$  NMR spectrum of **17** ( $d^5$ -pyridine, 298 K) is shown in Figure 3.16 and is similar to that found for the parent lead compound **15**. The phosphinodimethyl protons resonate as a doublet  $\delta$  1.11 [ $^2J_{H-P} = 12.5$  Hz], slightly upfield from those found in the parent plumbocene while the two methyl groups on the methylene backbone are represented by a doublet at  $\delta$  0.65 [ $^3J_{H-P} = 2.5$  Hz]. The cyclopentadienyl protons resonate as two broadened singlets at  $\delta$  5.82 and  $\delta$  5.84.



This feature differs considerably from the standard AA'BB' multiplets expected for mono-substituted cyclopentadienyl complexes and demonstrated by the  $^1\text{H}$  NMR spectrum of compound **15**. It is most likely a result of the effect of the quadrupolar  $^{11}\text{B}$  nucleus.

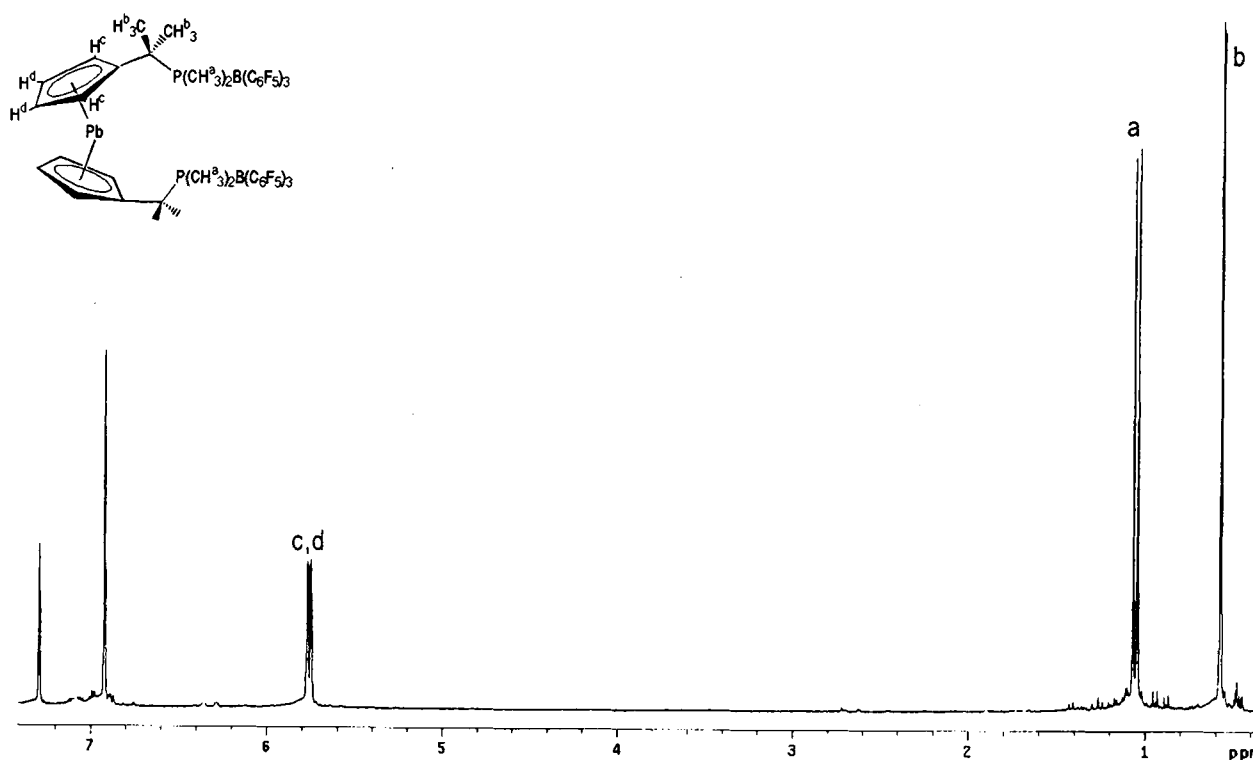


**Figure 3.16**  $^1\text{H}$  NMR spectrum of  $[\text{Pb}\{(\eta\text{-C}_5\text{H}_4)\text{CMe}_2\text{PMe}_2\text{B}(\text{C}_6\text{F}_5)_3\}_2]$  (**17**) ( $d^5$ -pyridine)

The  $^{13}\text{C}\{^1\text{H}\}$  NMR spectrum is similar to that obtained for the parent plumbocene (**15**). A doublet  $\delta$  26.8 [ $J_{\text{C-P}} = 13$  Hz] is assigned to the dimethylphosphino protons while two further doublets at  $\delta$  10.9 [ $^2J_{\text{C-P}} = 20$  Hz] and  $\delta$  32.1 [ $J_{\text{C-P}} = 16$  Hz] account for the bridging methyl and methylene carbons respectively. The *ipso*-carbon signal appears as a singlet at  $\delta$  116.3, (a loss of  $J_{\text{P-C}}$  resolution on addition of the borane) and the other two cyclopentadienyl carbons resonate at  $\delta$  108.4 and  $\delta$  109.5. In the case of the latter two signals, there is no evidence of coupling between the carbon and lead atoms, implied the absence of  $^{207}\text{Pb}$  satellite signals. This is further evidence for the proposed structure of the  $\text{P-B}(\text{C}_6\text{F}_5)_3$  complex in that the effect of the quadrupolar  $\text{B}(\text{C}_6\text{F}_5)_3$  ligand effects a broadening of the previously observed  $J_{\text{C-Pb}}$  coupling. The  $^{13}\text{C}$  signals for the  $\text{B}(\text{C}_6\text{F}_5)_3$  ligand appear at  $\delta$  139.4, 147.5 and 149.5.

The  $^{31}\text{P}\{^1\text{H}\}$  NMR spectrum (**Figure 3.17**) displays a singlet at  $\delta$  -11, which is a downfield shift of approximately 5 ppm from that of the parent complex **15**. In

addition, the three-bond P-Pb coupling is no longer evident. This is once again likely to be a result of the interaction between the  $^{11}\text{B}$  nucleus and the P-group. The  $^{11}\text{B}\{^1\text{H}\}$  spectrum displays a doublet at  $\delta$  0.65 [ $J_{\text{B-P}} = 70.5$  Hz] typical of a neutral, tetra-co-ordinate boron species which is well within the realms of  $\text{PR}_3$ -boron coupling constants.[55, 56]

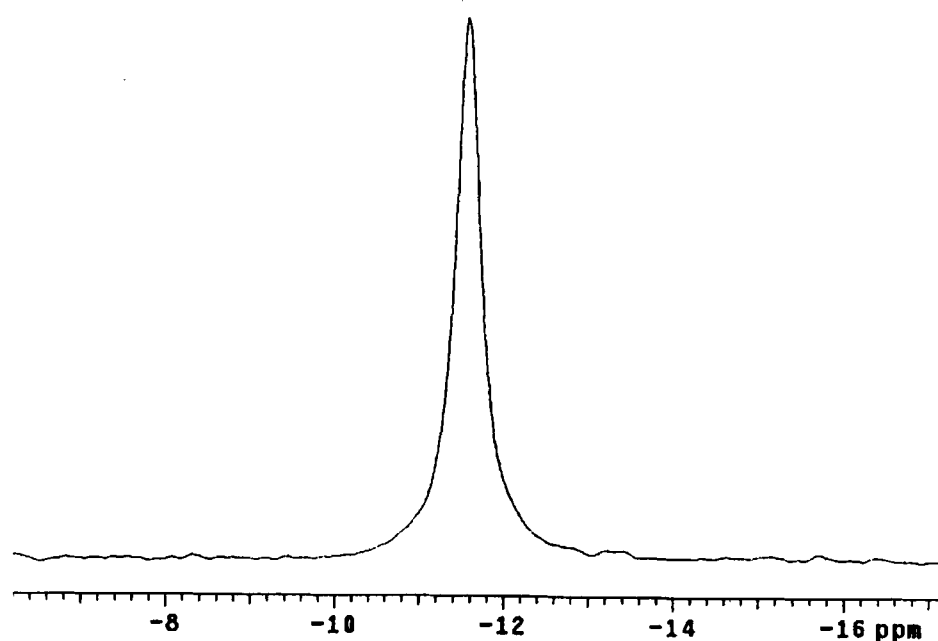
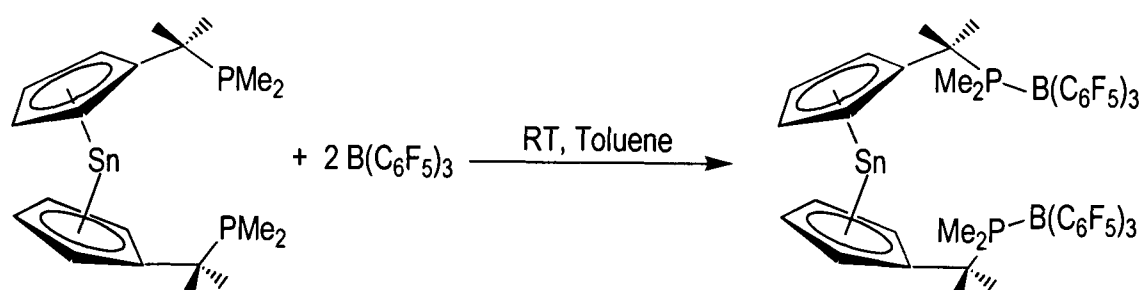


**Figure 3.17**  $^{31}\text{P}\{^1\text{H}\}$  NMR spectrum of  $[\text{Pb}\{(\eta\text{-C}_5\text{H}_4)\text{CMe}_2\text{PMe}_2\text{B}(\text{C}_6\text{F}_5)_3\}_2]$  (**17**) ( $\text{d}^5$ -pyridine)

### 3.4.3 Attempted Preparation of $[\text{Sn}\{(\eta\text{-C}_5\text{H}_4)\text{CMe}_2\text{PMe}_2\text{B}(\text{C}_6\text{F}_5)_3\}_2]$

A solution of two equivalents of  $\text{B}(\text{C}_6\text{F}_5)_3$  in toluene was added dropwise to a solution of **16** at room temperature and the resulting solution was stirred for 12 hours. Volatiles were removed under reduced pressure from the yellow solution and resulting pale yellow solid washed with pentane. Final removal of volatiles under reduced pressure yielded the compound as a pale yellow powder. (**Scheme 3.6**)



**Scheme 3.6** Attempted synthesis of  $[\text{Sn}\{(\eta\text{-C}_5\text{H}_4)\text{CMe}_2\text{PMe}_2\text{B}(\text{C}_6\text{F}_5)_3\}_2]$

The compound resulting from the reaction between **16** and two equivalents of  $\text{B}(\text{C}_6\text{F}_5)_3$  is a yellow solid, which decomposes in air and is soluble in polar solvents. Microanalysis results are inconsistent with the empirical formula  $\text{B}_2\text{C}_{56}\text{F}_{30}\text{H}_{32}\text{P}_2\text{Sn}$ .

The  $^1\text{H}$  NMR spectrum ( $d^5$ -pyridine) is more complex than that of **17** and suggests that a mixture of products have been formed. Instead of the expected set of signals analogous to those found for **17**, there were several groups of protons resonating between  $\delta$  0.4 and 1.0. The region between  $\delta$  5.5 and 6.5 also exhibited a number of broad signals.

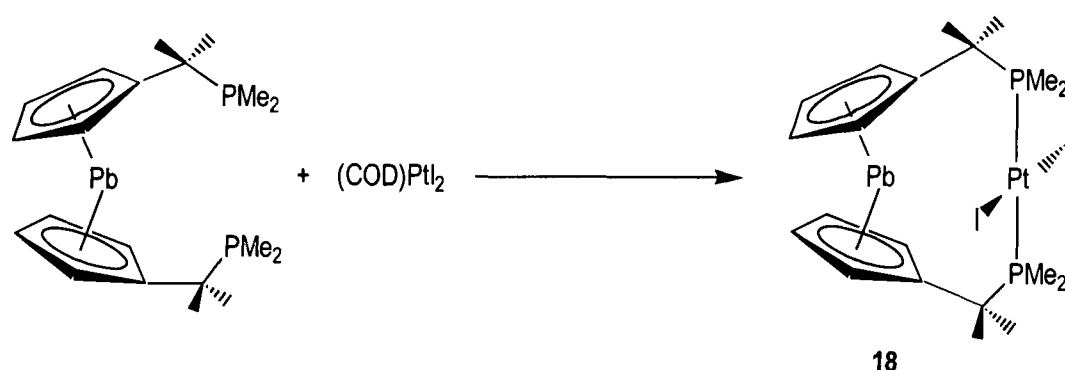
The  $^{31}\text{P}\{^1\text{H}\}$  NMR spectrum displays a number of signals between  $\delta$  - 40 and 80 rather than the single signal found in the spectrum of **17**. The experiment was repeated and resulted in similar findings, so further studies were discontinued.

### 3.5 Preparation of Heterobimetallic Group 14 - Transition Metal Complexes

In **Chapter 2** the preparation of heterobimetallic complexes by reacting a substituted early transition metal metallocene with a later transition metal complex *via* chelation of the metallocene substituent was illustrated. In the preliminary experiments carried out in this study, the Group 14 complexes **15** and **16** were employed in reactions with palladium and platinum dihalide salts. The products are generated by displacement of the cyclooctadiene (COD) ligand by the organometallic chelating phosphine system.<sup>[57, 58]</sup>

#### 3.5.1 Preparation of $[\text{Pb}\{(\eta\text{-C}_5\text{H}_4)\text{CMe}_2\text{PMe}_2\}_2\text{PtI}_2]$ (**18**)

To yellow solution of  $\text{PtI}_2(\text{COD})$  in THF was slowly added a solution of **15** in THF at room temperature. The resulting yellow solution was stirred overnight after which time volatiles were removed under reduced pressure and the yellow solid washed with pentane before the compound  $[\text{Pb}\{(\eta\text{-C}_5\text{H}_4)\text{CMe}_2\text{PMe}_2\}_2\text{PtI}_2]$  **18** was isolated as an orange powder in 50 % yield (**Scheme 3.7**).



**Scheme 3.7** Synthesis of  $[\text{Pb}\{(\eta\text{-C}_5\text{H}_4)\text{CMe}_2\text{PMe}_2\}_2\text{PtI}_2]$  (**18**)

### 3.5.2 Characterisation of $[\text{Pb}\{(\eta\text{-C}_5\text{H}_4)\text{CMe}_2\text{PMe}_2\}_2\text{PtI}_2]$ (**18**)

The compound **18** is an air-sensitive orange solid, which is sparingly soluble in THF. Microanalysis results are consistent with the empirical formula  $\text{C}_{20}\text{H}_{32}\text{P}_2\text{PbPtI}_2$ . The Fast Atom Bombardment mass spectrum (NOBA matrix) of compound **18** contains two peaks and although the signal due to the molecular ion ( $m/z = 990$ ) is not present, signals at  $m/z = 863$  [M-I] and  $m/z = 736$  [M-2I] with the correct isotope patterns are observed.

The complex exhibits a  $^{31}\text{P}\{^1\text{H}\}$  NMR resonance at  $\delta -11.0$ , which is shifted upfield by approximately 7 ppm from the parent dimethylphosphino-substituted plumbocene **15**. As a result of the presence of the  $^{195}\text{Pt}$  isotope (33.7 % relative abundance,  $I = 1/2$ ) a splitting due to the  $^{31}\text{P}$ - $^{195}\text{Pt}$  coupling is observed (**Figure 3.18**). It is well known that the magnitude of the  $^1J_{\text{P-Pt}}$  coupling constant in  $\text{L}_2\text{PtCl}_2$  complexes is a useful diagnostic tool for the identification as the *cis*- or *trans*- isomers.<sup>[59]</sup> For example, for *cis*- $\text{PtCl}_2(\text{PMe}_3)_2$ ,  $^1J_{\text{P-Pt}} = 3480$  Hz while for *trans*- $\text{PtCl}_2(\text{PMe}_3)_2$   $^1J_{\text{P-Pt}} = 2379$  Hz.<sup>[60]</sup> Similarly, for *cis*- and *trans*- $\text{PtCl}_2\{\text{P}(p\text{-tolyl})_3\}_2$ ,  $^1J_{\text{P-Pt}} = 3694$  and 2595 Hz respectively.<sup>[61]</sup> The observed  $J_{\text{P-Pt}}$  coupling constant in the compound **18** is 2320 Hz which suggests a *trans*-structure is most likely.

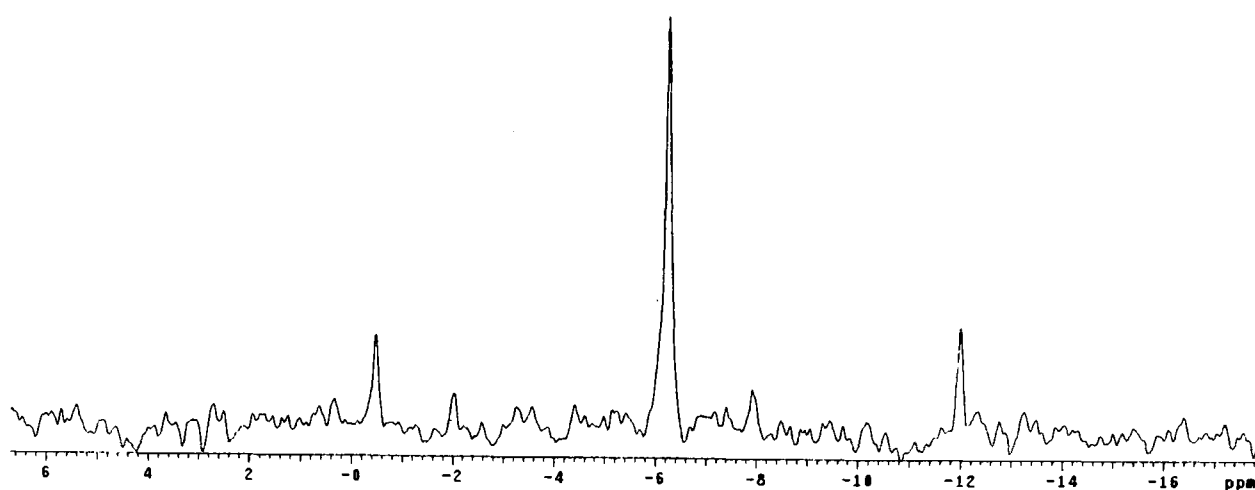


**Figure 3.18**  $^{31}\text{P}\{^1\text{H}\}$  NMR spectrum of  $[\text{Pb}\{(\eta\text{-C}_5\text{H}_4)\text{CMe}_2\text{PMe}_2\}_2\text{PtI}_2]$  (**18**) ( $\text{d}^8\text{-THF}$ )

It is characteristic for *trans*-co-ordinated chelating-phosphines to exhibit a virtual triplet in the  $^1\text{H}$  NMR spectrum where in the previously uncoordinated ligand, a doublet ( $^2J_{\text{P-H}}$ ) was exhibited. This is due to an additional P-P coupling through the Pt-P bonds resulting from a *trans*-effect, which leads to the protons on the methylphosphino groups interacting with two phosphorus environments.[62] In the case of **18**, a doublet, which occurs at  $\delta$  0.72 in the parent compound **15** is now exhibited as a triplet [ $J_{\text{P-H}} = 6.9$  Hz] at  $\delta$  1.01.

One objective of this work was to synthesise a bimetallic main group-late transition metal complex containing a main group metallocene and a transition metal (Pb and Pt in this study). This work is in some respects comparable with that of Graham and Erker described in **Section 1.6**. [57, 58, 62, 63] Graham *et al.* reported oligomeric products in which tetranuclear complexes containing Rh and Pd were favoured over the binuclear species. Work by Erker, however, demonstrated the formation of heterobinuclear complexes involving Group 4 and 10 metals.[62] The main difference between the two ligand systems was in the substituent ( $\text{R} = \text{H}$  or  $\text{Me}$ ) on the carbon ‘spacer’ ( $\text{CR}_2$ ) linking the cyclopentadienyl and phosphine groups. [57, 58, 63]

Considering the complex **A** incorporating the metallocene  $[\text{Ti}\{(\eta\text{-C}_5\text{H}_4)\text{CH}_2\text{PPh}_2\}_2\text{Cl}_2]$  in **Figure 3.19** which is synthesised using an analogue of the  $[\text{Zr}\{(\eta\text{-C}_5\text{H}_4)\text{CMe}_2\text{PAr}_2\}_2\text{Cl}_2]$  ligand reported by Erker, with the modification of a non-methylated backbone. The H-atoms contained in the methylene bridge of the

titanocene in **A** come into close contact with the chloride ligands on the Rh or Ti centres. In the case of the methylated-backbone ligands used by Erker in example **C**, the substitution of hydrogen for a more sterically demanding group brings the alkyl groups into unacceptably close contact with the chloride ligands, destabilising the tetranuclear structure and possibly favouring a binuclear arrangement.[58]

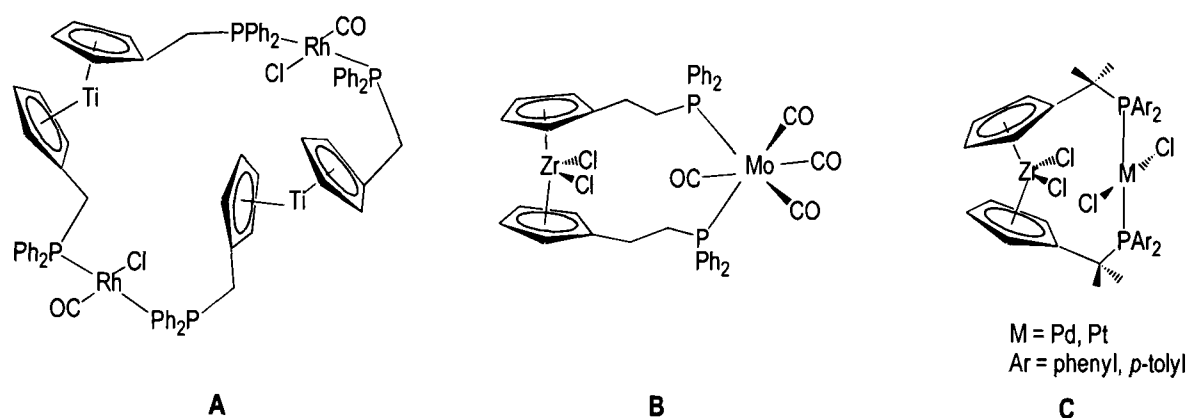
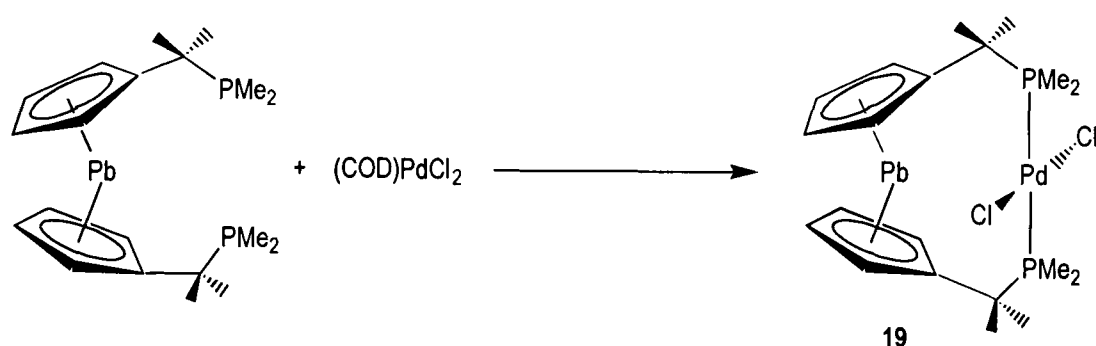


**Figure 3.19** Examples of binuclear and tetranuclear ELHB complexes

Utilising these arguments for the case of **18**, it seems likely that the bimetallic complex proposed would be formed favourably over the tetranuclear version due to the presence of substituents on the backbone carbon.

### 3.5.3 Attempted Preparation of $[\text{Pb}\{(\eta\text{-C}_5\text{H}_4)\text{CMe}_2\text{PMe}_2\}_2\text{PdCl}_2]$ (**19**)

To yellow solution of  $\text{Pd}(\text{COD})\text{Cl}_2$  in THF was slowly added a solution of **15** in THF at room temperature. The resulting yellow solution was stirred overnight after which time volatiles were removed under reduced pressure and the residual yellow solid was washed with pentane and dried under reduced pressure (**Scheme 3.8**) to yield  $[\text{Pb}\{(\eta\text{-C}_5\text{H}_4)\text{CMe}_2\text{PMe}_2\}_2\text{PdCl}_2]$  (**19**).



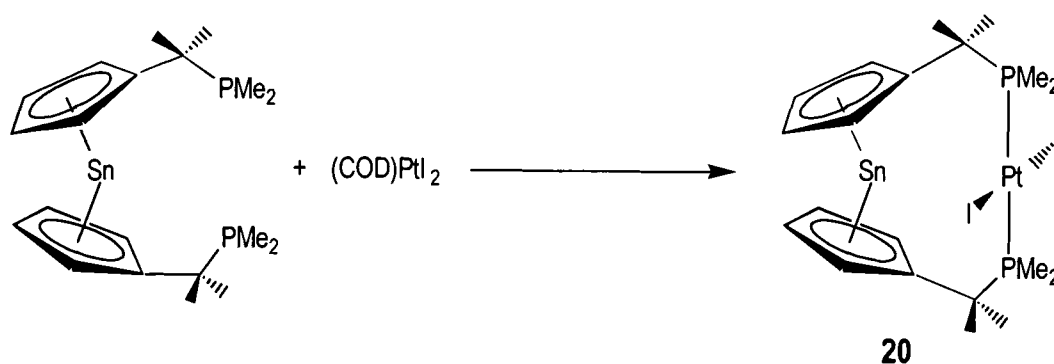
**Scheme 3.8** Attempted Synthesis of  $[\text{Pb}\{(\eta\text{-C}_5\text{H}_4)\text{CMe}_2\text{PMe}_2\}_2\text{PdCl}_2]$  (**19**)

The product **19** is an air-sensitive orange solid, which is poorly soluble in THF. Microanalysis results are consistent with the empirical formula  $C_{20}H_{32}P_2PbPdCl_2$ . Unfortunately, however, the mass spectrum (FAB) does not show any signals attributable to the desired compound; peaks for the molecular ion  $[M^+]$ , or for the fragments  $[M-Cl]$  and  $[M-2Cl]$  were absent.

Analogy with the platinum analogue **18** suggests that the compound **19** has a *trans*-arrangement. In the  $^{31}P\{^1H\}$  NMR spectrum ( $d^8$ -THF, 298 K), however, two signals are observed at  $\delta$  -3.1 and -5.7, suggesting that both the *cis*- and *trans*-isomers of the compound  $[Pb\{(\eta-C_5H_4)CMe_2PMe_2\}_2PdCl_2]$  could be present. Unfortunately, palladium does not exhibit any NMR activity, so this assignment is based purely on the comparable chemical shift of the two product signals are downfield from that of the starting material by approximately the same amount as that observed for the platinum analogue **18**.

#### 3.5.4 Attempted Preparation of $[Sn\{(\eta-C_5H_4)CMe_2PMe_2\}_2PtI_2]$ (**20**)

To yellow solution of  $PtI_2(COD)$  in THF was slowly added a solution of **16** in THF at room temperature. The resulting yellow solution was stirred overnight after which time volatiles were removed under reduced pressure and the yellow solid washed with pentane before the compound  $[Sn\{(\eta-C_5H_4)CMe_2PMe_2\}_2PtI_2]$  (**20**) was isolated as an orange powder in 60 % yield (**Scheme 3.9**).



**Scheme 3.9** Attempted Synthesis of  $[Sn\{(\eta-C_5H_4)CMe_2PMe_2\}_2PtI_2]$  (**20**)

### 3.5.5 Characterisation of compound **20**

The compound **20** is an air-sensitive orange solid, which is poorly soluble in all common solvents. Microanalysis results are consistent with the empirical formula  $\text{C}_{20}\text{H}_{32}\text{P}_2\text{PtSnI}_2$ . The mass spectrum did not exhibit any assignable peaks. The poor solubility of compound **20**, like that of compound **19**, precluded any NMR studies and in addition the mass spectrum did not display any assignable peaks. A polymeric structure like that proposed for **14** is a likely arrangement with the substituted stannocene (**16**) acting as a bridging rather than a chelating ligand.



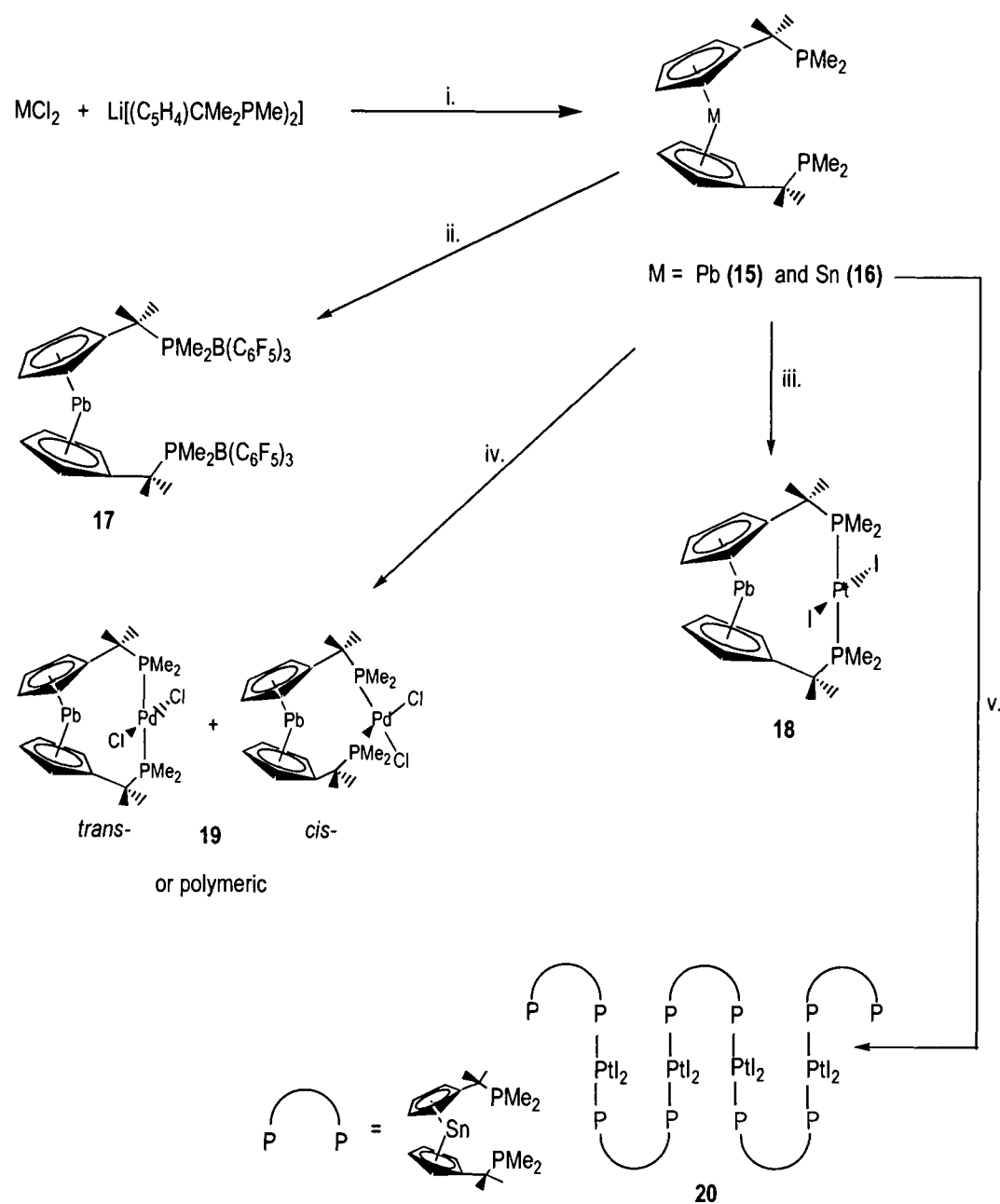
### 3.6 Summary

This chapter describes the synthesis of the main group metallocene compounds  $[\text{Pb}\{(\eta\text{-C}_5\text{H}_4)\text{CMe}_2\text{PMe}_2\}_2]$  (**15**) and  $[\text{Sn}\{(\eta\text{-C}_5\text{H}_4)\text{CMe}_2\text{PMe}_2\}_2]$  (**16**) by the reaction of the respective Group 14 metal(II) chloride salts with the lithium salt of the substituted cyclopentadienyl ligand  $[\text{Li}(\text{C}_5\text{H}_4)\text{CMe}_2\text{PMe}_2]$ . The yields for both reactions were high and the compounds were fully characterised by multinuclear NMR spectroscopy techniques including  $^{207}\text{Pb}\{^1\text{H}\}$  and  $^{119}\text{Sn}\{^1\text{H}\}$  NMR methods, which demonstrated chemical shifts typical of those found for other main group metallocenes.

The reactivity of the pendant phosphine groups of these new complexes has been investigated through reactions with the Lewis acid  $\text{B}(\text{C}_6\text{F}_5)_3$  and through attempts to synthesise bimetallic main group-transition metal complexes. Reaction between compound **15** and two equivalents of  $\text{B}(\text{C}_6\text{F}_5)_3$  yields the disubstituted compound  $[\text{Pb}\{(\eta\text{-C}_5\text{H}_4)\text{CMe}_2\overline{\text{PMe}_2\text{B}(\text{C}_6\text{F}_5)_3}\}_2]$  (**17**), which has been characterised by NMR spectroscopy techniques. The attempted reaction between the tin analogue **16** and two equivalents of  $\text{B}(\text{C}_6\text{F}_5)_3$  resulted in a mixture of products as shown by  $^1\text{H}$  and  $^{31}\text{P}\{^1\text{H}\}$  NMR spectra.

The synthesis of  $[\text{Pb}\{(\eta\text{-C}_5\text{H}_4)\text{CMe}_2\overline{\text{PMe}_2}\}_2\text{PtI}_2]$  (**18**) was achieved by reaction between compound **15** and  $\text{PtI}_2(\text{COD})$ . The  $^{31}\text{P}\{^1\text{H}\}$  NMR spectrum demonstrates the presence of a singlet with  $^{195}\text{Pt}$  satellites with a  $J_{\text{P-Pt}}$  value consistent with a *trans*-arrangement of phosphine groups around the Pt-metal. An analogous reaction between compound **15** and  $\text{PdCl}_2(\text{COD})$  resulted in the formation of the compound **19** for which microanalysis results are consistent with the empirical formula for the compound  $[\text{Pb}\{(\eta\text{-C}_5\text{H}_4)\text{CMe}_2\overline{\text{PMe}_2}\}_2\text{PdCl}_2]$ , although the low solubility suggests a polymeric structure.

The new chemistry described in this chapter is summarised in **Scheme 3.10**.



- Reagents and conditions:
- i. THF,  $-78^\circ\text{C}$
  - ii. 2  $B(C_6F_5)_3$ , toluene
  - iii.  $PtI_2(COD)$ , THF
  - iv.  $PdCl_2(COD)$ , THF
  - v.  $PtI_2(COD)$ , THF

**Scheme 3.10** Summary of the new chemistry in this chapter

### 3.11 References for Chapter 3

- [1] D. J. Burkey and T. P. Hanusa, *Comments Inorg. Chem.*, **17** (1995) 41.
- [2] M. A. Beswick, J. S. Palmer and D. S. Wright, *Chem. Soc. Rev.*, **27** (1998) 225.
- [3] E. O. Fischer and H. Grubert, *Z. Anorg. Chem.*, **286** (1956) 237.
- [4] E. O. Fischer and H. Grubert., *Z. Naturforsch.*, **11b** (1956) 423.
- [5] L. D. Dave, D. F. Evans and G. Wilkinson, *J. Chem. Soc.*, (1959) 3684.
- [6] A. Almenningen, A. Haaland and T. Motzfeldt, *J. Organomet. Chem.*, **7** (1967) 97.
- [7] D. J. Burkey and T. P. Hanusa, *Organometallics*, **14** (1995) 11.
- [8] M. J. Heeg, R. H. Herber, C. Janiak, J. J. Zuckerman, H. Schumann and W. F. Manders, *J. Organomet. Chem.*, **346** (1988) 321.
- [9] M. J. Heeg, C. Janiak and J. J. Zuckerman, *J. Am. Chem. Soc.*, **106** (1984) 4259.
- [10] C. Pantattoni, G. Bombeieri and U. Croatto, *Acta Crystallogr.*, **21** (1966) 823.
- [11] M. A. Beswick, C. Lopez-Casideo, M. A. Paver, P. R. Raithby, C. A. Russell, A. Steiner and D. S. Wright, *Chem. Commun.*, (1997) 109.
- [12] J. L. Atwood, W. E. Hunter, A. H. Cowley, R. A. Jones and C. A. Stewart, *J. Chem. Soc. Chem. Commun.*, (1981) 925.
- [13] H. Schumann, C. Janiak, E. Hahn, C. Kolax, J. Loebel, M. D. Rausch, J. J. Zuckerman and M. J. Heeg, *Chem. Ber.*, **119** (1986) 2656.
- [14] H. Schumann, C. Janiak and J. J. Zuckerman, *Chem. Ber.*, **121** (1988) 207.
- [15] P. Jutzi and R. Dickbreder, *J. Organomet. Chem.*, **373** (1989) 301.
- [16] S. P. Constantine, P. B. Hitchcock and G. A. Lawless, *Organometallics*, **15** (1996) 3905.
- [17] W. J. Evans, K. J. Forrestal, J. T. Leman and J. W. Ziller, *Organometallics*, **15** (1996) 527.
- [18] W. J. Evans, R. D. Clark, K. J. Forrestal and J. W. Ziller, *Organometallics*, **18** (1999) 2401.
- [19] D. J. Burkey, T. P. Hanusa and J. C. Huffman, *Inorg. Chem.*, **39** (2000) 153.
- [20] P. Jutzi, D. Kanne and C. J. Kruger, *Angew. Chem. Int. Ed. Engl.*, **24** (1985) 773.
- [21] P. Jutzi, *Adv. Organomet. Chem.*, **26** (1986) 217.

- [22] S. P. Constantine, P. B. Hitchcock, G. A. Lawless and G. M. DeLima, *J. Chem. Soc., Chem. Commun.*, (1996) 1101.
- [23] S. P. Constantine, H. Cox, P. B. Hitchcock and G. A. Lawless, *Organometallics*, *19* (2000) 317.
- [24] H. Sitzmann, R. Boese and P. Stellberg, *Z. Anorg. Allg. Chem.*, *622* (1996) 751.
- [25] J. V. Scibelli and M. D. Curtis, *J. Am. Chem. Soc.*, *95* (1973) 924.
- [26] P. Jutzi, E. Schlueter, M. B. Hursthouse, A. M. Arif and R. L. Short, *J. Organomet. Chem.*, *299* (1986) 285.
- [27] P. Jutzi, U. Holtmann, D. Kanne, C. Kruger, R. Blom, R. Gleiter and I. Hyla-Kryspin, *Chem. Ber.*, *122* (1989) 1629.
- [28] J. L. Robbins, N. Edelstein, B. Spencer and J. C. Smart, *J. Am. Chem. Soc.*, *104* (1982) 1882.
- [29] P. Jutzi and B. Hielscher, *Organometallics*, *5* (1986) 2511.
- [30] T. V. Timofeeva, J.-H. Lii and N. L. Allinger, *J. Am. Chem. Soc.*, *117* (1995) 7452.
- [31] R. A. Williams, T. P. Hanusa and J. C. Huffman, *Organometallics*, *9* (1990) 1128.
- [32] J. S. Overby, T. P. Hanusa and V. G. Young Jr. , *Inorg. Chem.*, *37* (1998) 163.
- [33] P. Jutzi, F. Köhl, P. Hofmann, C. Kruger and Y.-H. Tsay, *Chem. Ber.*, *113* (1980) 757.
- [34] R. A. Williams, T. P. Hanusa and J. C. Huffman, *Organometallics* *9*, (1990) 1128.
- [35] B. Bosnich, *Chem. Soc. Rev.*, *23* (1994) 387.
- [36] D. R. Armstrong, M. J. Duer, M. G. Davidson, D. Moncrieff, C. A. Russell, C. Stourton, A. Steiner, D. Stalke and D. S. Wright, *Organometallics*, *16* (1997) 3340.
- [37] G. Bruno, E. Ciliberto and I. L. Fragala, *J. Organomet. Chem.*, *289* (1985) 263.
- [38] S. Cradock and W. Duncan, *J.C.S. Faraday Trans.*, *2* *74* (1978) 194.
- [39] S. G. Baxter, A. H. Cowley, J. G. Lasch, M. Lattman, W. P. Sharum and C. A. Stewart, *J. Am. Chem. Soc.*, *104* (1982) 4064.
- [40] T. S. Dory and J. J. Zuckerman, *J. Organomet. Chem.*, *264* (1984) 295.

- [41] S. P. Constantine, G. M. DeLima, P. B. Hitchcock, J. M. Keates and G. A. Lawless, *J. Chem. Soc., Chem. Commun.*, (1996) 2337.
- [42] S. P. Constantine, G. M. DeLima, P. B. Hitchcock, J. M. Keates, G. A. Lawless and I. Marziano, *Organometallics*, **16** (1997) 793.
- [43] M. L. Hays and T. P. Hanusa, *Adv. Organomet. Chem.*, **40** (1996) 117.
- [44] B. Wrackmeyer and K. Horschler, *Annu. Rep. NMR Spectrosc.*, **38** (1999) 202.
- [45] B. Wrackmeyer, A. Sebald and L. H. Merwin, *Magn. Reson. Chem.*, **29** (1991) 260.
- [46] P. A. W. Dean, D. D. Phillips and L. Polensek, *Can. J. Chem.*, **59** (1981) 50.
- [47] B. Wrackmeyer and K. Horschler, *Annu. Rep. NMR Spectrosc.*, **30** (1991) 249.
- [48] P. Jutzi, R. Dickbreder and H. Noth, *Chem. Ber.*, **122** (1989) 865.
- [49] F. X. Köhl, R. Dickbreder, P. Jutzi, G. Müller and B. Huber, *Chem. Ber.*, **122** (1989) 871.
- [50] C. Janiak, H. Schumann, C. Stader, B. Wrackmeyer and J. J. Zuckerman, *Chem. Ber.*, **121** (1988) 1745.
- [51] W.-W. DuMont and B. Neudert, *Z. Anorg. Allg. Chem.*, **441** (1978) 86.
- [52] H. H. Karsch, A. Appelt and G. Müller, *Organometallics*, **5** (1986) 1664.
- [53] B. Wrackmeyer, *Ann. Rep. NMR Spectrosc.*, **15** (1985) 73.
- [54] J. M. Keates, *Ph.D. Thesis*, University of Sussex, 1997.
- [55] T. Imamoto, T. Oshiki, T. Onozawa, T. Kusumoto and K. Sato, *J. Am. Chem. Soc.*, **112** (1990) 5244.
- [56] K. Bourumeau, A.-C. Gaumont and J.-M. Denis, *J. Organomet. Chem.*, **529** (1997) 205.
- [57] T. W. Graham, A. Llamazares, R. McDonald and M. Cowie, *Organometallics*, **18** (1999) 3490.
- [58] T. W. Graham, A. Llamazares, R. McDonald and M. Cowie, *Organometallics*, **18** (1999) 3502.
- [59] R. G. Pregosin, in J. G. Verkade and L. D. Quin (Eds.): *Stereochemistry of Metal Complexes: Unidentate Phosphorus Ligands, Phosphorus-31 NMR Spectroscopy in Stereochemical Analysis; Organic Compounds and Metal Complexes*, VCH, Weinheim 1987, p. 465.
- [60] P. L. Goggin, R. J. Goodfellow, S. R. Haddock, J. R. Knight, F. J. S. Reed and B. F. Taylor, *J. Chem. Soc., Dalton Trans.*, (1974) 523.

- [61] R. Favez, R. Roulet, A. A. Pinkerton and D. Schwarzenbach, *Inorg. Chem.*, **19** (1980) 1356.
- [62] B. Bosch, G. Erker and R. Fröhlich, *Inorg. Chim. Acta.*, **270** (1998) 446.
- [63] B. E. Bosch, I. Brummer, K. Künz, G. Erker, R. Frölich and S. Kotila, *Organometallics*, **19** (2000) 1255.

## **Chapter 4**

# **Introduction to Inorganic Fullerene-Like Materials**

## 4.0 Introduction to Chapter 4

This chapter provides a brief background into the structural characteristics, preparation and methods of analysis of inorganic fullerene (IF)-related materials. A comparison with carbon based fullerenic structures is given along with a brief review of the recent research into the area.

Since the discovery of  $C_{60}$  in 1985 by Kroto *et al.*,<sup>[1]</sup> world-wide research into the field of carbon fullerene chemistry has developed rapidly. A number of significant breakthroughs have allowed for the preparation of single walled carbon nanotubes (SWNTs),<sup>[2]</sup> multi-walled carbon nanotubes (MWNTs) as well as techniques for opening and filling these nano-structures with a plethora of elements and different types of compounds.<sup>[3-5]</sup>

More recently, inorganic analogues of these carbon fullerenic species have been discovered and their properties studied.<sup>[6]</sup> Layered metal chalcogenides derived from the parent  $2H-MX_2$  structure ( $M = W$  and  $Mo$ ;  $X = S$  and  $Se$ ) have been prepared by a number of synthetic routes ranging from encapsulation of  $MO_3$  particles to laser bombardment of bulk  $MS_2$  samples.<sup>[7, 8]</sup> As a result of their structural similarities with the carbon fullerenes IF-related materials as they are popularly known, have shown potential for use in the fields of solid lubricants,<sup>[9, 10]</sup> photovoltaic films,<sup>[11]</sup> hydrosulfurisation catalysts<sup>[12]</sup> and further applications besides.

The work presented in the second part of this thesis investigates the synthesis of novel IF-like materials (**Chapter 5**) and also describes an alternative method for preparing Group 5 transition metal oxide precursor materials, some of which show a propensity to form IF-related morphologies (**Chapter 6**). This study demonstrates that the tendency to form polyhedral structures is common among nanoparticles of compounds which commonly exhibit a 2D-layered structure.



## 4.1 The Carbon Fullerenes

Following the serendipitous discovery of  $C_{60}$  by Kroto and co-workers in 1985<sup>[1]</sup> and the advent of fullerene chemistry, attention has been focused on associated cylindrical and polyhedral forms of graphite.<sup>[2, 13-18]</sup> Kroto postulated that an anomalously stable species in the mass spectrum of vapourised carbon might have a structure containing 60 carbon atoms. He suggested that it would be comprised of 60 carbon atoms arranged in a truncated icosahedron (**Figure 4.1**), a structure analogous to that of an Association football. Instead of the lengthy IUPAC name\*, the species is known by its trivial name *Buckminsterfullerene*, after the architect Richard Buckminster Fuller whose geodesic domes had a similar appearance.

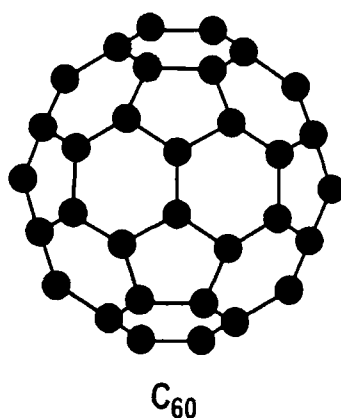


**Figure 4.1** Illustration of Buckminsterfullene ( $C_{60}$ )

Over the last decade, the chemistry of fullerenes has been widely studied by an ever-increasing number of groups around the world. The potential applications of carbon fullerenes are many and varied. Lubricants, scanning tunnelling microscopy (STM) tips, catalyst supports, superconductors, gas storage media and electronic displays have all been proposed as applications of the new technology.<sup>[19]</sup> Many of these ideas are still at the theoretical stage of development, but the current level of investment into these areas of research suggests that some projects will have a bright future.<sup>[20]</sup>

---

\*The IUPAC name of  $C_{60}$ : Hentricontacyclo[29.29.0.0<sup>2,14</sup>.0<sup>3,12</sup>.0<sup>4,59</sup>.0<sup>5,10</sup>.0<sup>6,58</sup>.0<sup>7,55</sup>.0<sup>8,53</sup>.0<sup>9,21</sup>.0<sup>11,20</sup>.0<sup>13,18</sup>.0<sup>15,30</sup>.0<sup>16,28</sup>.0<sup>17,25</sup>.0<sup>19,24</sup>.0<sup>22,52</sup>.0<sup>23,50</sup>.0<sup>26,49</sup>.0<sup>27,47</sup>.0<sup>29,45</sup>.0<sup>32,44</sup>.0<sup>33,60</sup>.0<sup>34,47</sup>.0<sup>35,43</sup>.0<sup>36,56</sup>.0<sup>38,54</sup>.0<sup>39,51</sup>.0<sup>40,48</sup>.0<sup>42,46</sup>] hexaconta-1, 3, 5(10), 6, 8, 11, 13 (18), 14, 16, 19, 21, 23, 25, 27, 29(45), 30, 32(44), 33, 35(43), 36, 38(54), 39(51), 40(48), 41, 46, 49, 52, 55, 57, 59-triacontaene.

## 4.2 The Structures of Carbon Fullerenes

The discovery of the remarkable stability of  $C_{60}$  and the carbon fullerenes has revolutionised the theories of molecular shape and structure with their multitudinous forms including nested fullerenes (buckyonions), nanotubes and helical coils among others.[2, 13, 14, 21, 22] With the basic building block being an essentially flat and rigid graphitic structure, how is it possible that these curved and closed morphologies can be formed?

Carbon is a common element found in a variety of forms. Graphite is one allotropic form of carbon which is stable under ambient conditions, existing as a structure comprised of planar layers of six-membered rings held together by relatively weak van der Waals (vdW) forces. Other carbon forms include the tetrahedrally ordered diamond arrangement as well as pit-coal, coke, charcoal and soot which are in principle 'graphite like' but have a lower degree of local ordering. Fullerenic species tend to exist as closed structures including fullerenes, nanotubes and nanoparticles.[23]

Curvature of the graphitic structure requires the presence of non-six-membered rings in the layers. It is precisely the ability of carbon to form five-membered rings, which allows for the formation of buckminsterfullerene, the most stable of all the fullerenes. The important role of *pentagonal* rings in the formation of curved structures is demonstrated in the structure of  $C_{60}$ . The molecule contains 12 pentagons, which are symmetrically dispersed among the other 20 hexagons and make up the 'soccer ball' spherical arrangement. Use of *heptagonal* rings on the other hand results in *negative* curvature and formation of a saddle shaped surface (**Figure 4.2**). Heptagonal carbon rings have not, as yet, been observed in molecular fullerenes, although their presence has been implied by the negative curvature observed by Iijima in fullerene derived structures such as nanotubes and other nanoparticles.[14]

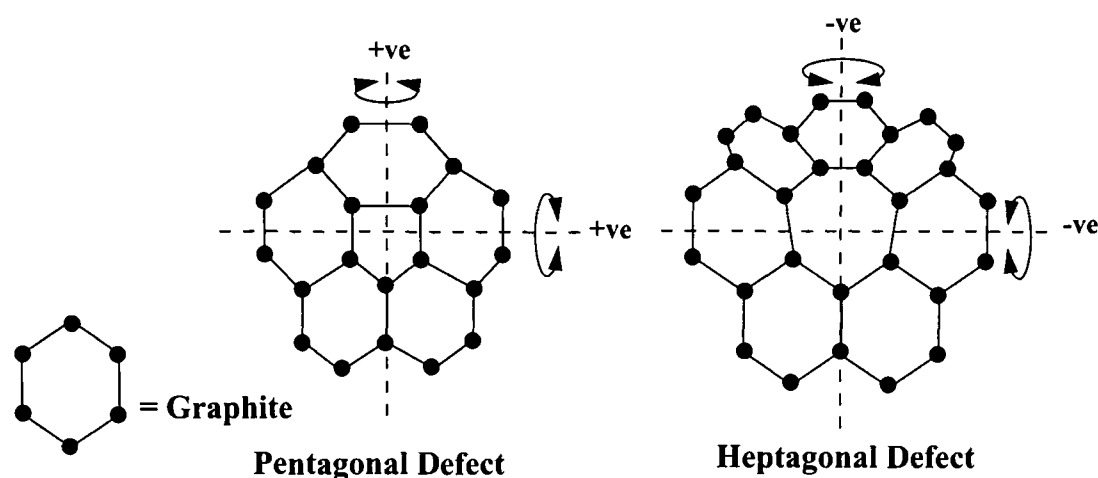


**Figure 4.2** Representation of 5- and 7-membered rings in  $C_{60}$

Although non-six membered carbon rings are required to form a spherical shape, a cylindrical carbon nanotube may form along its length without the need for defects. In 1991, Iijima reported the discovery of graphitic, cylindrical nanostructures or *nanotubes*.<sup>[2]</sup> In general, these tubes are analogous to rolled-up layers of 'graphite chicken wire' where the ends of the tubes are capped by half-spherical graphite domes, which contain the same pentagonal defects as buckminsterfullerene. It was also noted that these nanotubes could form one of three morphologies dependent upon the way in which the graphite layers were 'rolled up' in the cylinder arrangement: by joining opposite graphite hexagons at their lateral edges or by linking them such that they are displaced with respect to one another forming helical, twisted tubes.<sup>[24]</sup>

For carbon fullerene clusters of greater than 6000 atoms, double layer fullerenes are more energetically favourable than single walled structures.<sup>[17]</sup> In an independent study comparing the relative strengths of the two walls in a system consisting of two concentric carbon nanotubes, the second tube was found to stabilise the superstructure.<sup>[25]</sup> This stabilisation has been attributed to the weak vdW forces between the layers.

### 4.3 Non-Carbon 'Fullerene-Like' Materials

A group of related materials, thus far attracting less attention, are the non-carbon-based inorganic fullerenes. Known also as inorganic fullerene-related materials, they are so-called because of their similarity in structure and properties to their carbon-based counterparts. Until recently, boron was considered to be the element with the greatest number of cage structures. As a result, the chemistry of polyhedral borane structures has been well studied and the structures and properties of borohydride compounds have been expounded in detail.[7, 26]

Furthermore, the cage-like structure of boron nitride (BN) crystallises in a hexagonal, graphitic arrangement (**Figure 4.3**). It is therefore natural to view it as a precursor for the formation of inorganic-fullerene like structures. By replacing two carbon atoms with an isoelectronic B-N pair in fullerenes such as  $C_{60}$  and in carbon nanotubes, mixed  $C_{60-2n}B_nN_n$  and even  $B_nN_{60-n}$  structures have been prepared.[27]

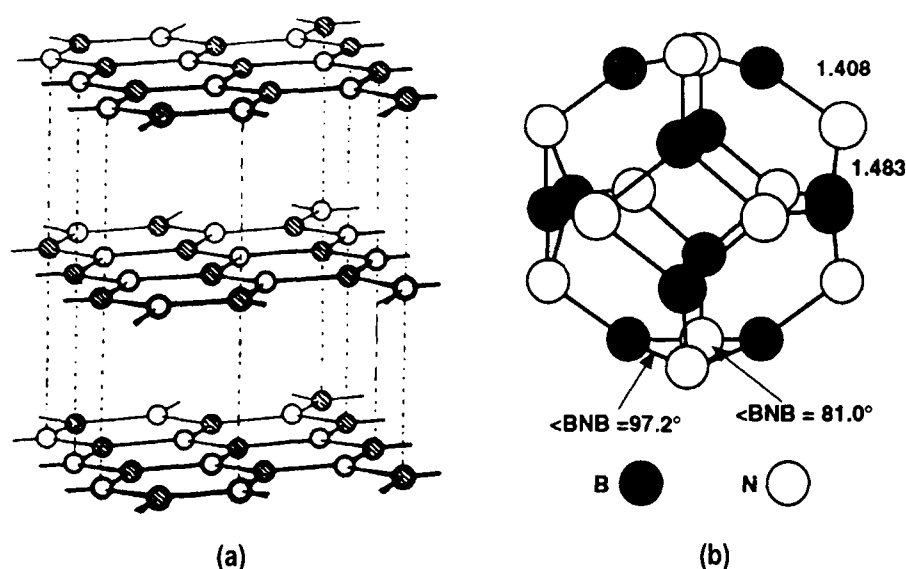


**Figure 4.3** The (a) quasi-graphitic and (b) cage-like structures of Boron Nitride

The initial work in the area of transition metal based IF-like materials was performed by Tenne and co-workers at the Weizmann Institute in Rehovot, Israel while preparing thin-film tungsten selenide ( $WSe_2$ ) and tungsten sulfide ( $WS_2$ ) solar cells.[6] Tenne considered the structures of carbon and the early transition metal sulfides; both graphitic carbon and molybdenum sulfide are comprised of layered structures. It was generally believed that geometrically closed structures were unique to carbon because the strain involved for other elements was thought to prevent stable

structures existing. One exception is the case of layered minerals like asbestos, which are known to exist in open, cylindrical forms not dissimilar to the concentric tubes found in graphite. [28, 29]

The structural similarities between IF-related materials and carbon-fullerenes can best be demonstrated by a direct comparison between the layered structure of graphite and that of the  $2H-MX_2$  arrangement as shown in **Figure 4.4**. The structure is accounted for by the crystal structure of the dichalcogenides of Mo and W in which each metal layer is sandwiched between two chalcogen layers (hence  $2H-MX_2$ ). Strong covalent bonds exist between the metal and chalcogen atoms within the layers and weak vdW interactions hold the layers together. Such a structure provides an atomically smooth and unreactive vdW surface.

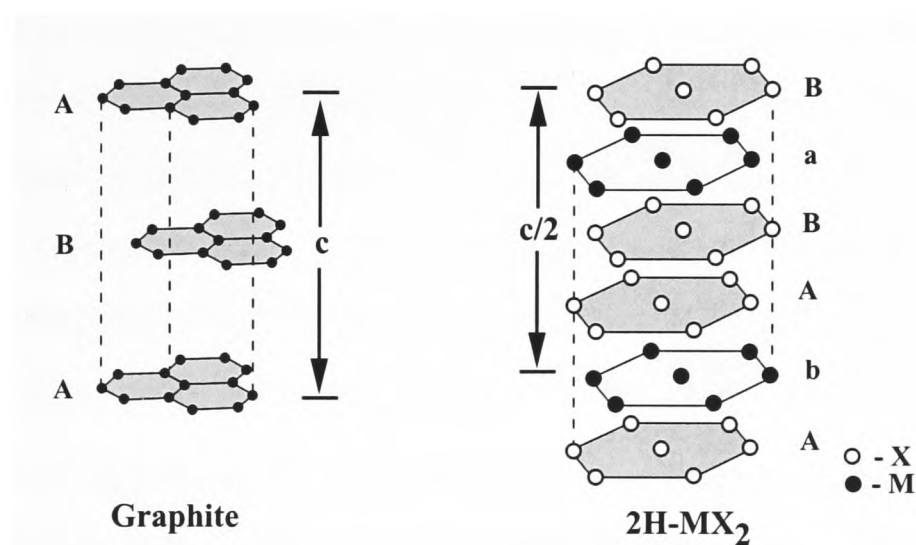


**Figure 4.4** Comparison between the layered structures of graphite and the  $2H-MX_2$  – type compounds

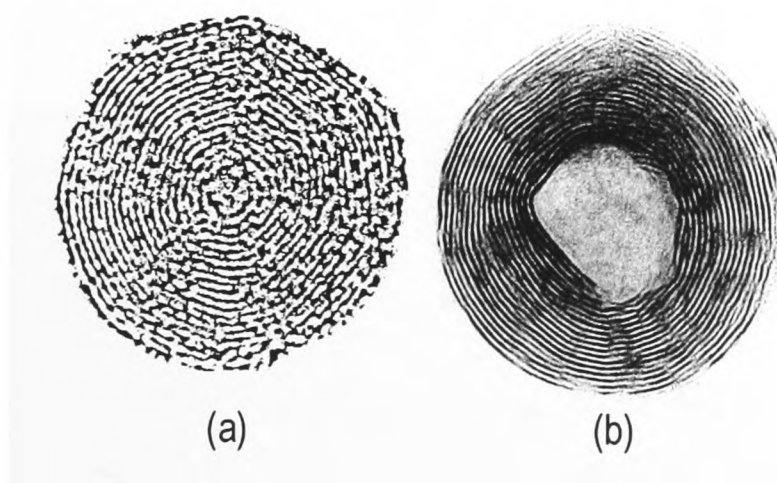


**Figure 4.5** TEM lattice images of carbon-nested fullerene (a) and IF-WS<sub>2</sub> (b). Each dark line represents an atomic layer. The distance between each two layers is 3.35 and 6.18 Å for carbon-nested fullerene and IF-WS<sub>2</sub>, respectively. The c-axis is always normal to the surface of the nested fullerenes in both cases. [7]

Like their carbon-based analogues, nanoclusters of inorganic layered compounds such as the metal dichalcogenides are also known to be unstable in the planar form and tend to metamorphasise into hollow cage, IF-like (IF-MX<sub>2</sub>) structures similar to those of nested fullerenes and nanotubes.[6, 30, 31] This is thought to be not entirely unrelated to the highly reactive nature of the dangling bonds on the MX<sub>2</sub> surface parallel to the *c* planes (see **Figure 4.4**). The excess surface energy resulting from these dangling bonds in nanoclusters can lead to the situation that, under certain conditions, the MS<sub>2</sub> sheets fold and form closed, hollow structures. In doing so, the dangling bonds are eliminated.[13] This, however, does not explain the closed structures from a geometrical point of view.

From this perspective, complete closure of the MX<sub>2</sub> structure requires the replacement of hexagons by other polygonal units in an analogous fashion to that discussed for carbon in the previous section (**Section 4.2**). It has been found that the IF-related structures also include defects, which allow for curvature and the formation of a three-dimensional nanostructure. In this case, however, the defects are not only pentagonal and heptagonal rings, but can also include *rhombohedral* and *triangular* irregularities. IF-like metal dichalcogenides exhibit both positive and negative curvature within their structures.[6] One example of this behaviour is shown by the structure of an IF-MoS<sub>2</sub> nanotubular structure (**Figure 4.5**). The regions at which the diameter of the tube increases or decreases demonstrates either positive or negative curvature effects as shown in **Figure 4.6**. [7, 32, 33].

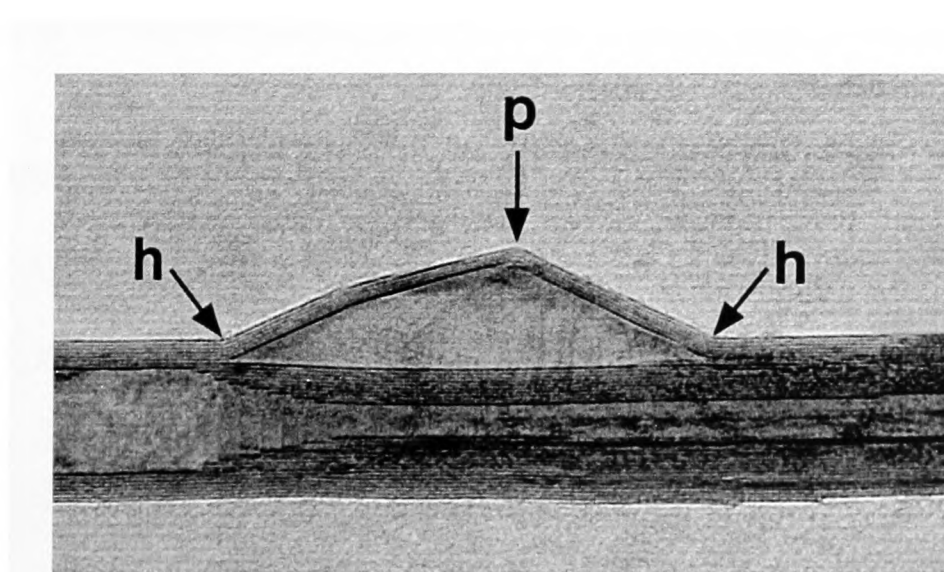


**Figure 4.5** Defects resulting in positive and negative curvature in a nanotube of IF-MoS<sub>2</sub>. [8]  
(h = heptagonal defect, p = pentagonal defect).

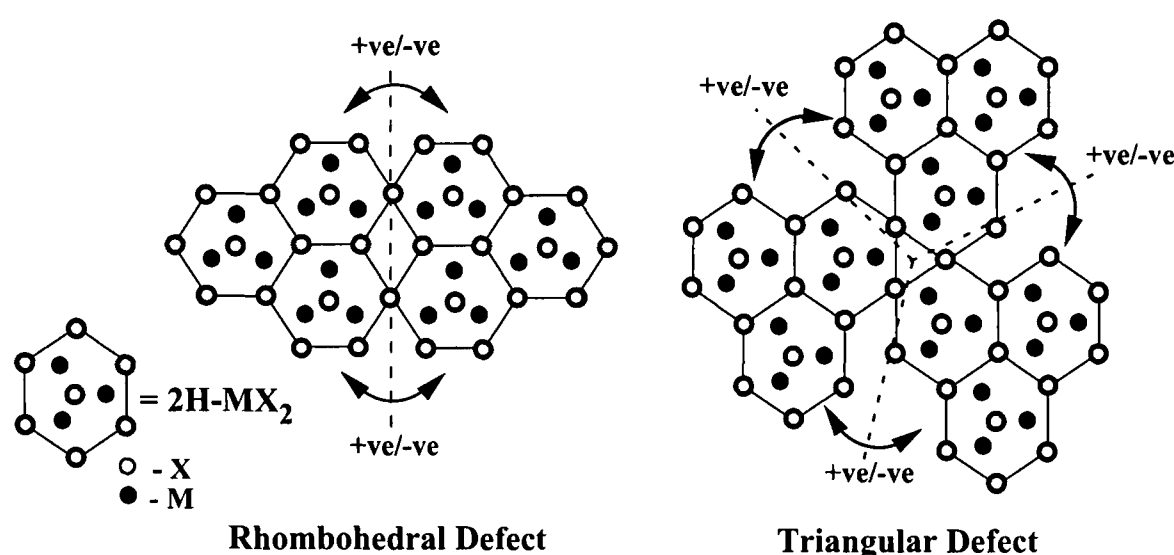


**Figure 4.6** Positive and negative curvature in  $2\text{H-MX}_2$  materials resulting from the presence of rhombohedral and triangular defects

#### 4.4 Methods of Preparation of IF-Like Materials

There are a number of both specific and general methods by which IF-related materials can be prepared. These currently include gas phase growth from ion beam sputtered molybdenum or tungsten films; spontaneous room temperature growth from reduced  $\text{WS}_3$  soot;<sup>[34]</sup> laser evaporation from non-fullerenic  $\text{MoS}_2$  films;<sup>[35]</sup> STM induced growth from finely divided, amorphous  $\text{MoS}_3$  particles<sup>[36]</sup> and finally, gas- and solid-phase growth from partially reduced Mo or W oxides.<sup>[30, 34]</sup> In the last three cases it is possible to obtain filled or partially filled encapsulates whereas the other techniques result in hollow, IF-like closed-cage structures. STM induced  $\text{MoS}_2$  growth produces partially filled encapsulates containing amorphous  $\text{MoS}_3$  filling while the gas- and solid-phase growth from reduced Mo and W oxides results in oxide-containing closed structures.<sup>[3, 22]</sup>

##### 4.4.1 Gas and Solid Phase Synthesis of IF-Like $\text{MS}_2$ (M = Mo and W)

Previous experimentation has been carried out on molybdenum oxide ( $\text{MoO}_3$ ) in the gas phase to synthesise IF-like  $\text{MoS}_2$ .<sup>[25, 30]</sup> The utility of this system is based upon the fact that reduced molybdenum oxide ( $\text{MoO}_{3-x}$ ) is volatile under reducing conditions above  $700^\circ\text{C}$ . In a typical experiment,  $\text{MoO}_3$  is heated to  $800^\circ\text{C}$  in a reducing atmosphere of forming gas (5 %  $\text{H}_2$  / 95 %  $\text{N}_2$ ) to yield reduced  $\text{MoO}_{3-x}$ . The reduced oxide then sublimates in a stream of hydrogen sulfide ( $\text{H}_2\text{S}$ ) gas admitted with the forming gas and sulfidisation generally occurs within five minutes (**Figure 4.7**).



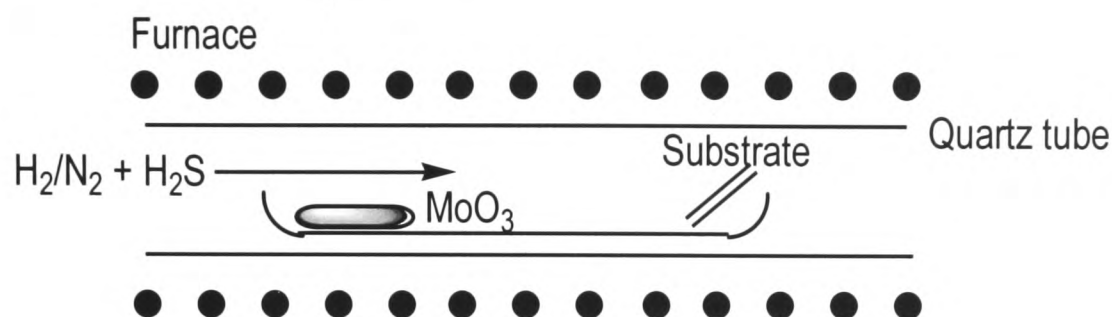


**Figure 4.7** Schematic of the gas-phase reactor used in the synthesis of IF-MoS<sub>2</sub>

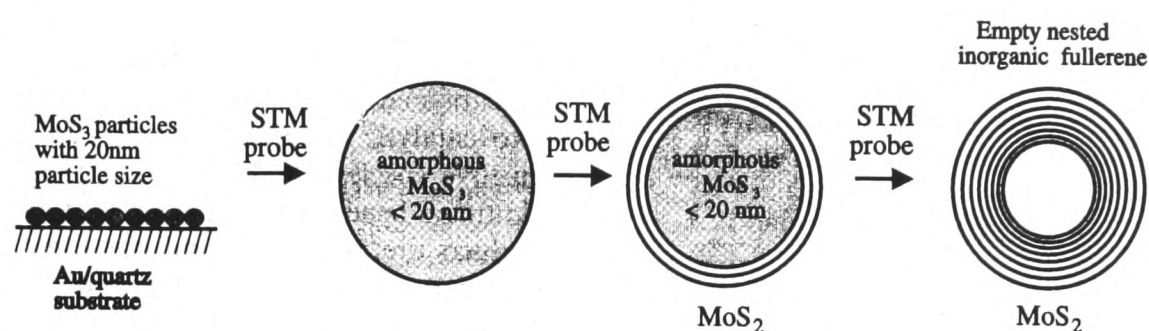
For the structurally analogous tungsten oxide WO<sub>3</sub>, the gas phase reaction is precluded by the lack of volatility of tungsten oxides. The reaction therefore occurs in a two phase system. Tungsten oxide nanoparticles are prepared by resistively heating a tungsten wire under vacuum in the presence of water vapour, generated by placing a beaker of pure water in the vacuum chamber containing the heated W wire. The reduced WO<sub>3-x</sub> particles with sizes of approximately 150 nm are then heated to 900°C. In this case, H<sub>2</sub>S and H<sub>2</sub> gases are passed over the sample to simultaneously reduce and sulfidise the sample to IF-like WS<sub>2</sub>. The short reaction time ensures that incomplete conversion of the oxide occurs and that IF-encapsulated oxides are produced as a result.<sup>[11]</sup> The process of growth of the IF-MS<sub>2</sub> species will be discussed in the next section (**Section 4.5**).

The synthesis of IF-WSe<sub>2</sub> is achieved using a similar technique, the only difference being the use of Se vapour instead of H<sub>2</sub>S. In this case, selenium shot is heated up to 350°C and, using forming gas as the carrier, passed over a sample of WO<sub>3</sub> heated to between 650°C and 850°C.<sup>[37]</sup>

#### 4.4.2 STM Induction of Amorphous Films

Amorphous sulfide precursors such as MoS<sub>3</sub> have also demonstrated themselves to be excellent precursors for the growth of IF-like material in a slow crystallisation process lasting from anything between one hour at 800-900°C to several years at ambient conditions (**Scheme 4.1**).<sup>[6, 22]</sup>





**Scheme 4.1** Mechanism of formation of MoS<sub>2</sub> induced by STM from MoS<sub>3</sub>

By applying very short electrical pulses from an STM tip onto amorphous MoS<sub>3</sub> particles, fast crystallisation into IF-like MoS<sub>2</sub> particles is induced.<sup>[36]</sup> A study of the EDX spectrum of both starting material and product demonstrates the presence of Mo and S only in the reaction mixture. While the ratio of S/Mo was found to be 3.0 for the amorphous nanoparticles, the ratio varied between 1.8 and 2.2 for the IF-related particles in accordance with the predicted change in morphology.<sup>[3]</sup>

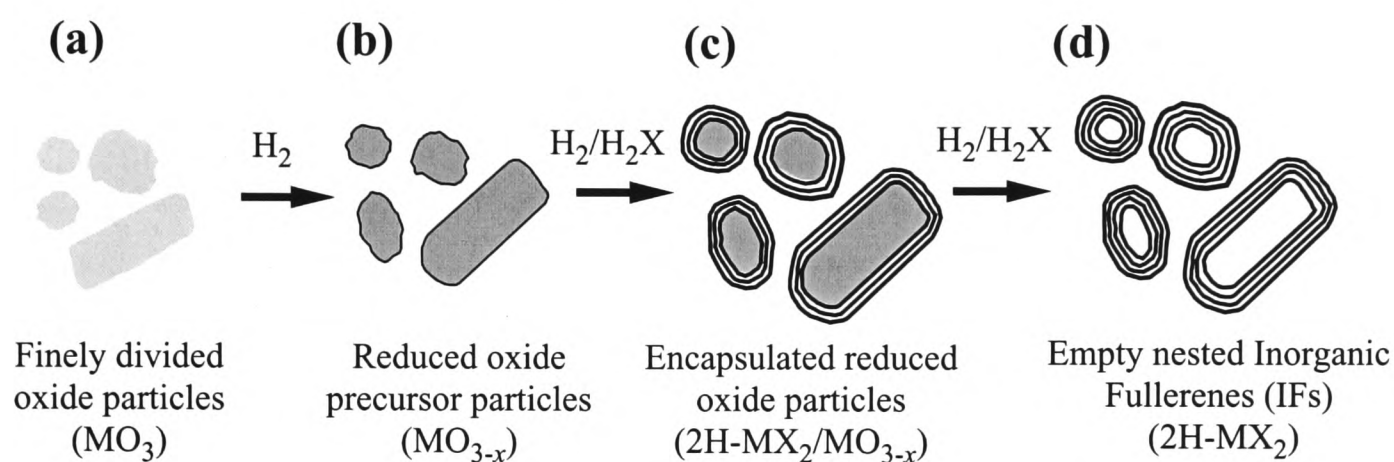
#### 4.5 Growth of IF-Like Materials: Encapsulation of Metal Oxides Within IF-Like Cages

The experimental results described above furnish some ideas for the growth mechanism of IF-like materials. Extensive bending of graphite layers has been reported and it has been noted that severe bending occurs at high temperatures.<sup>[13]</sup> Work by Tenne *et al.* has described the curling of WS<sub>2</sub> films at 1000°C, which implies that high temperatures may initiate either bending or faceting of the crystals, inducing the crystal to close in on itself.<sup>[38]</sup>

In the gas phase production of IF-MoS<sub>2</sub> nanoparticles, which contain only a very few sulfide layers, a spherically symmetrical morphology is the usual outcome. However, whereas these single- or double-layer species tend to be ‘evenly bent’, multiple-layer IFs like those formed in the gas-solid phase reactions between H<sub>2</sub>S and WO<sub>3</sub> contain faceted morphologies with sharp angles at the corners of the polyhedra. These observations were integral in the proposal of the growth mechanism described below.

The proposed growth mechanism for IF-like materials commences with a very fast reaction between the oxide surface layer in the first instant of the reaction and the growth of a closed single or double MS<sub>2</sub> layer. This inert layer of MS<sub>2</sub> isolates the

nanoparticle from its nearest neighbours and prohibits fusion of the oxide into larger particles which would then form  $2\text{H-MS}_2$  platelets. Simultaneously, fast hydrogen diffusion into the oxide particles leads to reduction of the oxide core into  $\text{MoO}_2$  or  $\text{W}_{18}\text{O}_{49}$  within several minutes. The remaining oxide core is then progressively transformed into the respective sulfide (IF) (**Scheme 4.2**). Consequently, the size of the IF-particle is determined by the size of the incipient oxide nanoparticle.[31, 32]



**Scheme 4.2** Schematic of the proposed growth mechanism of IF-like materials from metal oxide precursors

The rate determining step in the process has been attributed to the intercalation of the sulfide in the top few layers followed by slow diffusion towards the ‘growth front’ at the interface between the sulfide and the sub-oxide. Following the very rapid formation of the first few sulfide layers over the entire surface of the metal oxide particle, further growth is limited by the rate of inward (outward) migration of sulfide (oxygen/water) species through the  $\text{MS}_2$  barrier. Hence, the second stage of the process is diffusion controlled.[8]

In order to penetrate through the top one or two  $\text{MS}_2$  layers, diffusion through dislocations and kinks *parallel* to the  $\text{MS}_2$  layers takes place followed by intercalation of sulfur atoms between the  $\text{WS}_2$  layers *perpendicular* to the sulfide layers. Additionally, it has been observed that when the structure of the oxide changes from a smooth spherical surface to a faceted one (upon reduction *via* annealing), more ‘growth fronts’ are observed. This observation is in agreement with the fact that as more layers are formed, the number of dislocations increases leading to more paths for diffusion into (S) and out of (O,  $\text{H}_2\text{O}$ ) the IF particle.



Thus, for smooth layered nanoparticles containing a ‘dislocation free’ surface, it is expected that termination of the sulfidisation process occurs after formation of one or at most two  $\text{MS}_2$  layers. For those particles consisting of a faceted morphology, the extent of sulfidisation and therefore, number of  $\text{MS}_2$  layers is limited only by the annealing time and the availability (amount) of the sub-oxide core.

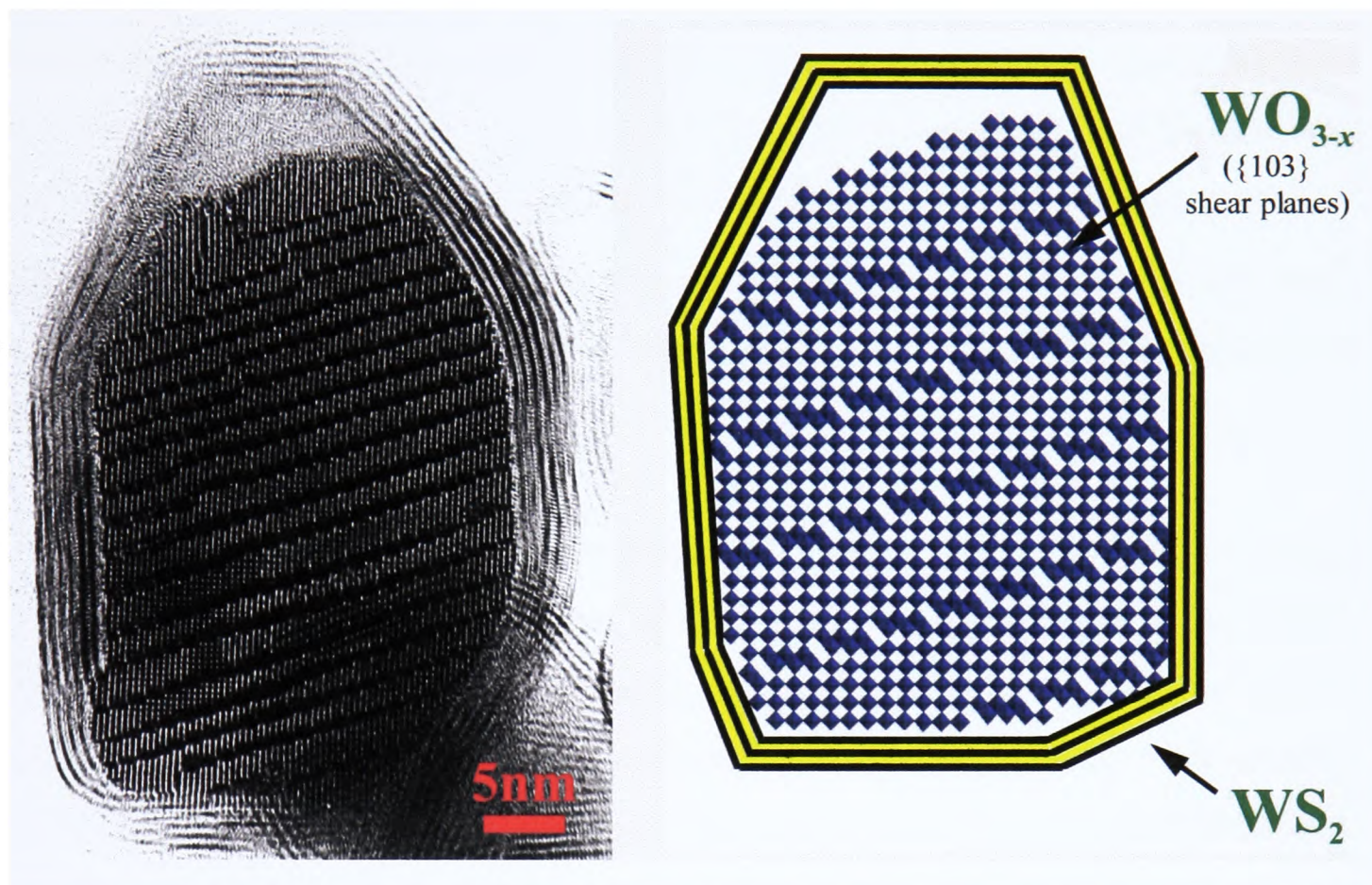


**Figure 4.9** Micrograph and schematic of a large  $\text{WO}_{3-x}$  encapsulate comprising a  $\text{ReO}_3$ -type  $\text{WO}_3$  sublattice containing a Wadsley-type defect encapsulated in multi-layer IF- $\text{WS}_2$  material.

The proposed mechanism is corroborated by experimental observations[8, 33] including the synthesis of the nanoparticle exhibited in **Figure 4.9**. It shows a micrograph of a sample of IF- $\text{WS}_2$  grown from a reduced  $\text{WO}_3$  substrate *via* reaction with  $\text{H}_2\text{S}$ . [33] The morphology of the encapsulated species has clearly been determined by the morphology of the reduced oxide precursor. In this case, the encapsulate is a quasi-spherical crystallite of  $\text{WO}_{3-x}$  and in addition to the curved IF- $\text{WS}_2$  ‘skin’, the presence of other defects and structural features is also observed. These are common in encapsulates formed by this method and closer inspection of the micrograph reveals the presence of a Wadsley-type defect which is simulated in the schematic.[3] This ‘crystallographic shear’ defect arises as a result of the corner-sharing  $\text{WO}_3$  octahedra network partially collapsing to form shear planes consisting now of edge-sharing  $\text{WO}_3$  octahedra. Collapse of the corner sharing network is a



result of the decrease of oxide sites in the lattice upon reduction from  $\text{WO}_3$  to  $\text{WO}_{3-x}$ .<sup>[39]</sup> Towards the top of **Figure 4.9** can be seen a void. This has resulted from partial consumption of the oxide.<sup>[33]</sup>

#### 4.6 Growth of IF-like Materials: Encapsulation of WC Within IF-Like Cages

As described above, transition metal dichalcogenide IF-like materials can be prepared from the metal oxides by a variety of routes. The encapsulation of IF-like  $\text{WS}_2$  material around nanoparticles of tungsten carbide (WC) has recently been reported by Sloan *et al.*<sup>[40]</sup> In this instance, the product incorporates a much denser and hard-wearing core-material than any of the precursors previously utilised in materials of this genre.

In these preparations, three samples of WC were utilised. A high surface area (high  $S_g$ ) precursor was prepared by reaction of  $\text{WO}_3$  with a mixture of  $\text{CH}_4/\text{H}_2$  at  $750^\circ\text{C}$ . Carburisation was confirmed by XRD analysis. Low  $S_g$  WC was purchased from a commercial supplier and finally, a second high  $S_g$  sample prepared by ‘ball milling’ the commercial WC for forty-eight hours. The particle size ranges were 200-2000 Å for both high  $S_g$  samples and 0.3 – 2.5  $\mu\text{m}$  for the low  $S_g$  material. As for the sulfidisation processes employed for  $\text{WO}_3$ , the conditions comprised passing a mixture of  $\text{N}_2/\text{H}_2$  gas and  $\text{H}_2\text{S}$  over the carbide at  $820^\circ\text{C}$ .

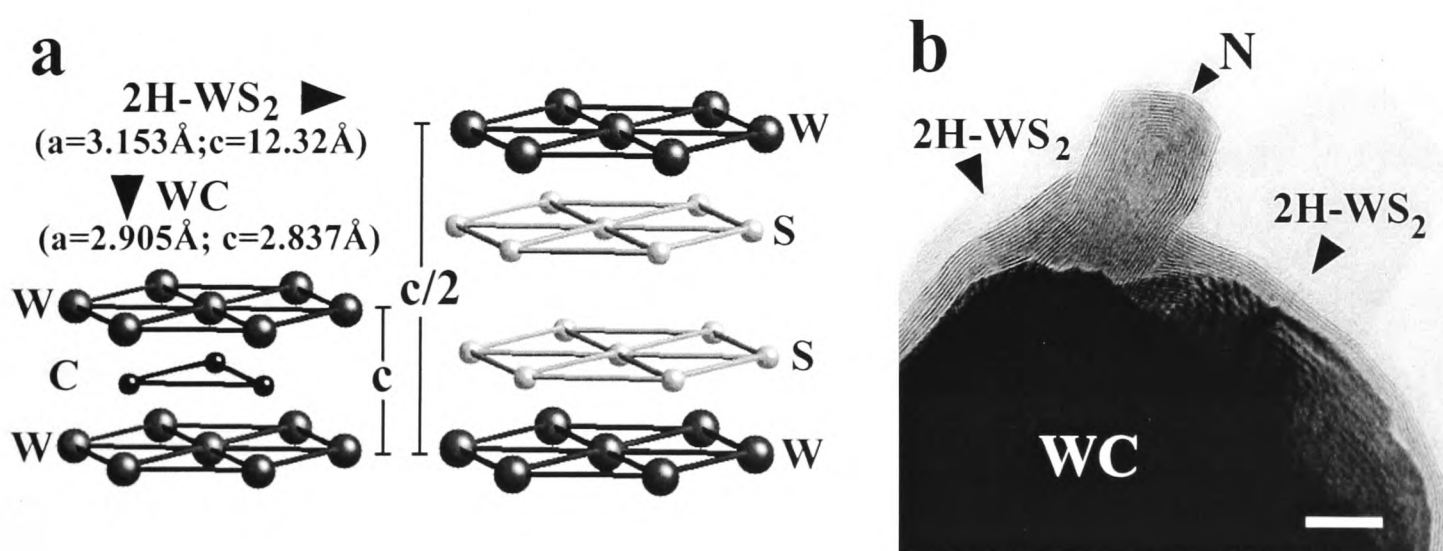


**Figure 4.10** (a) Schematic depiction of the WC hexagonal and 2H- $\text{WS}_2$  structures demonstrating the differences in the size of  $c$  versus stacking. (b) HTREM micrograph showing the 2H- $\text{WS}_2$  encapsulated particle resulting from sulfidisation of low surface area WC. A small defect on the carbide surface has resulted in the formation of a small nanotube (N) on the encapsulate. (Scale bar = 140 nm)

**Figure 4.10 (a)** shows the relationship between the crystallographic forms of the carbide precursor and IF-WS<sub>2</sub> product. In general, the low  $S_g$  WC precursors were totally encased by the IF-WS<sub>2</sub> layers, consisting of between two and twenty layers per encapsulate producing particles in the same size range as the precursor carbide. The micrograph in **Figure 4.10 (b)** shows one of these large encapsulates coated with a non-uniform 2H-WS<sub>2</sub> network, the morphology of which follows closely that of the WC precursor. Additionally, with the exception of the nanotube feature (N) it was found that irrespective of the length of sulfidisation process, the IF-WS<sub>2</sub> material showed no penetration beyond a depth of 100 Å.

The encapsulates formed from the high  $S_g$  precursors from carburised WO<sub>3</sub> tended to consist of almost completely converted IF-WS<sub>2</sub> structures. This was explained as a result of the residual oxygen content of the precursor, present as oxycarbide or as an oxidised layer on the surface of the carbide. **Figure 4.11 (a)** displays one such particle demonstrating complete conversion and an ellipsoidal IF-WS<sub>2</sub> structure. **Figure 4.11 (b)** shows a small carbide encapsulate formed from the ball-milled WC precursor encased in approximately ten layers of IF-WS<sub>2</sub> material. This illustrates the main difference between those IF materials grown from the carburised WO<sub>3</sub> material, and those prepared from commercially available WC.

The structures of the smaller encapsulates illustrated in **Figures 4.11 (a)** and **4.11 (b)** provide information about the growth mechanism of the encapsulating sulfide. The fast Fourier transform (FFT) in **Figure 4.11 (c)**, calculated for the boxed area in **Figure 4.11 (a)**, allows the reflections to be indexed according to the (01–10) projection of WC and superimposed upon this pattern is a blurred reflection which corresponds to the <002> planes of the IF-WS<sub>2</sub> material. **Figure 4.11 (d)** displays the microstructure of the carbide at the interface with the 2H-WS<sub>2</sub> sulfide and a small, disordered area of WC is visible (DS). A further enlargement in **Figure 4.11 (e)** demonstrates how two distorted layers of carbide intergrow with one layer of sulfide. The overall morphology of the precursor, however, plays a more important role in determining the final shape of the encapsulates.

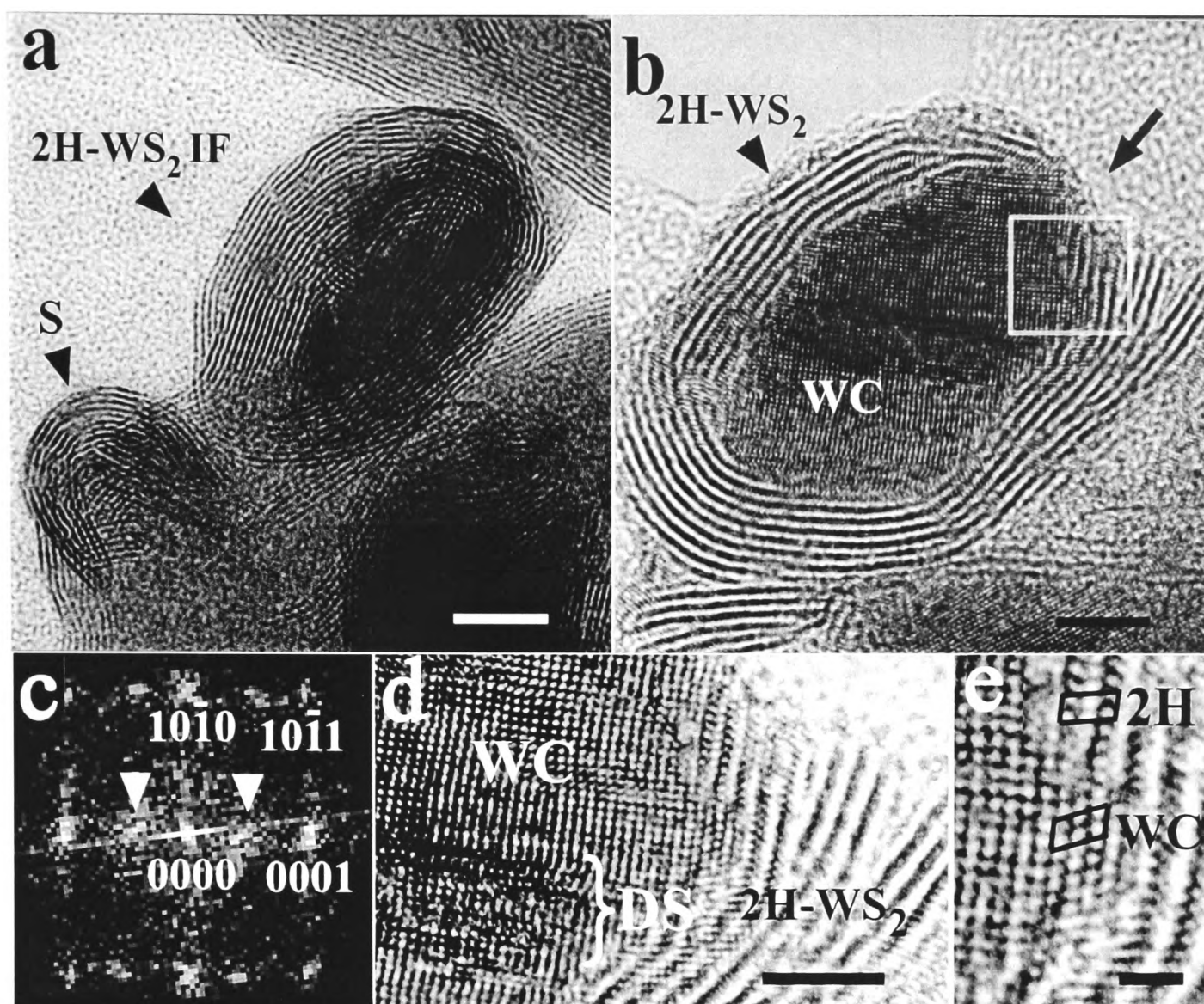


**Figure 4.11** (a) HRTEM micrograph of 2H-WS<sub>2</sub> IF nanoparticle grown from high S<sub>g</sub> precursors (scale bar = 75 Å) (b) IF-WS<sub>2</sub> nanoparticle formed from ball milled WC precursor (c) Calculated ED pattern from a FFT of the boxed region in Fig. 4.11(b) showing an interface between WC and IF-WS<sub>2</sub> phases. (d) HRTEM micrograph showing the interface and a distorted region (DS) in the WC microstructure (scale bar = 35 Å) (e) Enlargement of the WC/WS<sub>2</sub> interface showing intergrowth between one layer of sulfide (2H) and two layers of distorted carbide (WC) (scale bar = 10 Å)

The main consequence of encapsulation of WC inside IF-WS<sub>2</sub> shells with respect to the physical properties of the composite material is an enhancement of the structural rigidity or hardness, which may improve its properties in tribological applications (see **Section 4.8.1**). In addition, the conductive attributes afforded by inclusion of the more metallic carbide enhance this feature of the composite material.[40]

#### 4.7 Non-Oxide and Non-Carbide Based IF-Like Materials

The synthesis of cage structures of nickel(II) chlorides illustrates that the formation of nanoparticles (**Figure 4.12**) with layered and hollow cage structures is not confined either to the Group 6 metals, or to oxide and carbide species. The additional point of interest in this case is that because layered Ni atoms couple antiferromagnetically, the structures may demonstrate different magnetic behaviour depending on the parity of



the closed  $\text{NiCl}_2$  layers in the particulates. Those with an odd number of layers should behave as nanomagnets.[41]

$\text{NiCl}_2$  crystallises in the  $\bar{R}3m$  space group like other three-dimensional transition metal chloride complexes and in the IF-like morphology there are strong, mixed ionic-covalent bonds between the metal and halide moieties. The inter-layer adhesiveness is provided by weak van der Waals forces as in other IF- $\text{MX}_2$  materials.[41] Further investigations into other transition metal sulfide and chloride materials suggest that some systems may afford species suitable for ferromagnetic devices or even high temperature superconductors.[20]

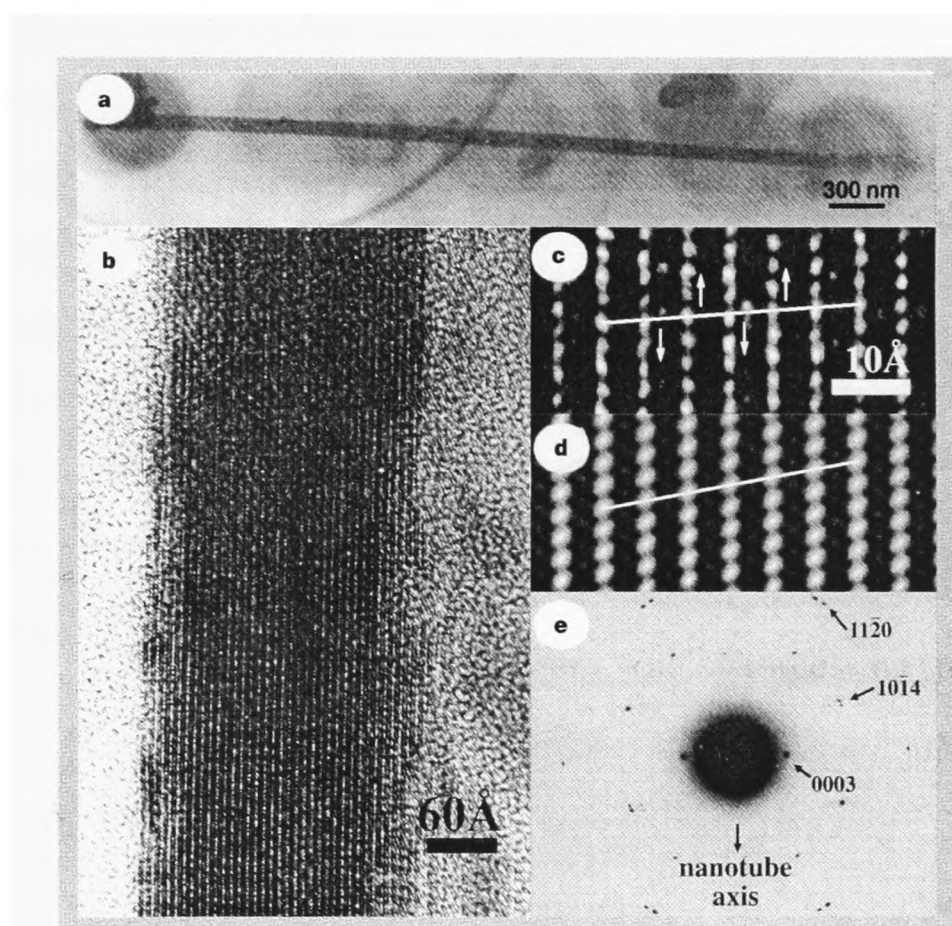


**Figure 4.12** Micrograph showing the IF-nature of layered  $\text{NiCl}_2$  (a) HRTEM image of the IF- $\text{NiCl}_2$  nanotube; (b) nanotube microstructure, demonstrating the layered character of the material; (c) higher magnification and (d) simulation of the layered structure; (e) electron diffraction pattern of the IF- $\text{NiCl}_2$  material.

## 4.8 Intercalation of IF-Like Structures

Intercalation compounds are formed by the insertion of atomic or molecular guest species between the layers of the host material. Examples of host lattices include graphite, transition metal dichalcogenides and metal oxides.[23]

IF-like materials containing intercalated alkali metals have also been prepared by sulfidisation of sodium-doped tungsten oxides. By dissolving  $10^{-2} - 10^{-3}$  M of alkali-metal salt - such as sodium chloride - in the water reservoir, the subsequent water vapour contained a proportion of sodium cations which then reacted with the heated tungsten wire to form alkali-metal doped oxides. These were then converted to the sulfides by a similar route to that described above. **Figure 4.13** shows an illustration of the apparatus used to prepare the intercalation compounds. The bell-jar is evaporated to approximately  $10^{-5}$  bar and the W-wire is then resistively heated close to its melting temperature for several minutes. After allowing the system to cool for a few minutes, a beaker of alkali-metal solution ( $10^{-2}$  M) is inserted into the bell jar and the chamber re-evacuated to  $10^{-3}$  bar at which point the water in the beaker freezes, the gate valve to the vacuum pump is closed and the W wire heated again. After several minutes, the wall of the bell-jar is coated with a blue oxide powder which can then be collected.[11]

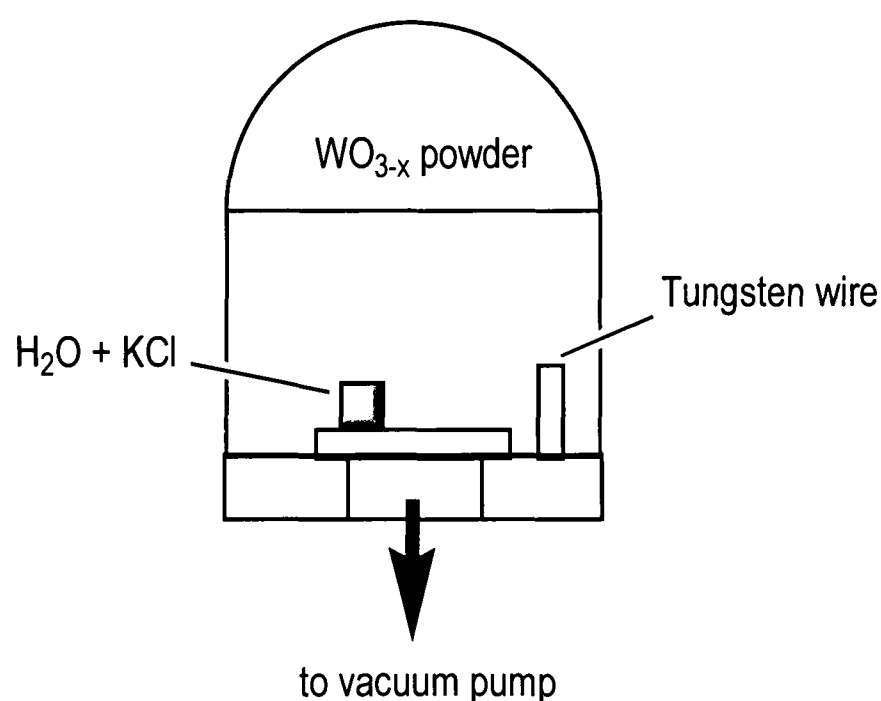


**Figure 4.13** Schematic representation of the evaporation apparatus utilised in the synthesis of oxide nanoparticles.



## 4.9 Applications of IF-Like Materials

### 4.9.1 Solid Lubricants

The most obvious physical parallel between graphite and layered 2H-MX<sub>2</sub> structures to speculate upon is the ability of the latter to act as lubricant. The need for solid lubricants arises from environmental reasons mainly because liquid lubricants cannot be recycled and because of the need to replace them after longer intervals. The suitability of 2H-MX<sub>2</sub> materials arises as a result of the sheets of hexagonally bonded metal atoms with weak vdW forces affording low adhesion between layers. Whereas C<sub>60</sub> has been experimentally proven to demonstrate poor lubrication properties, the same cannot be said of 2H-MX<sub>2</sub> materials, which are commonly used as a lubricant for work in vacuum and space technology as well as in automotive transport applications where a liquid lubricant would prove unsuitable.[42, 43]

The main advantage of IF-like nested particles in lubrication applications is their seamless structure, which inhibits the sticking and abrasiveness of the nanocluster by the surface of the metal pieces during work. It has been proposed that the absence of 'dangling bonds' from the IF-related material surface results in far poorer adhesion to the underlying substrate.[10] In addition, these spheroidal nanoparticles can also act as spacers, prohibiting contact between two metal surfaces where liquid lubricants would be squeezed out; under heavy loads for example (**Figure 4.14**). Evidence of the improved properties of IF-related MoS<sub>2</sub> over conventional 2H-MoS<sub>2</sub> materials has been demonstrated by substantially reduced wear and improved mechanical operation.[44] These IF-materials can in fact be thought of as 'nanoballbearings', rolling to reduce friction between two surfaces rather than sliding.

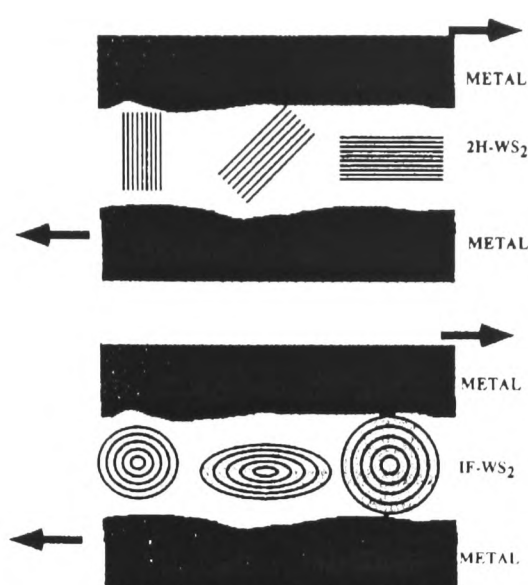


**Figure 4.14** Schematic Representation of the action of a solid lubricant between two metal surfaces

### 4.9.2 Photovoltaic Films

The formation of stable suspensions of intercalated IF-like materials allows deposition of thin films, which potentially have a wide range of applications including use as photosensitive elements in solar cells and also *via* fabrication into STM tips.<sup>[11]</sup> The preparation of these thin films involves essentially identical procedures to those for preparing intercalated IF-like materials described in **Section 4.7**. After preparation of the intercalated IF-material, IF-films are deposited on a gold substrate by electrophoretic deposition. Analysis of the thin films demonstrated that the intercalation of alkali atoms into the IF lattice induces n-type conductivity in the host.<sup>[11]</sup>

## 4.10 Structural Analysis of IF-Like Materials

In order to analyse and characterise this novel class of materials, there is number of criteria, which must be taken into consideration. Relevant aspects to consider include the chemical composition of the material and the compositional homogeneity. In addition, it is important to know the structure of the crystallite and finally identification of the species involved and analysis of defects and impurities. Using a combination of powder X-ray diffraction, electron microscopy and energy dispersion X-ray diffraction (EDX) these criteria can be satisfied. The techniques are described below.

### 4.10.1 Powder X-Ray Diffraction

X-Ray diffraction has been an important analytical technique since the beginning of the twentieth century for the identification and characterisation of solids. It is commonly used for routine characterisation and detailed structural elucidation, particularly phase identification and quantitative analysis of mixtures of materials.[39] X-Ray diffraction is a technique whereby the sample is exposed to monochromatic X-rays resulting in a diffraction pattern. From the angles of diffraction afforded, the  $d$ -spacing between the crystal planes in the sample can be calculated using the Bragg equation.[45]

$$n \lambda = 2 d_{hkl} \sin \theta \quad \text{(Equation 4.1)}$$

where  $n$  is the order of reflection,  $\lambda$  is the wavelength of the X-rays,  $d$  is the distance between crystal planes and  $\theta$  is the angle of reflection. Each crystal sample affords a characteristic diffraction pattern that can be identified using data reported in the literature.[46]

A Philips PW1710 diffractometer using  $\text{CuK}\alpha$  radiation and operating in the  $\theta - 2\theta$  mode was used for obtaining the diffraction data. This was interfaced with a microcomputer for manipulation of the collected data. Samples were ground to a fine powder using a pestle and mortar, mounted on an aluminium plate with a 1 mm groove cut into it and smoothed flat with a microscope slide.

Bragg's Law (equation 4.1) is only strictly valid for perfect crystals and perfectly monochromatic radiation. In practice, deviations from the ideal are observed which must be taken into account when considering real X-ray phenomena. In powder XRD, the sample consists of a large collection of very small crystals randomly orientated. The diffracted X-rays, instead of being single points, consist of a series of non-uniformly spaced cones, whose spacings are determined by the prominent planes of the crystallites. In powder X-ray diffraction the most important deviation from ideal behaviour occurs as a result the effect that particle size has on diffracted radiation. If crystals are very small, broadening of the diffracted beam occurs. That is, scattering at angles near to but not equal to the exact Bragg angles, occurs and a broadening in the diffracted beam results. The reason for this effect for thin crystals is interference by successive layers of atoms does not necessarily cause complete destructive interference when the Bragg angle is not observed. The extent to which this broadening occurs is given by the Scherrer formula (equation 4.2) in which  $t$  is the crystal thickness,  $\lambda$  the radiation wavelength,  $\theta_B$  the Bragg angle and  $B$  the width of the diffracted intensity measured at half the maximum intensity and expressed in terms of radians.[47]

$$t = \frac{0.9 \lambda}{B \cos \theta_B} \quad (\text{Equation 4.2})$$

It can be seen that as the crystal thickness decreases, the peak width increases.

#### **4.10.2 High Resolution Transmission Electron Microscopy (HRTEM)**

Currently, the two most important microscopy techniques used are scanning electron microscopy (SEM) and transmission electron microscopy (TEM). The difference between the two is that SEM provides images of the external morphology of a sample, while TEM provides information about the internal structure. The microscopes used in the studies in this thesis were high-resolution transmission electron microscopes (HRTEMs).[48]

HRTEM involves exposure of a sample to an electron beam, which is generated from a tungsten wire or lanthanum boride ( $\text{LaB}_6$ ) crystal electron gun - accelerated through

a potential difference and directed onto the sample by a series of electron lenses. [49] The whole system operates under high vacuum conditions generated by a series of diffusion and turbomolecular pumps. Electrons diffracted by the sample create a diffraction pattern, which can be transformed into an image using an array of lenses. The resultant pattern and/or image can then be projected onto a viewing screen.

JEOL 2000FX TEMSCAN, JEOL 4000X and JEOL 3000F microscopes were used for the studies in this thesis. With the microscope operating at the stated voltage, the relativistically corrected wavelength of the electron corresponds to 0.0251 Å for 200 kV electrons. Two of the microscopes are also fitted with a Link Pentafet detector incorporating LINK eXl or ISIS microanalysis systems for EDX analysis. This allowed for elemental analysis of samples from their characteristic X-rays to be undertaken. Hard copies of the images can be obtained by either of two methods. All of the microscopes incorporate a 50 plate camera allowing negatives to be obtained and developed. In addition, the 3000F microscope allows images to be obtained digitally using a 1 k x 1 k CCD (charge cooled device) and Gatan Digital Micrograph software. Utilising HRTEM at higher magnifications allows selection of single crystals for identification of phases through electron diffraction patterns. In addition, lattice images of the sample can be obtained.

Samples were ground to a fine powder and placed in a glass vial, then dispersed in AR grade ethanol or chloroform. The vial was then held in an ultra sonic bath for 2-3 minutes before several drops of the suspension were placed on a lacy carbon-coated, copper grid. The grid was placed in a specimen holder, and was inserted into the side-entry port of the microscope and then the whole system was evacuated. After the microscope was tuned, the sample could be analysed.

Like X-rays, electrons are diffracted by the net plane of a crystal lattice. For thin crystals ( $< 500$  Å) aligned with a specific  $hkl$  plane at an angle ( $\theta$ ) to the axis of the electron beam, mutually coherent scattered beams will interfere constructively when the Bragg conditions (4.1) are met. When short wavelengths are used as the diffracting medium, the Bragg angle  $\theta$  is very small and so  $\sin \theta \approx \theta$ . Therefore, when  $n = 1$  the Bragg condition simplifies to

$$d_{hkl} \sin \theta = \lambda \quad (\text{Equation 4.3})$$

In the electron microscope, the film is placed at a distance,  $L$ , corresponding to the camera length with respect to the crystal (**Figure 4.15**). If  $O$  is the centre spot and  $H$  is the diffraction spot then  $r$ , the distance between  $O$  and  $H$  can be expressed by

$$r = L \tan 2\theta \quad (\text{Equation 4.4})$$

Combining 4.3 and 4.4 gives

$$r d_{hkl} = L \lambda \quad (\text{Equation 4.5})$$

If  $r$  can be determined and  $L$  and  $\lambda$  are known, then  $d_{hkl}$  can be calculated.[48]

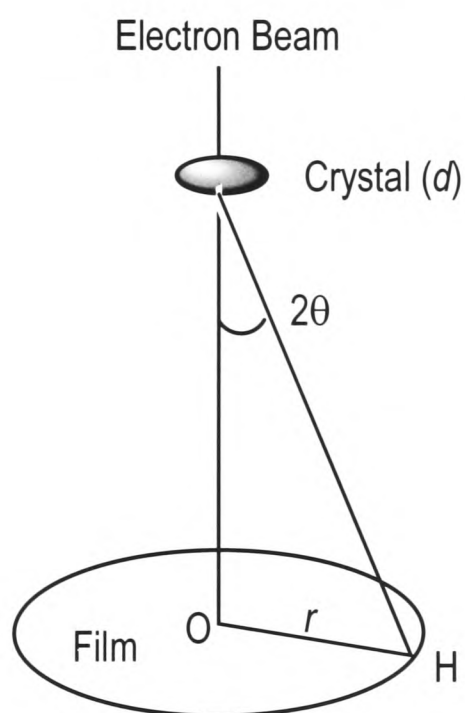


**Figure 4.15** Illustration of the arrangement of the film, crystal sample and electron beam as described in equation 4.5.

## 4.11 Summary

This chapter has provided a brief review of the recent studies in the field of inorganic fullerenes. The relationship between carbon and non-carbon fullerene types has been explored along with current theories about the growth mechanism, methods of preparation and examples of novel structures.

The relationship between the oxide precursors and the product encapsulates, in terms of the microstructures and morphologies has been demonstrated by some of the examples described. As a result of the wide variety of applications for both the encapsulated oxides and the encapsulating chalcogenides, these novel materials are potentially of great significance to materials science.

The remainder of this part of the thesis explores new avenues in the synthesis of IF-like materials through utilising existing available precursors (**Chapter 5**) and also *via* the synthesis of transition metal oxide precursors by an alternative method and their subsequent sulfidisation (**Chapter 6**).

**4.12 References for Chapter 4**

- [1] H. W. Kroto, J. R. Heath, S. C. O'Brien, R. F. Curl and R. E. Smalley, *Nature*, **318** (1985) 162.
- [2] S. Iijima, *Nature*, **354** (1991) 56.
- [3] J. Sloan, J. Cook, M. L. H. Green, J. L. Hutchison and R. Tenne, *J. Mater. Chem.*, **7** (1997) 1089.
- [4] S. C. Tsang, Y. K. Chen, P. J. F. Harris and M. L. H. Green, *Nature*, **372** (1994) 159.
- [5] S. C. Tsang, J. J. Davis, M. L. H. Green, H. A. O. Hill, Y. C. Leung and P. J. Sadler, *J. Chem. Soc., Chem. Commun.*, (1995) 2579.
- [6] R. Tenne, L. Margulis, M. Genut and G. Hodes, *Nature*, **360** (1992) 444.
- [7] R. Tenne, H. M. and Y. Feldman, *Chem. Mater.*, **10** (1998) 3225.
- [8] M. Homyonfer, *Ph.D. Thesis*, Weizmann Institute, Rehovot, Israel, (1998).
- [9] Y. Golan, C. Drummond, M. Homyonfer, Y. Feldman, R. Tenne and J. Israelachivili, *Adv. Mater.*, **11** (1999) 934.
- [10] L. Rapoport, Y. Feldman, M. Homyonfer, H. Cohen, J. Sloan, J. L. Hutchison and R. Tenne, *Wear*, **225-229** (1999) 975.
- [11] M. Homyonfer, B. Alperson, Y. Rosenberg, L. Sapir, S. R. Cohen, G. Hodes and R. Tenne, *J. Am. Chem. Soc.*, **119** (1997) 2693.
- [12] E. Furimsky and C. H. Amberg, *Can. J. Chem.*, **53** (1975) 3567.
- [13] D. Ugarte, *Nature*, **359** (1992) 707.
- [14] H. W. Kroto, *Nature*, **329** (1987) 529.
- [15] W. Kratschmer, L. D. Lamb, K. Fostiropoulos and D. R. Huffman, *Nature*, **347** (1990) 354.
- [16] D. Ugarte, *Europhys. Let.*, **22** (1993) 45.
- [17] A. Maiti, C. J. Brabec and J. Bernholc, *Phys. Rev. Let.*, **70** (1993) 3023.
- [18] S. Iijima, T. Ichihashi and Y. Ando, *Nature*, **356** (1992) 776.
- [19] M. Schluter, M. Lannoo, M. Needels, G. A. Baraff and D. Tomanek, in H. W. Kroto, J. E. Fischer and D. E. Cox (Eds.): *The Fullerenes*, Pergamon Press Ltd., Oxford 1993, p. 303.
- [20] A. P. E. York, *Chemistry in Britain*, **36** (2000) 40.
- [21] J. P. Lu and W. Yang, *Phys. Rev.*, **49B** (1994) 11421.
- [22] L. Margulis, G. Salitra and R. Tenne, *Nature*, **365** (1993) 113.



- 
- [23] U. Müller, *Inorganic Structural Chemistry*, Wiley, Stuttgart 1991.
- [24] W. Tremel, *Angew. Chem. Int. Ed. Engl.*, **38** (1999) 2175.
- [25] D. J. Srolovitz, S. A. Safran, M. Homyonfer and R. Tenne, *Phys. Rev. Lett.*, **74** (1995) 1779.
- [26] N. N. Greenwood and A. Earnshaw, *Chemistry of the Elements*, Pergamon Press, Oxford 1990.
- [27] O. Stephan, P. M. Ajayan, C. Colliex, P. Redlich, J. M. Lambert, P. Bernier and P. Lefin, *Science*, **266** (1994) 1683.
- [28] T. F. Bates, L. B. Sand and J. F. Mink, *Science*, **111** (1950) 512.
- [29] R. Tenne, L. Margulis and G. Hodes, *Adv. Mater.*, **5** (1993) 386.
- [30] Y. Feldman, E. Wasserman, D. J. Srolovitz and R. Tenne, *Science*, **267** (1995) 222.
- [31] Y. Feldman, G. L. Frey, M. Homofonyer, V. Lyakhovitskaya, L. Marguilis, H. Cohen, G. Hodes, J. L. Hutchison and R. Tenne, *J. Am. Chem. Soc.*, **118** (1996) 5362.
- [32] R. Tenne, *Adv. Mater.*, **7** (1995) 965.
- [33] J. Sloan, J. L. Hutchison, R. Tenne, Y. Feldman, T. Tsirlina and M. Homyonfer, *J. Solid State Chem.*, **144** (1999) 100.
- [34] M. Hershfinkel, L. H. Gheber, V. Volterra, J. L. Hutchison, L. Marguilis and R. Tenne, *J. Am. Chem. Soc.*, **116** (1994) 1914.
- [35] M. S. Donley, N. T. McDevitt, T. W. Hass, P. T. Murray and J. T. Grant, *Thin Solid Films*, **168** (1989) 335.
- [36] M. Homyonfer, Y. Mastai, M. Hershfinkel, V. Volterra, J. L. Hutchison and R. Tenne, *J. Am. Chem. Soc.*, **118** (1996) 7804.
- [37] T. Tsirlina, Y. Feldman, M. Homyonfer, J. Sloan, J. L. Hutchison and R. Tenne, *Fullerene Sci. Technol.*, **6** (1998) 157.
- [38] M. Genut, L. Marguilis, G. Hodes and R. Tenne, *Thin Solid Films*, **217** (1992) 91.
- [39] C. N. R. Rao and B. Raveau, *Transition Metal Oxides*, VCH Publishers, Cambridge 1995.
- [40] A. Rothschild, J. Sloan, A. P. E. York, M. L. H. Green, J. L. Hutchison and R. Tenne, *J. Chem. Soc., Chem. Commun.*, (1999) 363.
- [41] Y. Rosenfeld Hacoheh, E. Grunbaum, R. Tenne, J. Sloan and J. L. Hutchison, *Nature*, **395** (1998) 336.

- [42] I. L. Singer, in I. L. Singer and H. M. Pollock (Eds.): *Fundamentals of Friction: Macroscopic and Microscopic Processes*, Kluwer, Dordrecht 1992, p. 237.
- [43] J. S. Zabinski, M. S. Donley, V. J. Dryhouse and N. T. McDevitt, *Thin Solid Films*, 214 (1992) 156.
- [44] L. Rapoport, Y. Bilik, Y. Feldman, M. Homiyonfer, S. R. Cohen and R. Tenne, *Nature*, 387 (1997) 791.
- [45] W. L. Bragg, *Proc. Roy. Soc.*, 89A (1913) 248.
- [46] Inorganic Crystal Structure Database, International Centre for Diffraction Data 1982.
- [47] H. P. Klug and L. E. Alexander, *X-Ray Procedures for Polycrystalline and Amorphous Materials*, Wiley Scientific, New York 1974.
- [48] J. B. Claridge, *D. Phil. Thesis*, University of Oxford, 1996.
- [49] P. J. Goodhew and F. J. Humphreys, *Electron Microscopy and Analysis*, Taylor and Francis, London 1988.

## **Chapter 5**

### **Synthesis of IF-Like Materials (I)**

## 5.0 Introduction to Chapter 5

In **Chapter 4**, the methods of preparation of IF-like materials from precursor oxides, carbides and sulfides were described. Generally, the simplest route involves sulfidisation of either a transition metal oxide such as  $\text{WO}_3$  or carbide (WC).[1-10] In this chapter, a number of novel precursors are sulfidised and shown to afford IF-type structures as a result. The materials have been chosen on the basis of their suitability for forming IF-nanostructures and include molybdenum carbide (MoC) and two mixed-metal binary oxides  $\text{Nb}_4\text{W}_{13}\text{O}_{47}$  and  $\text{Nb}_8\text{W}_9\text{O}_{47}$ . Finally, a study of the epitaxial growth of  $\text{WO}_3$  from a WC substrate and the sulfidised products is detailed. The work described in this chapter was undertaken under the supervision of Dr. Jeremy Sloan who performed all the HRTEM studies described below.

### 5.1 Synthesis of IF-Molybdenum Sulfide (IF-MoS<sub>2</sub>) from Molybdenum Carbide (MoC)

Tungsten carbide (WC) has been shown to lend itself to the formation of IF-WS<sub>2</sub> when reacted with  $\text{H}_2\text{S}$  under the correct conditions (**Section 4.4**).[6, 11] Given that it has a similar crystal structure to its W analogue (molybdenum carbide crystallises in the  $\text{P6}_3/\text{mmm}$  space group with hexagonal symmetry), MoC was considered to be a feasible starting material from which to synthesise IF-MoS<sub>2</sub>. The stable polytype of MoS<sub>2</sub> (WS<sub>2</sub>) is **2H**, i.e. hexagonal packing of layers in the sequence AbA BaB.[12, 13] The other known polytype is **3R** in which the unit cell contains three layers as a repeat unit in a unit cell with rhombohedral symmetry.

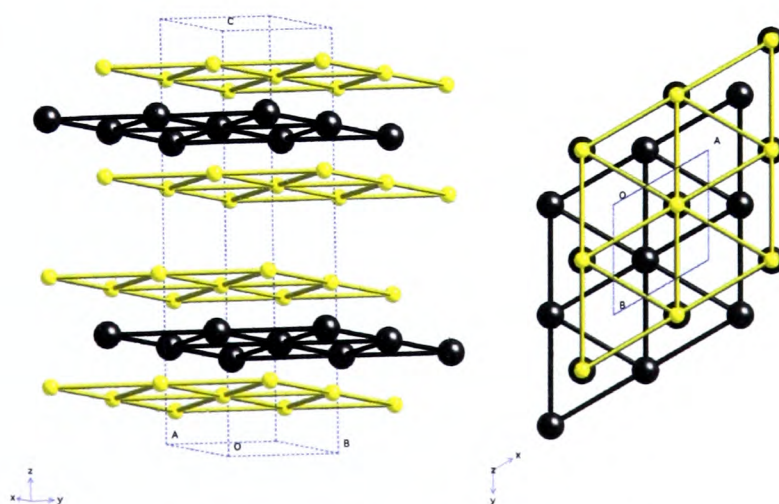


**Figure 5.1** Schematic of the layered structure of MoS<sub>2</sub> demonstrating the 2H-stacking and the hexagonal arrangement within the Mo and S layers. The Mo-S bonds are covalent and tetrahedral with weak van der Waals interactions holding the adjacent sulfur sheets together. Note that the molybdenum layers are staggered and the MoS<sub>2</sub> layers are stacked in an AbA BaB arrangement.

### 5.1.1 Sulfidisation of MoC

The experimental conditions employed for this synthesis are based on those described for the synthesis of IF-WS<sub>2</sub> from a WC precursor.[6] A porcelain crucible containing a sample of commercially available MoC (Aldrich Chemical Co., 99.95 %) was placed in a silica glass tube, which was inserted into a tube furnace as illustrated in **Figure 5.1**. The tube was purged with N<sub>2</sub> and heated up to 650°C at which temperature N<sub>2</sub> was replaced by H<sub>2</sub>S flowing at a rate of 15 ml min<sup>-1</sup> for 20 minutes. After this time, the N<sub>2</sub> supply was reconnected and the sample allowed to cool.

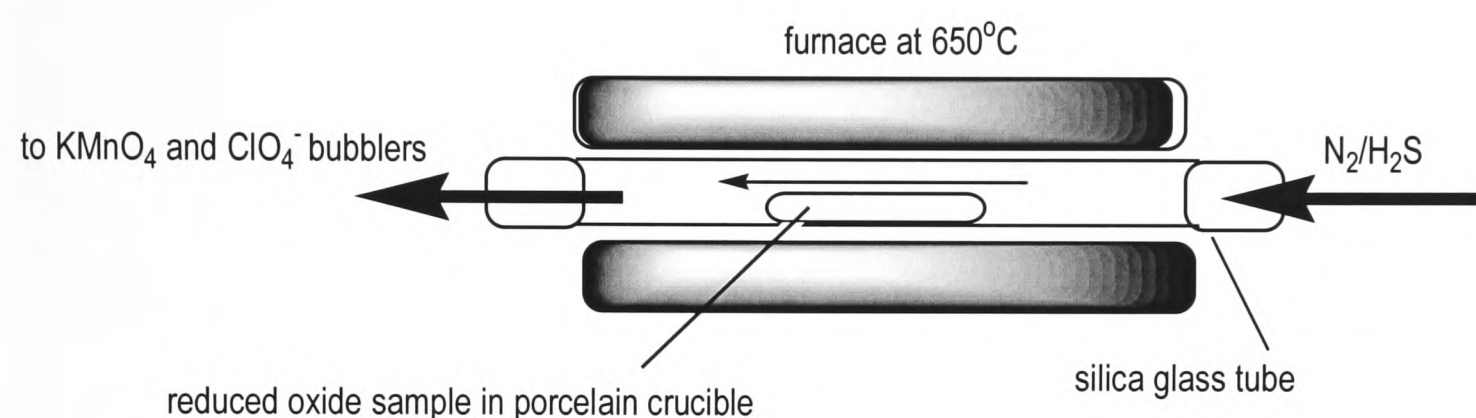


**Figure 5.1** Apparatus used to sulfidise the molybdenum carbide sample

### 5.1.2 Characterisation of Sulfidised Product

Upon sulfidisation, the brown-black molybdenum carbide changed to a blue-black microcrystalline material. Powder X-ray diffraction studies revealed a spectrum identical to that reported for IF-MoS<sub>2</sub> with a hexagonal symmetry and in the P6<sub>3</sub>/mmm space group, displaying a strong signal at  $2\theta = 15^\circ$  which is characteristic of the (002) reflection in layered MX<sub>2</sub>-type structures.



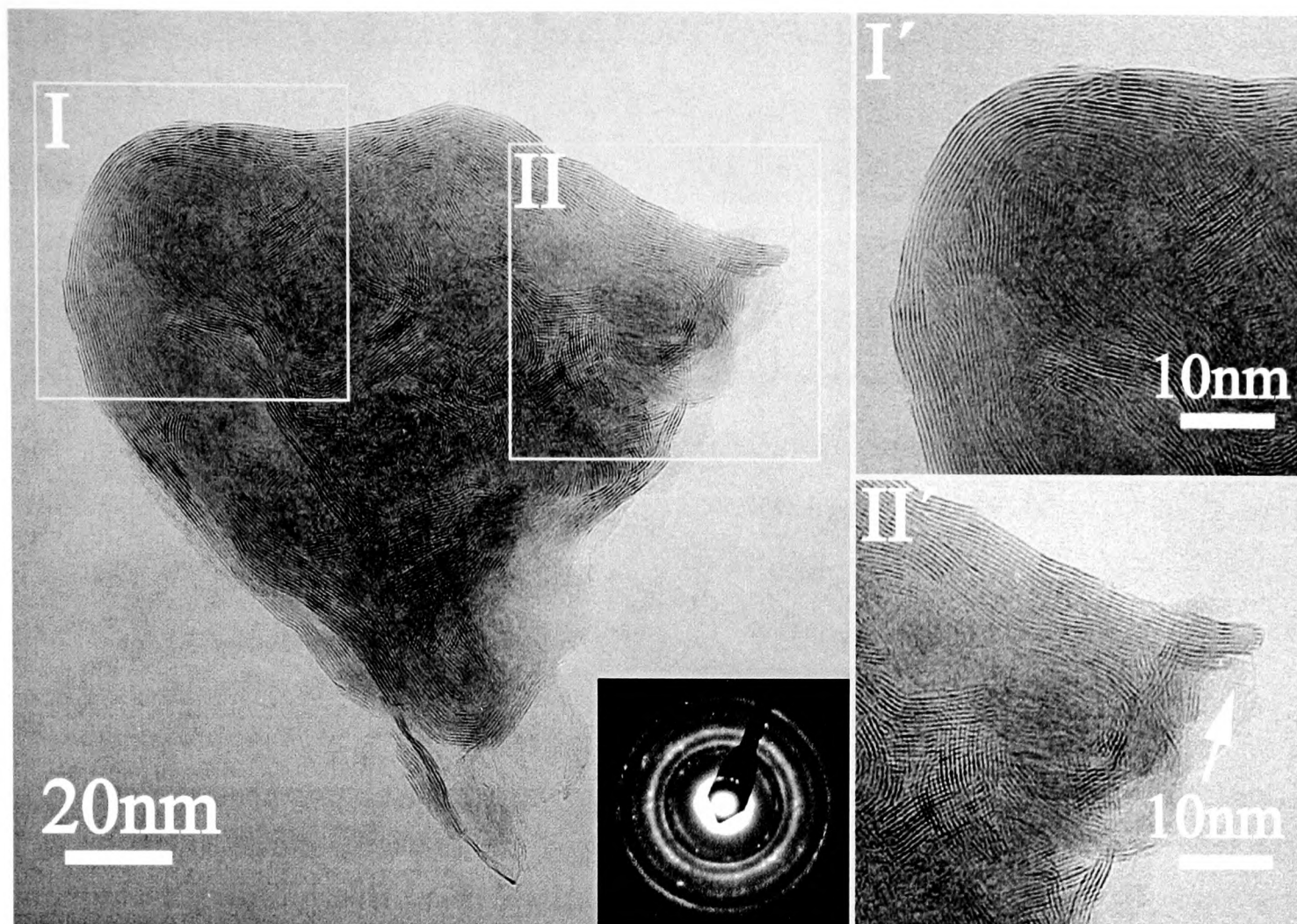


**Figure 5.3** Micrograph exhibiting IF-MoS<sub>2</sub> particles synthesised from Mo<sub>2</sub>C and H<sub>2</sub>S. The insets I' and II' show examples of curvature and discontinuous growth respectively. The SAED pattern (inset) shows a typical ring-pattern attributable to MoS<sub>2</sub>. A ring pattern rather than a spot pattern is observed because the MoS<sub>2</sub> layers are in multiple orientations.

The micrographs in **Figure 5.3** illustrate a nanoparticle typical of those found in the product sample. Particles tend to exhibit spheroidal morphologies with diameters ranging between 80 and 150 nm. The main picture shows an irregularly shaped IF-MoS<sub>2</sub> nanoparticle and the inset contains the electron diffraction pattern obtained from the same species. The ring pattern is typical of IF-MoS<sub>2</sub> with the rings demonstrating multiple orientations of the molybdenum sulfide structure.<sup>[14]</sup> The images show that the material has been completely sulfidised with multiply orientated, layered MoS<sub>2</sub> throughout the sample. The insets I and II show higher magnification images of two regions, which display features of particular interest. The inset I' illustrates curvature of the MoS<sub>2</sub> layers typically exhibited by IF-like materials. Several different growth fronts are also visible which have suddenly ceased at points where the parent metal carbide supply was exhausted. The second inset II' reveals examples of discontinuous growth at the edge of the IF-particle where instead of curving around the corner of the particle, the growth front abruptly halts. This may provide an insight into the growth mechanism of the molybdenum sulfide.

The sulfidisation mechanism of  $\text{MoO}_3$  and WC is considered to proceed *via* fast formation of one or two layers on the surface of the starting material, followed by a diffusion controlled process of oxide or carbide consumption *via* a number of growth fronts.[7, 8, 14] For the molybdenum carbide in this example however, the process occurs very rapidly. In order to attempt isolation of partially sulfidised MoC, the sulfidisation process was repeated with the time reduced to five minutes. It was observed that even after five minutes, complete conversion had occurred. This increased reactivity of the molybdenum carbide over tungsten carbide is also evidenced by the number of different orientations of layered- $\text{MoS}_2$  within the particle, contrasting with the more ordered circular growth pattern observed in IF- $\text{WS}_2$  encapsulated carbides.[6]

An EDX scan was obtained from the same specimen from which the HRTEM micrographs were taken. The spectrum clearly shows signals attributable to X-ray emissions from Mo and S only, with no evidence to suggest any remaining unreacted molybdenum carbide.

## 5.2 Mixed-Metal Binary Oxide Systems, $\text{Nb}_4\text{W}_{13}\text{O}_{47}$ and $\text{Nb}_8\text{W}_9\text{O}_{47}$

This section of the chapter concerns the reactions between  $\text{H}_2\text{S}$  and two mixed-metal binary tungsten-niobium oxides of the compositions  $\text{Nb}_4\text{W}_{13}\text{O}_{47}$  and  $\text{Nb}_8\text{W}_9\text{O}_{47}$  supplied by Prof. F. Krumeich of the Laboratory of Inorganic Chemistry, ETH Zürich, Switzerland.

### 5.2.1 Tetragonal Tungsten Bronzes (TTBs): $\text{Nb}_4\text{W}_{13}\text{O}_{47}$ and $\text{Nb}_8\text{W}_9\text{O}_{47}$

The compounds  $\text{Nb}_4\text{W}_{13}\text{O}_{47}$  and  $\text{Nb}_8\text{W}_9\text{O}_{47}$  are members of a group of compounds known as tetragonal tungsten bronzes (TTBs). They result from a modification of the  $\text{WO}_3$  ( $\text{ReO}_3$ -type) corner sharing octahedra structure shown in **Figure 5.4**. The tetragonal tungsten bronze type represents another  $\text{ReO}_3$ -related structure in which tunnels of different shapes occur inside a framework of corner-sharing  $\text{MO}_6$  octahedra.

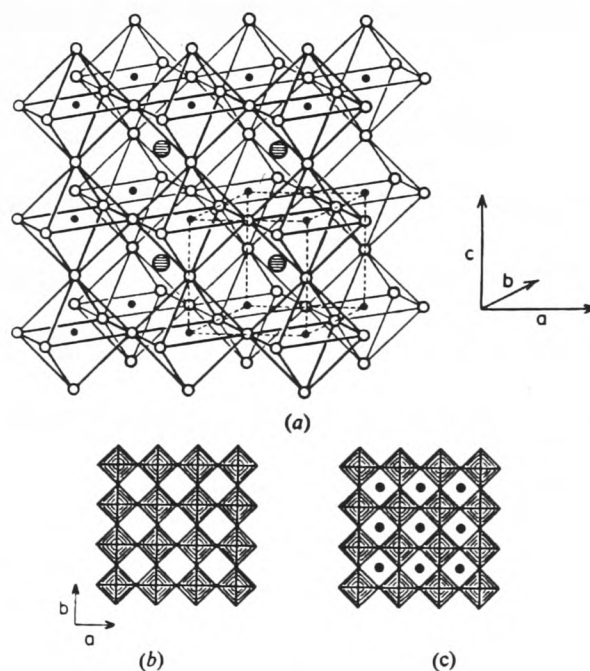


**Figure 5.4** the  $\text{ReO}_3$  (a) and (b) and perovskite (c) open structure types. (a) The filled circles are the Re-type atoms; open circles are anions (O); hatched circles, cation sites, unoccupied in  $\text{ReO}_3$ , occupied in perovskites. The dashed lines indicate one unit cell. In (b) and (c) the two structure types are represented as  $\text{MO}_6$  octahedra and projected along the (001) axis. [15]

In **Figure 5.5**, the skeleton structure of TTB and its unit cell are illustrated. The sequence is built up from corner sharing  $\text{MO}_6$  octahedra arranged such that there are three-, four-, and five-sided ‘channels’ which can accommodate small cations. The structural building unit formed from this arrangement is a pentagonal bipyramid, which shares edges with five corner-sharing octahedra. The reduction in the overall oxygen:metal ratio required by the composition  $x\text{Nb}_2\text{O}_5 \cdot y\text{WO}_3$  is achieved by edge sharing of some octahedra and by filling of a fraction of the pentagonal columns (PCs) with  $-\text{M}-\text{O}-\text{M}-\text{O}-$  strings ( $\text{M} = \text{W}$  or  $\text{Nb}$ ) in the tunnel structures.



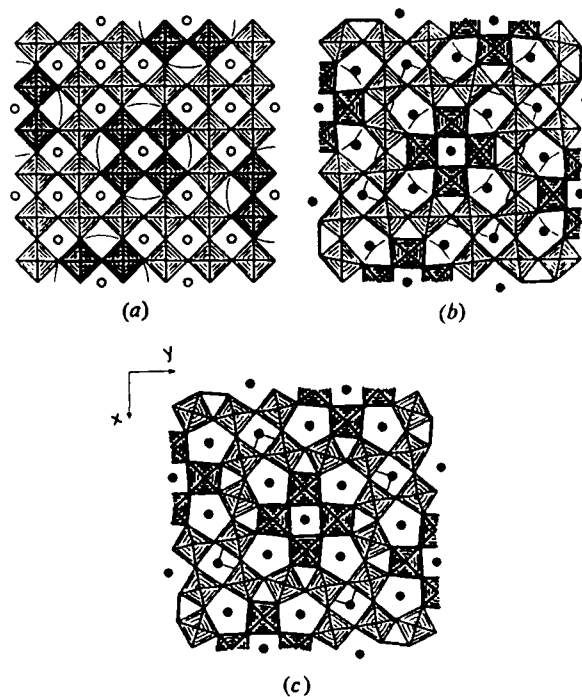


**Figure 5.5** Formation of the pentagonal column (PC) TTB structure from the  $\text{MO}_6(\text{ReO}_3)$ -type framework viewed along the (001) projection. The groups to be rotated are outlined and the progression (a)-(b)-(c) demonstrates how rotation of the  $\text{MO}_6$  octahedra results in the formation of pentagonal columns. [15]

It is known that over the compositional range of the  $\text{Nb}_2\text{O}_5$ - $\text{WO}_3$  system, crystal structures of compounds consist of sub-cells of the tetragonal tungsten bronze (TTB) type. The TTB arrangement consists of corner sharing  $\text{MO}_6$  octahedra arranged to form TTB sub-cells where M is a cation: in this case W and Nb. The unit cell comprises three TTB sub-cells (**Figure 5.6**). Four of the resulting twelve pentagonal columns (PCs) per unit cell are occupied by  $-\text{M}-\text{O}-\text{M}-\text{O}-\text{M}-$  strings which run parallel to the  $c$  axis (**Figure 5.7**). [16]

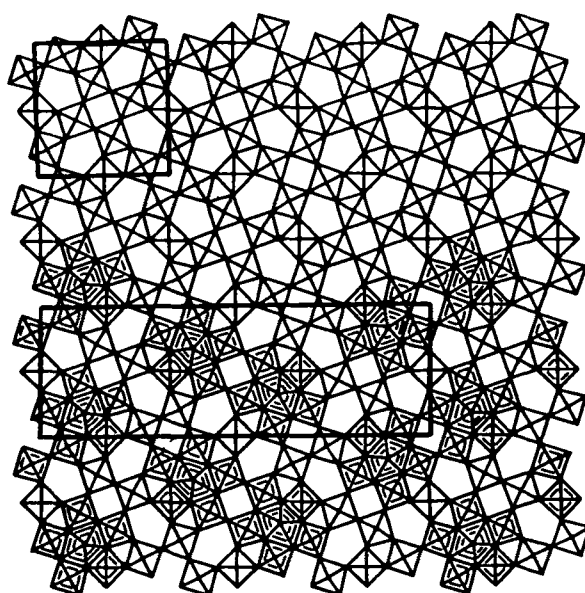


**Figure 5.6** Figure of the basic TTB framework as found in mixed-metal binary oxides such as  $\text{Nb}_8\text{W}_9\text{O}_{47}$  and  $\text{Nb}_4\text{W}_{13}\text{O}_{47}$ . The unit cell is made up from three TTB sub-cells. The projection is along the (001) axis.[17]

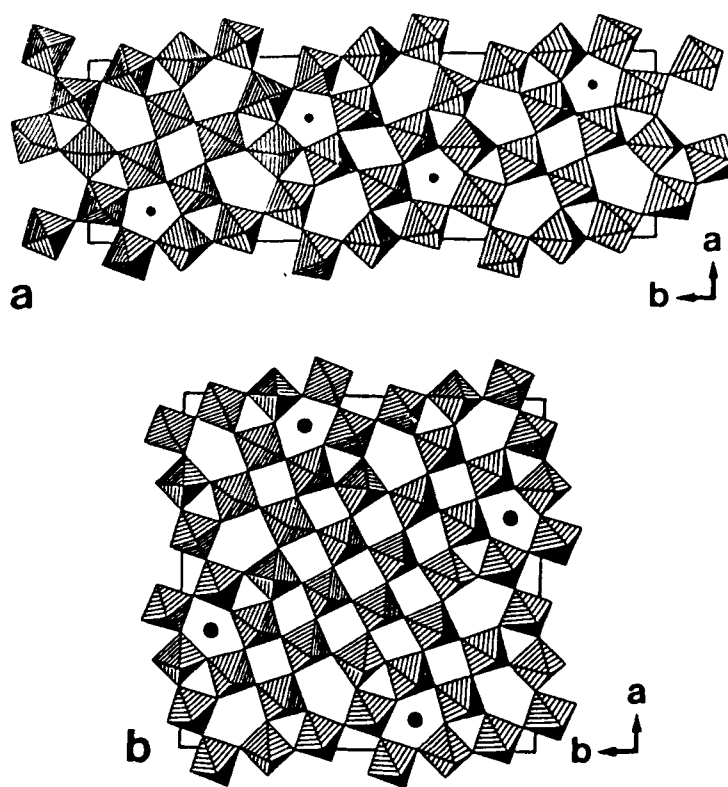


**Figure 5.7** Structural models of the 4:9 and the 2:7 phases of Nb/W TTB structure viewed along the (001) projection; (a) demonstrates how 4 out of the 12 pentagonal columns (PCs) are filled with -M-O-M-O-strings in structures such as  $\text{Nb}_8\text{W}_9\text{O}_{47}$  while (b) for an alternative phase the unit cell is comprised differently. [18]

The mixed-metal binary oxide  $\text{Nb}_8\text{W}_9\text{O}_{47}$  is prepared from the compounds  $\text{Nb}_2\text{O}_5$  and  $\text{WO}_3$  in the molar ratio of 4:9. The powder mixture is heated to  $900^\circ\text{C}$  for 100 h in air and is then ground in an agate mortar and closely packed in sealed platinum capsules. The capsules are heated at  $1300^\circ\text{C}$  and quenched in iced water after heating for 45 h. The oxide  $\text{Nb}_4\text{W}_{13}\text{O}_{47}$  was prepared in an analogous fashion.[16]

### 5.2.2 Effects of Sulfidisation on the Mixed-Metal Binary Oxide Systems $\text{Nb}_4\text{W}_{13}\text{O}_{47}$ and $\text{Nb}_8\text{W}_9\text{O}_{47}$

The mixed-metal binary oxides  $\text{Nb}_4\text{W}_{13}\text{O}_{47}$  and  $\text{Nb}_8\text{W}_9\text{O}_{47}$  were sulfidised in a similar fashion to the molybdenum carbide, as described in **Section 5.2**. Prior to sulfidisation, however, the oxides were ground in an agate mortar in order to shear the crystals in the *ab*-plane as shown in **Figure 5.8** below. This was to ensure that the surface containing the pentagonal columns (PCs) was available for reaction with the  $\text{H}_2\text{S}$  reagent. Of interest was the potential for sulfidisation to progress *via* growth along the columns into the inner structure of the TTB material, and from there into the layered structure. Thus, the prepared oxides were sulfidised in analogous apparatus to that shown in **Figure 5.1** at  $750^\circ\text{C}$  for 30 minutes with a flow rate of  $30 \text{ ml min}^{-1}$ .

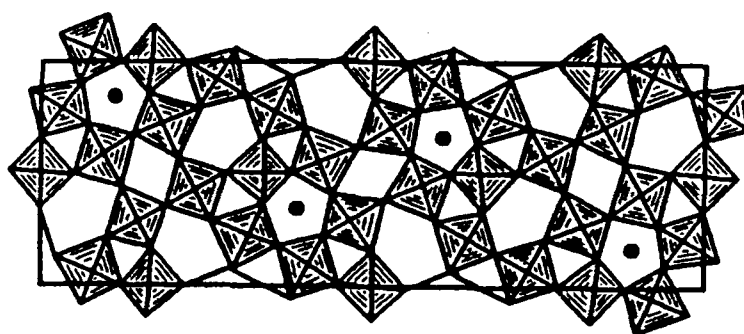


**Figure 5.8** Projection of the unit cell structure of  $\text{Nb}_8\text{W}_9\text{O}_{47}$  along the (001) axis.<sup>[19]</sup> The pentagonal tunnels marked with a black dot are those occupied by the -M-O-M-O-M- strings while the others remain as empty channels. This is the surface made available by grinding of the crystals in an agate mortar.

The sulfidised products were isolated as finely divided dark-grey, microcrystalline powders. Analysis by HRTEM demonstrates some novel and interesting results arising from the sulfidisation process. The particle sizes varied between 800 and 1500 nm in diameter and a typical example is shown below in **Figure 5.9**. This particulate is synthesised from sulfidisation of the  $\text{Nb}_4\text{W}_{13}\text{O}_{47}$  binary oxide but is also representative of products formed from  $\text{Nb}_8\text{W}_9\text{O}_{47}$ . The material consists of a mixture of unreacted oxide (TTB Region) and areas clearly demonstrating a layered  $(\text{W}, \text{Nb})\text{S}_2$  morphology around the edges of the particle. These observations are consistent with the IF- $\text{MX}_2$  growth mechanisms described in **Chapter 4**. The sulfidisation process in this instance has probably occurred in a similar manner *via* fast, initial sulfidisation of the binary oxide surface, followed by progressive consumption of the oxide on a number of growth fronts.

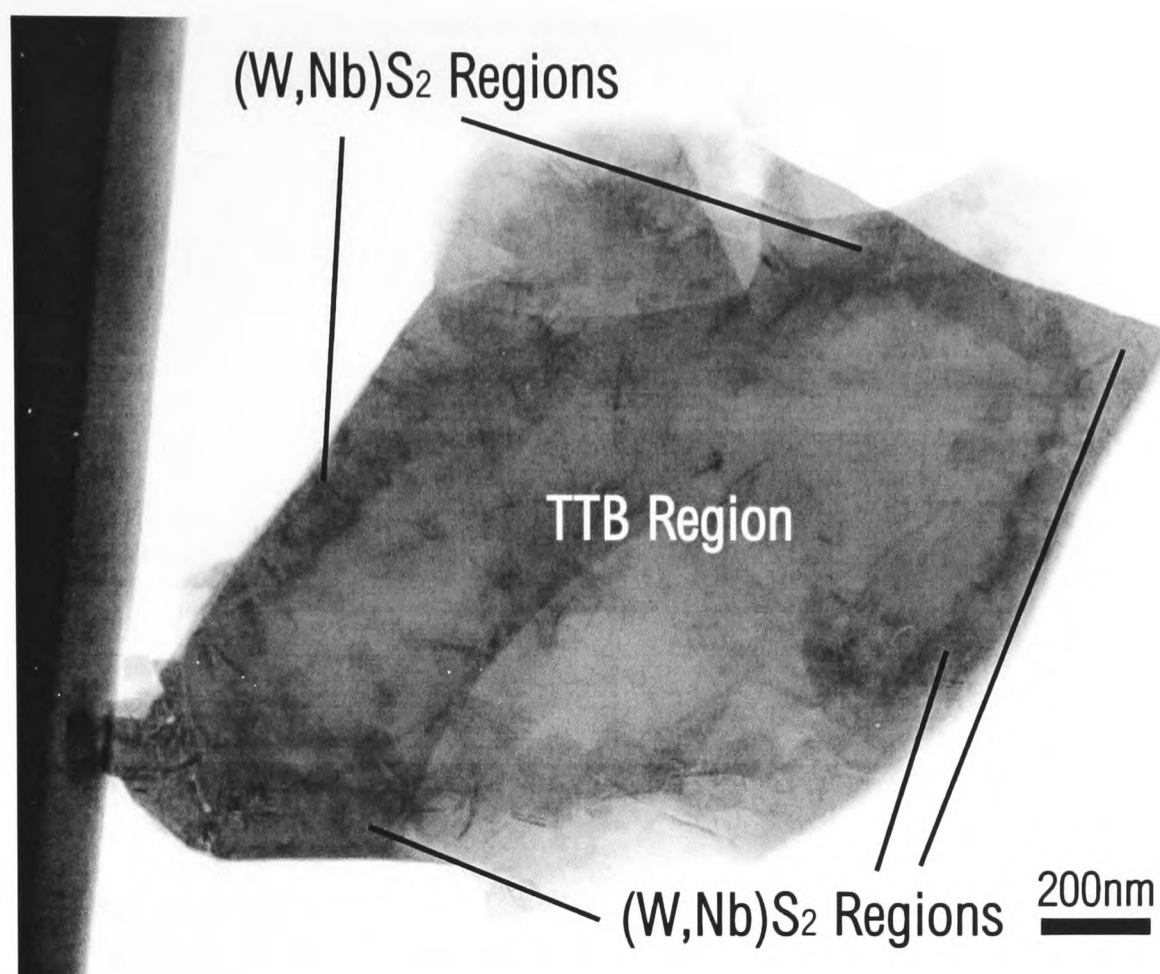


**Figure 5.9** Micrograph demonstrating typical particle size for a sulfidised  $\text{Nb}_4\text{W}_{13}\text{O}_{47}$  particle. Those of  $\text{Nb}_8\text{W}_9\text{O}_{47}$  exhibited similar morphologies. Illustrated are regions of sulfidised and unreacted oxide. This image corresponds to the SAED pattern in Figure 5.10.

Further evidence for the occurrence of sulfidisation of the binary oxide has been obtained from the electron diffraction patterns of the two product materials. The two SAED patterns in **Figure 5.10** have been taken from regions in **Figure 5.9** and from images of sulfidised  $\text{Nb}_8\text{W}_9\text{O}_{47}$ . Viewed along the  $c$  axis or (001) projection and thus, perpendicular to the  $ab$ -plane containing the pentagonal column openings in the parent oxide, two distinct patterns are evident. The first is the characteristic spot pattern of the TTB material in the  $ab$ -plane. The second feature is the ring-pattern, which is an attribute of layered  $\text{MS}_2$  structures such as  $\text{WS}_2$ ,  $\text{MoS}_2$  and  $\text{NbS}_2$ .<sup>[14]</sup> These reflections have been indexed according to the calculated  $d$ -spacings obtained from the diffraction patterns. From these data it is not possible to assign the reflections specifically to  $\text{WS}_2$  or  $\text{NbS}_2$ , rather, it is more likely that they are a result of a composite  $(\text{W}, \text{Nb})\text{S}_2$  structure.

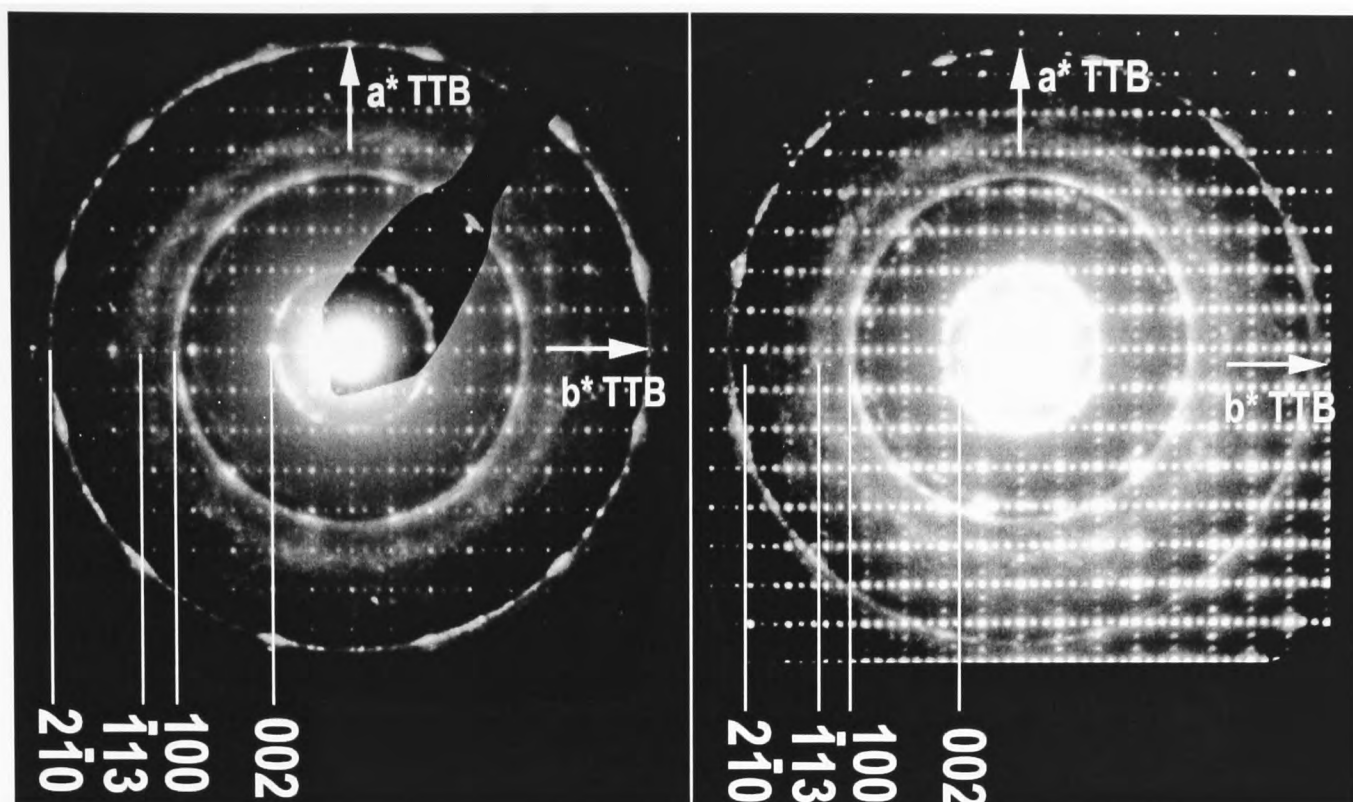


**Figure 5.10** Composite electron diffraction patterns of sulfidised samples of  $\text{Nb}_8\text{W}_9\text{O}_{47}$  (left) and  $\text{Nb}_4\text{W}_{13}\text{O}_{47}$  (right) indicating the presence of two types of crystal in the lattice. The ring pattern results from the IF-(W, Nb) $\text{S}_2$  material within the binary oxide and the reflections have been indexed accordingly. The Bragg reflections of the TTB matrix give the characteristic  $\langle 001 \rangle$  reflections (along the  $c^*$  axis) as bright spots in a square arrangement. The  $a^*$  and  $b^*$  labels indicate the reciprocal lattice planes of the TTB crystals.

Lending additional weight to the proposed formation of (W, Nb) $\text{S}_2$  is the EDX scan (**Figure 5.11**) obtained from the same specimens from which the SAED patterns were taken. The spectra clearly demonstrate the presence of sulfidised material in addition to that of the starting oxides.

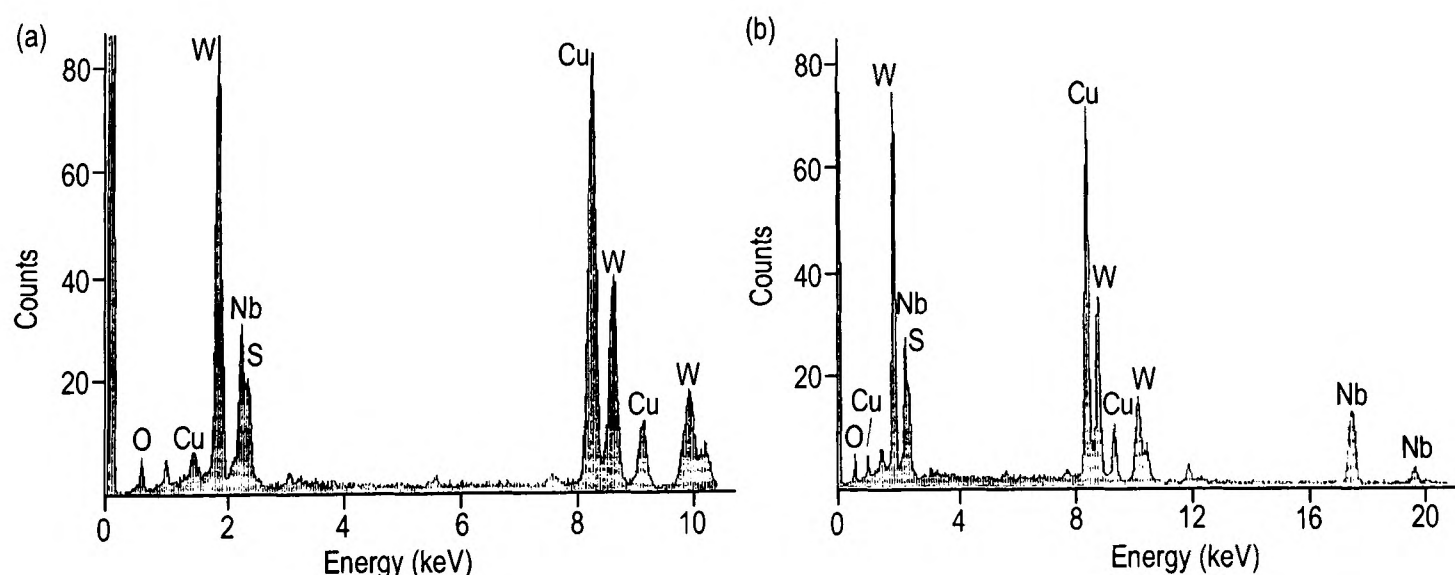


**Figure 5.11** EDX Scans taken from sulfidised samples of (a)  $\text{Nb}_8\text{W}_9\text{O}_{47}$  and (b)  $\text{Nb}_4\text{W}_{13}\text{O}_{47}$  indicating the presence of (W, Nb) $\text{S}_2$ .



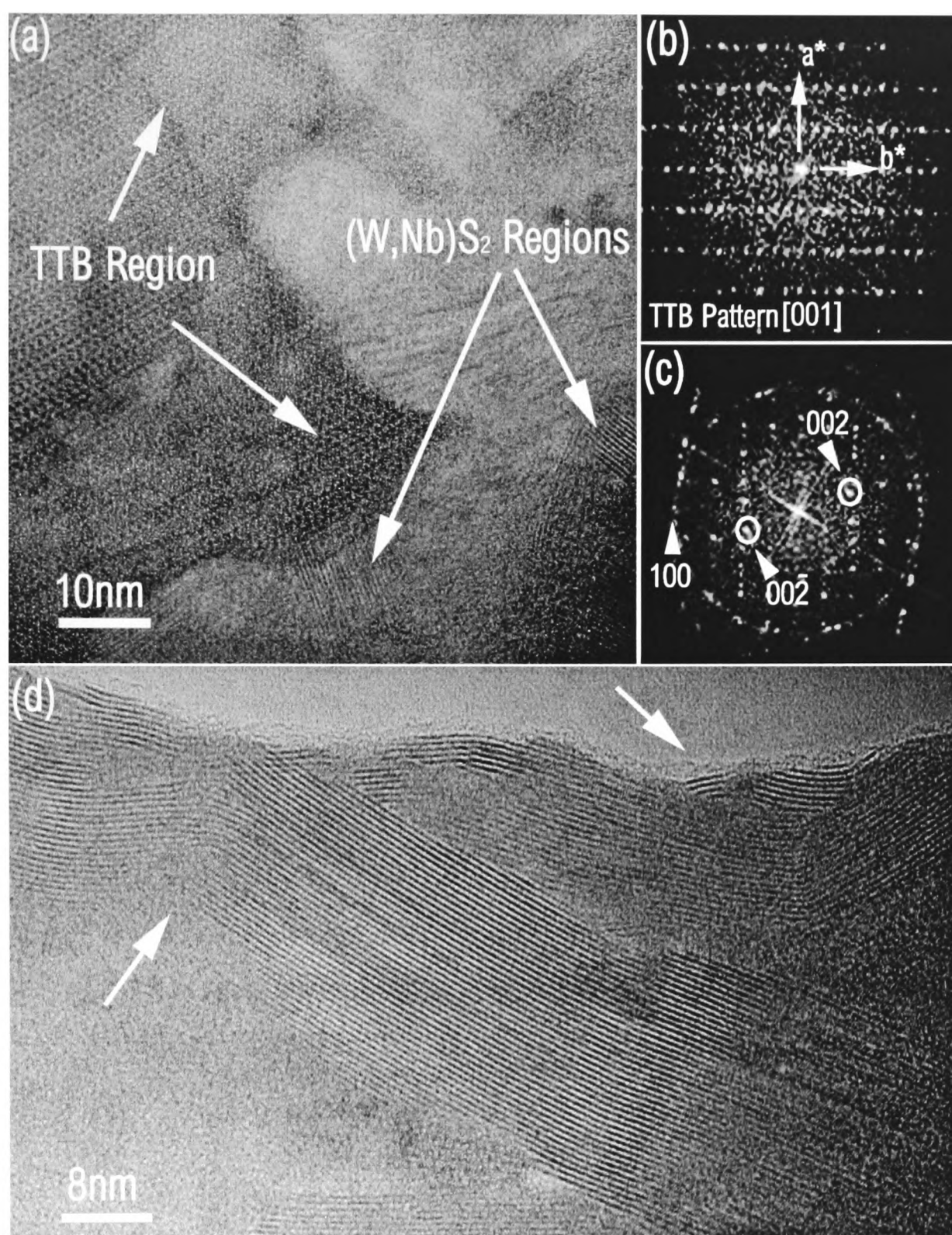


**Figure 5.12** (a) Illustration of the intergrowth between TTB regions and those of (W, Nb) $S_2$  material; (b) FFT of the TTB-oxide region shown in (a); (c) FFT of the sulfidised (W, Nb) $S_2$  region denoted in (a); (d) micrograph of the surface of a sulfidised  $Nb_8W_9O_{47}$  particle.

The micrographs above show an enlargement of an area of intergrowth in a sample of sulfidised  $Nb_8W_9O_{47}$ . **Figure 5.12 (a)** clearly shows the microstructures of both the TTB-type oxide and curved IF-(W, Nb) $S_2$  with a region of indeterminate stoichiometry in between. To confirm these assignments, Fast Fourier Transformations (FFT) on the two regions were carried out affording the simulated diffraction patterns (b) and (c). These are consistent with those expected for TTB- and mixed TTB-IF- $MS_2$  systems respectively. The latter pattern has been indexed and the  $\langle 002 \rangle$  and  $\langle 100 \rangle$  reflections are labelled. Finally, **Figure 5.12 (d)** shows a magnification of a region near the surface of the particle. The layered (W, Nb) $S_2$

strata are clearly visible and regions of intergrowth or growth-fronts are highlighted by the two arrows. There are regions of indeterminate composition – possibly a partially reduced form of the original TTB structure, to the left of the image.

As a result of thickness of the crystals obtained, it was not possible to observe the effect of sulfidisation along the pentagonal channels and thus, determine whether sulfide growth occurred from within the channels. The thickness could be greatly reduced by ball-milling the precursors and obtaining smaller particulates.

### **5.3 Epitaxial and Bulk Formation of IF-WS<sub>2</sub> Structures and Encapsulates from Tungsten Carbide (WC) Precursors**

This work was undertaken as part of a programme of collaboration between the Carbon Nanotechnology Group and Department of Materials, University of Oxford and the Department of Materials and Interfaces, Weizmann Institute, Rehovot, Israel.

Tungsten carbide (WC) has recently been shown to be active as a catalyst for the conversion of methane and carbon dioxide to synthesis gas ( $\text{CO} + \text{H}_2$ ).<sup>[20]</sup> It was also found, however, that deactivation of the WC catalyst by  $\text{CO}_2$  results in the formation of tungsten oxides, which are inactive for methane reforming. These oxides do have applications such as catalysts for metathesis, optoelectronic devices and as gas sensor materials. They have also demonstrated to be useful precursors in the synthesis of IF-WS<sub>2</sub> encapsulates.<sup>[11]</sup>

In this study, the formation of IF-WS<sub>2</sub> structures consisting of nanoparticles, nanotubes and various intermediate composites, starting from a WC precursor is described. In order to produce the IF-structures, commercially available tungsten carbide (WC) has been oxidised by  $\text{CO}_2$  for varying lengths of time ranging from one to forty-eight hours. The resulting products include a WC/WO<sub>3-x</sub> composite in which WO<sub>3-x</sub> needles of varying size and shape are grown epitaxially on the surfaces of carbide precursor crystals and fully oxidised WO<sub>3-x</sub> needles.

Sulfidisation has been introduced at different stages of the oxidation to produce different types of IF-materials. These include WC/WS<sub>2</sub> IF-nanoparticle encapsulates,

formed by partial sulfidisation of the carbide, and WC/WO<sub>3-x</sub>/IF-WS<sub>2</sub> nanotube composites formed by partial sulfidisation of the WC/WO<sub>3-x</sub>. In addition, partially filled WO<sub>3-x</sub>/IF-WS<sub>2</sub> composites formed by partial sulfidisation of the WO<sub>3-x</sub> needles and hollow IF-WS<sub>2</sub> nanotubes formed by total sulfidisation of the WO<sub>3-x</sub> product have been identified.

### 5.3.1 Oxidation of WC by CO<sub>2</sub>

The oxidation of WC by CO<sub>2</sub> was originally investigated *in situ* using a controlled environment transmission electron microscope. The work was performed *ex situ* by York *et al.*[11] by heating commercially available WC samples in a gas-flow reactor at 600-800°C using a CO<sub>2</sub> flow rate of 100 ml min<sup>-1</sup> for twenty-four hours. Partially oxidised WC showing growth of multiple epitaxial WO<sub>3-x</sub> needles was observed. The figure below (**Figure 5.12**) illustrates a high magnification HRTEM analysis of a typical region of intergrowth between the carbide and epitaxial tungsten oxide needle.

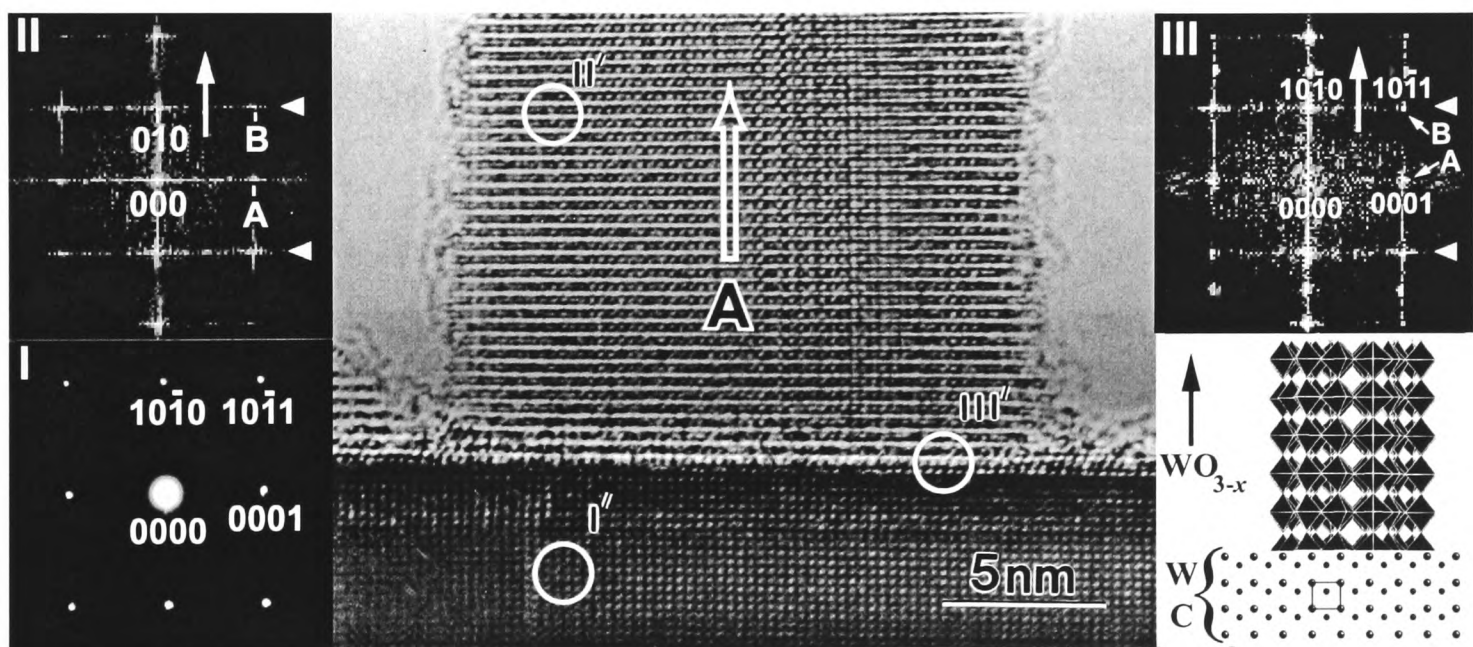


**Figure 5.12** Micrograph showing the interface between the WO<sub>3-x</sub> needle and the parent WC crystal. The inset patterns correspond to: I (0110) SAED pattern obtained from region I' corresponding to the parent crystal. II FFT obtained from region II' corresponding to the WO<sub>3-x</sub> needle. III FFT obtained from region III' corresponding to the WO<sub>3-x</sub> / WC interface. The schematic at the lower right represents the composite microstructure at the interface. The unit cell of the parent carbide ( $a = 0.2907$  nm;  $c = 0.2837$  nm) is indicated.

The central micrograph of **Figure 5.12** shows a HRTEM image of the interface between a WO<sub>3-x</sub> needle grown on the surface of a WC crystallite. The inset I shows the SAED pattern from area I', corresponding to the [0110] projection of the parent carbide. The carbide crystal microstructure is visible below the carbide/oxide



interface in the micrograph. The inset II is a Fast Fourier Transform (FFT) obtained from region II' and shows the calculated diffraction behaviour of the oxide needle. The strong reflections in the centre of II indicated by the long arrow correspond to the 0.375 nm layers in the oxide needle. The inset III obtained from the oxide/carbide interface in region III' is an FFT, which shows the composite diffraction behaviour at the interface. The strong reflections in this pattern correspond to the oxide layers that have been realigned along the [1010] direction of the WC pattern, which suggests that the substructure of the oxide is constrained by that of the carbide.[11]

The mechanism of needle formation on the carbide surface has been discussed.[11] The first step involves dissociation of CO<sub>2</sub> on the WC surface to afford WO<sub>x</sub> and CO. After formation of the surface WO<sub>3-x</sub>, a possible needle propagation mechanism has been envisaged. This entails a gas-phase reaction, which transports the oxide (WO<sub>x</sub>) from the carbide surface to the oxide needle tips. This mechanism allows for the epitaxial growth of needles from the WC crystal surface and is supported by the observation of amorphous material on the surface of the needle and carbide.

Commercially available tungsten carbide (Aldrich, 99.95%) was placed in a silica tube of diameter 5 mm and heated in a Eurotherm tube furnace at 750°C under a flow of CO<sub>2</sub> (50 ml min<sup>-1</sup>) for periods of two, six, twelve and twenty-four hours. After the respective time period the sample was removed from furnace and slowly cooled to room temperature.

Each of the oxidised samples was analysed by powder X-ray diffraction and a series of XRD spectra for samples ranging from the unreacted, commercial WC material to the fully oxidised (24 hour oxidation) WO<sub>3-x</sub> is shown below in **Figure 5.13**. The progression from carbide to oxide can be clearly followed by observing the diminution in intensity of the signals at 31.5, 36.8 and 48.2° with the concomitant intensification of those sets at 23 and 34° resulting from formation of WO<sub>3-x</sub>. The set of signals for the carbide after 24 hour oxidation is virtually identical to that reported for WO<sub>3-x</sub>. [2] These samples contain similar epitaxially grown WO<sub>3-x</sub> needles to those observed in the study described above and confirm the composition of the bulk sample. The next

stage involves the sulfidisation of these needle structures to form IF-like  $\text{WS}_2$  nanotubes and other composite structures.

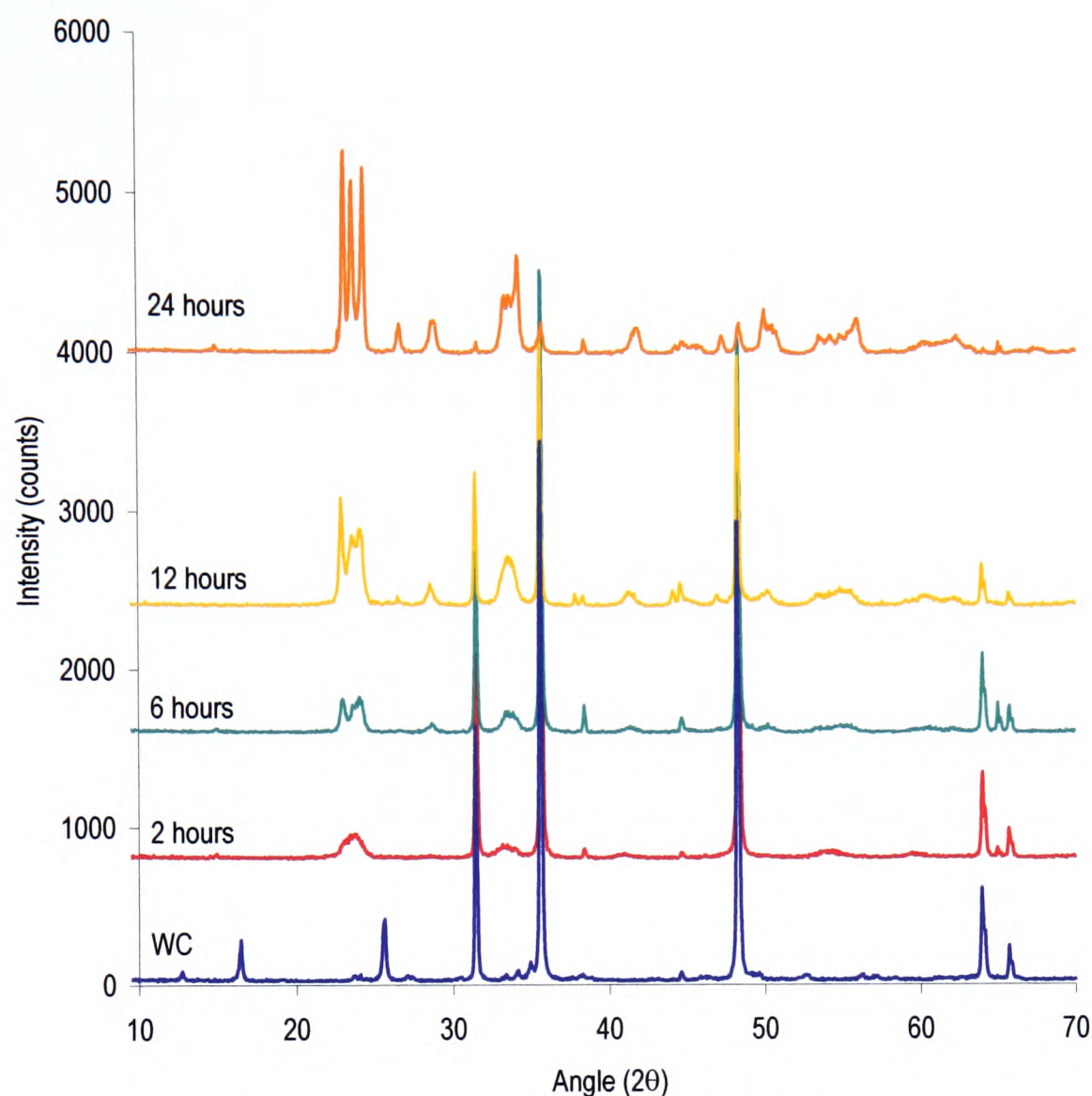


**Figure 5.13** Transformation of WC to  $\text{WO}_{3-x}$  via oxidation by  $\text{CO}_2$  followed by powder X-ray diffraction: (a) WC precursor; (b) after 2 hours of oxidation; (c) after 6 hours of oxidation; (d) after 12 hours of oxidation (e) after 24 hours of oxidation

### 5.3.2 Sulfidisation of $\text{WC}/\text{WO}_{3-x}$ Nanoparticles

The series of partially and fully oxidised WC samples prepared as described above, were then sulfidised in a similar fashion to the molybdenum carbide, as detailed in **Section 5.2**. Thus, the materials were reacted with  $\text{H}_2\text{S}$  with a flow rate of  $30 \text{ ml min}^{-1}$  in analogous apparatus to that shown in **Figure 5.1** at  $750^\circ\text{C}$  for 30 minutes. Three of the analysed samples were analysed by powder X-ray diffraction and a series of XRD spectra obtained for the sulfidised samples of WC (0 hours oxidation), WC (12 hours oxidation) and WC (24 hours oxidation) is shown below in **Figure 5.14**. The progression from starting material to IF- $\text{WS}_2$  can be clearly followed by observing the intensification of those signals, particularly that due to the (002) plane of the sulfide at  $14.5^\circ$ , and also at  $28.0$  and  $58.4^\circ$  resulting from formation of IF- $\text{WS}_2$ .

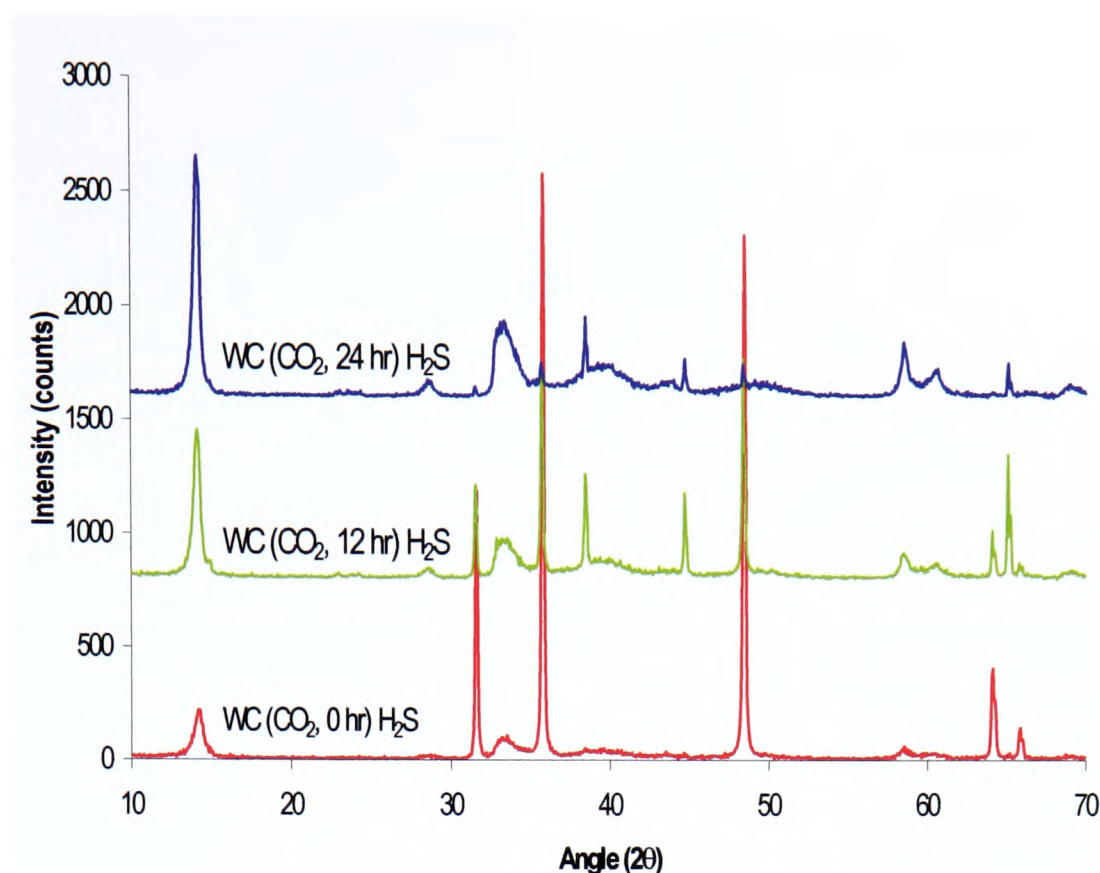


**Figure 5.14** Transformation of WC/ $\text{VO}_{3-x}$  to IF- $\text{WS}_2$  via sulfidisation by  $\text{H}_2\text{S}$  followed by powder X-ray diffraction: (A) WC precursor; (B) after 12 hours of oxidation; (C) after 24 hours of oxidation.

HRTEM studies were performed on the samples obtained after sulfidisation and several images are displayed in **Figure 5.15** below. **Figure 5.15 (a)** shows a tungsten carbide particle whereupon there are several epitaxially grown  $\text{VO}_{3-x}$  needles, partially sulfidised, yielding IF- $\text{WS}_2$  nanotubes containing some unreacted tungsten oxide. In **Figure 5.15 (b)**, the epitaxial nature of the  $\text{VO}_{3-x}$  needles with respect to the carbide surface is demonstrated. Additionally, this solid nanotube is encapsulated in a few layers of IF- $\text{WS}_2$ . Finally, **Figure 5.15 (c)** is a higher magnification image of some partially filled IF- $\text{WS}_2$  nanotubes, exhibiting hollow structures near the ‘top’ of the tube after complete consumption of the oxide in that region. Nearer the base of the nanotube, unreacted  $\text{VO}_{3-x}$  material remains.



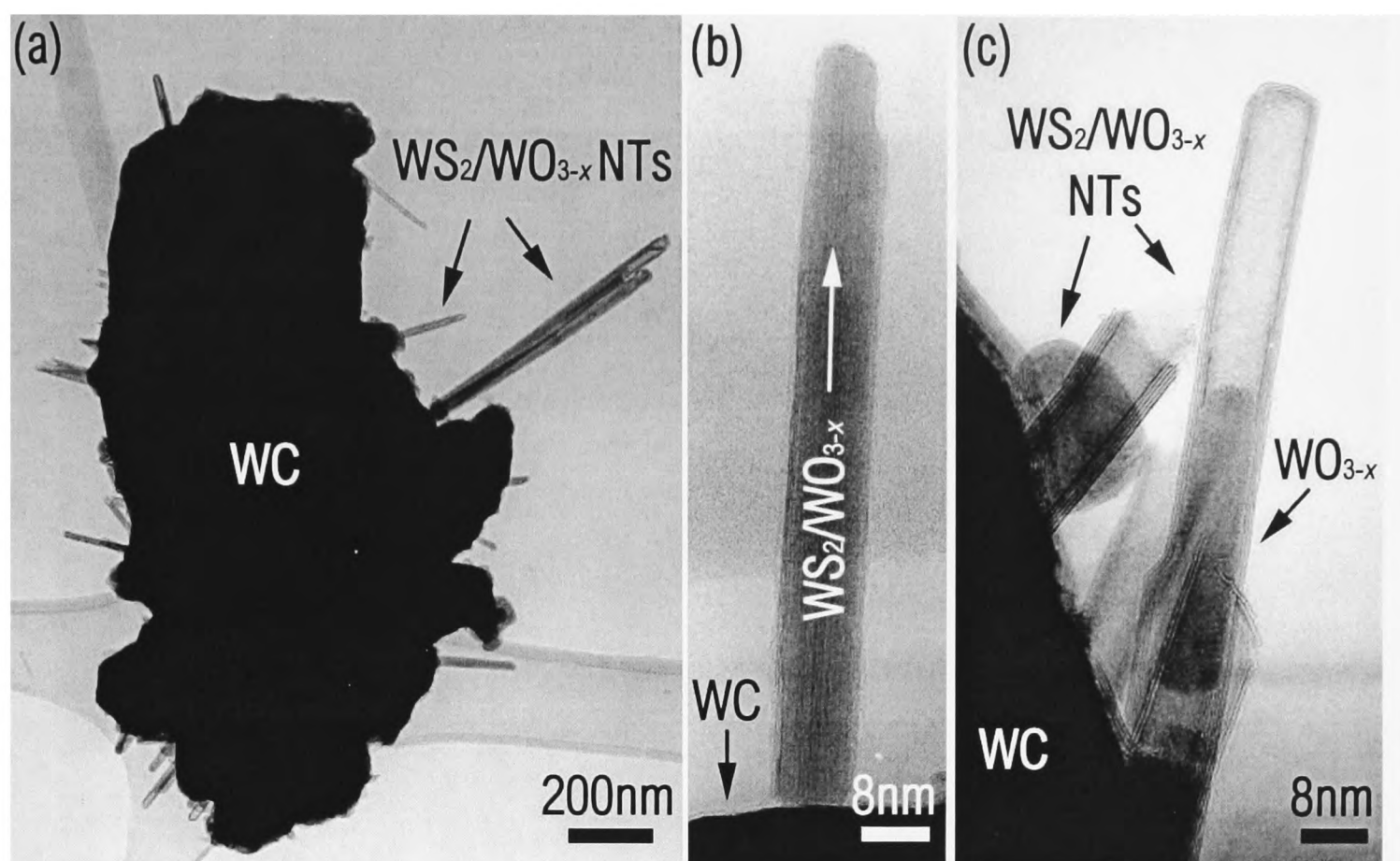


**Figure 5.15** Micrographs illustrating the product formation of the intermediate 'partially oxidised' tungsten carbide (WC) precursor. **(a)** Epitaxial growth of  $WO_{3-x}$  needles from the surface of the WC precursor; **(b)** nanotube comprising a  $WO_{3-x}$  core encapsulated in IF- $WS_2$ ; **(c)** hollow IF- $WS_2$  nanotube containing a small amount of tungsten oxide.

Taken in conjunction with the powder X-ray diffraction data in **Figures 5.13** and **5.14** these images clearly quantify and confirm the observations made about the nature of the bulk materials in both carbide-oxide and the sulfidised samples.

The main difference between the IF materials grown from the WC precursor and those grown from  $WO_{3-x}$  is that the tungsten carbide material is encapsulated within a maximum of about 10 layers of  $WS_2$ . The number of layers around the tungsten oxide precursor is much greater, as shown in **Figure 5.16**. In addition, the number of IF- $WS_2$  layers formed on the carbide substrate is independent of the length of the sulfidisation process. This is in contrast to the behaviour of the  $WO_{3-x}$  precursor, for which the sulfidisation step is only limited by the quantity of oxide available.

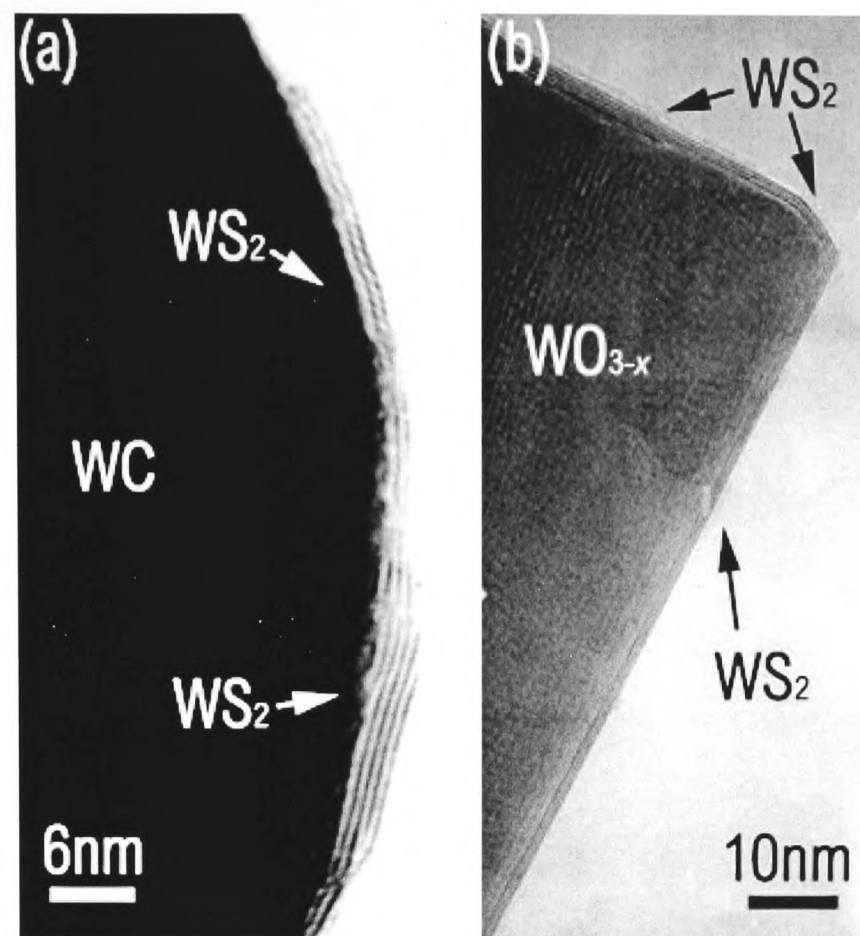


**Figure 5.16** Comparison between the sulfidised products of (a) WC prior to oxidation by CO<sub>2</sub> and (b) after complete oxidation to WO<sub>3-x</sub>. The most poignant difference is in the number of IF-WS<sub>2</sub> layers which is limited to approximately 10 for WC irrespective of the length of the sulfidisation process but apparently limited only by the amount of consumable oxide in the case of WO<sub>3-x</sub>.

The consequence of encapsulating a very dense and hardwearing compound such as WC inside IF-WS<sub>2</sub> shells, is to enhance the structural rigidity of the resulting IF-WS<sub>2</sub>/WC encapsulates: a feature which may enhance their performance in tribological applications. The fact that WC also exhibits a metallic character should enhance the conductive properties of the composite material.

## 5.4 Summary

The chemistry described in this chapter was concerned with the preparation of IF-like materials from a range of available precursors including molybdenum carbide (MoC), the mixed tungsten-niobium binary oxides  $\text{Nb}_8\text{W}_9\text{O}_{47}$  and  $\text{Nb}_4\text{W}_{13}\text{O}_{47}$  and from tungsten carbide (WC) and some sequentially oxidised (*via*  $\text{CO}_2$ ) derivatives.

Upon reaction with  $\text{H}_2\text{S}$  at  $750^\circ\text{C}$ , molybdenum carbide (MoC) was shown to undergo complete sulfidisation to  $\text{MoS}_2$  even after very short reaction times. The product material did not contain any encapsulated oxide, rather a structure consisting of  $\text{MoS}_2$  layers oriented in multiple directions. This behaviour contrasts with that of the tungsten analogue, WC, which only undergoes limited conversion to  $\text{WS}_2$ -encapsulated WC regardless of the length of sulfidisation process.

Sulfidisation of the binary oxides  $\text{Nb}_8\text{W}_9\text{O}_{47}$  and  $\text{Nb}_4\text{W}_{13}\text{O}_{47}$  has been described. The particle sizes range between 800 and 1500 nm, however, this could be greatly reduced by ball-milling the precursors and obtaining smaller particulates. The limited amount of starting material available prevented a study of the behaviour of different sized particles. The presence of  $(\text{W}, \text{Nb})\text{S}_2$  was confirmed by HRTEM studies and EDX analysis.

Finally, the stepwise oxidation of WC by  $\text{CO}_2$  and sulfidisation of the intermediate  $\text{WC}/\text{WO}_{3-x}$  materials has been described. The formation of a variety of partially oxidised and sulfidised products including  $\text{WO}_{3-x}$  nanotubes, empty and partially filled IF- $\text{WS}_2$  nanotubes and IF- $\text{WS}_2$  encapsulated WC was determined by powder X-ray diffraction and HRTEM studies.

## 5.5 References for Chapter 5

- [1] Y. Feldman, E. Wasserman, D. J. Srolovitz and R. Tenne, *Science*, **267** (1995) 222.
- [2] Y. Feldman, G. L. Frey, M. Homyonfer, V. Lyakhovitskaya, L. Marguilis, H. Cohen, G. Hodes, J. L. Hutchison and R. Tenne, *J. Am. Chem. Soc.*, **118** (1996) 5362.
- [3] M. Hershfinkel, L. H. Gheber, V. Volterra, J. L. Hutchison, L. Marguilis and R. Tenne, *J. Am. Chem. Soc.*, **116** (1994) 1914.
- [4] M. Homyonfer, Y. Mastai, M. Hershfinkel, V. Volterra, J. L. Hutchison and R. Tenne, *J. Am. Chem. Soc.*, **118** (1996) 7804.
- [5] L. Marguilis, G. Salitra and R. Tenne, *Nature*, **365** (1993) 113.
- [6] A. Rothschild, J. Sloan, A. P. E. York, M. L. H. Green, J. L. Hutchison and R. Tenne, *J. Chem. Soc., Chem. Commun.*, (1999) 363.
- [7] J. Sloan, J. L. Hutchison, R. Tenne, Y. Feldman, T. Tsirlina and M. Homyonfer, *J. Solid State Chem.*, **144** (1999) 100.
- [8] R. Tenne, L. Margulis and G. Hodes, *Adv. Mater.*, **5** (1993) 386.
- [9] R. Tenne, H. M. and Y. Feldman, *Chem. Mater.*, **10** (1998) 3225.
- [10] T. Tsirlina, Y. Feldman, M. Homyonfer, J. Sloan, J. L. Hutchison and R. Tenne, *Fullerene Sci. Technol.*, **6** (1998) 157.
- [11] A. P. E. York, J. Sloan and M. L. H. Green, *J. Chem. Soc., Chem. Commun.*, (1999) 269.
- [12] J. A. Wilson and A. D. Yoffe, *Adv. Phys.*, **18** (1969) 193.
- [13] M. Homyonfer, *Ph.D. Thesis*, Weizmann Institute, Rehovot, Israel, (1998).
- [14] R. Tenne, L. Marguilis, M. Genut and G. Hodes, *Nature*, **360** (1992) 444.
- [15] B. G. Hyde and M. O'Keeffe, *Acta Cryst.*, **A29** (1973) 243.
- [16] S. Horiuchi, K. Muramatsu and Y. Matsui, *Acta Cryst.*, **A 34** (1978) 939.
- [17] M. Sundberg and B.-O. Marinder, *J. Solid State Chem.*, **84** (1990) 23.
- [18] F. Krumeich, C. Bartsch and R. Gruehn, *J. Solid State Chem.*, **120** (1995) 268.
- [19] F. Krumeich, A. Hussain, C. Bartsch and R. Gruehn, *Z. Anorg. Allg. Chem.*, **621** (1995) 799.
- [20] A. P. E. York, J. B. Claridge, A. J. Brungs, S. C. Tsang and M. L. H. Green, *J. Chem. Soc., Chem. Commun.*, (1997) 39.

## **Chapter 6**

### **Synthesis of IF-Like Materials (II)**



## 6.0 Introduction to Chapter 6

This chapter describes the preparation of a range of Group 5 metal oxides synthesised *via* the metal vapour synthesis technique. These amorphous oxides have been annealed under reducing conditions to induce crystallinity before undergoing reaction with hydrogen sulfide gas to form layered  $\text{MS}_2$  ( $\text{M} = \text{V}, \text{Nb}, \text{Ta}$ ) materials, which exhibit IF-like characteristics. As in the previous chapter, this work was undertaken under the supervision of Dr. Jeremy Sloan, who performed the HRTEM studies described below.

The use of transition metal oxides as precursors in the synthesis of IF- $\text{MX}_2$  type materials is well established.<sup>[1-7]</sup> One of the main methods of preparation of these materials involves the reaction between an atomised metal source and water vapour, resulting in a microcrystalline oxide product.<sup>[4]</sup> During the course of the studies presented in this chapter, an alternative methodology has been utilised to prepare these precursors, namely that of metal vapour synthesis (MVS).

## 6.1 Metal Vapour Synthesis (MVS)

### 6.1.1 Introduction to the MVS Technique

Metal vapour synthesis is a technique used mainly in the synthesis of organometallic complexes. Originally developed by Skell<sup>[8-11]</sup> and co-workers in the early 1960s, it was employed by Timms<sup>[12]</sup> as an energetically favourable method for producing organometallic transition metal complexes from an ingot of the required metal and a supply of organic ligand. This technique also involves the co-condensation of metal atoms, generated *in situ* from a bulk sample of metal at a high temperature, with water vapour, although under much higher vacuum conditions than the previously reported oxide preparation methods. It is only recently that MVS has been used to produce ‘more classical’ inorganic materials. The advantage in using the technique is that materials with very small particle sizes can be made. Previously described MVS methods, however, involve the evaporation of first-row transition metals into molten alkali metal nitrates, which oxidise the metals to metal oxides.<sup>[13]</sup>

In **Figure 6.1**, the thermodynamic considerations of the process are illustrated. MVS is successful due to its unique advantage of removing the thermodynamic and kinetic barriers connected with reactions of bulk metals. The activation energy,  $\Delta G_A^\#$ , for the metal vapour synthesis of a ligand-metal complex is more favourable than that for the bulk reaction  $\Delta G_B^\#$ , by an amount approximating the free energy of sublimation of the metal,  $\Delta G_{\text{sub}}(\text{M})$ . Thermodynamically, the MVS route is more favourable because the free energy of formation of the ligand-metal complex,  $\Delta G_{\text{r}(\text{B})}$  is greater in magnitude than that of the conventional synthesis,  $\Delta G_{\text{r}(\text{A})}$  by an amount approximating  $\Delta G_{\text{sub}}(\text{M})$ .

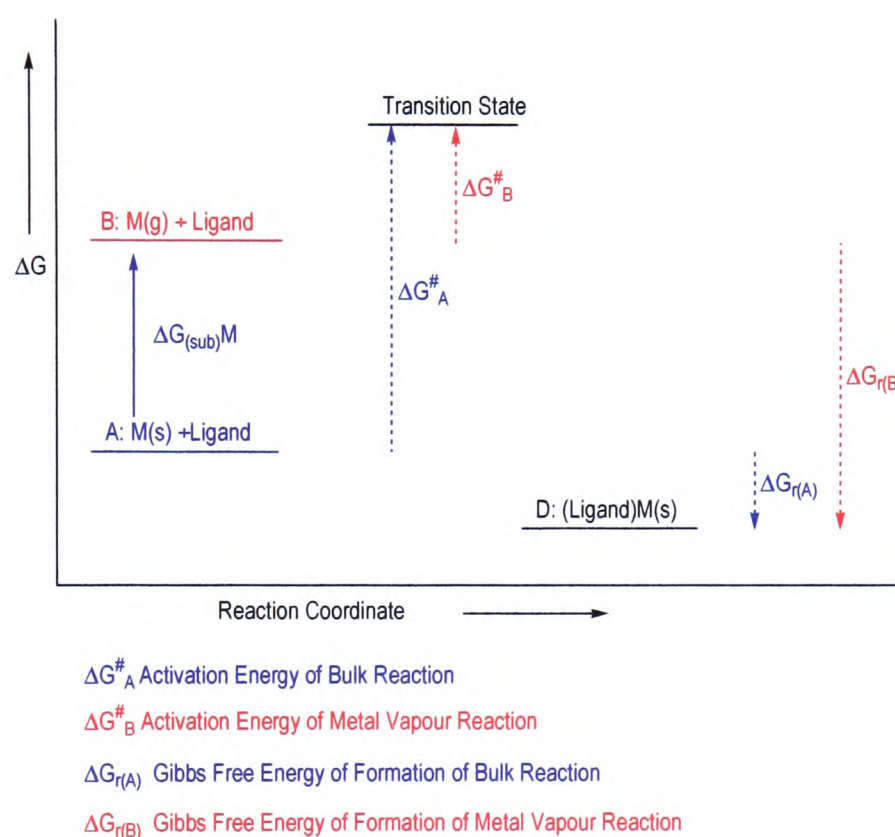


**Figure 6.1** Schematic energy diagram for the MVS Technique

The MVS apparatus consists of a ground glass bell-jar as the reaction vessel, evacuated to  $10^{-6}$  mbar using a series of two-stage backing and turbomolecular pumps. During the experiment, the surface of the glass bell jar is cooled to  $-196^\circ\text{C}$  by a liquid nitrogen jacket. The ligand is admitted to the vessel through a heated stainless steel inlet system, which allows for even coating and controlled rate of admission to the evacuated bell jar. This is important because the metal is evaporated utilising an electron-gun furnace, which operates only under high-vacuum conditions.

A diagram of the apparatus used in this laboratory is shown in **Figure 6.2**. In order to achieve the synthesis of oxide precursors for IF-like materials, the following modifications to the procedure have been implemented. Degassed water is admitted to the reaction chamber and condenses as a frozen matrix on the liquid nitrogen cooled walls of the bell jar. Simultaneously, a metal ingot is heated using an electron-gun furnace, a schematic of which is shown in **Figure 6.3**. The vapourised metal is co-condensed with the water vapour and the resulting frozen matrix consists of metal atoms trapped in frozen water in which the metal atoms are prevented from simply forming a metal aggregate or thin film. On warming to room temperature, the metal atoms react with the water to form a metal oxide. The material is rinsed out of the vessel as a suspension in ethanol and filtered through a glass frit then residual volatiles are removed under reduced pressure.

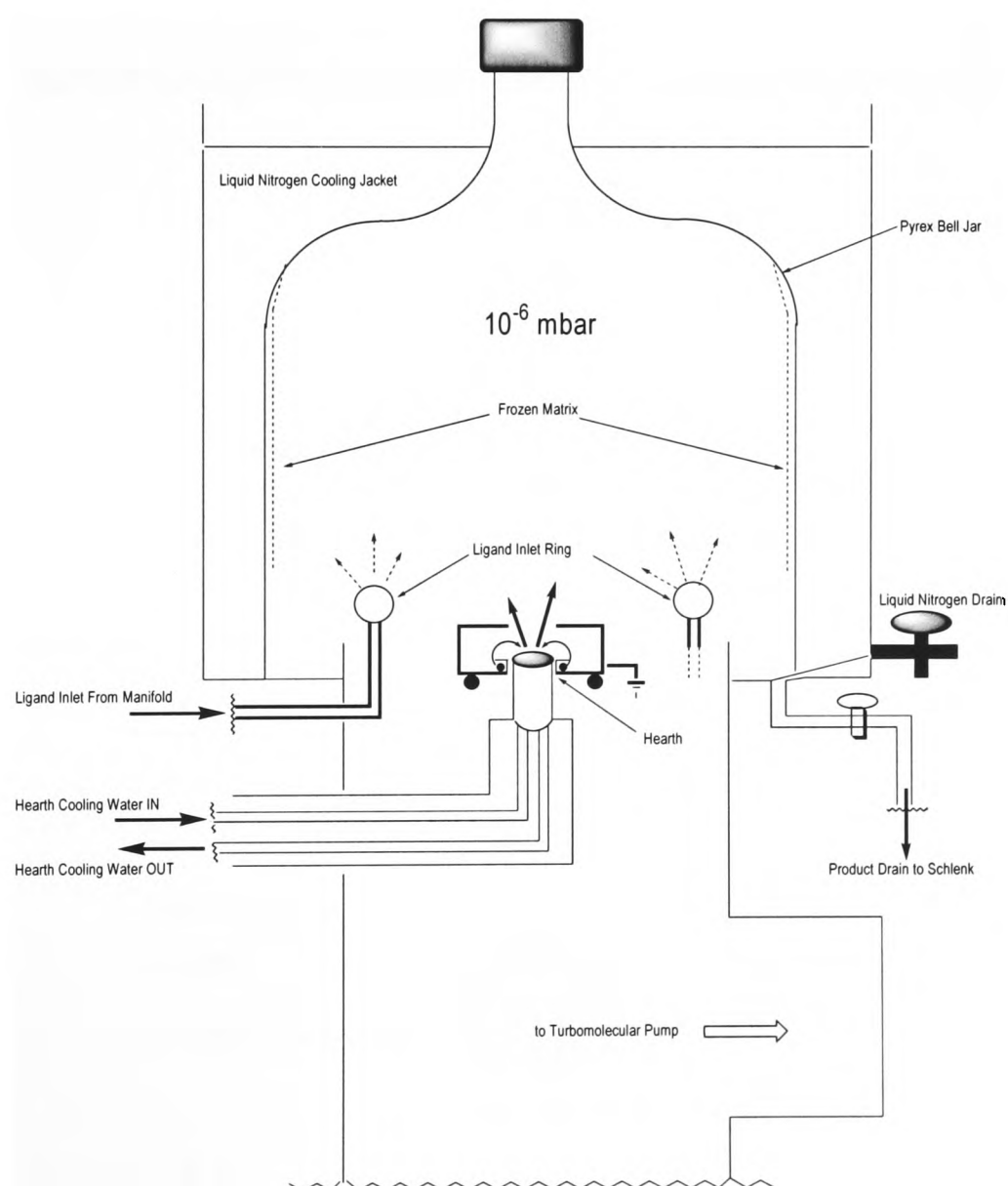


**Figure 6.2** Schematic of the MVS Apparatus used in the synthesis of the Group 5 metal oxides described in this chapter

6.2 Preparation of Group 5 Metal Oxides by MVS

Metal atoms generated from a molten ingot were co-condensed with distilled water over a three-hour period. After warming to room temperature, the coloured matrix was washed out of the reactor with analytical grade ethanol and the suspended product was filtered through a glass frit and dried. Solvent was removed under reduced pressure and the finely divided product was collected (see **Table 6.1** for details).

Metal	Power (kW)	Matrix Colour	Product Colour	Yield (g)
V	0.7	Olive green	black	2.8
Nb	3.2	Green	light grey	1.4
Ta	4.2	Grey	dark grey	2.3

**Table 6.1** Summary of reaction conditions for the MVS synthesis of Group 5 metal oxides

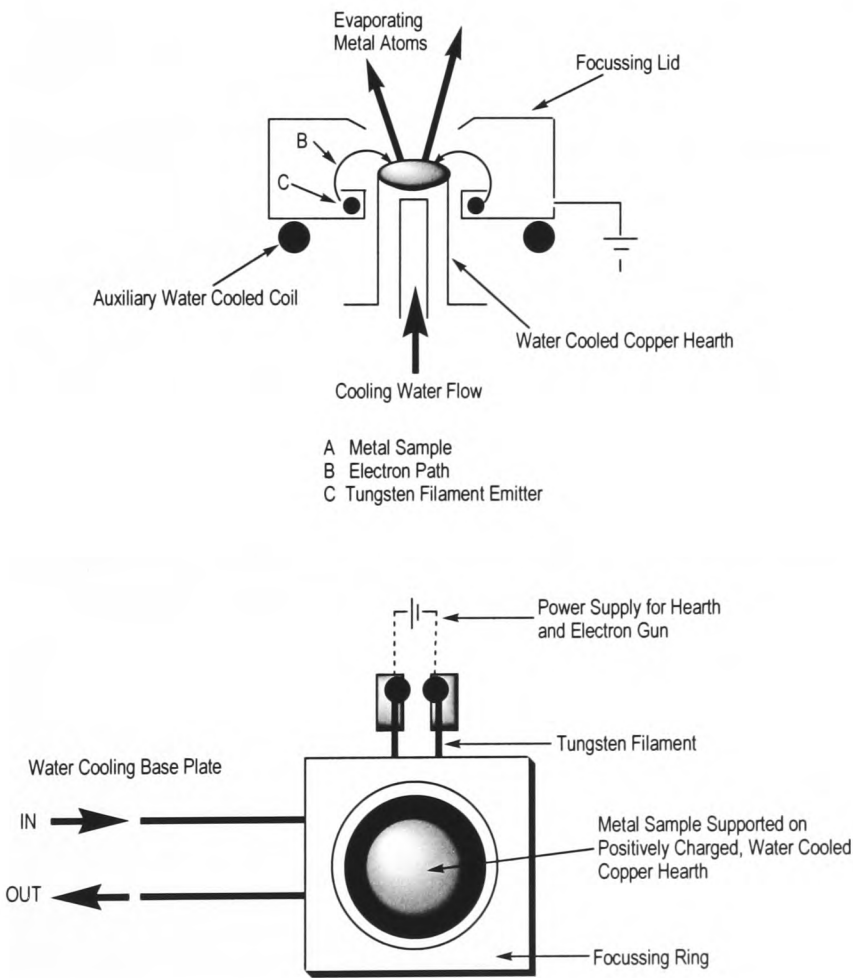


**Figure 6.3** Side-on and top views of the hearth used in the experiments



### 6.2.1 Analysis of MVS Products

The series of Group 5 metal oxides was analysed by a number of techniques to determine the particle size, morphology and composition. The powder X-ray diffraction spectra of the three products are shown in **Figure 6.4**. The absence of any sharp diffraction peaks indicates the amorphous nature of the materials and the presence of broad humps suggests that the particles are very small. An EDX scan has been obtained for each material from the same specimen from which the X-ray diffraction data were obtained. The spectra exhibit signals solely attributable to X-ray emissions from the respective transition metal (V, Nb or Ta) and oxygen as shown in **Figure 6.5 (a)-(c)**.

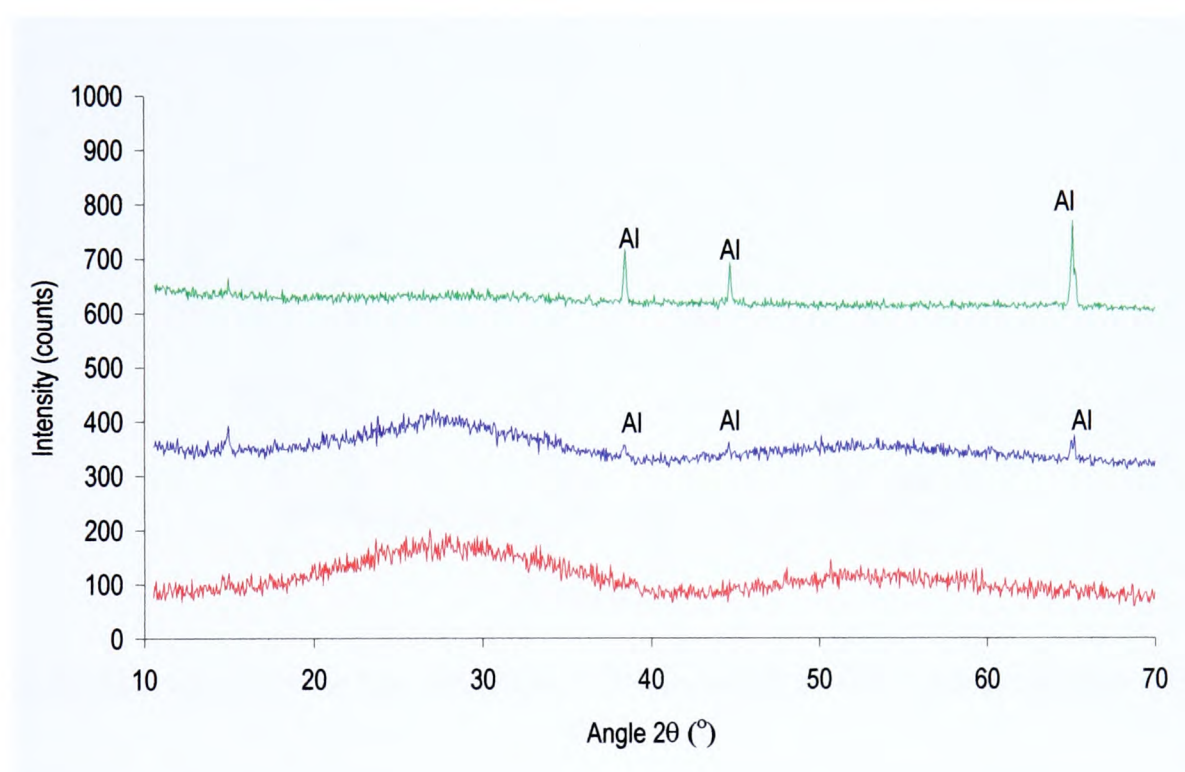


**Figure 6.4** Powder X-ray diffraction spectra for the Group 5 MVS products [V (red) , Nb (blue) and Ta (green) oxides]

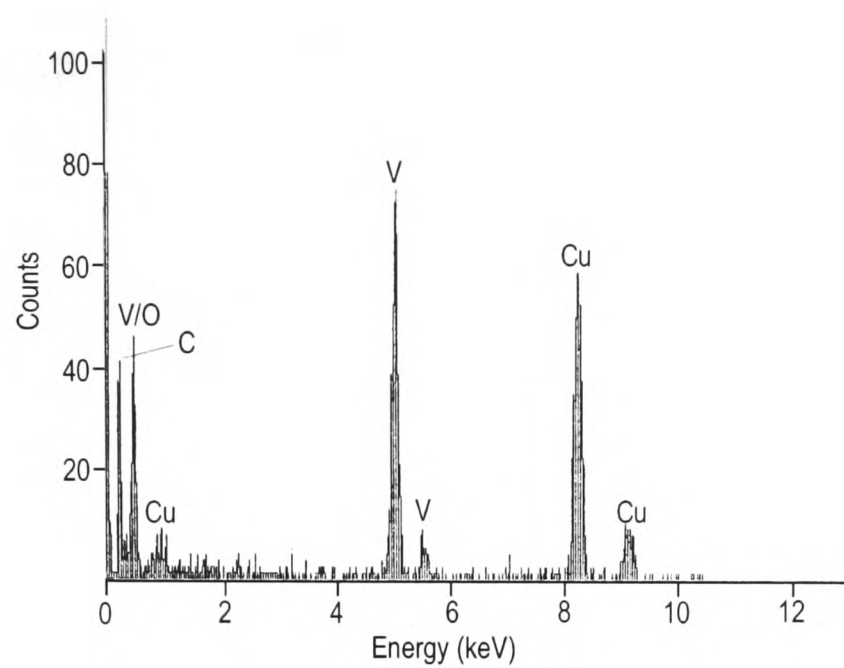


**Figure 6.5 (a)** EDX spectrum for the amorphous MVS product from the reaction between vanadium and water

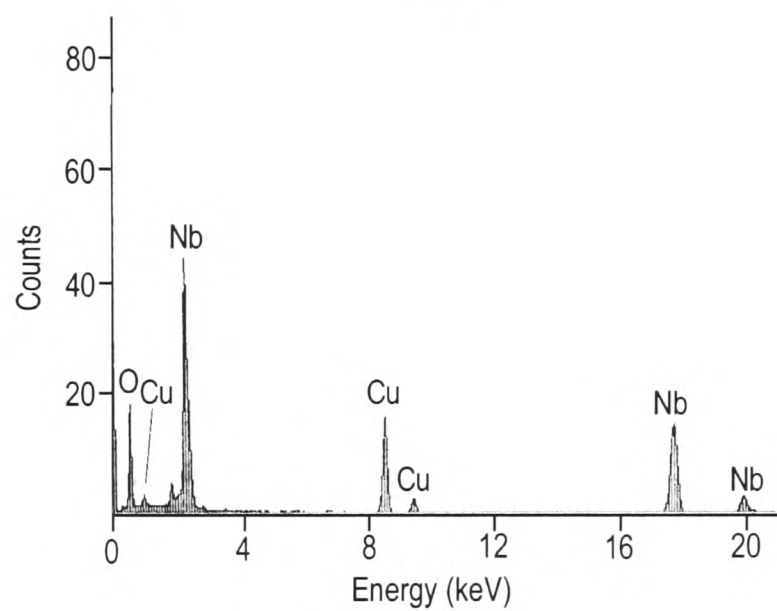


**Figure 6.5 (b)** EDX spectrum for the amorphous MVS product from the reaction between niobium and water

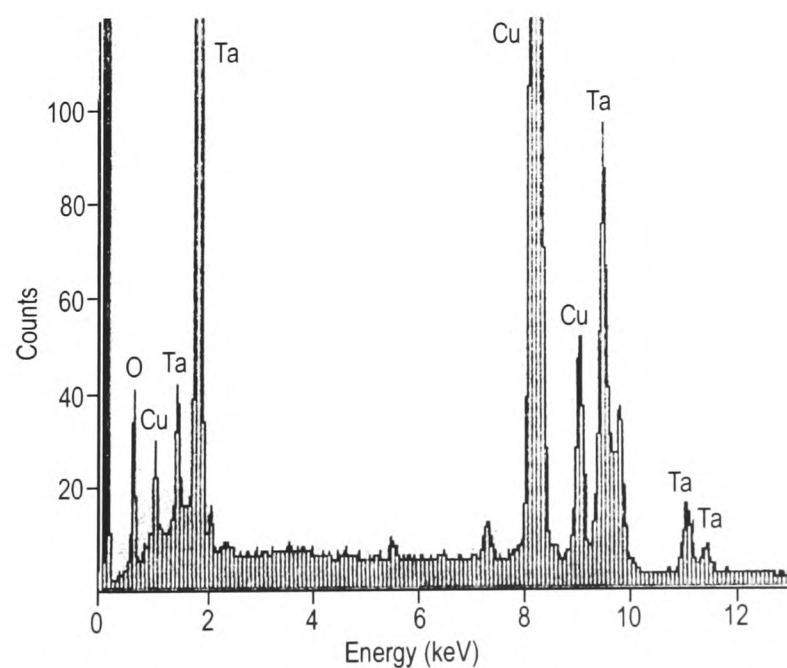


**Figure 6.5 (c)** EDX spectrum for the amorphous MVS product from the reaction between tantalum and water

The particle sizes and morphologies were determined from HRTEM studies. All three systems produced irregular shaped particles as shown below in **Figure 6.6**. The materials consisted of agglomerations of very small particles of between 5 and 10 nm in diameter. The high surface area resulting from this arrangement may be an advantage in the sulfidisation process, the first stage of which results in fast formation of one or two layers of metal sulfide, isolating the small oxide particles and preventing formation of larger platelets.[4, 5]

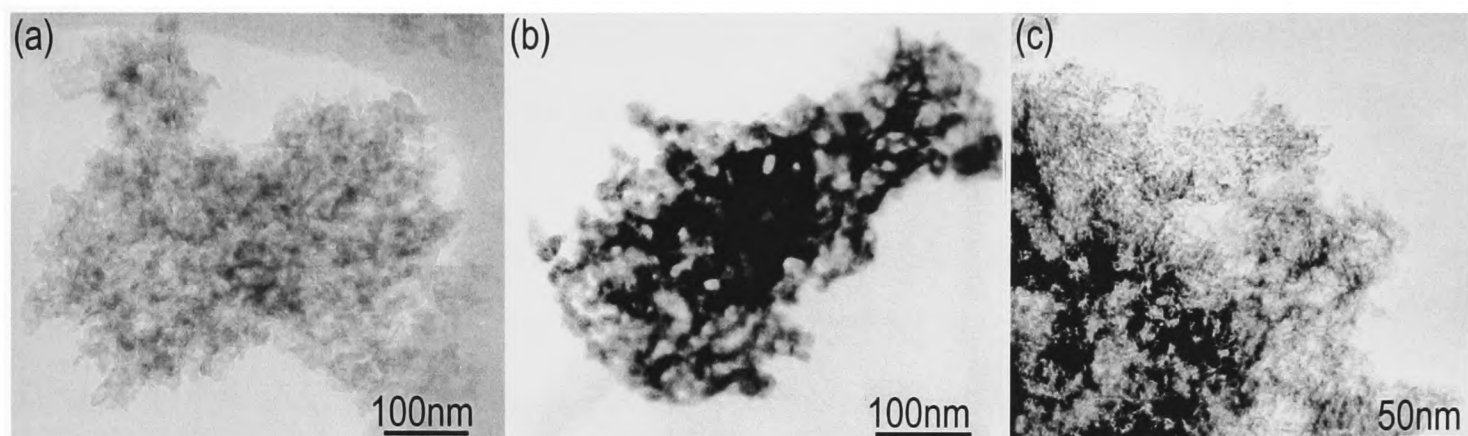


**Figure 6.6** HRTEM micrographs showing typical particle sizes and high surface area morphologies of amorphous MVS products for (a) vanadium, (b) tantalum and (c) niobium

Thus, MVS has been shown to be a viable technique for the synthesis of amorphous metal oxide nanoparticles which are of a suitable size to act as precursors for the synthesis of IF-like materials. Through annealing the oxides under a reducing atmosphere, it is proposed that suitable crystalline precursor morphologies for the formation of IF-like materials can be attained.

### 6.3 Preparation of Crystalline Group 5 Metal Oxides

Previous work by Tenne *et al.* has demonstrated the requirement of a reduced, nanocrystalline oxide to act as a precursor to IF-MS<sub>2</sub> synthesis.[2, 4, 6, 14] Furthermore, the microstructure of the precursors has shown to be an important factor in terms of influencing the growth mechanism of the encapsulating sulfides. To this end, the amorphous Group 5 metal oxides of indeterminate stoichiometry were annealed under reducing conditions in order to impart these properties. In addition, after the annealing stage of the process, the crystalline oxides were then analysed and the phases of these intermediate oxide materials were identified.

The oxides were heated under a dynamic atmosphere of hydrogen gas (H<sub>2</sub>) at between 700-850°C for about one hour in apparatus similar to that illustrated in **Figure 6.7**. Details of the specific conditions for each metal oxide are given in **Section 7.4**.

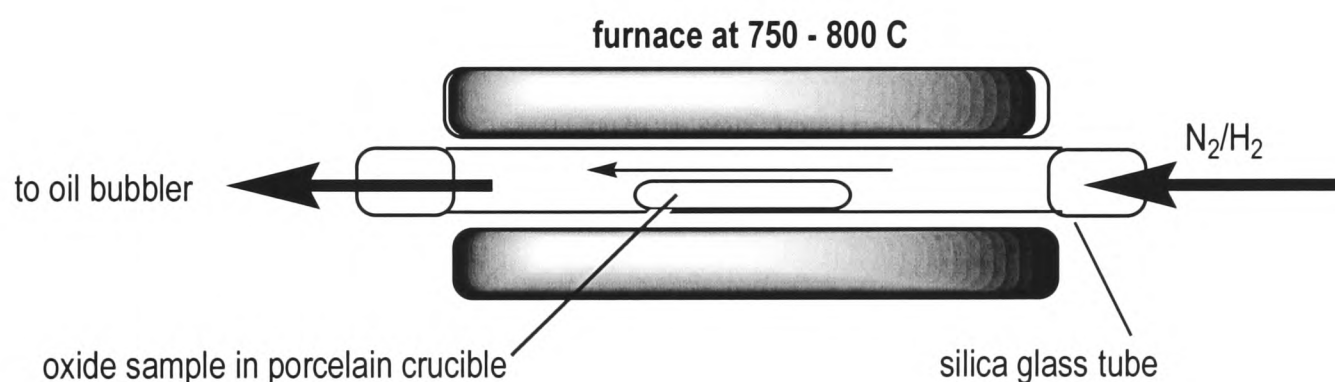


**Figure 6.7** Schematic of the annealing/reducing apparatus used in the experiments

In a typical experiment, a porcelain crucible charged with a sample of amorphous oxide was placed in a silica glass tube. The silica tube was inserted into an electrothermal furnace and purged with N<sub>2</sub> gas for 20 minutes. The furnace was then heated to the appropriate temperature. At this point, the N<sub>2</sub> supply was replaced with H<sub>2</sub>, which was passed over the oxide for 30 minutes at a rate of 60 ml min<sup>-1</sup>. After this time, the N<sub>2</sub> supply was reconnected and the sample slowly returned to room temperature.



### 6.3.1 Preparation of Reduced Vanadium Oxide, $\alpha$ - $V_2O_3$

A microcrystalline sample of vanadium oxide ( $V_2O_3$ ) was prepared as described in **Section 6.1** by heating the precursor at 750°C for 30 minutes under a dynamic atmosphere of  $H_2$  gas, before cooling to room temperature under an inert atmosphere.

The powder X-ray diffraction spectrum for the product, shown in **Figure 6.8**, is virtually identical to that reported for a common, reduced form of vanadium oxide,  $\alpha$ - $V_2O_3$  or Karelite.[15, 16] This oxide exhibits the common *corundum* oxide structure also shared by  $Al_2O_3$ ,  $Ti_2O_3$  and  $Cr_2O_3$ . The structure consists of a hexagonal close-packed array of O-atoms with the metal atoms occupying two-thirds of the octahedral holes. The result is a series of face-sharing octahedra in which every octahedron shares three edges within a layer and three vertices with octahedra from an adjacent layer to which it has no face-sharing connection.[17] Two polyhedral representations of  $V_2O_3$  are shown in **Figure 6.9**.

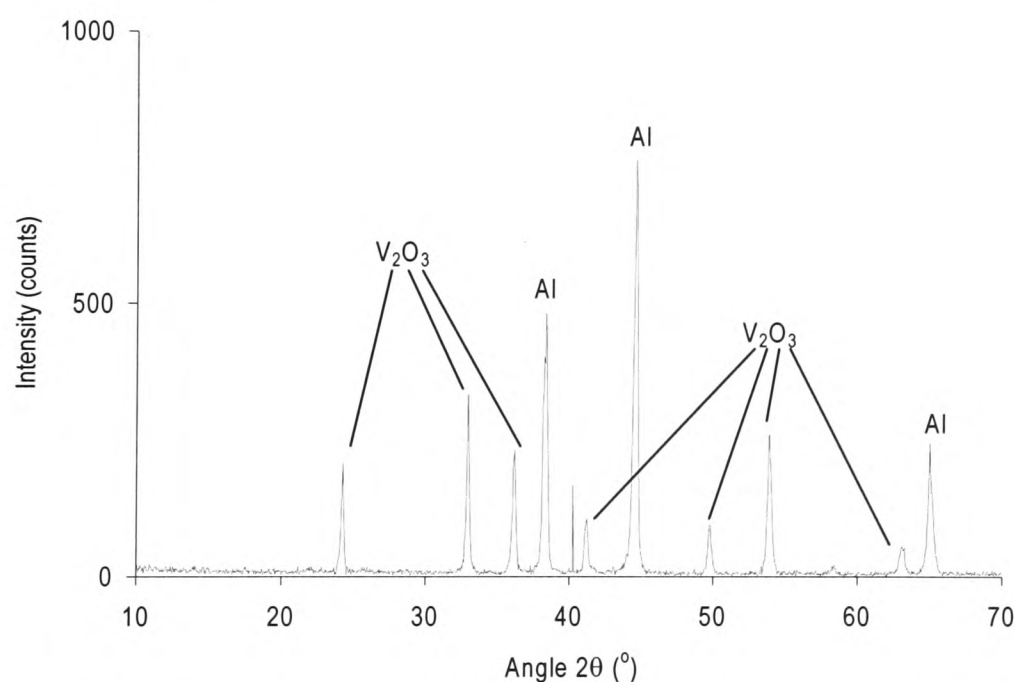


**Figure 6.8** Powder X-ray diffraction plot for reduced vanadium oxide ( $\alpha$ - $V_2O_3$ )

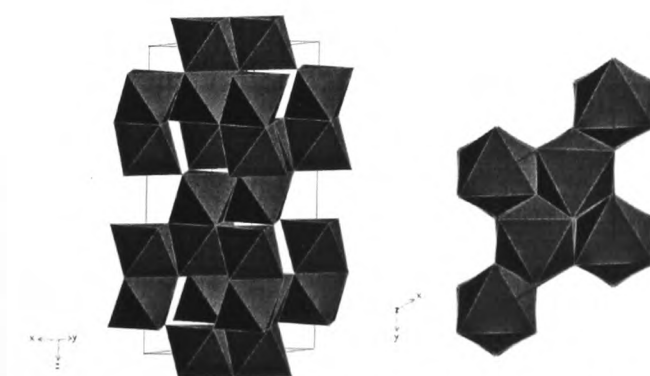


**Figure 6.9** Two representations of the Karelite form of  $\alpha$ - $V_2O_3$

An EDX scan of the reduced vanadium oxide provides evidence for the presence of only vanadium and oxygen and is similar to the spectrum obtained for the amorphous MVS product.

### 6.3.2 Preparation of Reduced Niobium Oxide, $\text{NbO}_2$

Microcrystalline niobium oxide was prepared as described in **Section 6.1** *via* heating the precursor at  $750^\circ\text{C}$  for 30 minutes under a dynamic atmosphere of  $\text{H}_2$  gas. The product afforded is a dark-grey microcrystalline solid. The powder X-ray diffraction spectrum shown in **Figure 6.10** confirms the presence of single-phase, crystalline  $\text{NbO}_2$  (**Figure 6.11**) by comparison of the data with that contained on the Inorganic Crystal Structural Database.<sup>[15]</sup> The X-ray diffraction data is consistent with that reported by Bolzan *et al.* for the synthesis of  $\text{NbO}_2$  from fully oxidised  $\text{Nb}_2\text{O}_5$  upon reduction under flowing hydrogen at  $950^\circ\text{C}$  for 48 hours.<sup>[18]</sup>

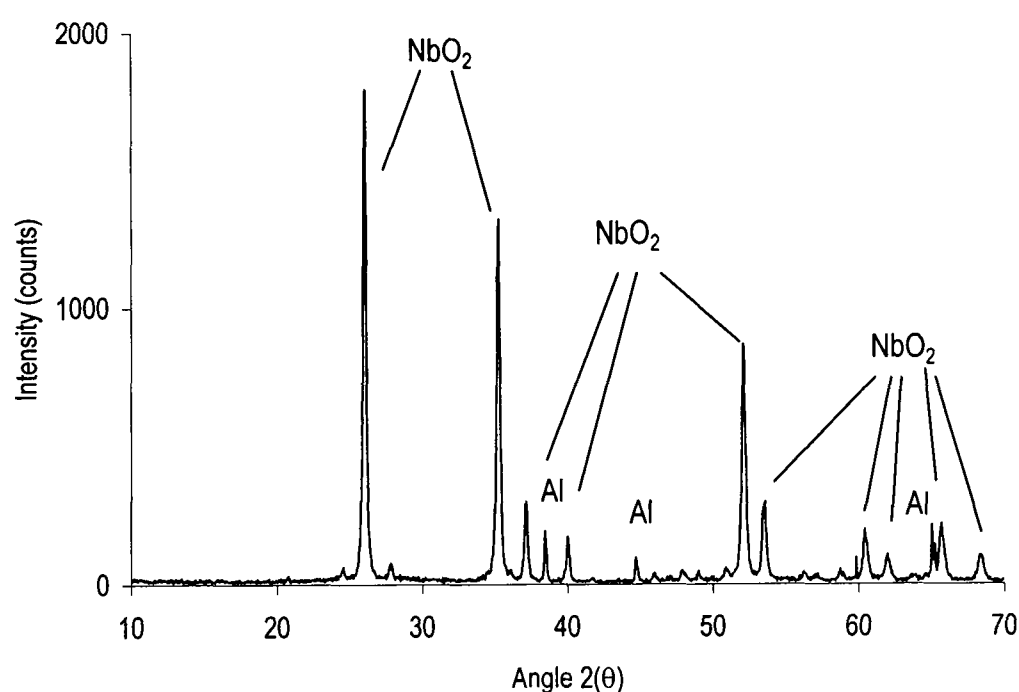


**Figure 6.10** Powder X-ray diffraction plot for reduced niobium oxide ( $\text{NbO}_2$ )

Thus, the oxide has been identified as  $\text{NbO}_2$ , which adopts a regular rutile structure in high-temperature forms while the low temperature structures (below  $800^\circ\text{C}$ ) are usually described as ‘distorted rutiles’. Despite the relative stability of the +4 oxidation state, at high temperatures  $\text{NbO}_2$  is rapidly oxidised under air to  $\text{Nb}_2\text{O}_5$  or can be further reduced to the Nb(II) species,  $\text{NbO}$ .<sup>[18]</sup>

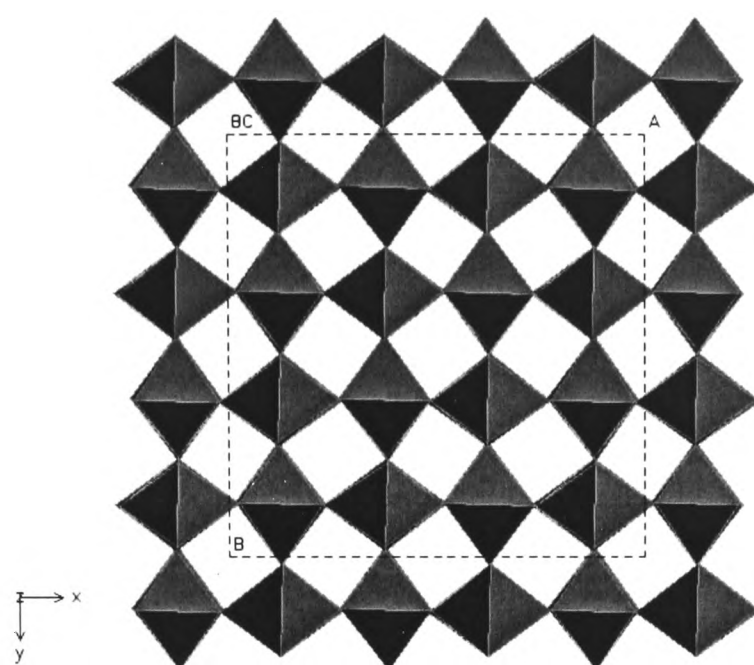


**Figure 6.11** Projection of the rutile-structure of the reduced oxide  $\text{NbO}_2$  along the  $c$  axis. The polyhedra represent octahedral  $\text{NbO}_6$  units.

The rutile structure is one of the most common transition metal oxide structures. The ideal structure consists of corner sharing  $\text{MO}_6$  octahedra which form long ‘square tunnels’ along the  $c$  axis (**Figure 6.11**).<sup>[17, 19]</sup> HRTEM studies reveal that the  $\text{NbO}_2$  particles comprise of nanocrystalline spheroidal units with diameters ranging between 50 and 150 nm. In addition, an EDX scan confirmed detection only of the two composite elements in the observed spectrum.

Thus, the reduced, crystalline niobium oxide  $\text{NbO}_2$  has been identified as the product from the amorphous MVS synthesised  $\text{NbO}_x$  starting material. These properties suggest that the sulfidisation process should result in formation of  $\text{MS}_2$  structures exhibiting IF-like properties as for the vanadium oxide  $\alpha\text{-V}_2\text{O}_3$ .

### 6.3.3 Preparation of Tantalum Oxide, TT- $\text{Ta}_2\text{O}_5$

The amorphous tantalum oxide was treated as described in **Section 6.1** by heating at  $750^\circ\text{C}$  for 30 minutes under a dynamic atmosphere of  $\text{H}_2$  gas. The material afforded was a blue-black microcrystalline solid.

The powder X-ray diffraction spectrum for the product is shown in **Figure 6.12**. The data confirm the presence of a single-phase, crystalline material by comparison with the data contained on the Inorganic Crystal Structural Database.<sup>[15]</sup> The X-ray

diffraction data correlate with that reported by Hummel *et al.* for the synthesis of TT-Ta<sub>2</sub>O<sub>5</sub>, prepared *via* a reaction between layered 2H-TaS<sub>2</sub> and water under high pressure at 200°C.[20] Hence, the product is fully oxidised with Ta in the +5 oxidation state.

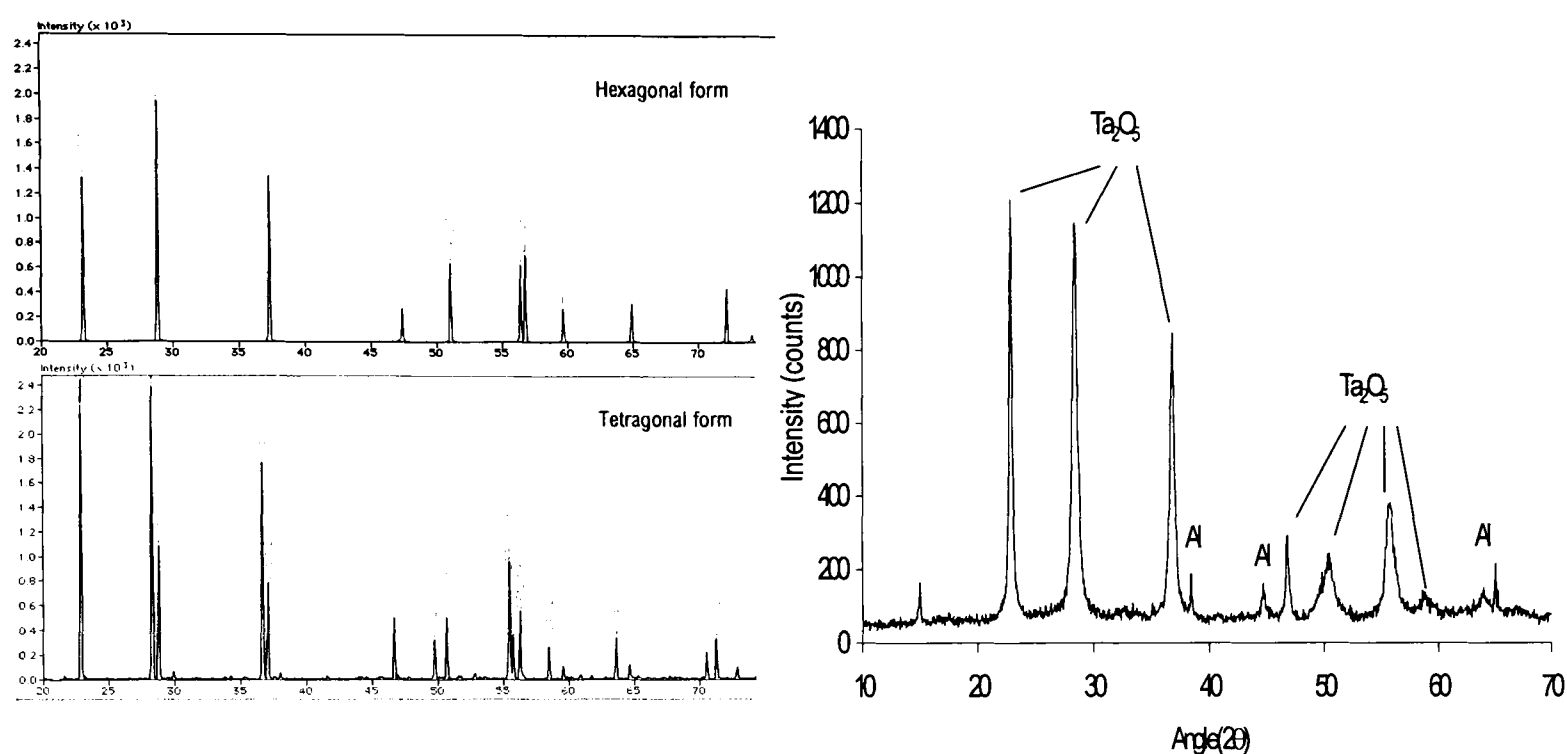


**Figure 6.12** Calculated X-ray diffraction plots for the hexagonal and tetragonal forms of tantalum oxide (T-Ta<sub>2</sub>O<sub>5</sub> and TT-Ta<sub>2</sub>O<sub>5</sub>) and the observed powder X-ray diffraction plot for reduced tantalum oxide (TT-Ta<sub>2</sub>O<sub>5</sub>)

Pure tantalum oxide (Ta<sub>2</sub>O<sub>5</sub>) has a number of structurally distinct polymorphs including a high temperature form, first reported by Magnéli in 1952 which crystallises in a rhombohedral space group.[21] The  $\delta$ -form of Ta<sub>2</sub>O<sub>5</sub> has several different types including the high-temperature (HT) and low-temperature (LT) tetragonal forms which all have similar parent structures in which the metal atoms are arranged in sheets and are surrounded by oxygen atoms arranged to form either distorted octahedral or pentagonal bipyramidal polyhedra.[22]

The oxide TT-Ta<sub>2</sub>O<sub>5</sub> crystallises in the space group P6/mmm with hexagonal symmetry and 75% oxygen occupancy. It consists of repeating hexagonal bipyramidal units as shown in **Figure 6.11**. This hexagonal arrangement undergoes a phase transition upon heating to 900°C to the T-Ta<sub>2</sub>O<sub>5</sub> (high temperature) form, which crystallises in an orthorhombic space group Pmm2 and consists of tantalum atoms with a pentagonal-bipyramidal array of O-atoms, interspersed with distorted TaO<sub>6</sub> octahedra.[20]

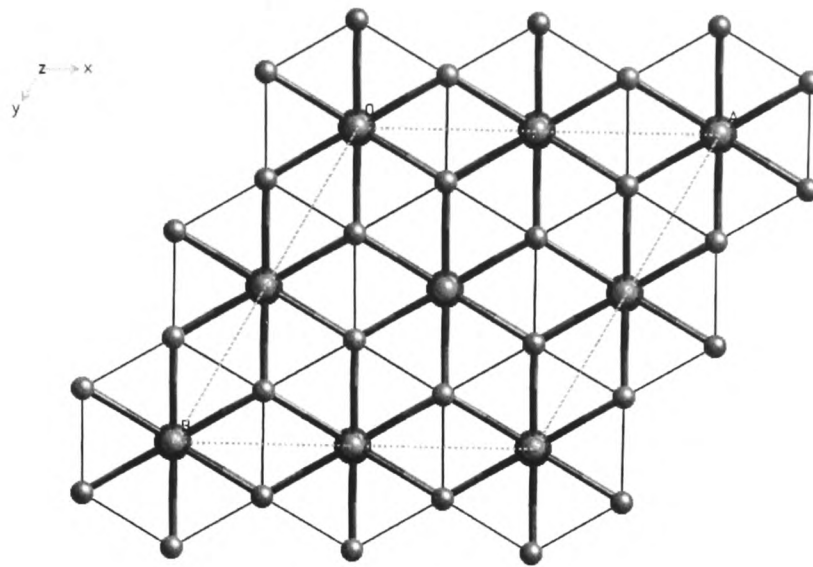


**Figure 6.11** Hexagonal form of TT-Ta<sub>2</sub>O<sub>5</sub> which crystallises in the P6/mmm space group. Ta atoms (large spheres) O atoms (small spheres).

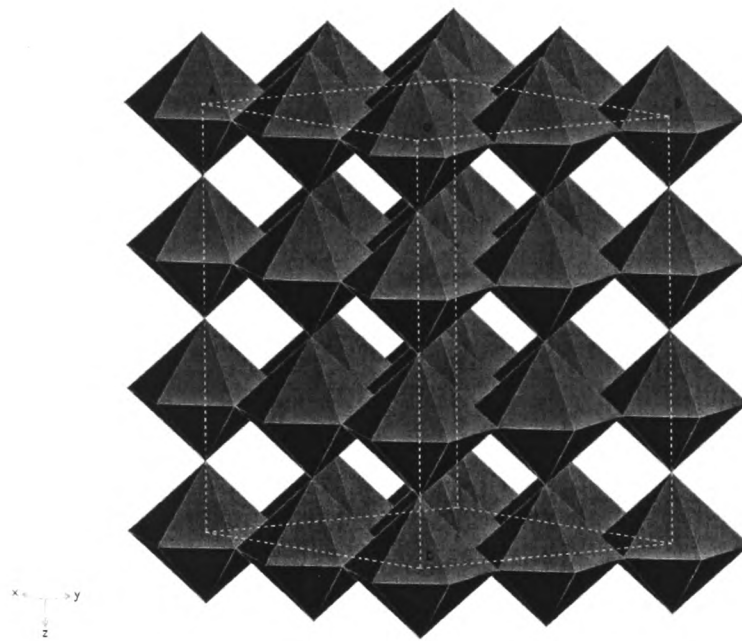


**Figure 6.12** Hexagonal form of Ta<sub>2</sub>O<sub>5</sub> assigned to the MVS synthesised tantalum oxide. It crystallises in the P6/mmm space group and the layers are made up of a series of edge sharing hexagonal bipyramids.

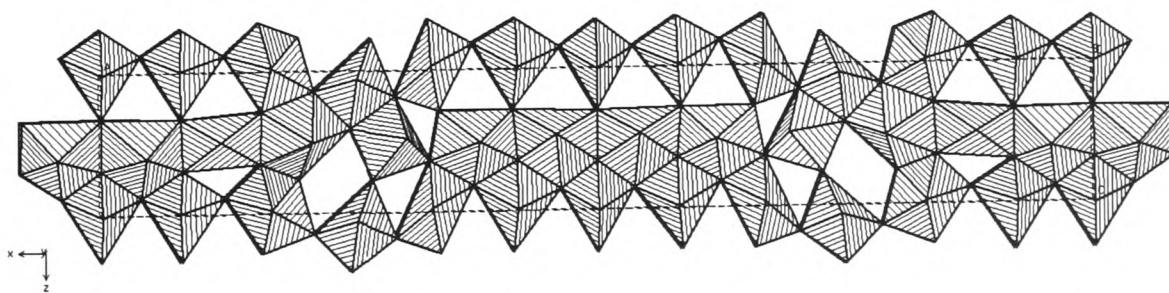


**Figure 6.13** Tetragonal form of Ta<sub>2</sub>O<sub>5</sub> which crystallises in the Pmm2 space group. The structure is derived from a complex network of pentagonal bipyramidal co-ordination polyhedra and distorted octahedra.



The EDX scan of the tantalum oxide is similar to the spectrum obtained for the amorphous MVS product confirming the presence of tantalum and oxygen only.

#### 6.4 Preparation of Group 5 Metal Sulfides ( $\text{MS}_2$ )

The metals vanadium, niobium and tantalum are all capable of forming layered  $2\text{H-MS}_2$  type sulfides analogous to those of molybdenum and tungsten.[2, 17] Thus, the crystalline oxides  $\alpha\text{-V}_2\text{O}_3$ ,  $\text{NbO}_2$  and  $\text{TT-Ta}_2\text{O}_5$  were sulfidised using an analogous procedure to that described in Chapter 5 in an attempt to form IF- $\text{MS}_2$  encapsulates ( $\text{M} = \text{V}$ ,  $\text{Nb}$  and  $\text{Ta}$ ). The layered arrangement of  $\text{VS}_2$  is shown below in **Figure 6.18**.

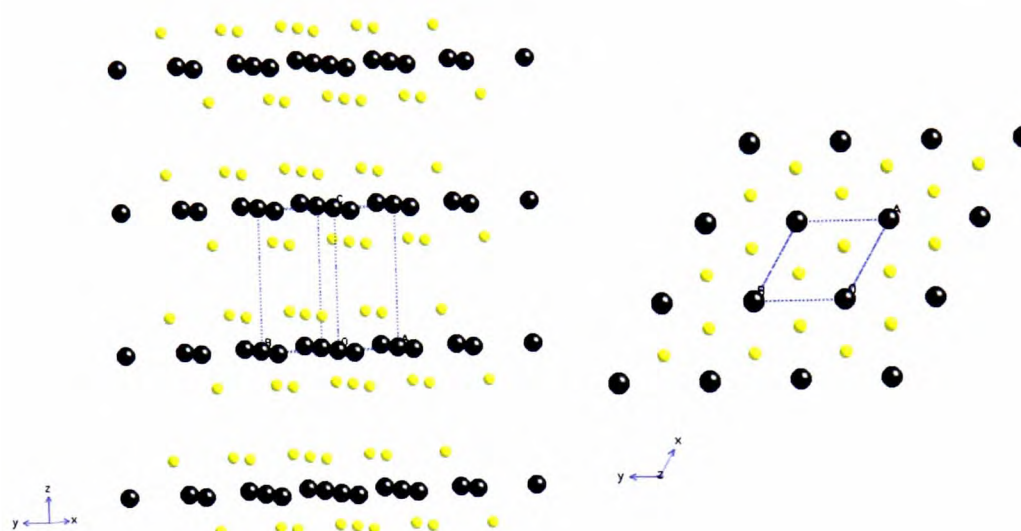


**Figure 6.18** Schematic of the layered structure of IF-like vanadium sulfide ( $\text{VS}_2$ )

The layer structures of transition metal sulfides are of two main types exhibiting either octahedral or trigonal prismatic co-ordination of the metal atoms.  $\text{TiS}_2$ ,  $\text{ZrS}_2$  and  $\text{HfS}_2$  exhibit the octahedral arrangement. Structures exhibiting the trigonal prismatic arrangement include  $\text{MoS}_2$ ,  $\text{WS}_2$  and  $\text{NbS}_2$ .<sup>[17]</sup>

### 6.4.1 Sulfidisation of the Oxide $\alpha\text{-V}_2\text{O}_3$

Following sulfidisation of the  $\alpha\text{-V}_2\text{O}_3$  oxide phase, a black crystalline solid was isolated. The powder X-ray diffraction spectrum is shown in **Figure 6.19**. The data confirms the presence of both  $\text{VS}_2$  and  $\text{V}_2\text{O}_3$  by comparison with the data contained on the Inorganic Crystal Structural Database.[15] The signals are consistent with those reported by Ouvrard *et al.* for the rhombohedral form of  $\text{VS}_2$  which crystallises in the  $\bar{R}3m$  space group.[23]

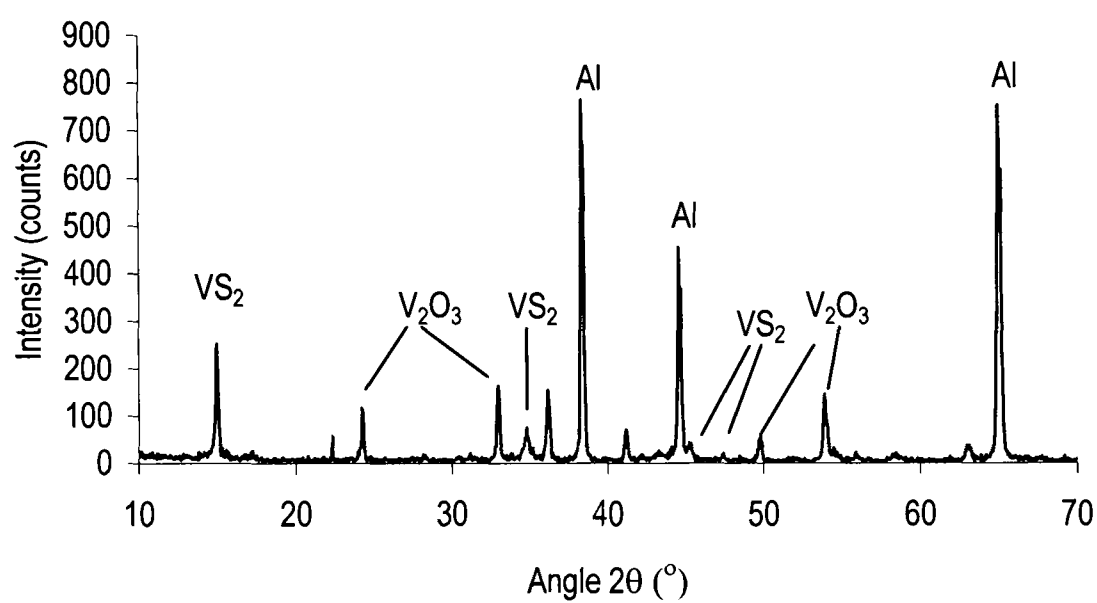


**Figure 6.19** Powder X-ray diffraction spectrum of sulfidised  $\alpha\text{-V}_2\text{O}_3$

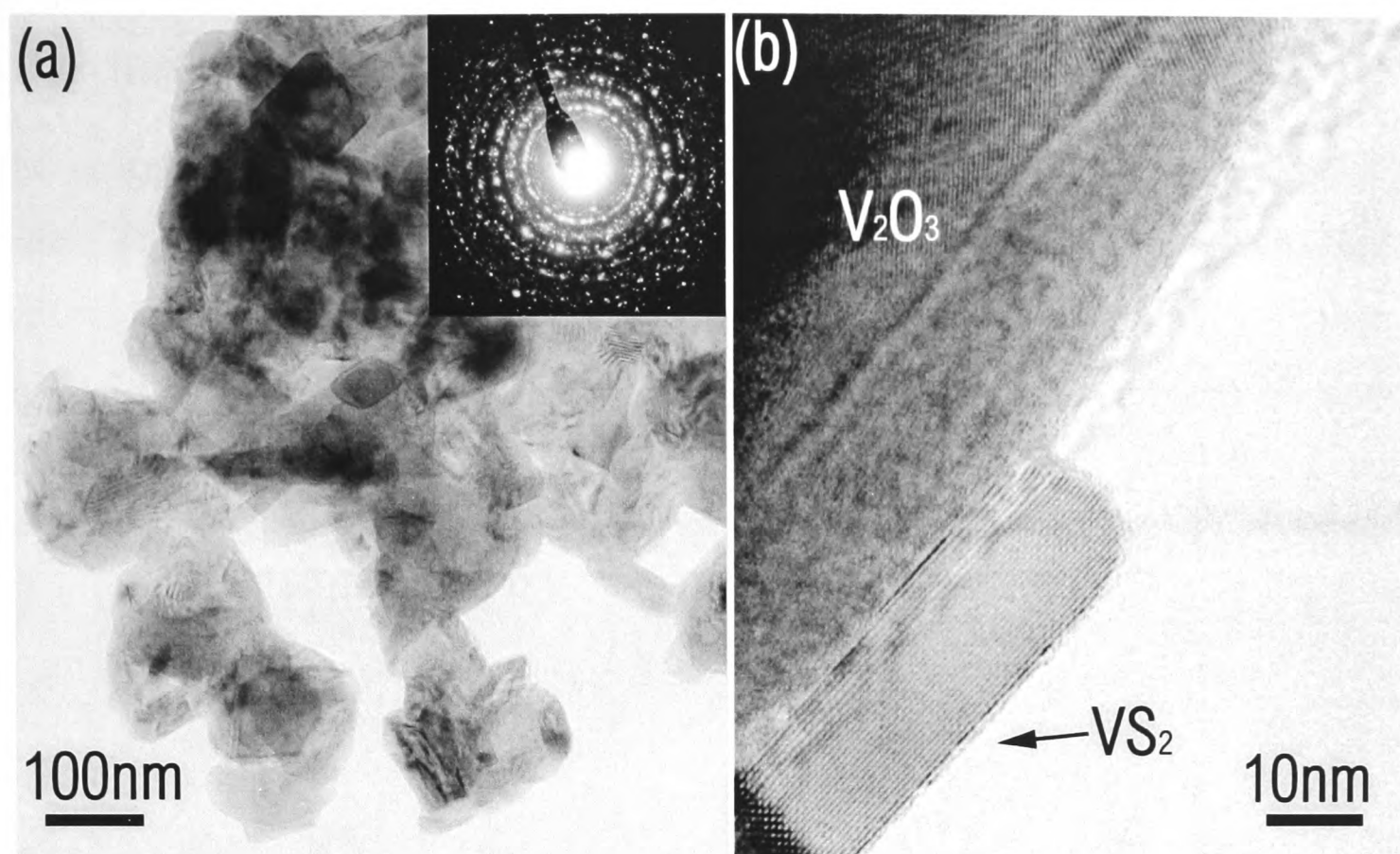


**Figure 6.16** Micrographs showing (a) the general particle size and SAED pattern of  $\alpha$ - $V_2O_3$  particles (b) higher magnification micrograph demonstrating the formation of layered  $VS_2$  material on the surface of a  $V_2O_3$  particle.

HRTEM studies provide evidence that sulfidisation of  $V_2O_3$  has resulted in the formation of a layered  $VS_2$  structure as shown in the micrographs in **Figure 6.16**. **Figure 6.16 (a)** provides a representative example of sulfidised  $V_2O_3$  particles. They display spherical morphologies with diameters of approximately 100 nm and in general consist of non-sulfidised  $V_2O_3$  interspersed with isolated regions of layered  $VS_2$ . **Figure 6.16 (b)** shows one such region under higher magnification. The arrow indicates a region of  $VS_2$  material which has grown from the oxide surface. The inter-layer (V-V) distance of 0.61 nm is consistent with that reported for IF- $VS_2$ [2] although there is no evidence of curvature of the sulfide around the oxide material. Although HRTEM illustrated that some  $VS_2$  material was produced during the sulfidisation process, only approximately 5 % of the oxide material demonstrated any significant sulfidisation. The lack of any quantitative formation of IF- $VS_2$  may have been a result of a mismatch between the oxide structure ( $V_2O_3$ ) and that required for IF- $VS_2$  propagation.

An EDX scan of the sulfidised material also implied the presence of both sulfide and oxide within the sample given that signals attributable to V, S and O were observed.



### 6.4.2 Sulfidisation of the Oxide NbO<sub>2</sub>

The material produced after the sulfidisation of reduced NbO<sub>2</sub> is a black crystalline solid. The powder X-ray diffraction spectrum is shown in **Figure 6.19**. The data confirm the presence of both NbS<sub>2</sub> and niobium oxide by comparison with the data contained on the Crystal Structural Database.[15] Thus, a structural change has also occurred within the oxide upon sulfidisation. The signals are consistent with those reported by Jellinek for the hexagonal form of NbS<sub>2</sub> which crystallises in the P6<sub>3</sub>/mmm space group. [24]

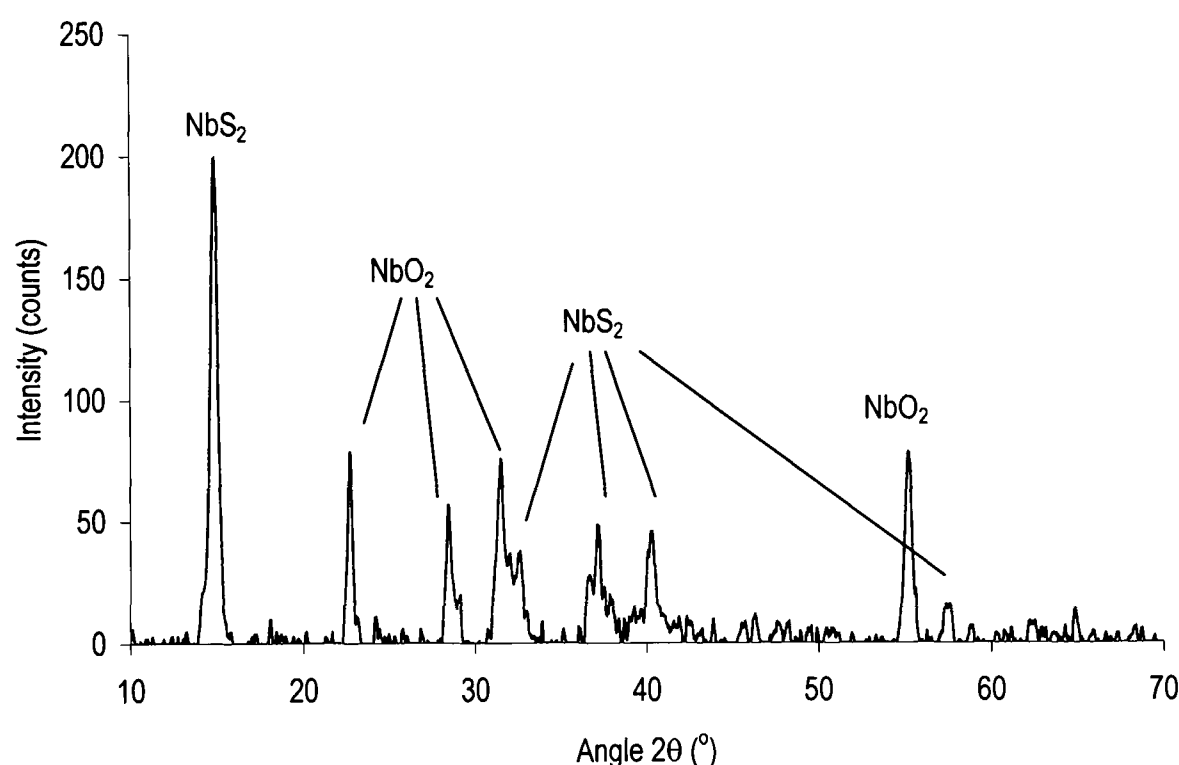


**Figure 6.19** Powder X-ray diffraction plot for IF-like niobium sulfide (NbS<sub>2</sub>)

HRTEM studies provide evidence that sulfidisation of NbO<sub>2</sub> has resulted in the formation of IF-like NbS<sub>2</sub> nanoparticles as shown in the micrographs in **Figure 6.20**. **Figure 6.20 (a)** provides a representative example of a sulfidised NbO<sub>2</sub> particle, which displays a distorted spherical morphology with dimensions of approximately 50 nm by 100 nm. The arrow indicates a region displaying possible formation of layered NbS<sub>2</sub> material. The micrograph in **Figure 6.20 (b)** shows a hollow IF-NbS<sub>2</sub> encapsulate containing approximately 10 layers. The inter-layer (Nb-Nb) distance of 0.594 nm is consistent with that reported for the (002) spacing 2H-NbS<sub>2</sub>. [24] There is evidence of curvature of the sulfide around the cavity as well as discontinuous sulfide growth towards the top of the micrograph. A Fast Fourier Transform (FFT) operation on the layered sulfide region results in the diffraction pattern displayed in the inset. This

shows spots resulting from reflections in the  $\langle 002 \rangle$  and  $\langle 00\bar{2} \rangle$  lattice planes, which are typical of those expected from IF-like materials.

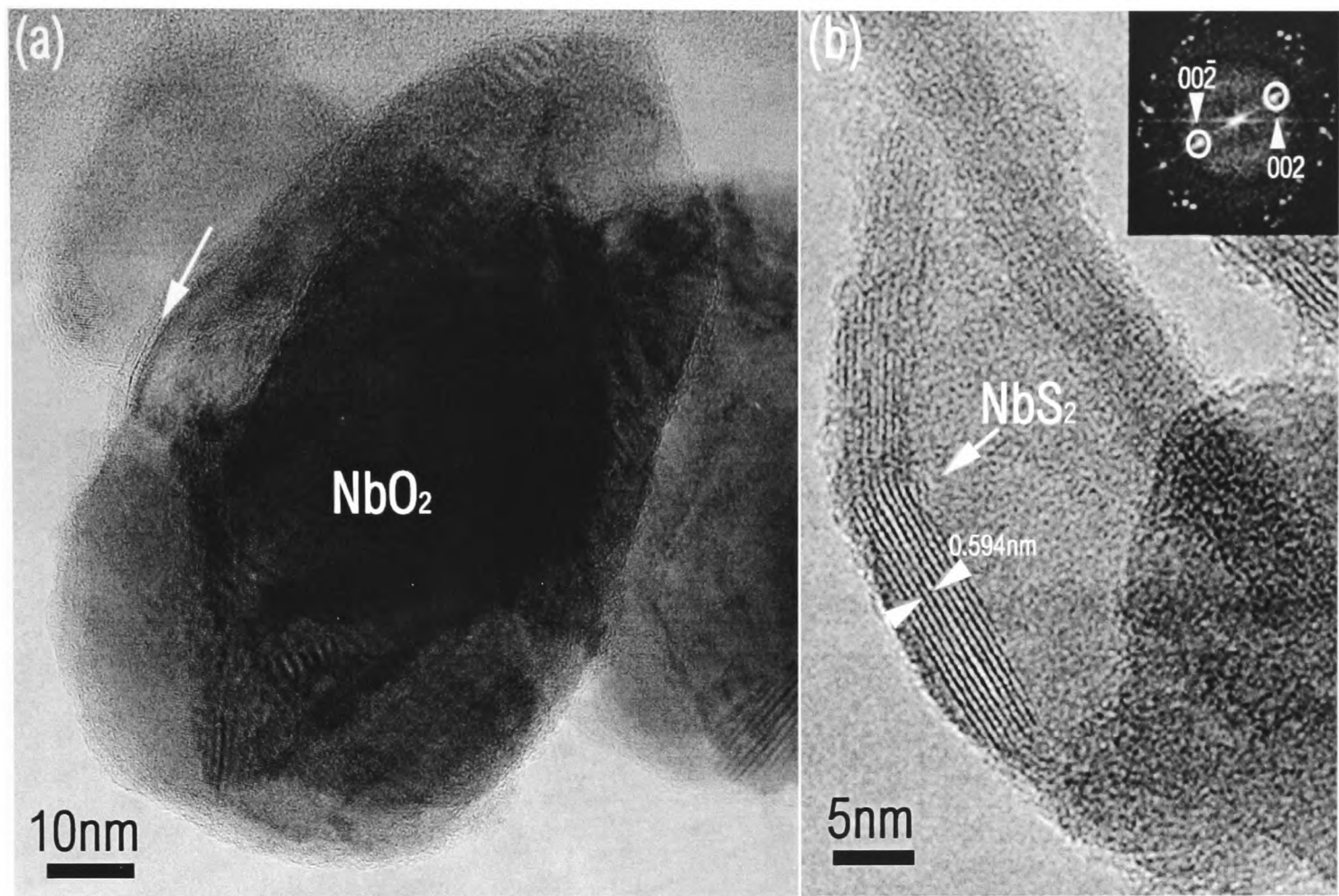


**Figure 6.20** (a) Micrograph demonstrating the morphology of a reduced  $\text{NbO}_2$  particle exposed to sulfidisation. The arrow denotes a region, which shows evidence of partial sulfidisation. (b) Micrograph and FFT SAED pattern (inset) of IF- $\text{NbS}_2$  prepared from a MVS synthesised precursor. The arrows show the inter-layer spacings between successive Nb-layers within an IF- $\text{NbS}_2$  encapsulate of approximately 10 layers.

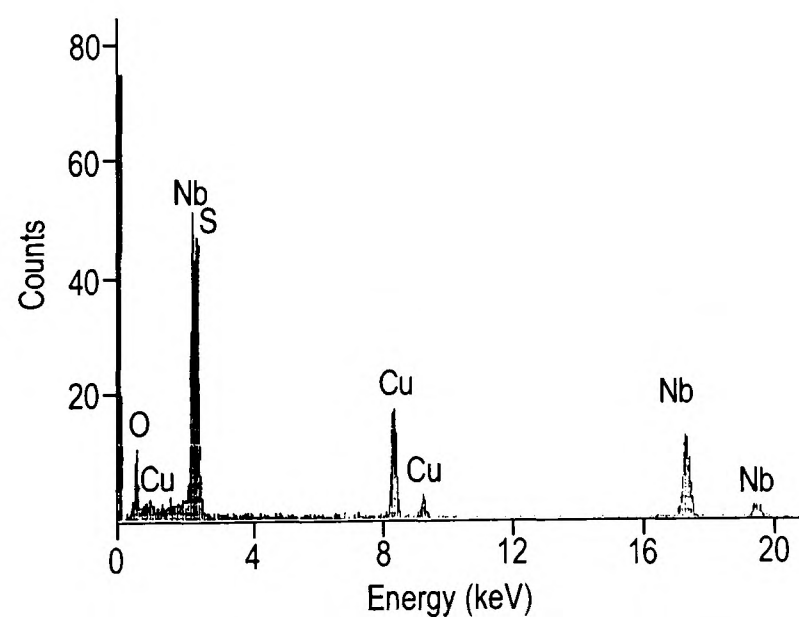


**Figure 6.21** EDX spectrum for the sulfidised  $\text{NbO}_2$  sample

### 6.4.3 Sulfidisation of the Oxide TT-Ta<sub>2</sub>O<sub>5</sub>

The material produced after the sulfidisation of reduced Ta<sub>2</sub>O<sub>5</sub> is a blue-black crystalline solid. The powder X-ray diffraction spectrum is shown in **Figure 6.22**. The data confirm the presence of both TaS<sub>2</sub> and Ta<sub>2</sub>O<sub>5</sub> by comparison with the data contained on the Inorganic Crystal Structural Database.[15] The signals are consistent with those reported by Meetsma for the hexagonal form of TaS<sub>2</sub>, which crystallises in the P6<sub>3</sub>/mmm space group. [25]

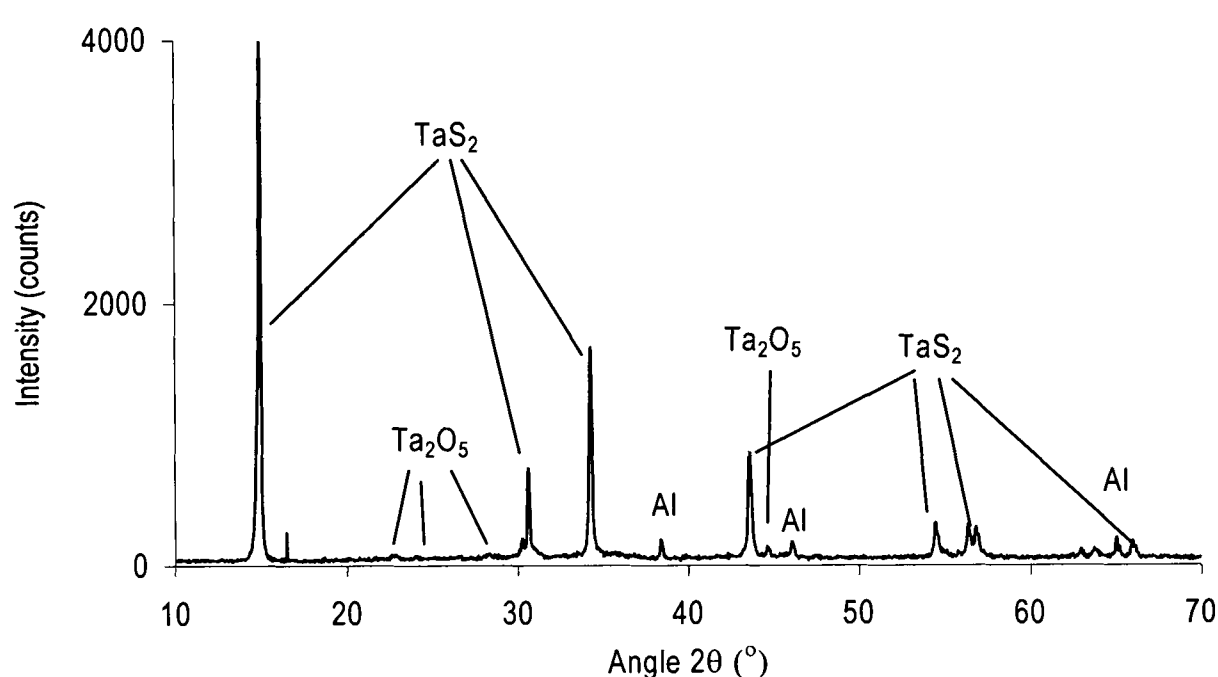


**Figure 6.21** Powder X-ray diffraction plot for sulfidised Ta<sub>2</sub>O<sub>5</sub>

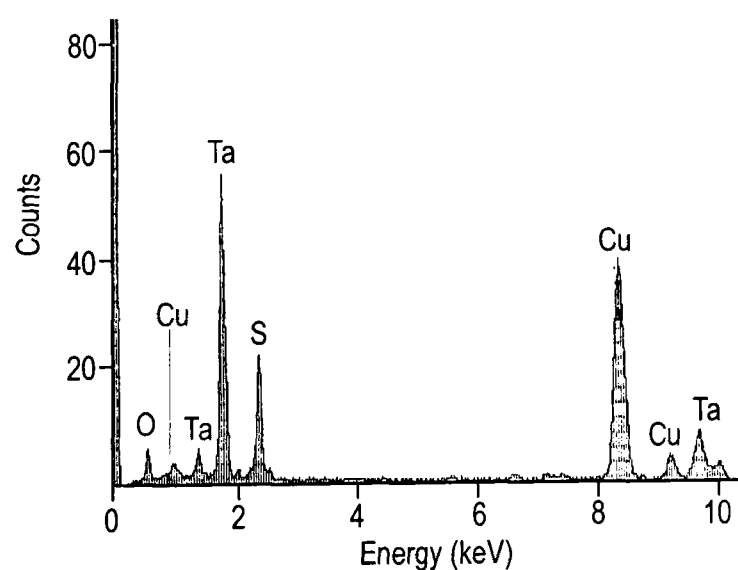


**Figure 6.21** EDX spectrum for sulfidised Ta<sub>2</sub>O<sub>5</sub>

An EDX scan of the crystalline tantalum oxide after sulfidisation shown in **Figure 6.21** confirms the presence of tantalum, sulfur and oxygen.

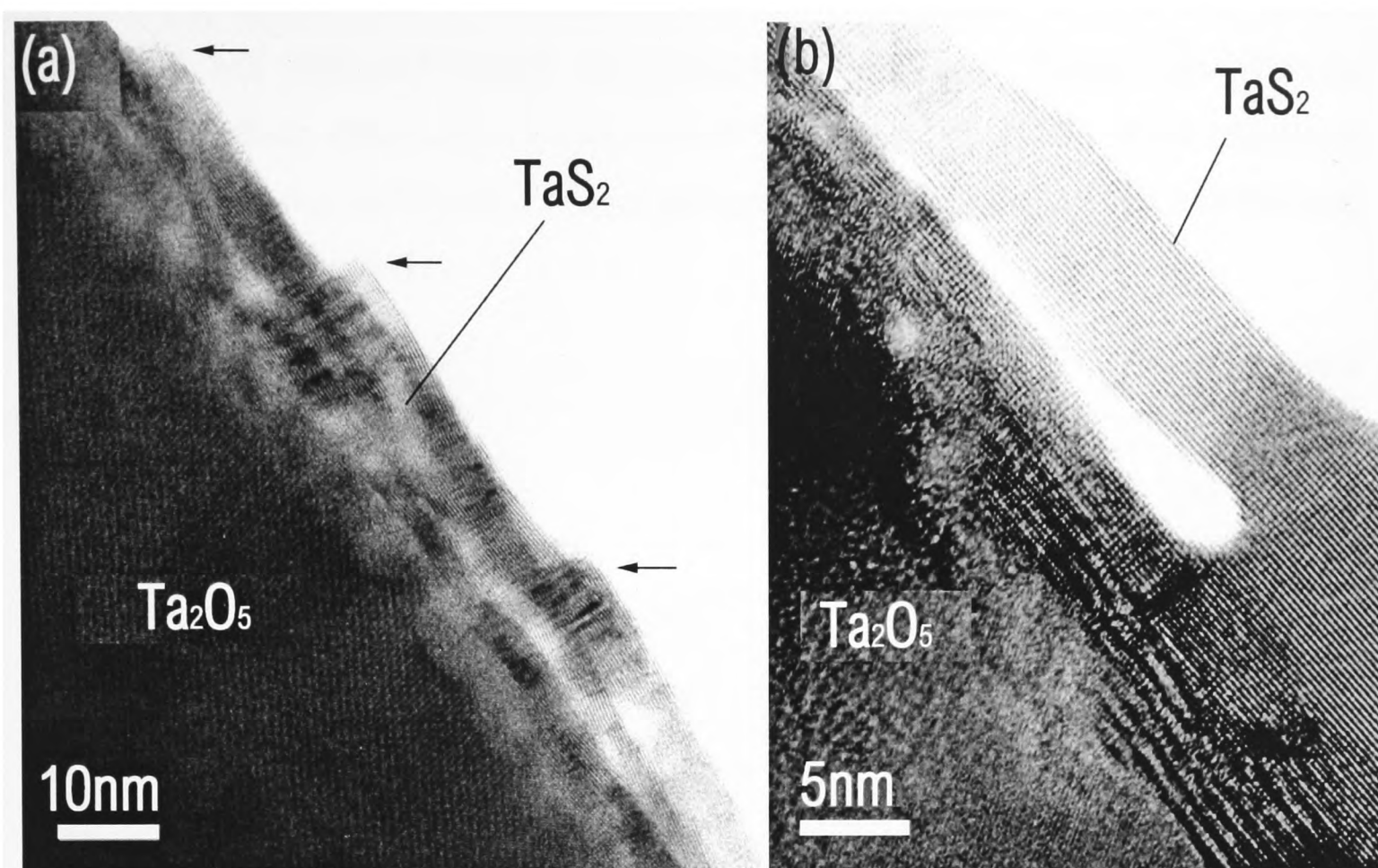


**Figure 6.22** (a) HRTEM micrograph illustrating the material produced following sulfidisation of the  $\delta$ - $\text{Ta}_2\text{O}_5$  reduced oxide.  $2\text{H-TaS}_2$  is clearly visible on the surface of the encapsulated reduced oxide, however, the layers of  $\text{TaS}_2$  tend to overlap and discontinuities are evident; (b) shows an enlargement of one region of the material and demonstrates intergrowth between the oxide and sulfide phases as well as a void which has become encapsulated beneath the  $\text{TaS}_2$  structure.

The micrographs in **Figure 6.22** demonstrate the discontinuous nature of  $\text{TaS}_2$  growth and a lack of curvature in the structure. **Figure 6.22** (a) provides evidence for a number of discontinuous sulphide growth fronts, which overlap. The inter-layer distance of 0.605 nm is consistent with that reported for  $\text{TaS}_2$  by Meetsma[25] although there is a distinct lack of curvature. Instead of following the morphology of the oxide particle, the  $\text{TaS}_2$  layers cease growing at the points indicated by arrows. **Figure 6.22** (b) displays a region under higher magnification and demonstrates that intergrowth between oxide and sulphide has occurred. The presence of a void in the structure suggests that the oxide supply has been exhausted in that particular area.

In **Figure 6.23** below, the regions of discontinuous growth are shown more clearly. **Figures 6.23** (a) and (e) illustrate discontinuities in sulphide growth. A magnification of the region of oxide-sulphide intergrowth is shown in **Figure 6.23** (b) where the hexagonal sub-structure of the oxide and layered structure of the sulphide are clearly distinguishable. Utilising the known parameters for the crystal structures of TT- $\text{Ta}_2\text{O}_5$



and  $\text{TaS}_2$  it has been possible to simulate this interface. **Figure 6.22 (c)** shows that the simulated and observed images are remarkably similar. Finally, the electron diffraction pattern obtained by a Fast Fourier Transformation (FFT) of the interfacial region displays the combination of spot patterns expected for the layered sulphide and hexagonal tantalum oxide.

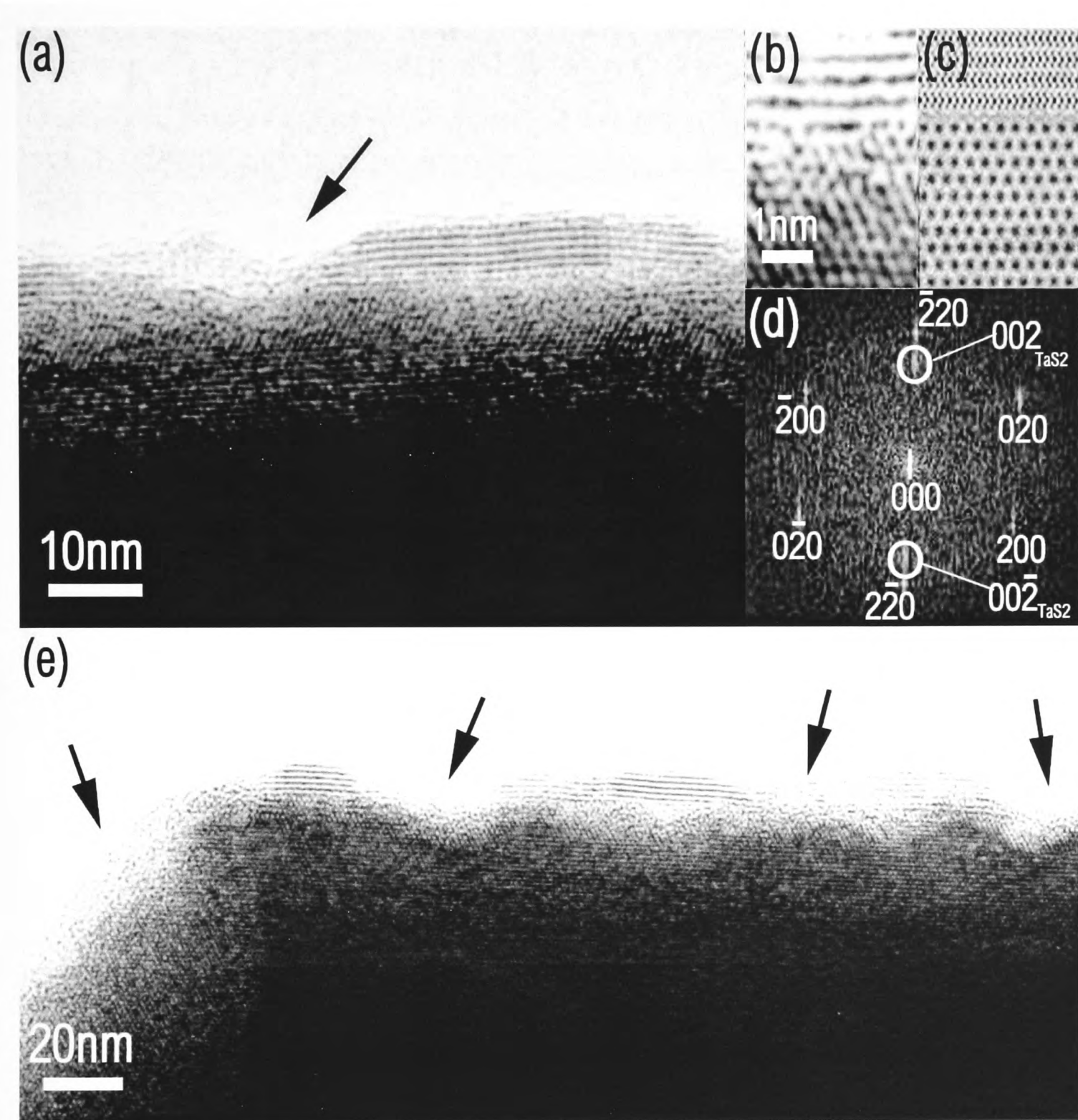


**Figure 6.23** (a) Micrograph demonstrating the presence of discontinuous  $2\text{H-TaS}_2$  on the oxide surface; (b) enlargement of the interfacial region of the sulfide/oxide and (c) simulation of the region showing the hexagonal nature of the encapsulated oxide; (d) FFT SAED pattern exhibiting a diffraction pattern typical of a 6-fold symmetrical species ( $\text{Ta}_2\text{O}_5$ ) and the (002) reflections typically found in layered transition metal sulfides ( $\text{TaS}_2$ ); (e) lower magnification detail of the surface showing the frequency of discontinuities in the sulfide layers.

Thus, the tantalum oxide precursor does show evidence of intergrowth with layered- $\text{TaS}_2$ , and the propensity to form IF-like structures. There is, however, a distinct lack of curvature in the observed sulfide. Possible explanations for this behaviour include the fact that TT- $\text{Ta}_2\text{O}_5$  contains tantalum in the +5 oxidation state and is not a 'reduced oxide'. This situation could have precluded the diffusion-controlled growth process in that the dearth of surface defects in the material prevented diffusion of sulfide species into the parent oxide. By annealing the oxide under more reducing conditions, it may be possible to isolate an alternative phase, such as  $\text{TaO}_2$ , with an oxide structure more accessible towards the sulfidisation process.

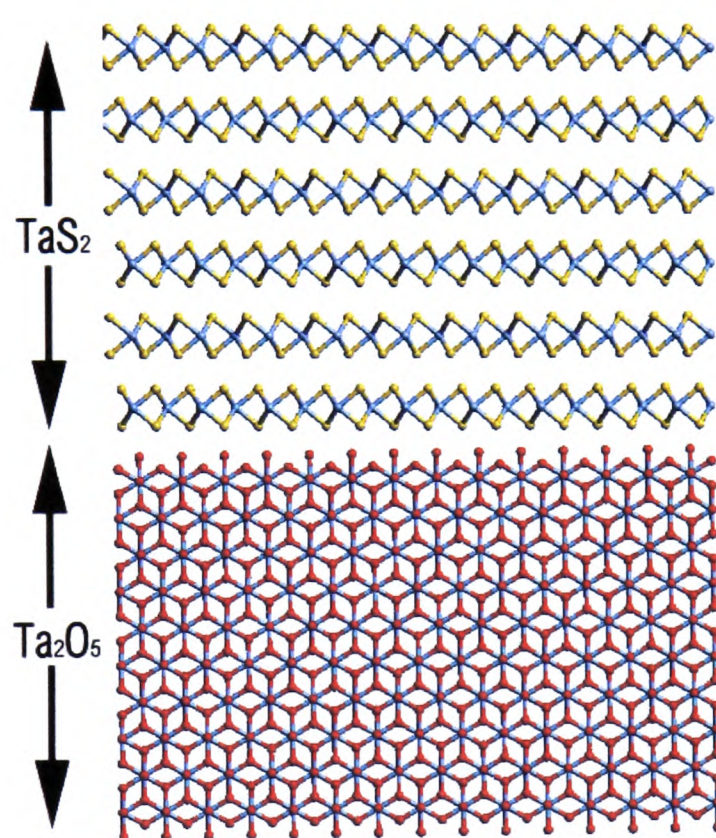


**Figure 6.24** Schematic of the interfacial region between  $\text{TaS}_2$  and  $\text{Ta}_2\text{O}_5$  phases

## 6.5 Attempted Sulfidisation of Amorphous MVS Products

For completion, attempts were made to sulfidise the amorphous transition metal oxides prior to crystallisation in an effort to see if IF- $\text{MS}_2$  materials could result after an *in situ* crystallisation of the amorphous oxide. The oxides were heated at  $750^\circ\text{C}$  under an atmosphere of  $\text{H}_2\text{S}$  for 40 minutes then slowly cooled to room temperature. Neither the tantalum nor the vanadium oxides showed any evidence of sulfidisation *via* this route, however, analysis of the niobium oxide product yielded some interesting results.

The material produced after the sulfidisation of amorphous niobium oxide is a black crystalline solid. The powder X-ray diffraction spectrum is shown in **Figure 6.25**. The data confirm the presence of  $\text{NbS}_2$  by comparison with the data contained on the Inorganic Crystal Structural Database.[15] The signals are consistent with those reported by Jellenik for the hexagonal form of  $\text{NbS}_2$  which crystallises in the  $\text{P6}_3/\text{mmm}$  space group as observed for the sample obtained after pre-crystallisation of the oxide, described in **Section 6.4.2**. [24]

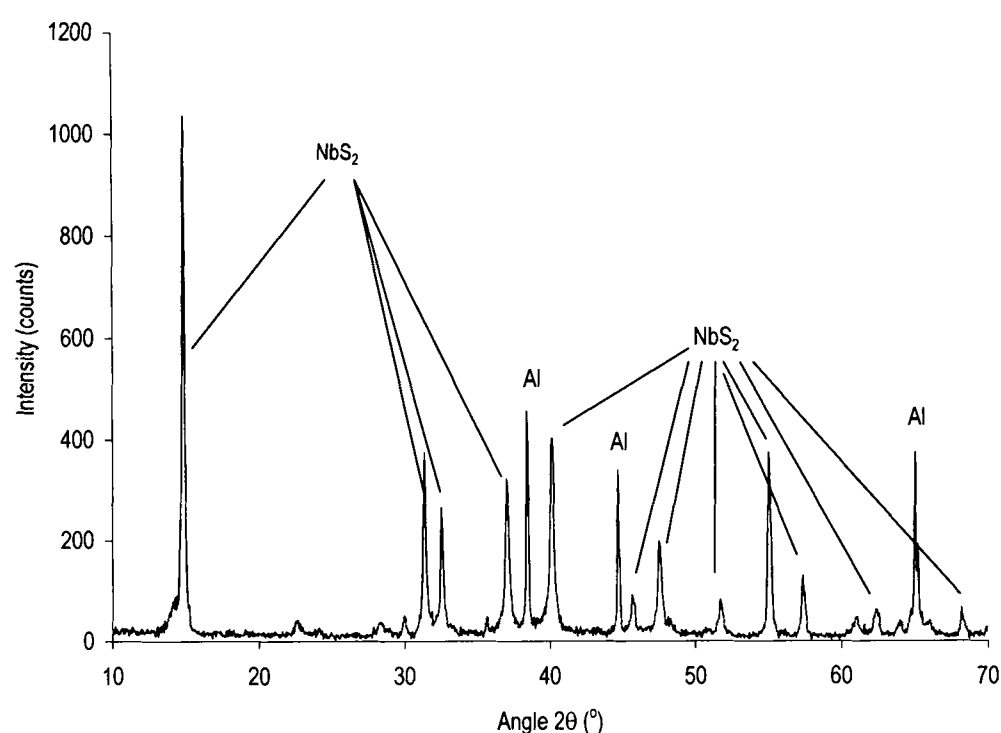


**Figure 6.25** Powder X-ray diffraction plot for IF-like niobium sulfide ( $\text{NbS}_2$ ) produced directly from amorphous niobium oxide

Compared to the powder X-ray diffraction data from IF- $\text{NbS}_2$  material obtained after pre-annealing the oxide, the conversion to IF- $\text{NbS}_2$  is much greater, with virtually no evidence of any unreacted oxide. An EDX scan of the material shows signals assignable to the elements Nb and S, confirming the complete conversion to sulfide. One reason for this difference in behaviour might be that the particle size in the amorphous material is smaller than that observed in the crystalline oxide, exposing more surface oxide to sulfidisation. The morphology of the resulting sulfide, however, is virtually identical to that found for the pre-crystallised sample.

## 6.6 Summary

This chapter has described a novel method for the preparation of amorphous transition metal oxides using the MVS technique. Such materials have been fêted as possible precursors for forming IF-like materials. The elemental compositions, particle sizes and morphologies of these materials have been determined using powder X-ray diffraction, HRTEM and EDX analysis. Annealing the amorphous oxides in a reducing atmosphere was successful in producing the nanocrystalline oxides identified as  $\alpha$ -V<sub>2</sub>O<sub>3</sub>, NbO<sub>2</sub> and TT-Ta<sub>2</sub>O<sub>5</sub> from their powder X-ray diffraction spectra.

The preliminary investigations described here have illustrated that there are a number of factors that determine the nature of the transition metal sulfide formed and whether or not IF-like materials result, like those observed for common forms of WS<sub>2</sub> and MoS<sub>2</sub> including particle size and oxide structure. All of the sulfidised materials displayed evidence of intergrowth between oxide and layered-sulfide, a pre-requisite for the growth of IF-MS<sub>2</sub> species and at least one of the oxides (NbO<sub>2</sub>) clearly formed IF-like nanoparticles, which were observed by HRTEM.

The oxides  $\alpha$ -V<sub>2</sub>O<sub>3</sub> and TT-Ta<sub>2</sub>O<sub>5</sub> did not display evidence of significant quantities of IF-like material, although layered sulfides were observed. This may be a result of inappropriate oxide morphology and, in the case of tantalum oxide, due to the fully oxidised form, which have inhibited the diffusion growth mechanism of IF-TaS<sub>2</sub>.

It may well be possible to induce IF-formation from the vanadium and tantalum oxides by using more reducing conditions during the annealing stages to produce crystalline oxides exhibiting structures more amenable to sulfidisation.



## 6.7 References for Chapter 6

- [1] Y. Feldman, G. L. Frey, M. Homyonfer, V. Lyakhovitskaya, L. Marguilis, H. Cohen, G. Hodes, J. L. Hutchison and R. Tenne, *J. Am. Chem. Soc.*, **118** (1996) 5362.
- [2] M. Homyonfer, *Ph.D. Thesis*, Weizmann Institute, Rehovot, Israel, (1998).
- [3] L. Marguilis, G. Salitra and R. Tenne, *Nature*, **365** (1993) 113.
- [4] J. Sloan, J. L. Hutchison, R. Tenne, Y. Feldman, T. Tsirlina and M. Homyonfer, *J. Solid State Chem.*, **144** (1999) 100.
- [5] R. Tenne, *Adv. Mater.*, **7** (1995) 965.
- [6] R. Tenne, H. M. and Y. Feldman, *Chem. Mater.*, **10** (1998) 3225.
- [7] A. P. E. York, J. Sloan and M. L. H. Green, *J. Chem. Soc. Chem. Commun.*, (1999) 269.
- [8] P. S. Skell, *J. Am. Chem. Soc.*, **85** (1963) 1023.
- [9] P. S. Skell and L. D. Westcott Jr., *J. Am. Chem. Soc.*, **88** (1965) 2829.
- [10] P. S. Skell and R. R. Engel, *J. Am. Chem. Soc.*, **88** (1965) 3749.
- [11] P. S. Skell and R. R. Engel, *J. Am. Chem. Soc.*, **88** (1965) 4883.
- [12] P. L. Timms, *J. Chem. Soc. Chem. Comm.*, (1968) 1025.
- [14] R. Tenne, L. Marguilis, M. Genut and G. Hodes, *Nature*, **360** (1992) 444.
- [15] I. C. S. Database, International Centre for Diffraction Data 1982.
- [16] C. E. Rice and W. R. Robinson, *J. Solid State Chem.*, **21** (1977) 145.
- [17] A. F. Wells, *Structural Inorganic Chemistry*, Clarendon Press, Oxford 1993.
- [18] A. A. Bolzan, C. Fong and B. Kennedy, *J. Solid State Chem.*, **113** (1994) 9.
- [19] P. A. Cox, *Transition Metal Oxides: An Introduction to their Electronic Structure and Properties*, Clarendon Press, Oxford 1992.
- [20] H.-U. Hummel, R. Fackler and P. Remmert, *Chem. Ber.*, **125** (1992) 551.
- [21] S. Lagergren and A. Magneli, *Acta Chem. Scand.*, **6** (1952) 444.
- [22] N. C. Stephenson and R. S. Roth, *Acta Cryst.*, **B27** (1971) 1037.
- [23] G. Ouvrard, *Ann. Chim. (Paris)*, **7** (1982) 53.
- [24] F. Jellinek, G. Brauer and H. Müller, *Nature*, **185** (1960) 376.
- [25] A. Meetsma, G. A. Wiegers, R. J. Haange and J. L. de Boer, *Acta Cryst.*, **C39** (1990) 1983.

## **Chapter 7**

### **Experimental Details**

## 7.1 General Experimental Details

### 7.1.1 Techniques

All manipulations of air and/or moisture sensitive materials were performed under an inert atmosphere of pure argon or dry dinitrogen using standard Schlenk line techniques or in an inert atmosphere dry box containing dinitrogen. Inert gases were purified firstly by passage through columns filled with activated molecular sieves (4 Å) and then either manganese (II) oxide suspended on vermiculite, for the Schlenk line, or BASF catalyst, for the dry box. Celite<sup>®</sup> filtration aid was purchased from Fluka Chemie and oven-dried at 150 °C prior to use. Filtrations were generally performed using modified stainless steel cannulae, which had been fitted with glass fibre filter discs. All glassware and cannulae were dried overnight at 150 °C before use.

### 7.1.2 Solvents

Solvents were pre-dried over activated 4 Å molecular sieves and then distilled from Na/K alloy (light petroleum ether (b. p. 40-60 °C), diethyl ether, pentane and DME), from sodium (petroleum ether (b. p. 100-120 °C) and toluene), from potassium (THF), phosphorus pentoxide (methanol) or from calcium hydride (dichloromethane), under a slow continuous stream of dinitrogen. Solvents were thoroughly degassed by the pump-fill technique followed by re-admission of argon or by purging with argon for approximately 15 min. prior to use. Deuterated NMR solvents (Aldrich, Goss Scientific) were refluxed and distilled from potassium metal ( $d^6$ -benzene,  $d^8$ -toluene,  $d^8$ -THF), from calcium hydride ( $d^2$ -dichloromethane and  $d^5$ -pyridine) or from magnesium sulfate ( $d^6$ -acetone), distilled and degassed by the freeze-pump-thaw technique prior to use. and stored in Young's ampoules under argon. D<sub>2</sub>O was degassed by purging with argon for approximately 15 min. prior to use. NMR solvents were transferred using a teat pipette in an inert atmosphere dry box, or by vacuum distillation using an all-glass apparatus.

### 7.1.3 General Materials

The compounds  $\text{MnCl}_2$ ,  $\text{TiCl}_4$ ,  $\text{NH}_4\text{PF}_6$ ,  $\text{KN}(\text{SiMe}_3)_2$ ,  $\text{NaN}(\text{SiMe}_3)_2$ ,  $\text{ZnMe}_2$  (2.0 M solution in hexanes),  $^t\text{BuLi}$  (1.7 M solution in pentane),  $^n\text{BuLi}$  [2.5 M solution in light petroleum ether (b.p. 40 - 60 °C)],  $\text{MeLi}$  (1.6 M solution in  $\text{Et}_2\text{O}$ ),  $\text{HCl}$  (1.0 M solution in diethyl ether), naphthalene ( $\text{C}_8\text{H}_{10}$ ), 6,6-dimethylfulvene,  $\text{CH}_3\text{I}$ ,  $\text{WC}$  and  $\text{MoC}$  were purchased from Aldrich Chemical Company and used without further purification. 1,2,3,4-Tetramethylcyclopent-2-enone was purchased from Aldrich and distilled before use.  $\text{ZrCl}_4$  and  $\text{HfCl}_4$  were purchased from Aldrich and sublimed prior to use.  $\text{LiN}(\text{SiMe}_3)_2$  was purchased from Aldrich and was recrystallised from THF before use. Trimethylphosphine ( $\text{PMe}_3$ ),<sup>[1]</sup>  $\text{LiCH}_2\text{PMe}_2$ ,<sup>[2]</sup>  $\text{TiCl}_4(\text{THF})_2$ ,<sup>[3]</sup>  $\text{ZrCl}_4(\text{THF})_2$ ,<sup>[3]</sup>  $\text{HfCl}_4(\text{THF})_2$ <sup>[3]</sup> and  $\text{B}(\text{C}_6\text{F}_5)_3$ <sup>[4]</sup> were prepared according to published literature procedures. V, Nb and Ta metals were used as supplied by the STREM Chemical Company. The compounds  $\text{Nb}_4\text{W}_{13}\text{O}_{47}$  and  $\text{Nb}_8\text{W}_9\text{O}_{47}$  were kindly donated by Prof. F. Krumiech of the Laboratory of Inorganic Chemistry, ETH Zürich, Switzerland. The compounds  $\text{PtI}_2(\text{COD})$  and  $\text{PdCl}_2(\text{COD})$ ,  $[\text{Fe}(\eta\text{-C}_5\text{H}_5)_2][\text{PF}_6]$  and  $\text{LiPMe}_2 \cdot 0.22\text{Et}_2\text{O}$  were kindly donated by S.I. Pascu, S. Barlow and R.M. Bellabarba, all of this laboratory.

### 7.1.4 Instrumentation

**Solution NMR spectra** were recorded using either a Varian Mercury 300 ( $^1\text{H}$  300 MHz,  $^{13}\text{C}$  75.5 MHz,  $^{19}\text{F}$  282.3 MHz,  $^{31}\text{P}$  121.6 MHz,  $^{119}\text{Sn}$  111.9 MHz and  $^{207}\text{Pb}$  62.7 MHz) or a Varian UNITYplus ( $^1\text{H}$  500 MHz,  $^{11}\text{B}$  160.4 MHz,  $^{13}\text{C}$  125.7 MHz,  $^{31}\text{P}$  202.4 MHz) spectrometer and are at room temperature unless otherwise stated. The spectra were referenced internally relative to the residual protio-solvent ( $^1\text{H}$ ) and solvent ( $^{13}\text{C}$ ) resonances relative to tetramethylsilane ( $^1\text{H}$ ,  $^{13}\text{C}$ ,  $\delta = 0$ ) or externally to  $\text{BF}_3 \cdot \text{Et}_2\text{O}$  ( $^{11}\text{B}$ ,  $\delta = 0$ );  $\text{H}_3\text{PO}_3$  ( $^{31}\text{P}$ ,  $\delta = 0$ );  $\text{SnMe}_4$  ( $^{119}\text{Sn}$ ,  $\delta = 0$ );  $\text{PbOAc}_4$  ( $^{207}\text{Pb}$ ,  $\delta = -2675$  ppm) or  $\text{CFCl}_3$  ( $^{19}\text{F}$ ,  $\delta = 0$ ). Chemical shifts ( $\delta$ ) are expressed in ppm and coupling constants ( $J$ ) in Hz. The  $^1\text{H}$ - $^{13}\text{C}$  Heteronuclear Multiple Quantum Coherence (HMQC) spectra were recorded by either Dr Nick Rees or by the author. All chemical shifts are in ppm and coupling constants are in Hz.

**Electrospray mass spectra** were recorded using a Micromass LC TOF electrospray ionisation mass spectrometer. **FAB mass spectrometry** was performed by the EPSRC Mass Spectrometry Service at Swansea.

**Elemental analyses** were performed by the Microanalytical Department of the Inorganic Chemistry Laboratory, Oxford.

**X-ray Crystallography** was performed by Dr Leigh Rees. Crystals were isolated under dinitrogen, covered with a polyfluoroether, and mounted on a glass fibre. Data were collected on an Eraf-Nonius DIP2000 image plate diffractometer with graphite-monochromated Mo-K $\alpha$  radiation ( $\lambda = 0.71069$  Å). All solution, refinement, and graphical calculations were performed using the CAMERON<sup>[5]</sup> software package. Crystal structures were solved by direct methods using the SIR 92 program<sup>[6]</sup> and were refined by full-matrix least squares on  $F^2$ . Non-hydrogen atoms were refined with anisotropic displacement parameters. Hydrogen atoms were generated and allowed to ride on their corresponding carbon atoms with fixed thermal parameters.

**Powder X-ray diffraction** was performed using a Philips 1729 diffractometer equipped with Cu-K $\alpha_1$  radiation operated at 40 kV and 30 mA.

**High resolution transmission electron microscopy (HRTEM)** was performed by Dr. Jeremy Sloan using a JEOL 2010 electron microscope operated at 200 kV, or a JEOL 3000FX HRTEM operated at 400 kV. The 2010 microscope was fitted with a Link Pentafet energy dispersive X-ray (EDX) detector, linked to a Link eXL system, so that analysis of the characteristic X-rays produced by the samples could be undertaken. Samples were ground to a fine powder and dispersed in AR grade chloroform or ethanol. The dispersed sample was placed in an ultrasonic bath for 5-10 minutes before a drop of the suspension was placed on a lacy carbon coated copper grid and placed in the specimen holder. The specimen holder was placed in the side entry port of the microscope and the system was evacuated. After the microscope was tuned the sample was analysed.

## 7.2 Experimental Details for Chapter 2

### 7.2.1 Preparation of $[\text{HC}_5\text{Me}_4\text{CH}_2\text{PMe}_2\text{H}][\text{Cl}]$ (1)

To a yellow solution of  $\text{LiCH}_2\text{PMe}_2$  (3.12 g, 38 mmol) in THF (125 ml) at  $-78^\circ\text{C}$  was added dropwise *via* cannula, a THF solution (75 ml) of tetramethylcyclopent-2-eneone (5.25 g, 38 mmol). The resulting yellow solution was allowed to warm to room temperature and was stirred for a further 12 hours. Upon further cooling to  $-78^\circ\text{C}$  a 1.0 M solution of HCl in  $\text{Et}_2\text{O}$  (79.8 ml, 2.1 equivalents) was added over 2.5 hours and formation of a white precipitate ensued. The mixture was then stirred for 2 hours and the white solid isolated on a glass frit after transfer *via* a wide bore Teflon cannula. The product was washed with THF (2 x 20 ml) and pentane (2 x 30 ml) before residual solvent was removed under reduced pressure to yield the compound **1** as a white powder.

Crude yield : 7.2 g. (80 %)

### 7.2.2 Preparation of $[\text{HC}_5\text{Me}_4\text{CH}_2\text{PMe}_2\text{H}][\text{PF}_6]$ (2)

To a pale yellow solution of **1** (12.19 g, 52 mmol) in degassed  $\text{H}_2\text{O}$  (50 ml) was added *via* cannula a solution of  $\text{NH}_4\text{PF}_6$  (10.24 g, 57 mmol) in degassed  $\text{H}_2\text{O}$  (50 ml) with the immediate precipitation of a white solid. The product was transferred to a glass frit and filtered then washed with degassed  $\text{H}_2\text{O}$  (2 x 30 ml). Residual water was removed from the resulting white solid under reduced pressure to yield the compound **2** as a white powder.

Yield: 15.1 grams (85 %).

### 7.2.3 Preparation of $[\text{HC}_5\text{Me}_4\text{CH}_2\text{PMe}_2]$ (3)

To a suspension of **2** (13.81 g, 40 mmol) in methanol (50 ml) was added a solution of KOH (2.25 g, 40 mmol) in methanol (20 ml). The suspension changed to a cloudy solution with the concomitant evolution of a phosphine odour. Pentane (50 ml) was added to the solution, which was stirred for 10 minutes. On separation of the two layers, the top, pentane layer was transferred *via* cannula into a Schlenk tube containing  $\text{MgSO}_4$  (3.0 grams) and the suspension stirred. The suspension was then

filtered into a clean Schlenk tube to yield a colourless solution from which solvent was removed under reduced pressure. The compound **3** was isolated as a very pale, yellow oil.

Yield: 3.50 grams (45%).

#### 7.2.4 Preparation of $[\text{K}(\text{C}_5\text{Me}_4)\text{CH}_2\text{PMe}_2]$ (**4**)

To a THF solution (25 ml) of **3** (1.00 g, 5.1 mmol) at  $-78^\circ\text{C}$  was added *via* cannula a THF solution (25 ml) of  $\text{KN}(\text{SiMe}_3)_2$  (1.03 grams, 5.1 mmol). The solution was allowed to warm to room temperature and stirred for 12 hours. Solvent was removed under reduced pressure from the resulting yellow solution. The off-white product was washed with pentane (2 x 10 ml) and isolated by filtration. After residual solvent was removed under reduced pressure the compound **4** was obtained as a pyrophoric, white powder.

Yield: 0.95 grams, (79 %).

#### 7.2.5 Preparation of $[\text{Na}(\text{C}_5\text{Me}_4)\text{CH}_2\text{PMe}_2]$ (**5**)

To a THF (25 ml) solution of **3** (1.34 g, 6.2 mmol) at  $-78^\circ\text{C}$  was added *via* cannula a THF solution (25 ml) of  $\text{NaN}(\text{SiMe}_3)_2$  (1.05 grams, 6.2 mmol). The solution was allowed to warm to room temperature and stirred for 12 hours. Solvent was removed under reduced pressure from the resulting yellow solution. The off-white product was washed with pentane (2 x 10 ml) and isolated by filtration. After residual solvent was removed under reduced pressure the compound **5** was obtained as a pyrophoric, white powder.

Yield: 1.19 g, (87 %).

#### 7.2.6 Preparation of $[\text{Li}(\text{C}_5\text{Me}_4)\text{CH}_2\text{PMe}_2]$ (**6**)

To a stirred THF solution (25 ml) of **3** (0.80 g, 4.0 mmol) at  $-78^\circ\text{C}$  was added *via* cannula a THF solution (25 ml) of  $\text{LiN}(\text{SiMe}_3)_2$  (0.63 grams, 4.1 mmol). The solution was allowed to warm to room temperature and stirred for 12 hours. Solvent was

removed under reduced pressure from the resulting yellow solution. The off-white product was washed with pentane (2 x 10 ml) and isolated by filtration. After residual solvent was removed under reduced pressure the compound **6** was obtained as a pyrophoric, white powder.

Yield: 0.60 g (74 %).

### 7.2.7 Preparation of $[\text{Zr}\{(\eta\text{-C}_5\text{Me}_4)\text{CH}_2\text{PMe}_2\}_2\text{Cl}_2]$ (**7**)

To a stirred THF solution (25 ml) of  $\text{ZrCl}_4(\text{THF})_2$  (259 mg, 0.69 mmol) at 0°C was added dropwise a solution of **5** (306 mg 1.40 mmol) in THF (20 ml). The colour changed from pale yellow to orange before reverting to yellow again on warming to room temperature. The yellow solution was then stirred for 12 hours, solvent was removed under reduced pressure and the yellow solid triturated with pentane (2 x 10 ml) then extracted into dichloromethane (2 x 20 ml). Solvent was removed from the resulting yellow solution under reduced pressure to yield the compound **7** as pale yellow microcrystals.

Yield: 267 mg (70 %).

### 7.2.8 NMR scale reaction between $[\text{Zr}\{(\eta\text{-C}_5\text{Me}_4)\text{CH}_2\text{PMe}_2\}_2\text{Cl}_2]$ (**7**) and 2 $\text{B}(\text{C}_6\text{F}_5)_3$

To a Young's tap NMR tube was added a  $d^8$ -toluene solution of compound **7** (10.0 mg, 0.018 mmol) and two equivalents of  $\text{B}(\text{C}_6\text{F}_5)_3$  (18.5 mg, 0.036 mmol).

### 7.2.9 Attempted preparation of $[\text{Zr}\{(\eta\text{-C}_5\text{Me}_4)\text{CH}_2\text{PMe}_2\}_2\text{Me}_2]$ (**9**)

To a stirred THF solution (25 ml) of **7** (140 mg, 0.26 mmol) at 0°C was added dropwise a solution of MeLi in diethyl ether (1.0 M, 0.52 ml, 0.52 mmol.). The pale yellow solution was stirred for 12 hours, solvent was removed under reduced pressure and the off-white solid triturated with pentane (2 x 5 ml) then extracted into toluene (2 x 10 ml). Solvent was removed from the resulting pale-yellow solution to yield the crude compound **9** as a white solid. Selected NMR data (298 K,  $d^2$ -dichloromethane)



$^1\text{H}$   $\delta$  0.85 [d, 6H,  $\text{P}(\text{CH}_3)_2$ ], 1.71 [s, 6H,  $\text{C}_5(\text{CH}_3)_4$ ], 1.87 [s, 6H,  $\text{C}_5(\text{CH}_3)_4$ ] and 2.48 [s, 2H,  $-\text{CH}_2-$ ].  $^{31}\text{P}\{^1\text{H}\}$   $\delta$  -45.5 [s, 3P] and -45.8 [s, 1P].

#### 7.2.10 Attempted preparation of $[\text{Hf}\{(\eta\text{-C}_5\text{Me}_4)\text{CH}_2\text{PMe}_2\}_2\text{Cl}_2]$

To a stirred THF solution (25 ml) of  $\text{HfCl}_4(\text{THF})_2$  (319 mg, 0.69 mmol) at  $0^\circ\text{C}$  was added dropwise a solution of **5** (300 mg 1.38 mmol) in THF (20 ml). The orange-yellow solution was then stirred at room temperature for 12 hours, solvent was removed under reduced pressure and the yellow solid triturated with pentane (2 x 10 ml) then extracted into dichloromethane (2 x 20 ml). Solvent was removed from the resulting yellow solution to yield a pale yellow solid. Selected NMR data (298 K,  $\text{d}^2$ -dichloromethane)  $^1\text{H}$   $\delta$  0.61 [d, 6H,  $\text{P}(\text{CH}_3)_2$ ], 1.84 [s, 6H,  $\text{C}_5(\text{CH}_3)_4$ ], 1.92 [s, 6H,  $\text{C}_5(\text{CH}_3)_4$ ] and 2.48 [s, 2H,  $-\text{CH}_2-$ ].

#### 7.2.11 Preparation of $[\text{Zr}\{(\eta\text{-C}_5\text{Me}_4)\text{CH}_2\text{PMe}_2\}_2\text{Cl}_2\text{PtI}_2]$ (**10**)

To a Schlenk tube containing stirred THF (25 ml) at  $-78^\circ\text{C}$  were simultaneously added dropwise *via* dual cannulae, solutions of **7** (100 mg, 0.18 mmol) and  $\text{PtI}_2(\text{COD})$  (105 mg, 0.18 mmol) in THF (25 ml each) over 30 minutes. The resulting orange solution was stirred at room temperature for one hour after which time a pale orange precipitate began to form. The solution was filtered and solvent was removed under reduced pressure. The resulting red-orange solid was triturated with pentane (10 ml), solvent was removed under reduced pressure and the compound **10** was isolated as an orange solid.

Yield: 53 mg (30 %).

#### 7.2.12 Preparation of $[\text{Mn}\{(\eta\text{-C}_5\text{Me}_4)\text{CH}_2\text{PMe}_2\}_2]$ (**11**)

To a stirred solution of **5** (1.0 g, 4.6 mmol) in THF (30 ml) at  $-78^\circ\text{C}$  was added *via* a solid addition Schlenk tube,  $\text{MnCl}_2$  (289 mg, 2.3 mmol). The mixture was slowly warmed to  $40^\circ\text{C}$  using a water bath and maintained at that temperature for 1 hour. The resulting orange solution was stirred for a further 12 hours, cooling slowly to room temperature. Solvent was removed under reduced pressure and the oily, orange product triturated with pentane (30 ml). The orange product was then extracted into

pentane (3 x 30 ml) and filtered *via* cannula into a Schlenk tube. Solvent was removed under reduced pressure to leave a concentrated solution (20 ml) which was cooled to 4 °C for 2 days. The compound **11** was isolated as orange, cubic, X-ray quality crystals.

Yield: 0.68 g (66%).

### 7.2.13 Attempted preparation of $[\text{Mn}\{(\eta\text{-C}_5\text{Me}_4)\text{CH}_2\text{PMe}_2\}_2][\text{Na}]$

In an analogous procedure to that reported by Robbins,<sup>[7]</sup> to a freshly prepared solution of sodium naphthalide (7.0 mg 0.23 mmol sodium, 30 mg; 0.23 mmol naphthalene) in THF (15 ml) was added a solution of compound **11** (103 mg, 0.23 mmol) in THF at room temperature. The resulting orange solution was stirred for 30 minutes after which time solvent was removed under reduced pressure to yield an intractable brown solid.

### 7.2.14 Attempted preparation of $[\text{Mn}\{(\eta\text{-C}_5\text{Me}_4)\text{CH}_2\text{PMe}_2\}_2][\text{PF}_6]$

In an analogous procedure to that reported by Robbins,<sup>[7]</sup> to an admixture of the two solids **11** (60 mg, 0.14 mmol) and  $[\text{FeCp}_2][\text{PF}_6]$  (44.6 mg, 0.14 mmol) was added THF (15 ml) at room temperature. Acetone (10 ml) was added to dissolve all the solids and the orange-red solution was stirred for 30 minutes after which time solvents were removed under reduced pressure. The orange solid was extracted into pentane, solvent was removed to yield a pink solid.

### 7.2.15 Preparation of $[\text{Mn}\{(\eta\text{-C}_5\text{Me}_4)\text{CH}_2\text{PMe}_2\text{B}(\text{C}_6\text{F}_5)_3\}_2] (\mathbf{12})$

To a stirred solution of **11** (98 mg, 0.22 mmol) in toluene (50 ml) was added *via* cannula a toluene solution (25 ml) of  $\text{B}(\text{C}_6\text{F}_5)_3$  (225 mg, 0.44 mmol). The orange solution was stirred for a further 12 hours. Solvent was removed from the resulting yellow suspension under reduced pressure and the solid, pale orange-yellow product washed with pentane (30 ml) and residual volatiles were removed under reduced pressure. The compound **12** was isolated as a yellow solid.

Yield: 203 mg (63 %).

### 7.2.16 Preparation of $[\text{Mn}\{(\eta\text{-C}_5\text{Me}_4)\text{CH}_2\text{PMe}_3\}_2][\text{I}]_2$ (**13**)

To a stirred solution of **11** (59 mg, 0.13 mmol) in pentane (20 ml) at room temperature was added *via* cannula  $\text{CH}_3\text{I}$  (1.0 ml, 2.1 eq.). The orange solution was allowed to warm to room temperature and stirred for a further 12 hours. A yellow precipitate resulted and solvent was removed under reduced pressure. The orange-yellow product was washed with pentane (10 ml) and any remaining volatiles were removed under reduced pressure. The compound **13** was isolated as a yellow solid.

Yield: 80 mg (83 %) Microanalysis results for a compound with the empirical formula  $\text{C}_{60}\text{H}_{40}\text{B}_2\text{MnP}_2$  (MW = 725.34 amu) C: 42.5 (42.8) H: 6.36 (6.36) found (calculated).

### 7.2.17 Attempted Preparation of $[\text{Mn}\{(\eta\text{-C}_5\text{Me}_4)\text{CH}_2\text{PMe}_2\}_2\text{PtI}_2]$ (**14**)

To a solution of  $\text{PtI}_2(\text{COD})$  (131 mg, 0.22 mmol) in THF (25 ml) at room temperature was added a solution of **11** (100 mg, 0.22 mmol) over 60 minutes. The orange-red solution was stirred for 2 hours after which time the solution was filtered and solvent was removed under reduced pressure. The resulting red-orange solid was triturated with pentane (10 ml), remaining volatiles were removed under reduced pressure and the compound **14** was isolated as a red-orange solid.

Yield: 86 mg (44 %) Microanalysis results for a compound with the empirical formula  $\text{C}_{24}\text{H}_{40}\text{I}_2\text{MnP}_2\text{Pt}$  (MW = 894.36 amu) C: 32.76 (32.23) H: 4.52 (4.80) P: 6.80 (6.92) found (calculated).

### 7.2.18 Preparation of $[\text{Li}(\text{C}_5\text{H}_4)\text{CMe}_2\text{PMe}_2]$

In an analogous procedure to that reported by Bellabarba,<sup>[8]</sup> to a stirred solution of  $\text{LiPMe}_2 \cdot 0.22\text{Et}_2\text{O}$  (3.58 g, 43 mmol) in THF (40 ml) at  $-78^\circ\text{C}$  was added dropwise a THF solution of 6,6-dimethylfulvene (5.42 g, 0.51 mmol) and the reaction mixture left to stir overnight after slowly warming to room temperature. Solvent was then removed from the yellow solution under reduced pressure affording a sticky, yellow solid. The product was triturated and then washed with pentane (3 x 15 ml) and filtration of the supernatant followed by removal of residual volatiles under reduced pressure yielded the compound  $[\text{Li}(\text{C}_5\text{H}_4)\text{CMe}_2\text{PMe}_2]$  as a fine, white powder.

Yield: 4.7 g (63 %) Selected NMR data (298 K,  $d^5$ -pyridine)  $^1\text{H}$   $\delta$  6.11 [m, 2H,  $\text{C}_5\text{H}_4$ ],  $\delta$  5.99 [m, 2H,  $\text{C}_5\text{H}_4$ ],  $\delta$  1.27 [d, 3H,  $\text{P}(\text{CH}_3)_2$ ;  $^2J_{\text{H-P}} = 15.0$  Hz],  $\delta$  0.92 [s, 6H,  $\text{C}(\text{CH}_3)_2$ ;  $^2J_{\text{H-P}} = 3.0$  Hz].  $^{31}\text{P}\{^1\text{H}\}$   $\delta$  -28.

#### 7.2.19 Attempted preparation of $[\text{Mn}\{(\eta\text{-C}_5\text{H}_4)\text{CMe}_2\text{PMe}_2\}_2]$

To an admixture of  $\text{MnCl}_2$  (59 mg, 0.46 mmol) and  $\text{Li}(\text{C}_5\text{H}_4)\text{CMe}_2\text{PMe}_2$  (200 mg, 0.93 mmol) in at  $-78^\circ\text{C}$  was added THF (50 ml). The mixture was slowly warmed to  $40^\circ\text{C}$  using a water bath and maintained at that temperature for 1 hour. The orange solution was then allowed to cool back to room temperature and was stirred for a further 12 hours. Solvent was removed under reduced pressure and the oily, orange product triturated with pentane (30 ml). The orange product was then extracted into pentane (3 x 30 ml) and filtered *via* cannula into a Schlenk tube. Residual volatiles were removed under reduced pressure to yield a waxy orange solid.  $^1\text{H}$  and  $^{31}\text{P}\{^1\text{H}\}$  NMR studies exhibited numerous signals indicating that a variety of products had formed during the reaction.

### 7.3 Experimental details for Chapter Three

#### 7.3.1 Attempted Preparation of $[\text{Pb}\{(\eta\text{-C}_5\text{Me}_4)\text{CH}_2\text{PMe}_2\}_2]$

To a foil covered Schlenk tube containing an admixture of  $\text{PbCl}_2$  (137 mg, 0.49 mmol) and  $[\text{Li}(\text{C}_5\text{Me}_4)\text{CH}_2\text{PMe}_2]$  (200 mg, 0.98 mmol) was added THF (20 ml) at  $-78^\circ\text{C}$ . The resulting yellow suspension was stirred for 12 hours. The orange solution containing a white precipitate was filtered *via* cannula to yield a dark yellow solution from which solvent was removed under reduced pressure. An orange, oily solid resulted. The product was triturated with pentane (10 ml) and the solid then extracted into pentane. Removal of solvents afforded a waxy, orange solid.  $^1\text{H}$  and  $^{31}\text{P}\{^1\text{H}\}$  NMR studies ( $\text{d}^5$ -pyridine) exhibited numerous signals suggesting that a variety of products had formed during the reaction.

#### 7.3.2 Preparation of $[\text{Pb}\{(\eta\text{-C}_5\text{H}_4)\text{CMe}_2\text{PMe}_2\}_2]$ (**15**)

To a foil covered Schlenk tube containing an admixture of  $\text{PbCl}_2$  (300 mg, 1.1 mmol) and  $\text{Li}(\text{C}_5\text{H}_4)\text{CMe}_2\text{PMe}_2$  (368 mg, 2.2 mmol) was added THF (30 ml) at  $-78^\circ\text{C}$ . The resulting yellow suspension was stirred for 12 hours. The orange solution containing a white precipitate was filtered *via* cannula to yield a dark yellow solution from which solvent was removed under reduced pressure. An orange, oily solid resulted. The product was triturated with pentane (10 ml) and the solid then extracted into pentane and stored at  $-40^\circ\text{C}$  overnight. The compound **15** was isolated as a microcrystalline, orange solid.

Yield: 400 mg (68 %).

#### 7.3.3 Preparation of $[\text{Sn}\{(\eta\text{-C}_5\text{H}_4)\text{CMe}_2\text{PMe}_2\}_2]$ (**16**)

To a foil covered Schlenk tube containing an admixture of  $\text{SnCl}_2$  (300 mg, 1.6 mmol) and  $\text{Li}(\text{C}_5\text{H}_4)\text{CMe}_2\text{PMe}_2$  (555 mg, 3.2 mmol) was added THF (20 ml) at  $-78^\circ\text{C}$ . The resulting yellow suspension was stirred for 12 hours. The dark yellow solution containing a white precipitate was filtered *via* cannula to yield a yellow solution from which solvent was removed under reduced pressure. A yellow, waxy solid was isolated. The product was triturated with pentane (10 ml) and the solid then extracted

into pentane and solvent was removed under reduced pressure. The compound **16** was isolated as a waxy, yellow solid and stored at -40°C in a dark place.

Yield: 650 mg (91 %).

#### 7.3.4 Preparation of $[\text{Pb}\{(\eta\text{-C}_5\text{H}_4)\text{CMe}_2\text{PMe}_2\text{B}(\text{C}_6\text{F}_5)_3\}_2]$ (**17**)

A solution of  $\text{B}(\text{C}_6\text{F}_5)_3$  (95 mg, 0.18 mmol) in toluene (25 ml) was added dropwise to a solution of **15** (50 mg, 0.09 mmol) in toluene (25 ml) at room temperature. The resulting yellow solution was stirred for 72 hours. Solvent was removed under reduced pressure from the yellow solution and the resulting yellow solid washed with pentane (2 x 20 ml). Final removal of volatiles under reduced pressure yielded compound **17** as a yellow powder.

Yield: 70 mg (50 %).

#### 7.3.5 Attempted preparation of $[\text{Sn}\{(\eta\text{-C}_5\text{H}_4)\text{CMe}_2\text{PMe}_2\text{B}(\text{C}_6\text{F}_5)_3\}_2]$

A solution of  $\text{B}(\text{C}_6\text{F}_5)_3$  (95 mg, 0.18 mmol) in toluene (25 ml) was added dropwise to a solution of **16** (50 mg, 0.09 mmol) in toluene (25 ml) at room temperature. The resulting yellow solution was stirred for 72 hours. Solvent was removed under reduced pressure from the yellow solution and the resulting pale yellow solid washed with pentane (2 x 20 ml). Final removal of volatiles under reduced pressure yielded a pale yellow product. Microanalysis results were inconsistent with those calculated for the proposed formula.

#### 7.3.6 Preparation of $[\text{Pb}\{(\eta\text{-C}_5\text{H}_4)\text{CMe}_2\text{PMe}_2\}_2\text{PtI}_2]$ (**18**)

A yellow solution of  $\text{PtI}_2(\text{COD})$  (83 mg, 0.14 mmol) in THF (30 ml) was slowly added to a solution of **15** (77 mg, 0.14 mmol) in THF (20 ml) at room temperature. The resulting yellow solution was stirred for 12 hours. Volatiles were removed under reduced pressure from the yellow-orange solution and the yellow solid washed with pentane (2 x 20 ml). Removal of residual pentane under reduced pressure yielded compound **18** as an orange powder.

Yield: 50 mg (36 %).

### 7.3.7 Attempted Preparation of $[\text{Pb}\{(\eta\text{-C}_5\text{H}_4)\text{CMe}_2\text{PMe}_2\}_2\text{PdCl}_2]$ (**19**)

A yellow solution of  $\text{PdCl}_2(\text{COD})$  (52 mg, 0.18 mmol) in THF (30 ml) was slowly (10 minutes) added to an orange solution of **15** (100 mg, 0.18 mmol) in THF (20 ml) at room temperature. The resulting orange solution was stirred for 12 hours. Solvent was removed under reduced pressure from the yellow-orange solution and the yellow solid washed with pentane (2 x 10 ml). Removal of residual pentane under reduced pressure yielded compound **19** as an orange-yellow powder.

Yield: 40 mg (32 %). Microanalysis results for a compound with the empirical formula  $\text{C}_{20}\text{H}_{32}\text{Cl}_2\text{PbP}_2\text{Pd}$  (MW = 718.9 amu) C: 33.4 (33.4) H: 4.48 (4.49) found (calculated).  $^{31}\text{P}\{^1\text{H}\}$  NMR spectrum ( $d^5$ -pyridine)  $\delta$  -3.4 (s),  $\delta$  -5.7 (s).

### 7.3.8 Attempted Preparation of $[\text{Sn}\{(\eta\text{-C}_5\text{H}_4)\text{CMe}_2\text{PMe}_2\}_2\text{PtI}_2]$ (**20**)

A yellow solution of  $\text{PtI}_2(\text{COD})$  (103 mg, 0.18 mmol) in THF (30 ml) was slowly (10 minutes) added to an orange solution of **16** (80 mg, 0.18 mmol) in THF (20 ml) at room temperature. The resulting orange solution was stirred for 12 hours. Solvent was removed under reduced pressure from the yellow-orange solution and the yellow solid washed with pentane (2 x 10 ml). Removal of residual pentane under reduced pressure yielded compound **20** as an orange-yellow powder.

Yield: 40 mg (32 %). Microanalysis results for a compound with the empirical formula  $\text{C}_{20}\text{H}_{32}\text{I}_2\text{SnP}_2\text{Pt}$  (MW = 902.01 amu) C: 26.7 (26.6) H: 3.6 (3.6) found (calculated).

## 7.4 Experimental details for Chapter 5

### 7.4.0 General Procedure

All sulfidisation and annealing experiments were undertaken in a fumehood. The exhaust gases from the sulfidisation reactions were scrubbed through solutions of acidified potassium permanganate ( $\text{KMnO}_4$ ) and bleach to remove any  $\text{H}_2\text{S}$ .

#### 7.4.1 Sulfidisation of molybdenum carbide ( $\text{MoC}$ )

A porcelain crucible charged with black  $\text{MoC}$  (100 mg, 935  $\mu\text{mol}$ ) was inserted into a silica glass tube of diameter 25 mm. The silica tube was placed in an electrothermal furnace and purged with  $\text{N}_2$  for 20 minutes. The furnace was heated to  $700^\circ\text{C}$  and the  $\text{N}_2$  gas supply was replaced by pure  $\text{H}_2\text{S}$ , which was admitted to the reaction vessel at the rate of approximately  $40 \text{ ml min}^{-1}$ . After 20 minutes, the  $\text{H}_2\text{S}$  supply was replaced with  $\text{N}_2$  and the furnace power switched off to allow slow cooling of the sample back to room temperature. The blue-black, product was then removed from the furnace and analysed by HRTEM and powder X-ray diffraction. The reaction was repeated reducing the sulfidisation time from 20 min to 5 min.

#### 7.4.2 Sequential oxidation of tungsten carbide ( $\text{WC}$ ) to $\text{WC}/\text{WO}_{3-x}$ by $\text{CO}_2$

Black, tungsten carbide ( $\text{WC}$ ) (100 mg, 950  $\mu\text{mol}$ ) was placed in a 5.0 mm diameter tube in a furnace.  $\text{CO}_2$  Gas was passed over the sample at  $40 \text{ ml min}^{-1}$  and the temperature of the furnace was increased to  $750^\circ\text{C}$ . The samples were heated at this temperature for 2, 6, 12 and 24 hours before cooling to room temperature. Samples were then analysed by powder X-ray diffraction and HRTEM.

#### 7.4.3 Sulfidisation of $\text{WC}/\text{WO}_{3-x}$

A porcelain crucible charged with a sample of partially oxidised  $\text{WC}/\text{WO}_{3-x}$  (*ca.* 50 mg) was placed in a silica glass tube of diameter 25 mm. The tube was inserted into an electrothermal furnace and purged with  $\text{N}_2$  for 20 minutes. The furnace was then heated to  $700^\circ\text{C}$ . At this point, the  $\text{N}_2$  gas supply was replaced by pure  $\text{H}_2\text{S}$ , which was admitted to the reaction vessel at the rate of approximately  $40 \text{ ml min}^{-1}$ . After 20 minutes, the  $\text{H}_2\text{S}$  supply was replaced with  $\text{N}_2$  and the furnace power switched off to allow slow cooling of the sample back to room temperature. The



products were then removed from the furnace and analysed by HRTEM and powder X-ray diffraction.

#### 7.4.4 Sulfidisation of $\text{Nb}_4\text{W}_{13}\text{O}_{47}$

Pale grey,  $\text{Nb}_4\text{W}_{13}\text{O}_{47}$  (*ca.* 10 mg, 0.003 mmol) was suspended in chloroform and ground using an agate mortar and pestle before being pipetted into a porcelain crucible and the solvent allowed to evaporate. The crucible was placed in a silica glass tube of diameter 25 mm which was inserted into an electrothermal furnace and purged with  $\text{N}_2$  for 20 minutes. The furnace was heated to  $650^\circ\text{C}$  and the  $\text{N}_2$  gas supply was replaced by pure  $\text{H}_2\text{S}$ , which was admitted to the reaction vessel at the rate of approximately  $30 \text{ ml min}^{-1}$ . After 40 minutes, the  $\text{H}_2\text{S}$  supply was replaced with  $\text{N}_2$  and the furnace power switched off to allow slow cooling of the sample back to room temperature. A black, crystalline product was afforded.

#### 7.4.5 Sulfidisation of $\text{Nb}_8\text{W}_9\text{O}_{47}$

Black, crystalline  $\text{Nb}_8\text{W}_9\text{O}_{47}$  (*ca.* 10 mg, 0.003 mmol) was prepared for annealing as described for  $\text{Nb}_4\text{W}_{13}\text{O}_{47}$  in **Section 7.4.4**. The furnace was heated to  $650^\circ\text{C}$  and the  $\text{N}_2$  gas supply was replaced by pure  $\text{H}_2\text{S}$ , which was admitted to the reaction vessel at the rate of approximately  $30 \text{ ml min}^{-1}$  for 40 minutes. The  $\text{H}_2\text{S}$  supply was replaced with  $\text{N}_2$  and the furnace power switched off to allow slow cooling of the sample back to room temperature. A dark grey, crystalline product was afforded.

## **7.5 Experimental details for Chapter 6**

### **7.5.0 General Procedure**

The MVS apparatus and operational procedures have been described in **Chapter 6**. All annealing and sulfidisation experiments were undertaken in a fumehood. The exhaust gases from the sulfidisation reactions were scrubbed through solutions of acidified potassium permanganate ( $\text{KMnO}_4$ ) and bleach to remove any  $\text{H}_2\text{S}$ .

#### **7.5.1 Preparation of amorphous vanadium oxide by MVS**

Vanadium atoms (3.0g, 59 mmol) generated from a molten vanadium ingot (*ca.* 10 g) were co-condensed with water vapour (100 ml) over 3 hours. The input power was increased from 5.4 kV x 90 mA to 5.4 kV x 110 mA (486 W to 594 W). After warming to room temperature, the olive green matrix was washed out of the reactor with analytical grade ethanol (600 ml) and the suspended product filtered through a glass frit. Excess solvents were removed under reduced pressure and the finely divided, black product was collected.

Yield: 2.8 g.

#### **7.5.2 Preparation of amorphous niobium oxide by MVS**

Niobium atoms (2.0g, 21 mmol) generated from a molten niobium ingot (*ca.* 10 g) were co-condensed with water vapour (100 ml) over 3 hours. The input power was increased from 1.5 kV x 90 mA to 7kV x 3.5 mA (135 W to 2450 W). After warming to room temperature, the green matrix was washed out of the reactor with analytical grade ethanol (600 ml) and the suspended product filtered through a glass frit. Excess solvents were removed under reduced pressure and the finely divided, pale grey product collected.

Yield: 1.4 g.

#### **7.5.3 Preparation of amorphous tantalum oxide by MVS**

Tantalum atoms (2.0g, 11 mmol) generated from a molten tantalum ingot (*ca.* 10 g) were co-condensed with water vapour (100 ml) over 3 hours. The input power was

increased from 7.5 kV x 3.5 mA to 8.2 kV x 5.3 mA (2625 W to 4346 W). After warming to room temperature, the grey matrix was washed out of the reactor with analytical grade ethanol (600 ml) and the suspended product filtered through a glass frit. Volatiles were removed from the grey solid under reduced pressure and the resultant dark grey powder collected.

Yield: 2.3 g.

#### **7.5.4 Preparation of $\alpha$ -V<sub>2</sub>O<sub>3</sub>**

A porcelain crucible containing a sample of black, amorphous vanadium oxide (*ca.* 50 mg) was placed in a silica glass tube of diameter 25 mm. After insertion into a tube furnace, the silica tube was purged with N<sub>2</sub> for 20 minutes while the temperature was increased to 850°C. At this point, the N<sub>2</sub> gas supply was replaced by pure H<sub>2</sub>, which was admitted to the reaction vessel at the rate of approximately 60 ml min<sup>-1</sup>. After one hour, the H<sub>2</sub> supply was replaced with N<sub>2</sub> and the furnace power switched off to allow slow cooling of the sample back to room temperature. The blue-black, finely divided crystalline product was then removed from the furnace and collected.

#### **7.5.5 Preparation of NbO<sub>2</sub>**

A porcelain crucible containing a sample of light grey, amorphous niobium oxide (*ca.* 50 mg) was placed in a silica glass tube of diameter 25 mm. After insertion into a tube furnace, the silica tube was purged with N<sub>2</sub> for 20 minutes while the temperature was increased to 800°C. At this point, the N<sub>2</sub> gas supply was replaced by pure H<sub>2</sub>, which was admitted to the reaction vessel at the rate of approximately 60 ml min<sup>-1</sup>. After one hour, the H<sub>2</sub> supply was replaced with N<sub>2</sub> and the furnace power switched off to allow slow cooling of the sample back to room temperature. The dark grey, finely divided crystalline product was then removed from the furnace and collected.

### 7.5.6 Preparation of TT-Ta<sub>2</sub>O<sub>5</sub>

A porcelain crucible containing a sample of grey, amorphous tantalum oxide (50 mg) was placed in a silica glass tube of diameter 25 mm. After insertion into a tube furnace, the silica tube was purged with N<sub>2</sub> for 20 minutes while the temperature was increased to 850°C. At this point, the N<sub>2</sub> gas supply was replaced by pure H<sub>2</sub>, which was admitted to the reaction vessel at the rate of approximately 60 ml min<sup>-1</sup>. After one hour, the H<sub>2</sub> supply was replaced with N<sub>2</sub> and the furnace power switched off to allow slow cooling of the sample back to room temperature. The blue-black, finely divided crystalline product was then removed from the furnace and collected.

### 7.5.7 Preparation of VS<sub>2</sub>

A porcelain crucible containing a sample of black, reduced vanadium oxide ( $\alpha$ -V<sub>2</sub>O<sub>3</sub>) (20 mg) was placed in a silica glass tube of diameter 25 mm. After insertion into a tube furnace, the silica tube was purged with N<sub>2</sub> for 20 minutes while the temperature was increased to 750°C. At this point, the N<sub>2</sub> gas supply was replaced by pure H<sub>2</sub>S, which was admitted to the reaction vessel at the rate of approximately 40 ml min<sup>-1</sup>. After 40 minutes, the H<sub>2</sub>S supply was replaced with N<sub>2</sub> and the furnace power switched off to allow slow cooling of the sample back to room temperature. The black, finely divided product was then removed from the furnace and collected.

### 7.5.8 Preparation of NbS<sub>2</sub>

A porcelain crucible containing a sample of blue-black reduced niobium oxide (NbO<sub>2</sub>) (20 mg) was placed in a silica glass tube of diameter 25 mm. After insertion into a tube furnace, the silica tube was purged with N<sub>2</sub> for 20 minutes while the temperature was increased to 700°C. At this point, the N<sub>2</sub> gas supply was replaced by pure H<sub>2</sub>S, which was admitted to the reaction vessel at the rate of approximately 40 ml min<sup>-1</sup>. After 40 minutes, the H<sub>2</sub>S supply was replaced with N<sub>2</sub> and the furnace power switched off to allow slow cooling of the sample back to room temperature. The black, finely divided product was then removed from the furnace and collected.

### 7.5.9 Preparation of TaS<sub>2</sub>

A porcelain crucible containing a sample of grey-black reduced tantalum oxide ( $\delta$ -Ta<sub>2</sub>O<sub>5</sub>) (20 mg) was placed in a silica glass tube of diameter 25 mm. After insertion into a tube furnace, the silica tube was purged with N<sub>2</sub> for 20 minutes while the temperature was increased to 870°C. At this point, the N<sub>2</sub> gas supply was replaced by pure H<sub>2</sub>S, which was admitted to the reaction vessel at the rate of approximately 60 ml min<sup>-1</sup>. After 30 minutes, the H<sub>2</sub>S supply was replaced with N<sub>2</sub> and the furnace power switched off to allow slow cooling of the sample back to room temperature. The dark grey, finely divided product was then removed from the furnace and collected.

### 7.5.10 Preparation of NbS<sub>2</sub> from Amorphous Niobium Oxide

A porcelain crucible containing a grey, amorphous niobium oxide (50 mg) was placed in a silica glass tube of diameter 25 mm. After insertion into a tube furnace, the silica tube was purged with N<sub>2</sub> for 20 minutes while the temperature was increased to 750°C. At this point, the N<sub>2</sub> gas supply was replaced by pure H<sub>2</sub>S, which was admitted to the reaction vessel at the rate of approximately 40 ml min<sup>-1</sup>. After 60 minutes, the H<sub>2</sub>S supply was replaced with N<sub>2</sub> and the furnace power switched off to allow slow cooling of the sample back to room temperature. The black, finely divided product was then removed from the furnace and collected.

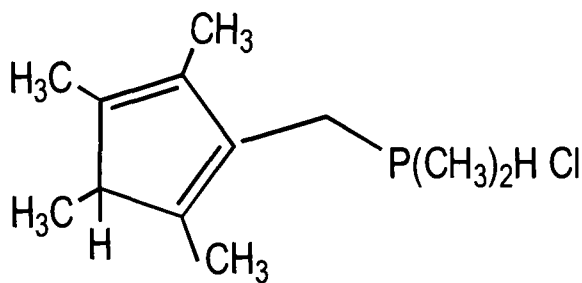
## 7.6 References for Chapter 7

- [1] M. L. Leutkens *Jr.*, A. P. Sattelberger, H. H. Murray, J. D. Basil, J. P. Fackler, *Inorg. Synth.*, 26 (1988) 7.
- [2] A. M. Martins, *Personal Communication*, (1998) .
- [3] L. E. Manzer, *Inorg. Synth.*, 21 (1982) 135.
- [4] C. P. Menhert, *D. Phil. Thesis*, University of Oxford, 1996.
- [5] D. J. Watkin, C. K. Prout, L. J. Pearce, *CAMERON*, Chemical Crystallography Laboratory, Oxford, U.K., 1996.
- [6] A. Altomare, G. Cascarano, A. Guagliardi, M. C. Burla, G. Polidori, M. Camalli, *J. Appl. Crystallogr.*, 27 (1994) 435.
- [7] J. L. Robbins, N. M. Edelstein, S. R. Cooper, J. C. Smart, *J. Am. Chem. Soc.*, 101 (1979) 3853.
- [8] R. M. Bellabarba, *D. Phil. Thesis*, University of Oxford, 2000.

## **Chapter 8**

### **Characterising Data**

8.1 Characterising data for [(HC<sub>5</sub>Me<sub>4</sub>)CH<sub>2</sub>PMe<sub>2</sub>H][Cl] (1)



Description

White solid

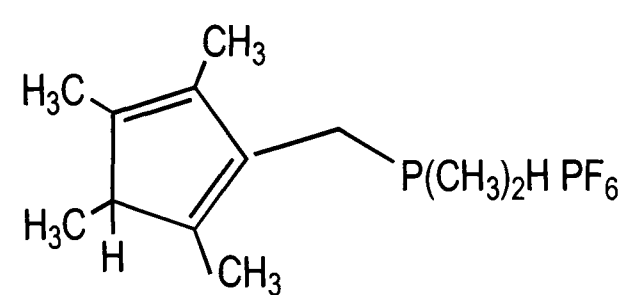
$C_{12}H_{22}PCl = 232.73$

<sup>1</sup> H NMR	d <sup>6</sup> -acetone 500 MHz	<sup>13</sup> C{ <sup>1</sup> H} NMR	D <sub>2</sub> O 125.7 MHz
δ 3.90	[t, 1H, CH <sub>b</sub> ] <sup>2</sup> J <sub>Hb-P</sub> = 14.0 Hz <sup>2</sup> J <sub>Hb-Ha</sub> = 15.0 Hz	δ 143.3	[s, C <sub>ring</sub> ]
		δ 134.3	[s, C <sub>ring</sub> ]
δ 3.51	[t, 1H, CH <sub>a</sub> ] <sup>2</sup> J <sub>Ha-P</sub> = 14.0 Hz <sup>2</sup> J <sub>Ha-Hb</sub> = 15.0 Hz	δ 127.2	[s, C <sub>ring</sub> ]
		δ 127.1	[s, C <sub>ring</sub> ]
δ 2.85	[m, 1H, H-C <sub>ring</sub> -CH <sub>3</sub> ]	δ 49.93	[s, H-C <sub>ring</sub> -CH <sub>3</sub> ]
δ 2.10	[d, 3H, P(CH <sub>3</sub> ) <sub>2</sub> ] <sup>2</sup> J <sub>H-P</sub> = 14.5 Hz	δ 17.96	[d, -CH <sub>2</sub> -] J <sub>P-C</sub> = 51.6 Hz
δ 2.06	[d, 3H, P(CH <sub>3</sub> ) <sub>2</sub> ] <sup>2</sup> J <sub>H-P</sub> = 14.5 Hz	δ 13.10	[s, H-CH <sub>3</sub> -C <sub>ring</sub> ]
δ 1.93	[s, 3H, C <sub>ring</sub> -CH <sub>3</sub> ]	δ 11.14	[s, CH <sub>3</sub> -C <sub>ring</sub> ]
δ 1.83	[s, 3H, C <sub>ring</sub> -CH <sub>3</sub> ]	δ 10.83	[s, CH <sub>3</sub> -C <sub>ring</sub> ]
δ 1.77	[s, 3H, C <sub>ring</sub> -CH <sub>3</sub> ]	δ 9.97	[s, CH <sub>3</sub> -C <sub>ring</sub> ]
δ 1.08	[d, 3H, CH <sub>3</sub> -C <sub>ring</sub> -H] <sup>3</sup> J <sub>H-H</sub> = 8.0 Hz	δ 2.93	[d, P(CH <sub>3</sub> ) <sub>2</sub> ] J <sub>P-C</sub> = 28.9 Hz
		δ 2.51	[d, P(CH <sub>3</sub> ) <sub>2</sub> ] J <sub>P-C</sub> = 28.9 Hz
<sup>31</sup> P{ <sup>1</sup> H} NMR	d <sup>6</sup> -acetone 121.6 MHz		
δ 40.38	[s, P(CH <sub>3</sub> ) <sub>2</sub> H]		

<sup>13</sup>C{<sup>1</sup>H} and <sup>1</sup>H NMR spectra were assigned using a <sup>1</sup>H-<sup>13</sup>C HMQC experiment



8.2 Characterising data for [(HC<sub>5</sub>Me<sub>4</sub>)CH<sub>2</sub>PMe<sub>2</sub>H][PF<sub>6</sub>] (2)



Description

White solid

C<sub>12</sub>H<sub>22</sub>F<sub>6</sub>P<sub>2</sub> = 342.24

Elemental Analysis	C %	H %	P %
Found	42.2	6.3	18.8
Required	42.1	6.5	18.1

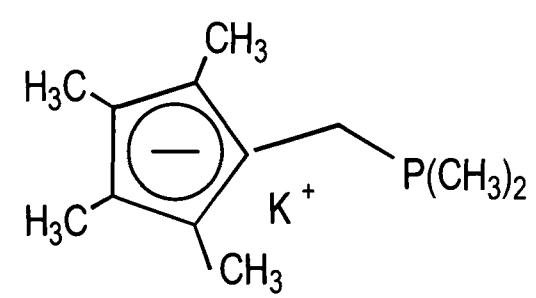
<sup>1</sup> H NMR	d <sup>6</sup> -acetone 500 MHz	<sup>13</sup> C{ <sup>1</sup> H} NMR	d <sup>6</sup> -acetone 125.7 MHz
δ 5.80	[d, 1H, <u>H</u> P(CH <sub>3</sub> ) <sub>2</sub> ] <sup>2</sup> J <sub>H-P</sub> = 4.5 Hz	δ 143.2	[s, <u>C</u> <sub>ring</sub> ]
		δ 142.5	[s, <u>C</u> <sub>ring</sub> ]
δ 3.69	[t, 1H, - <u>CH</u> <sub>b</sub> -] <sup>2</sup> J <sub>Ha-P</sub> = 14.0 Hz <sup>2</sup> J <sub>Ha-Hb</sub> = 15.0 Hz	δ 134.3	[s, <u>C</u> <sub>ring</sub> ]
		δ 127.3	[s, <u>C</u> <sub>ring</sub> ]
δ 3.35	[t, 1H, - <u>CH</u> <sub>a</sub> -] <sup>2</sup> J <sub>Ha-P</sub> = 14.0 Hz <sup>2</sup> J <sub>Ha-Hb</sub> = 15.0 Hz	δ 50.7	[s, H- <u>C</u> <sub>ring</sub> -CH <sub>3</sub> ]
		δ 17.8	[d, - <u>CH</u> <sub>2</sub> -] J <sub>C-P</sub> = 46.5 Hz
δ 2.86	[q, 1H, <u>H</u> -C <sub>ring</sub> -CH <sub>3</sub> ] <sup>3</sup> J <sub>H-H</sub> = 7.5 Hz	δ 13.8	[s, H- <u>CH</u> <sub>3</sub> -C <sub>ring</sub> ]
δ 2.00	[d, 3H, P( <u>CH</u> <sub>3</sub> ) <sub>2</sub> ] <sup>2</sup> J <sub>H-P</sub> = 13.5 Hz	δ 12.4	[s, <u>CH</u> <sub>3</sub> -C <sub>ring</sub> ]
δ 1.92	[s, 3H, C <sub>ring</sub> - <u>CH</u> <sub>3</sub> ]	δ 11.8	[s, <u>CH</u> <sub>3</sub> -C <sub>ring</sub> ]
δ 1.88	[d, 3H, P( <u>CH</u> <sub>3</sub> ) <sub>2</sub> ] <sup>2</sup> J <sub>H-P</sub> = 13.5 Hz	δ 11.3	[s, <u>CH</u> <sub>3</sub> -C <sub>ring</sub> ]
δ 1.86	[s, 3H, C <sub>ring</sub> - <u>CH</u> <sub>3</sub> ]	δ 3.32	[d, P( <u>CH</u> <sub>3</sub> ) <sub>2</sub> ] J <sub>C-P</sub> = 47.8 Hz
δ 1.80	[s, 3H, C <sub>ring</sub> - <u>CH</u> <sub>3</sub> ]	δ 2.50	[d, P( <u>CH</u> <sub>3</sub> ) <sub>2</sub> ] J <sub>C-P</sub> = 47.8 Hz
δ 1.07	[d, 3H, <u>CH</u> <sub>3</sub> -C <sub>ring</sub> -H] <sup>3</sup> J <sub>H-H</sub> = 15.0 Hz		
<sup>31</sup> P{ <sup>1</sup> H} NMR	d <sup>6</sup> -acetone 202.4 MHz	<sup>19</sup> F NMR	d <sup>6</sup> -acetone 282.3 MHz
δ 37.5	[s, <u>P</u> (CH <sub>3</sub> ) <sub>2</sub> ]	δ -195.51	[d, <u>PF</u> <sub>6</sub> ] J <sub>F-P</sub> = 710 Hz
δ -144.6	[spt, <u>PF</u> <sub>6</sub> ] J <sub>P-F</sub> = 710 Hz		

<sup>13</sup>C{<sup>1</sup>H} and <sup>1</sup>H NMR spectra were assigned using a <sup>1</sup>H-<sup>13</sup>C HMQC experiment

8.3 Characterising data for [(HC<sub>5</sub>Me<sub>4</sub>)CH<sub>2</sub>PMe<sub>2</sub>] (3)

		<b>Description</b>	
		Pale yellow oil	
		C <sub>12</sub> H <sub>21</sub> P = 196.27	
<b>Elemental Analysis</b>		C %	H %
Found		76.3	8.3
Required		73.4	10.8
		(very air sensitive)	
<b><sup>1</sup>H NMR</b>	d <sup>6</sup> -benzene 500 MHz	<b><sup>13</sup>C{<sup>1</sup>H} NMR</b>	d <sup>6</sup> -benzene 125.7 MHz
δ 2.85	[m, 1H, <u>H</u> -C <sub>ring</sub> -CH <sub>3</sub> ]	δ 138.6	[s, <u>C</u> <sub>ring</sub> ]
δ 2.42	[m, 1H, CH <sub>2</sub> ] <sup>2</sup> J <sub>Hb-Ha</sub> = 12.5 Hz <sup>2</sup> J <sub>H-P</sub> = 3.0 Hz	δ 138.2	[s, <u>C</u> <sub>ring</sub> ]
		δ 135.8	[s, <u>C</u> <sub>ring</sub> ]
δ 2.31	[m, 1H, CH <sub>2</sub> ] <sup>2</sup> J <sub>Ha-Hb</sub> = 12.5 Hz	δ 134.0	[s, <u>C</u> <sub>ring</sub> ]
δ 1.79	[s, 3H, C <sub>ring</sub> -CH <sub>3</sub> ]	δ 50.42	[s, H- <u>C</u> <sub>ring</sub> -CH <sub>3</sub> ]
δ 1.77	[s, 3H, C <sub>ring</sub> -CH <sub>3</sub> ]	δ 31.10	[d, <u>CH</u> <sub>2</sub> ] J <sub>C-P</sub> = 10.0 Hz
δ 1.75	[s, 3H, C <sub>ring</sub> -CH <sub>3</sub> ]	δ 14.57	[d, P( <u>CH</u> <sub>3</sub> ) <sub>2</sub> ] J <sub>C-P</sub> = 11.0 Hz
δ 1.07	[d, 3H, H-C <sub>ring</sub> CH <sub>3</sub> ] <sup>2</sup> J <sub>H-H</sub> = 12.5 Hz	δ 14.50	[s, H-C <sub>ring</sub> - <u>CH</u> <sub>3</sub> ]
δ 0.93	[d, 3H, P(CH <sub>3</sub> ) <sub>2</sub> ] <sup>2</sup> J <sub>P-H</sub> = 3.0 Hz	δ 14.46	[d, P( <u>CH</u> <sub>3</sub> ) <sub>2</sub> ] J <sub>C-P</sub> = 11.0 Hz
δ 0.85	[d, 3H, P( <u>CH</u> <sub>3</sub> ) <sub>2</sub> ] <sup>2</sup> J <sub>P-H</sub> = 3.0 Hz	δ 12.40	[s, C <sub>ring</sub> - <u>CH</u> <sub>3</sub> ]
		δ 11.79	[s, C <sub>ring</sub> - <u>CH</u> <sub>3</sub> ]
		δ 11.22	[s, C <sub>ring</sub> - <u>CH</u> <sub>3</sub> ]
<b><sup>31</sup>P{<sup>1</sup>H} NMR</b>	d <sup>6</sup> -benzene 202.4 MHz		
δ - 46.0	[s, <u>P</u> (CH <sub>3</sub> ) <sub>2</sub> ]		

8.4 Characterising data for  $[K(C_5Me_4)CH_2PMe_2]$  (4)



**Description**

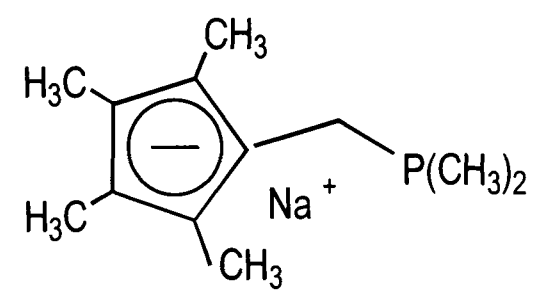
White Solid

$$C_{12}H_{20}KP = 234.36$$

Elemental Analysis	C %	H %	(very air sensitive)
Found	57.9	8.8	
Required	61.5	8.6	

$^1H$ NMR	d <sup>8</sup> -THF 500 MHz	$^{13}C\{^1H\}$ NMR	d <sup>8</sup> -THF 125.7 MHz
$\delta$ 2.44	[d, 2H, $\underline{CH_2}$ ] $^2J_{H-P} = 1.5$ Hz	$\delta$ 107.93	[s, $\underline{C_{ipso}}$ ]
$\delta$ 1.85	[s, 6H, $C_{ring}-\underline{CH_3}$ ]	$\delta$ 107.13	[s, $\underline{C_{ring}}-CH_3$ ]
$\delta$ 1.84	[s, 6H, $C_{ring}-\underline{CH_3}$ ]	$\delta$ 106.44	[s, $\underline{C_{ring}}-CH_3$ ]
$\delta$ 0.92	[d, 6H, $P(\underline{CH_3})_2$ ] $^2J_{H-P} = 2.5$ Hz	$\delta$ 31.64	[d, $\underline{CH_2}$ ] $J_{C-P} = 8.0$ Hz
		$\delta$ 15.73	[d, $P(\underline{CH_3})_2$ ] $J_{C-P} = 17.0$ Hz
$^{31}P\{^1H\}$ NMR	d <sup>8</sup> -THF 202.4 MHz	$\delta$ 12.06	[s, $C_{ring}-\underline{CH_3}$ ]
$\delta$ - 45.4	[s, $\underline{P(CH_3)_2}$ ]	$\delta$ 11.63	[s, $C_{ring}-\underline{CH_3}$ ]

8.5 Characterising data for [Na(C<sub>5</sub>Me<sub>4</sub>)CH<sub>2</sub>PMe<sub>2</sub>] (5)



**Description**  
White Solid

$C_{12}H_{20}NaP = 218.25$

Elemental Analysis	C %	H %	P %	(very air sensitive)
Found	63.1	9.2	14.3	
Required	66.0	9.2	14.2	

**<sup>1</sup>H NMR**      d<sup>5</sup>-pyridine 500 MHz

δ 2.71	[d, 2H, CH <sub>2</sub> ] <sup>2</sup> J <sub>H-P</sub> = 1.5 Hz
δ 2.22	[s, 6H, C <sub>ring</sub> -CH <sub>3</sub> ]
δ 2.17	[s, 6H, C <sub>ring</sub> -CH <sub>3</sub> ]
δ 0.86	[d, 6H, P(CH <sub>3</sub> ) <sub>2</sub> ] <sup>2</sup> J <sub>H-P</sub> = 2.5 Hz

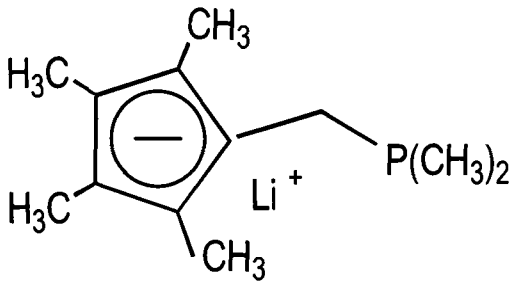
**<sup>31</sup>P{<sup>1</sup>H} NMR**      d<sup>5</sup>-pyridine 202.4 MHz

δ -46.0	[s, P(CH <sub>3</sub> ) <sub>2</sub> ]
---------	--

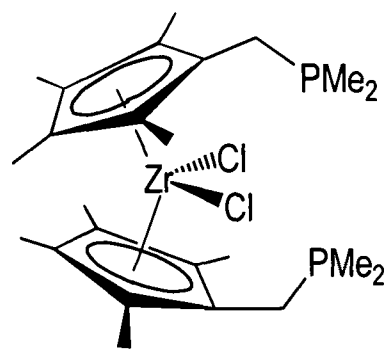
**<sup>13</sup>C{<sup>1</sup>H} NMR**      d<sup>5</sup>-pyridine 125.7 MHz

δ 105.58	[s, C <sub>ipso</sub> ]
δ 105.42	[s, C <sub>ring</sub> -CH <sub>3</sub> ]
δ 105.34	[s, C <sub>ring</sub> -CH <sub>3</sub> ]
δ 31.10	[d, CH <sub>2</sub> ] J <sub>C-P</sub> = 7.5 Hz
δ 14.40	[d, P(CH <sub>3</sub> ) <sub>2</sub> ] J <sub>C-P</sub> = 16 Hz
δ 12.40	[s, C <sub>ring</sub> -CH <sub>3</sub> ]
δ 11.96	[s, C <sub>ring</sub> -CH <sub>3</sub> ]

8.6 Characterising data for [Li(C<sub>5</sub>Me<sub>4</sub>)CH<sub>2</sub>PMe<sub>2</sub>] (6)

		<b>Description</b> White Solid  $C_{12}H_{20}LiP = 202.20$	
<b>Elemental Analysis</b>	C %	H %	P % (very air sensitive)
Found	64.8	9.3	15.0
Required	71.3	10.0	15.3
<b><sup>1</sup>H NMR</b>	d <sup>5</sup> -pyridine 500 MHz	<b><sup>13</sup>C{<sup>1</sup>H} NMR</b>	d <sup>5</sup> -pyridine 125.7 MHz
δ 2.66	[d, 2H, CH <sub>2</sub> ] <sup>2</sup> J <sub>H-P</sub> 1.5 Hz	δ 105.15	[s, C <sub>ring</sub> -CH <sub>3</sub> ]
δ 2.04	[s, 6H, C <sub>ring</sub> -CH <sub>3</sub> ]	δ 104.91	[s, C <sub>ring</sub> -CH <sub>3</sub> ]
δ 1.98	[s, 6H, C <sub>ring</sub> -CH <sub>3</sub> ]	δ 104.80	[s, C <sub>ipso</sub> ]
δ 0.73	[d, 6H, P(CH <sub>3</sub> ) <sub>2</sub> ] <sup>2</sup> J <sub>H-P</sub> 2.5 Hz	δ 29.20	[d, CH <sub>2</sub> ] J <sub>C-P</sub> = 7.76 Hz
<b><sup>31</sup>P{<sup>1</sup>H} NMR</b>	d <sup>8</sup> -THF 202.4 MHz	δ 13.37	[d, P(CH <sub>3</sub> ) <sub>2</sub> ] J <sub>C-P</sub> = 17.2 Hz
δ - 46.0	[s, P(CH <sub>3</sub> ) <sub>2</sub> ]	δ 10.87	[s, C <sub>ring</sub> -CH <sub>3</sub> ]
		δ 10.37	[s, C <sub>ring</sub> -CH <sub>3</sub> ]

8.7 Characterising data for  $[\text{Zr}\{(\eta\text{-C}_5\text{Me}_4)\text{CH}_2\text{PMe}_2\}_2\text{Cl}_2]$  (7)



**Description**  
Pale-yellow solid

$$\text{C}_{24}\text{Cl}_2\text{H}_{40}\text{P}_2\text{Zr} = 552.65$$

Elemental Analysis	C %	H %	P %	Zr %
Found	49.8	7.30	11.1	17.4
Required	52.1	7.29	11.2	16.5

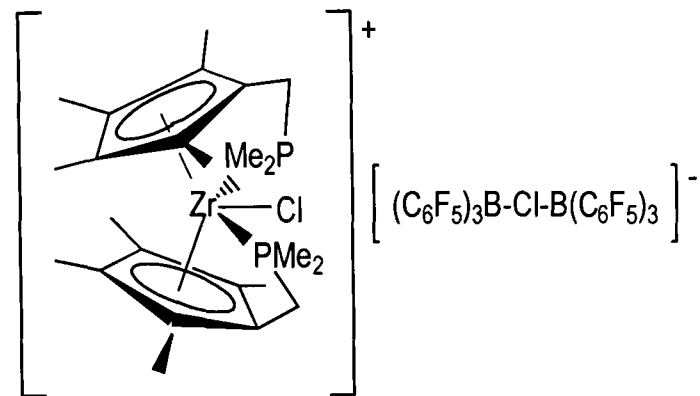
**Mass Spectrometry (FAB)**

<i>m/z</i>	547	$[\text{M}-\text{Cl} + 2\text{O}]$	50%
------------	-----	------------------------------------	-----

$^1\text{H}$ NMR	$\text{d}^5\text{-pyridine}$ 500 MHz	$^{13}\text{C}\{^1\text{H}\}$ NMR	$\text{d}^5\text{-pyridine}$ 125.7 MHz
$\delta$ 2.52	[s, 2H, $\text{CH}_2$ ]	$\delta$ 125.3	[d, $\text{C}_{\text{ipso}}$ $^2J_{\text{C-P}} = 12.9$ Hz]
$\delta$ 1.81	[s, 6H, $\text{C}_{\text{ring}}\text{-CH}_3$ ]	$\delta$ 121.9	[s, $\text{C}_{\text{ring}}\text{-CH}_3$ ]
$\delta$ 1.65	[s, 6H, $\text{C}_{\text{ring}}\text{-CH}_3$ ]	$\delta$ 121.6	[s, $\text{C}_{\text{ring}}\text{-CH}_3$ ]
$\delta$ 0.62	[s, 6H, $\text{P}(\text{CH}_3)_2$ ] <sup>*</sup>	$\delta$ 30.1	[d, $\text{CH}_2$ $J_{\text{C-P}} = 14.0$ Hz]
$^{31}\text{P}\{^1\text{H}\}$ NMR	$\text{d}^2\text{-dichloromethane}$ 500 MHz	$\delta$ 13.25	[d, $\text{P}(\text{CH}_3)_2$ $J_{\text{C-P}} = 15.0$ Hz]
$\delta$ - 44.5	[d, 6H, $\text{P}(\text{CH}_3)_2$ ] <sup>*</sup> $^2J_{\text{H-P}} = 3.0$ Hz]	$\delta$ 11.6	[d, $\text{C}_{\text{ring}}\text{-CH}_3$ $^4J_{\text{C-P}} = 4.2$ Hz]
		$\delta$ 10.5	[s, $\text{C}_{\text{ring}}\text{-CH}_3$ ]

<sup>\*</sup> Collected data again using  $\text{CD}_2\text{Cl}_2$  as the solvent to allow resolution of the doublet

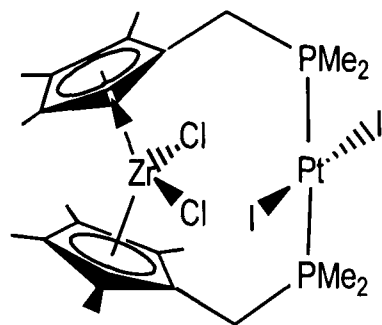
8.8 Characterising data for  $[\text{Zr}\{(\eta\text{-C}_5\text{Me}_4)\text{CH}_2\text{PMe}_2\}_2\text{Cl}]$   
 $[(\text{C}_6\text{F}_5)_3\text{BClB}(\text{C}_6\text{F}_5)_3]$  (8)



**Description**  
Pale-yellow solution in toluene  
 $B_2C_{60}Cl_2F_{30}H_{40}P_2Zr = 1576.62$

<b><math>^1\text{H}</math> NMR</b>	$d^8$ -toluene 500 MHz	<b><math>^{13}\text{C}\{^1\text{H}\}</math> NMR</b>	$d^8$ -toluene 125.7 MHz
$\delta$ 2.52	[d, 2H, $\text{CH}_2$ ] $^2J_{\text{H-P}} = 7.0$ Hz	$\delta$ 149.2	[d, $o\text{-C}_6\text{F}_5$ ] $J_{\text{C-F}} = 247$ Hz
$\delta$ 1.66	[s, 6H, $\text{C}_{\text{ring}}\text{-CH}_3$ ]	$\delta$ 140.7	[d, $p\text{-C}_6\text{F}_5$ ] $J_{\text{C-F}} = 252$ Hz
$\delta$ 1.65	[s, 6H, $\text{C}_{\text{ring}}\text{-CH}_3$ ]	$\delta$ 137.8	[d, $m\text{-C}_6\text{F}_5$ ] $J_{\text{C-F}} = 257$ Hz
$\delta$ 0.62	[d, 6H, $\text{P}(\text{CH}_3)_2$ ] $^2J_{\text{H-P}} = 10.6$ Hz	$\delta$ 124.4	[s, $\text{C}_{\text{ring}}\text{-CH}_3$ ]
<b><math>^{19}\text{F}</math> NMR</b>	$d^8$ -toluene 282.3 MHz	$\delta$ 123.4	[s, $\text{C}_{\text{ring}}\text{-CH}_3$ ]
$\delta$ - 163.0	[m, 1F, $p\text{-C}_6\text{F}_5$ ]	$\delta$ 118.0	[d, $\text{C}_{\text{ipso}}$ ] $^2J_{\text{C-P}} = 7.25$ Hz
$\delta$ - 158.0	[m, 2F, $m\text{-C}_6\text{F}_5$ ]	$\delta$ 115.4	[s, $\text{C}_{\text{ipso}}$ ]
$\delta$ - 133.0	[m, 2F, $o\text{-C}_6\text{F}_5$ ]	$\delta$ 22.4	[d, $\text{CH}_2$ ] $J_{\text{C-P}} = 31.4$ Hz
		$\delta$ 13.9	[s, $\text{C}_{\text{ring}}\text{-CH}_3$ ]
		$\delta$ 11.6	[s, $\text{C}_{\text{ring}}\text{-CH}_3$ ]
		$\delta$ 7.89	[d, $\text{P}(\text{CH}_3)_2$ ] $J_{\text{C-P}} = 36.7$ Hz
<b><math>^{31}\text{P}\{^1\text{H}\}</math> NMR</b>	$d^8$ -toluene 202.4 MHz	<b><math>^{11}\text{B}\{^1\text{H}\}</math> NMR</b>	$d^8$ -toluene 160.4 MHz
$\delta$ 8.26	[s, $\text{P}(\text{CH}_3)_2$ ]	$\delta$ - 13.0	[s, $\text{B}(\text{C}_6\text{F}_5)_3$ ]

8.9 Characterising data for  $[\text{Zr}\{(\eta\text{-C}_5\text{Me}_4)\text{CH}_2\text{PMe}_2\}_2\text{PtI}_2]$  (10)



**Description**

Yellow-Orange solid

$\text{C}_{20}\text{H}_{32}\text{Cl}_2\text{P}_2\text{ZrI}_2\text{Pt} = 1001.55$

Elemental Analysis	C %	H %
Found	28.5	4.1
Required	28.8	4.5

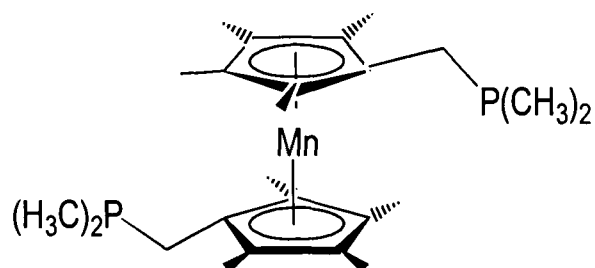
**Mass Spectrometry (FAB)**

<i>m/z</i>	747	$[\text{M} - 2\text{I}]$	50 %
------------	-----	--------------------------	------

$^{31}\text{P}\{^1\text{H}\}$  NMR     $\text{d}^8\text{-THF}$  202.4 MHz

$\delta$  - 12.0     $[\text{s}, \text{PMe}_2]$   
Pt Satellites  $J_{\text{P-Pt}} = 2304$  Hz



**8.10 Characterising data for  $[\text{Mn}\{(\eta\text{-C}_5\text{Me}_4)\text{CH}_2\text{PMe}_2\}_2]$  (11)****Description**

Orange crystalline solid

 $\text{C}_{24}\text{H}_{40}\text{MnP}_2 = 445.47$ **X-Ray crystal structure: Appendix A**

<b>Elemental Analysis</b>	<b>C %</b>	<b>H %</b>	<b>P %</b>
Found	62.8	10.4	13.6
Required	64.7	9.1	13.9

**Mass Spectrometry (FAB)**

$m/z$	445	$[\text{M}^+]$	50%
$m/z$	195	$[\text{M} - \text{C}_5\text{Me}_4\text{CH}_2\text{PMe}_2]$	100%

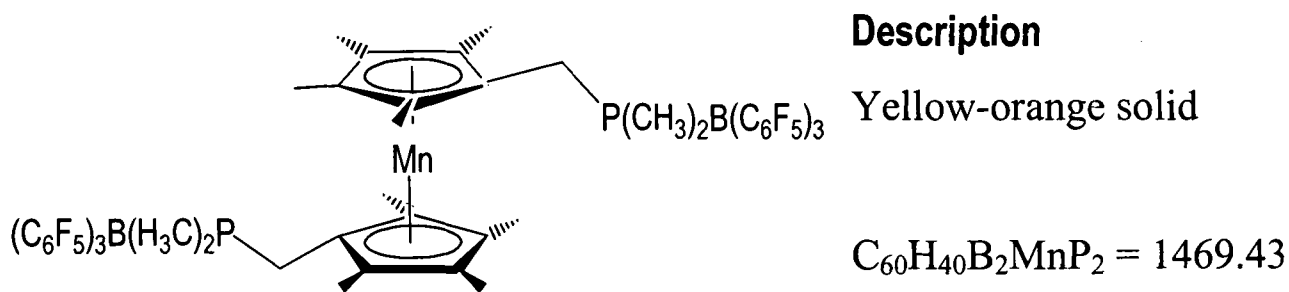
 **$^1\text{H}$  NMR**  $\text{d}^6\text{-benzene}$  500 MHz

$\delta$ 4.96	[s, 6H, $\text{P}(\text{CH}_3)_2$ ]
$\delta$ -2.51	[br.s, 6H, $\text{C}_{\text{ring}}\text{-CH}_3$ ]
$\delta$ -4.21	[br.s, 6H, $\text{C}_{\text{ring}}\text{-CH}_3$ ]
$\delta$ -11.29	[br.s, 2H, $\text{CH}_2$ ]

 **$^{31}\text{P}\{^1\text{H}\}$  NMR**  $\text{d}^8\text{-toluene}$  202.4 MHz

$\delta$ - 210.0	[s, $\text{P}(\text{CH}_3)_2$ ]
------------------	---------------------------------

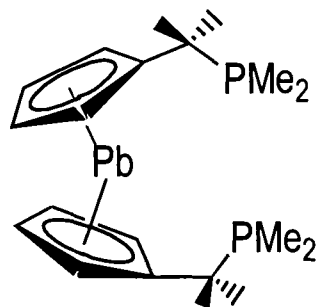
8.11 Characterising data for  $[\text{Mn}\{(\eta\text{-C}_5\text{Me}_4)\text{CH}_2\text{PMe}_2\text{B}(\text{C}_6\text{F}_5)_3\}_2]$  (12)



Elemental Analysis	C %	H %
Found	42.5	6.36
Required	42.8	6.36

Mass Spectrometry	(FAB)			
$m/z$	1469	$[\text{M}^+]$	5	%
$m/z$	957	$[\text{M}-\text{B}(\text{C}_6\text{F}_5)_3]$	10	%
$m/z$	445	$[\text{M}-2 \text{ B}(\text{C}_6\text{F}_5)_3]$	100	%

8.12 Characterising data for [Pb{(η-C<sub>5</sub>H<sub>4</sub>)CMe<sub>2</sub>PMe<sub>2</sub>}<sub>2</sub>] (15)



**Description**  
Orange crystalline solid

C<sub>20</sub>H<sub>32</sub>P<sub>2</sub>Pb = 541.62

Elemental Analysis	C %	H %
Found	43.2	6.0
Required	44.4	6.0

**<sup>1</sup>H NMR** d<sup>8</sup>-toluene 500 MHz

δ 5.73	[m, 2H, C <sub>ring</sub> H <sub>4</sub> ]
δ 5.68	[m, 2H, C <sub>ring</sub> H <sub>4</sub> ]
δ 1.22	[d, 6H, P(CH <sub>3</sub> ) <sub>2</sub> ] <sup>2</sup> J <sub>H-P</sub> = 12.0 Hz
δ 0.77	[d, 6H, C(CH <sub>3</sub> ) <sub>2</sub> ] <sup>3</sup> J <sub>H-P</sub> = 3.5 Hz

**<sup>31</sup>P{<sup>1</sup>H} NMR** d<sup>8</sup>-toluene 202.4 MHz

δ -15.6	[s, P(CH <sub>3</sub> ) <sub>2</sub> ] <sup>3</sup> J <sub>P-Pb</sub> = 276 Hz
---------	---

**<sup>207</sup>Pb{<sup>1</sup>H} NMR** d<sup>8</sup>-toluene 62.66 MHz

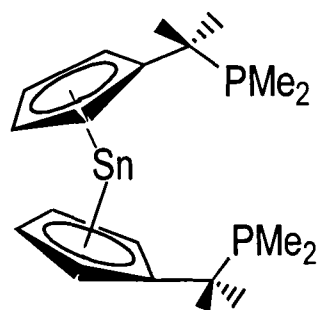
δ - 4925.2	[t, Pb] <sup>3</sup> J <sub>Pb-P</sub> = 270 Hz
------------	--

**<sup>13</sup>C{<sup>1</sup>H} NMR** d<sup>8</sup>-toluene 125.7 MHz

δ 139.5	[s, C <sub>ipso</sub> ]
δ 109.4	[d, C <sub>ring</sub> H <sub>4</sub> ] J <sub>C-Pb</sub> = 106 Hz
δ 108.8	[d, C <sub>ring</sub> H <sub>4</sub> ] J <sub>C-Pb</sub> = 82 Hz
δ 31.7	[d, C(CH <sub>3</sub> ) <sub>2</sub> ] J <sub>C-P</sub> = 16 Hz
δ 26.8	[d, P(CH <sub>3</sub> ) <sub>2</sub> ] J <sub>C-P</sub> = 13 Hz
δ 11.8	[d, C(CH <sub>3</sub> ) <sub>2</sub> ] <sup>2</sup> J <sub>C-P</sub> = 21 Hz

<sup>13</sup>C{<sup>1</sup>H} and <sup>1</sup>H NMR spectra were assigned using a <sup>1</sup>H-<sup>13</sup>C HMQC experiment

8.13 Characterising data for [Sn{(η-C<sub>5</sub>H<sub>4</sub>)CMe<sub>2</sub>PMe<sub>2</sub>}<sub>2</sub>] (16)



Description

Yellow solid

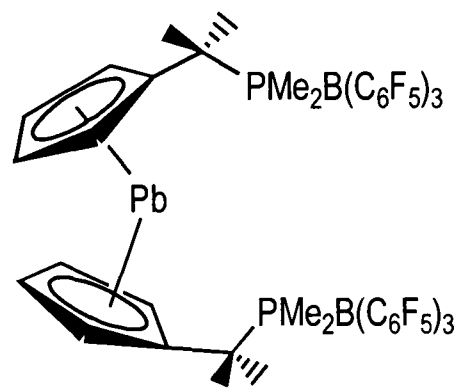
$$C_{20}H_{32}P_2Sn = 453.11$$

Elemental Analysis	C %	H %
Found	51.6	7.3
Required	53.0	7.1

<sup>1</sup> H NMR	d <sup>8</sup> -toluene 500 MHz	<sup>13</sup> C{ <sup>1</sup> H} NMR	d <sup>8</sup> -toluene 125.7 MHz
δ 5.67	[m, 2H, C <sub>ring</sub> H <sub>4</sub> ]	δ 140.0	[s, C <sub>ipso</sub> ]
δ 5.62	[m, 2H, C <sub>ring</sub> H <sub>4</sub> ]	δ 109.9	[s, C <sub>ring</sub> H <sub>4</sub> ]
δ 1.26	[d, 3H, P(CH <sub>3</sub> ) <sub>2</sub> ] <sup>2</sup> J <sub>H-P</sub> = 11.5 Hz	δ 107.9	[s, C <sub>ring</sub> H <sub>4</sub> ]
δ 0.74	[d, 6H, C(CH <sub>3</sub> ) <sub>2</sub> ] <sup>3</sup> J <sub>H-P</sub> = 3.5 Hz	δ 31.8	[d, C(CH <sub>3</sub> ) <sub>2</sub> ] J <sub>C-P</sub> = 16 Hz
<sup>31</sup> P{ <sup>1</sup> H} NMR	d <sup>8</sup> -toluene 202.4 MHz	δ 26.6	[d, P(CH <sub>3</sub> ) <sub>2</sub> ] <sup>4</sup> J <sub>C-Sn 117</sub> = 360 Hz <sup>4</sup> J <sub>C-Sn 119</sub> = 180 Hz J <sub>C-P</sub> = 13 Hz
δ -21.4	[s, P(CH <sub>3</sub> ) <sub>2</sub> ] <sup>3</sup> J <sub>P-Sn</sub> = 111 Hz	δ 10.0	[d, C(CH <sub>3</sub> ) <sub>2</sub> ] <sup>3</sup> J <sub>C-Sn 117</sub> = 471 Hz <sup>3</sup> J <sub>C-Sn 119</sub> = 230 Hz <sup>2</sup> J <sub>C-P</sub> = 21 Hz
<sup>119</sup> Sn{ <sup>1</sup> H} NMR	d <sup>8</sup> -toluene 111.9 MHz		
δ -2162.8	[t, Sn] <sup>3</sup> J <sub>Sn-P</sub> = 110 Hz		

<sup>13</sup>C{<sup>1</sup>H} and <sup>1</sup>H NMR spectra were assigned using a <sup>1</sup>H-<sup>13</sup>C HMQC experiment

8.14 Characterising data for  $[\text{Pb}\{(\eta\text{-C}_5\text{H}_4)\text{CMe}_2\text{PMe}_2\text{B}(\text{C}_6\text{F}_5)_3\}_2]$  (17)



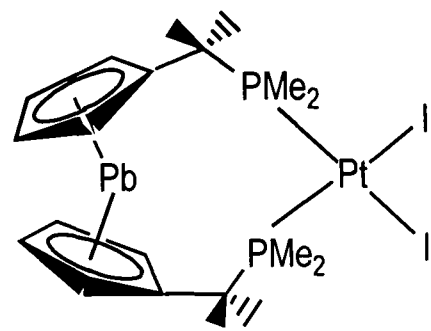
**Description**  
Yellow solid

$$\text{B}_2\text{C}_{36}\text{F}_{30}\text{H}_{32}\text{P}_2\text{Pb} = 1565.59$$

Elemental Analysis	C %	H %	P %
Found	42.5	2.6	3.43
Required	42.7	2.1	3.96

$^1\text{H}$ NMR	d <sup>5</sup> -pyridine 500 MHz	$^{13}\text{C}\{^1\text{H}\}$ NMR	d <sup>5</sup> -pyridine 125.7 MHz
$\delta$ 5.84	[m, 2H, C <sub>ring</sub> H <sub>4</sub> ]	$\delta$ 149.5	[br, C <sub>6</sub> F <sub>5</sub> ]
$\delta$ 5.82	[m, 2H, C <sub>ring</sub> H <sub>4</sub> ]	$\delta$ 147.5	[br, C <sub>6</sub> F <sub>5</sub> ]
$\delta$ 1.13	[d, 6H, P(CH <sub>3</sub> ) <sub>2</sub> ] $^2J_{\text{H-P}} = 12.0$ Hz	$\delta$ 139.4	[br, C <sub>6</sub> F <sub>5</sub> ]
$\delta$ 0.65	[d, 6H, C(CH <sub>3</sub> ) <sub>2</sub> ] $^3J_{\text{H-P}} = 3.0$ Hz	$\delta$ 116.3	[s, C <sub>ipso</sub> ]
		$\delta$ 109.5	[s, C <sub>ring</sub> H <sub>4</sub> ]
		$\delta$ 108.4	[s, C <sub>ring</sub> H <sub>4</sub> ]
$^{31}\text{P}\{^1\text{H}\}$ NMR	d <sup>5</sup> -pyridine 202.4 MHz	$\delta$ 32.12	[d, C(CH <sub>3</sub> ) <sub>2</sub> ] $J_{\text{C-P}} = 11.8$ Hz
$\delta$ -11.6	[s, P(CH <sub>3</sub> ) <sub>2</sub> ]	$\delta$ 26.82	[d, P(CH <sub>3</sub> ) <sub>2</sub> ] $J_{\text{C-P}} = 15.9$ Hz
$^{11}\text{B}\{^1\text{H}\}$ NMR	d <sup>5</sup> -pyridine 160.4 MHz	$\delta$ 10.94	[d, C(CH <sub>3</sub> ) <sub>2</sub> ] $^2J_{\text{C-P}} = 19.6$ Hz
$\delta$ 0.61	[d., (C <sub>6</sub> F <sub>5</sub> ) <sub>3</sub> B-PMe <sub>2</sub> -] $J_{\text{B-P}} = 70.5$ Hz		

8.15 Characterising data for  $[\text{Pb}\{(\eta\text{-C}_5\text{H}_4)\text{CMe}_2\text{PMe}_2\}_2\text{PtI}_2]$  (18)



**Description**

Yellow-Orange solid

$$\text{C}_{20}\text{H}_{32}\text{I}_2\text{P}_2\text{PbPt} = 990.52$$

Elemental Analysis	C %	H %	P %	Pb %
Found	25.1	3.6	6.4	19.8
Required	24.3	3.3	6.3	20.9

**Mass Spectrometry (FAB)**

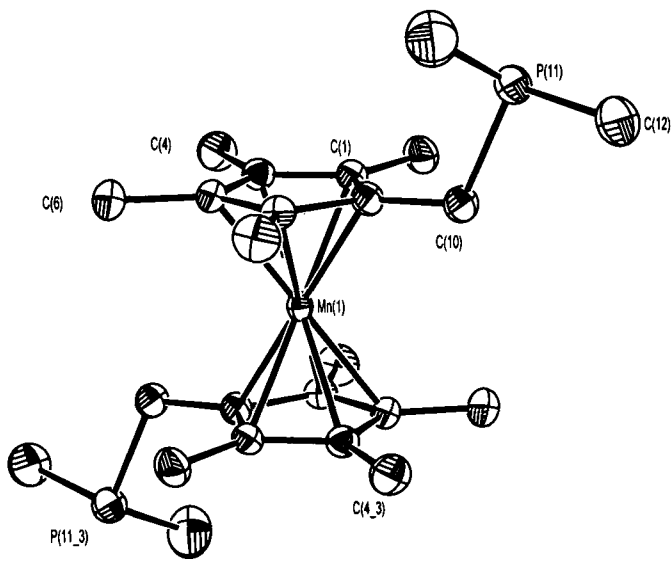
$m/z$	863	$[\text{M} - \text{I}]$	40 %
$m/z$	736	$[\text{M} - 2\text{I}]$	25 %

**$^{31}\text{P}\{^1\text{H}\}$  NMR**  $\text{d}^8\text{-THF}$  202.4 MHz

$\delta$  - 4.67       $[\text{s}, \text{PMe}_2]$   
Pt Satellites  $J_{\text{P-Pt}} = 2320$  Hz

## **Appendix A**

**A: Crystal Data and Structure Refinement for [Mn{(η-C<sub>5</sub>Me<sub>4</sub>)CH<sub>2</sub>PMe<sub>2</sub>}<sub>2</sub>] (11)**



Identification code	<b>11</b>	
Empirical formula	C <sub>24</sub> H <sub>40</sub> Mn P <sub>2</sub>	
Formula weight	445.44	
Temperature	293(2) K	
Wavelength	0.71073 Å	
Crystal system	Monoclinic	
Space group	<i>P</i> 2 <sub>1</sub> / <i>c</i>	
Unit cell dimensions	<i>a</i> = 8.6530(3) Å	<i>α</i> = 90°
	<i>b</i> = 16.2020(9) Å	<i>β</i> = 97.945(3)°
	<i>c</i> = 8.6100(5) Å	<i>γ</i> = 90°
Volume	1195.50(10) Å <sup>3</sup>	
<i>Z</i>	2	
Density (calculated)	1.237 mg/m <sup>3</sup>	
Absorption coefficient	0.693 mm <sup>-1</sup>	
<i>F</i> (000)	478	
Crystal size	0.3 x 0.3 x 0.4 mm <sup>3</sup>	
Theta range for data collection	2.38 to 26.52°	
Index ranges	0 ≤ <i>h</i> ≤ 10, 0 ≤ <i>k</i> ≤ 20, -10 ≤ <i>l</i> ≤ 10	
Reflections collected	2449	
Independent reflections	2449 [ <i>R</i> (int) = 0.0000]	
Refinement method	Full-matrix least-squares on <i>F</i> <sup>2</sup>	
Data / restraints / parameters	2449 / 0 / 131	
Goodness-of-fit on <i>F</i> <sup>2</sup>	1.355	
Final <i>R</i> indices [ <i>I</i> > 2σ( <i>I</i> )]	<i>R</i> = 0.0566, <i>R</i> <sub>w</sub> = 0.0947	
<i>R</i> indices (all data)	<i>R</i> = 0.0594, <i>R</i> <sub>w</sub> = 0.0957	
Largest diff. peak and hole	0.254 and -0.477 e.Å <sup>-3</sup>	



**Table 2** Atomic coordinates ( $\times 10^4$ ) and equivalent isotropic displacement parameters ( $\text{\AA}^2 \times 10^3$ ) for  $[\text{Mn}\{\{\eta\text{-C}_5\text{Me}_4\}\text{CH}_2\text{PMe}_2\}_2]$   $U_{\text{(eq)}}$  is defined as one third of the trace of the orthogonalized  $U^{\text{ij}}$  tensor.

	x	y	z	$U_{\text{(eq)}}$
Mn(1)	0	5000	0	17(1)
C(1)	1825(3)	5729(1)	-619(3)	22(1)
C(2)	3226(3)	5421(2)	-1282(3)	32(1)
C(3)	394(3)	5991(1)	-1506(3)	24(1)
C(4)	38(3)	6014(2)	-3249(3)	36(1)
C(5)	-619(3)	6257(2)	-440(3)	24(1)
C(6)	-2227(3)	6601(2)	-875(3)	37(1)
C(7)	175(3)	6161(1)	1106(3)	23(1)
C(8)	-474(3)	6388(2)	2573(3)	38(1)
C(9)	1694(3)	5835(1)	1004(3)	23(1)
C(10)	2955(3)	5671(2)	2344(3)	27(1)
C(12)	5474(4)	6174(2)	4537(4)	48(1)
C(13)	3334(4)	7338(2)	3219(5)	66(1)
P(11)	4467(1)	6482(1)	2616(1)	33(1)

**Table 3.** Bond lengths [Å] and angles [°] for [Mn{(η-C<sub>5</sub>Me<sub>4</sub>)CH<sub>2</sub>PMe<sub>2</sub>}<sub>2</sub>] (11)

Mn(1)-C(9)#1	2.092(2)
Mn(1)-C(9)	2.092(2)
Mn(1)-C(1)#1	2.099(2)
Mn(1)-C(1)	2.099(2)
Mn(1)-C(7)#1	2.105(2)
Mn(1)-C(7)	2.105(2)
Mn(1)-C(3)#1	2.120(2)
Mn(1)-C(3)	2.120(2)
Mn(1)-C(5)#1	2.127(2)
Mn(1)-C(5)	2.127(2)
C(1)-C(3)	1.426(3)
C(1)-C(9)	1.428(3)
C(1)-C(2)	1.495(3)
C(3)-C(5)	1.421(3)
C(3)-C(4)	1.491(3)
C(5)-C(7)	1.420(3)
C(5)-C(6)	1.497(3)
C(7)-C(9)	1.430(3)
C(7)-C(8)	1.497(3)
C(9)-C(10)	1.498(3)
C(10)-P(11)	1.846(2)
C(12)-P(11)	1.828(3)
C(13)-P(11)	1.816(4)
C(9)#1-Mn(1)-C(9)	180.000(1)
C(9)#1-Mn(1)-C(1)#1	39.86(9)
C(9)-Mn(1)-C(1)#1	140.14(9)
C(9)#1-Mn(1)-C(1)	140.14(9)
C(9)-Mn(1)-C(1)	39.86(9)
C(1)#1-Mn(1)-C(1)	180.000(1)
C(9)#1-Mn(1)-C(7)#1	39.84(9)
C(9)-Mn(1)-C(7)#1	140.16(9)
C(1)#1-Mn(1)-C(7)#1	66.57(9)
C(1)-Mn(1)-C(7)#1	113.43(9)
C(9)#1-Mn(1)-C(7)	140.16(9)
C(9)-Mn(1)-C(7)	39.84(9)
C(1)#1-Mn(1)-C(7)	113.43(9)

---

C(1)-Mn(1)-C(7)	66.57(9)
C(7)#1-Mn(1)-C(7)	180.0
C(9)#1-Mn(1)-C(3)#1	66.44(9)
C(9)-Mn(1)-C(3)#1	113.56(9)
C(1)#1-Mn(1)-C(3)#1	39.52(9)
C(1)-Mn(1)-C(3)#1	140.48(9)
C(7)#1-Mn(1)-C(3)#1	65.93(9)
C(7)-Mn(1)-C(3)#1	114.07(9)
C(9)#1-Mn(1)-C(3)	113.56(9)
C(9)-Mn(1)-C(3)	66.44(9)
C(1)#1-Mn(1)-C(3)	140.48(9)
C(1)-Mn(1)-C(3)	39.52(9)
C(7)#1-Mn(1)-C(3)	114.07(9)
C(7)-Mn(1)-C(3)	65.93(9)
C(3)#1-Mn(1)-C(3)	180.0
C(9)#1-Mn(1)-C(5)#1	66.35(9)
C(9)-Mn(1)-C(5)#1	113.65(9)
C(1)#1-Mn(1)-C(5)#1	66.16(9)
C(1)-Mn(1)-C(5)#1	113.84(9)
C(7)#1-Mn(1)-C(5)#1	39.20(9)
C(7)-Mn(1)-C(5)#1	140.80(9)
C(3)#1-Mn(1)-C(5)#1	39.09(9)
C(3)-Mn(1)-C(5)#1	140.91(9)
C(9)#1-Mn(1)-C(5)	113.65(9)
C(9)-Mn(1)-C(5)	66.35(9)
C(1)#1-Mn(1)-C(5)	113.84(9)
C(1)-Mn(1)-C(5)	66.16(9)
C(7)#1-Mn(1)-C(5)	140.80(9)
C(7)-Mn(1)-C(5)	39.20(9)
C(3)#1-Mn(1)-C(5)	140.91(9)
C(3)-Mn(1)-C(5)	39.09(9)
C(5)#1-Mn(1)-C(5)	180.0
C(3)-C(1)-C(9)	107.9(2)
C(3)-C(1)-C(2)	125.8(2)
C(9)-C(1)-C(2)	126.3(2)
C(3)-C(1)-Mn(1)	71.06(13)
C(9)-C(1)-Mn(1)	69.81(13)
C(2)-C(1)-Mn(1)	126.0(2)
C(5)-C(3)-C(1)	108.2(2)

---

C(5)-C(3)-C(4)	125.6(2)
C(1)-C(3)-C(4)	126.1(2)
C(5)-C(3)-Mn(1)	70.70(13)
C(1)-C(3)-Mn(1)	69.42(13)
C(4)-C(3)-Mn(1)	127.3(2)
C(7)-C(5)-C(3)	108.1(2)
C(7)-C(5)-C(6)	126.0(2)
C(3)-C(5)-C(6)	125.9(2)
C(7)-C(5)-Mn(1)	69.58(13)
C(3)-C(5)-Mn(1)	70.22(13)
C(6)-C(5)-Mn(1)	127.1(2)
C(5)-C(7)-C(9)	108.2(2)
C(5)-C(7)-C(8)	125.1(2)
C(9)-C(7)-C(8)	126.7(2)
C(5)-C(7)-Mn(1)	71.22(13)
C(9)-C(7)-Mn(1)	69.58(13)
C(8)-C(7)-Mn(1)	126.1(2)
C(1)-C(9)-C(7)	107.6(2)
C(1)-C(9)-C(10)	125.7(2)
C(7)-C(9)-C(10)	126.6(2)
C(1)-C(9)-Mn(1)	70.33(13)
C(7)-C(9)-Mn(1)	70.58(13)
C(10)-C(9)-Mn(1)	126.7(2)
C(9)-C(10)-P(11)	113.6(2)
C(13)-P(11)-C(12)	99.1(2)
C(13)-P(11)-C(10)	100.3(2)
C(12)-P(11)-C(10)	99.31(13)

---

Symmetry transformations used to generate equivalent atoms:

#1 -x,-y+1,-z

**Table 4** Anisotropic displacement parameters ( $\text{\AA}^2 \times 10^3$ )for **[Mn{( $\eta$ -C<sub>5</sub>Me<sub>4</sub>)CH<sub>2</sub>PMe<sub>2</sub>]<sub>2</sub> (11)**

	U <sup>11</sup>	U <sup>22</sup>	U <sup>33</sup>	U <sup>23</sup>	U <sup>13</sup>	U <sup>12</sup>
Mn(1)	16(1)	19(1)	15(1)	0(1)	1(1)	1(1)
C(1)	21(1)	23(1)	22(1)	0(1)	4(1)	-1(1)
C(2)	25(1)	35(1)	36(1)	-1(1)	9(1)	2(1)
C(3)	25(1)	24(1)	22(1)	1(1)	3(1)	-2(1)
C(4)	39(2)	44(2)	24(1)	7(1)	-1(1)	-5(1)
C(5)	22(1)	22(1)	29(1)	3(1)	3(1)	2(1)
C(6)	27(1)	35(1)	49(2)	9(1)	4(1)	6(1)
C(7)	26(1)	22(1)	23(1)	-2(1)	7(1)	0(1)
C(8)	43(2)	39(2)	33(1)	-9(1)	13(1)	2(1)
C(9)	23(1)	23(1)	23(1)	-2(1)	-1(1)	-2(1)
C(10)	29(1)	26(1)	26(1)	-1(1)	-5(1)	-3(1)
C(12)	46(2)	51(2)	41(2)	2(1)	-17(1)	-11(2)
C(13)	57(2)	35(2)	99(3)	-20(2)	-12(2)	0(2)
P(11)	31(1)	31(1)	34(1)	1(1)	-6(1)	-6(1)

